THEORETICAL STUDY ON PHASE TRANSITIONS AND CHEMICAL REACTIONS OF SELECTED MATERIALS UNDER HIGH PRESSURE

A Thesis Submitted to the College of

Graduate Studies and Research

In Partial Fulfillment of the Requirements

For The Degree of Doctor of Philosophy

In the Department of Physics and Engineering Physics

University of Saskatchewan

Saskatoon

By

Xue Yong

PERMISSION TO USE

In presenting this thesis in partial fulfilment of the requirements for a Postgraduate degree from the University of Saskatchewan, I agree that the Libraries of this University may make it freely available for inspection. I further agree that permission for copying of this thesis in any manner, in whole or in part, for scholarly purposes may be granted by the professor or professors who supervised my thesis work or, in their absence, by the Head of the Department or the Dean of the College in which my thesis work was done. It is understood that any copying or publication or use of this thesis or parts thereof for financial gain shall not be allowed without my written permission. It is also understood that due recognition shall be given to me and to the University of Saskatchewan in any scholarly use which may be made of any material in my thesis.

Requests for permission to copy or to make other use of material in this thesis in whole or part should be addressed to:

Head of the Department of Physics and Engineering Physics

116 Science Place

University of Saskatchewan

Saskatoon, Saskatchewan

Canada

S7N 5E2

ABSTRACT

The objective of this thesis is to investigate phase transitions and chemical reactions of selected materials under high pressure and high temperature using First-Principles electronic structure calculations and molecular dynamics (MD) simulations. This thesis is composed of three projects: (i) the design of new strategies for the synthesis of energetic materials based on fully extended CO_2 (X-CO_2) or CO (X-CO) solids at pressures amenable to industrial production, (ii) the investigation of novel chemical reactions of silica under Earth's mantle conditions, and (iii) the study of melting, nuclear quantum effects, and pressure-induced amorphization phenomena of ice Ih.

Extended X-CO_2 with fully sp^3 hybridized C and O atoms is a highly energetic material that can be synthesized at 41 GPa and 1800 K. The product obtained at high pressure was shown to be recoverable at ambient pressure using metadynamics. To alleviate the stringent synthetic conditions, new strategies including the addition of catalysts (H_2 and O_2) to solid CO_2 and CO and photochemical activation were proposed and investigated by performing *ab initio* molecular dynamics (AIMD) calculations. The addition of H_2 or O_2 was shown to successfully lower the formation pressure and produced different forms of polymeric X-CO_2/X-CO. The X-CO_2/X-CO obtained from H_2 activated polymerization of solid CO_2 and CO can be quench-recovered with estimated energy densities of 12.60 kJ/g and 11.50 kJ/g for CO_2+H_2 and CO+H_2, respectively. Photo-excitation was found to be the most efficient method that can lower the formation pressure for the polymerization of CO_2 solid to 15 GPa and 1200 K. The photochemical reaction produced a dense form of X-CO_2 consisting mainly of sp^3 C and O atoms with an estimated energy density of 8.63 kJ/g.

Chemical reactions between different silica with CO_2 and H_2 at high pressure and high temperature were investigated using AIMD. Crystalline and amorphous forms with the different stoichiometry SiO_2-CO_2 were found from the reactions between CO_2 with SiO_2 zeolite and stishovite. In MD calculations using the reactive force field on a large SiO_2/H_2 model system, H_2 was also found to react with quartz under moderate pressure and temperature. This chemical process produced a denser liquid water confined in the SiO_2/Si-H layers.

The structural evolution of pressure-induced amorphized (PIA) ice Ih was investigated by classical MD using the four-site TIP4P/ice water potential and AIMD calculations with non-local *van der Waals*-corrected exchange-correlation functional. The amorphization was revealed to be a multiple step process with an intermediate crystalline phase prior to amorphization. The existence of the intermediate crystalline structure is due to a shear instability. The results suggest that the PIA at low temperature is primarily governed by kinetics. An *ab initio*-based flexible and polarizable Thole-type TTM2.1-F water model was examined for the simulation of water properties with and without nuclear quantum effects (NQEs) by classical molecular dynamics and path integral molecular dynamics. The NQEs were shown to weaken the hydrogen bonds bringing the theoretical structure to a better agreement with experiment. NQEs also contributed to a decrease of 20 K in the melting temperature of ice of the TTM2.1-F water model.

ACKNOWLEDGMENTS

I would like to express my sincere gratitude to my supervisor, Professor John S. Tse, for the immeasurable amount of support and guidance he has provided. I am thankful for Professor Tse's knowledge and open-mindedness. During my Ph.D. study, Professor Tse and I had many deep discussions regarding my research. His sharp insight and serious attitude toward science have greatly influenced me and helped me to grow as a researcher. I am also very grateful for the great academic opportunities he has provided me. The workshops and conferences he sent me to attend have helped me to know more researchers and broadened my horizon. Professor Tse also supported my time in Ireland and work with our collaborators, which really helped me to complete my project. As a friend, Professor Tse gave me a lot of suggestions in daily life according to his experiences which helped me to go through good and bad days during my Ph.D. study. I am also grateful for his advice on my career and his strong reference to my new position in Singapore.

I would also like to thank Professor Niall J. English, my host at University College Dublin, for his careful guidance and full support during my stay in Ireland. He gave me great suggestions in my project related to anomalous properties of ice and water. I also owe big thanks to Dr. Christian J. Burnham and Dr. Zdenek Futera who were postdocs working with Dr. Naill J. English. I would also like to acknowledge Matt Probert (University of York) and Peter Kusalik (University of Calgary) for their suggestions on my project on water.

I would like to thank all the fellow students and postdocs, past and present, in Professor Tse's group, for the collaborations and the willingness to share their skills and interests with me. Special thanks goes to Hanyu Liu. We worked together on the CO_2 project and had the exciting results published. Other group members also helped me in many different ways, including Jacques Desmarais, Arnab Majumdar, Jianjun Yang, Niloofar Zarifi, Jianbao Zhao, Min Wu, Hui Wang,

and Yinwei Li. We had a great time together with useful discussions. Jacques Desmarais helped me parallel a path integral code and also proofread my thesis. Jianjun Yang and I were in the same office for two years, and she helped me a lot in both my work and personal life. I am also thankful to Arnab Majumdar, Adebayo Adeleke, Lindsay Goodwin, and Fred Sage who spent their weekends proofreading my thesis.

I appreciate all of my thesis committee members: Professor Alex Moewes, Professor Richard Bowles, and Professor Yansun Yao for their time, encouragement, and insightful comments. Particularly, Professor Yansun Yao who showed me how to perform meta-dynamic simulations.

I acknowledge the financial support received from the Chinese Scholarship Council.

I was so blessed to have many friends along this challenging and difficult journey, and I am glad that we had good time traveling, sharing, and growing together. They are Ning Qiao, Liu Wang, Wubing Deng, Zhibang Lv, Bing Zhang, Eileen Walliser and her husband Ed, Cam Janzen and his wife, Josie Janzen. They helped me a lot when my husband was away in Singapore. Eileen Walliser is like a host mom to me. She always invites my family to her place to have dinner with her family. We celebrated Christmas together for four times in the past five years.

The University of Saskatchewan is a special place for reasons beyond academics. It is where I met my husband, Lin Cao. Without his deep love and unhesitating support, this thesis would not have been possible. I would like to thank my son, Timothy Cao, for his unconditional love. He made all the difficult moments melt away with his smile. This thesis work demanded a lot of my time that he deserved to have. My sincerest thanks also go to my mom Xingrong Wang and my dad Xianlin Yong for their unconditional love and support. In particular, I am forever grateful to my mom who helped me care for my son since he was born and to my dad who

supported me by giving his blessing to my mom to be here with me. Last but not least, I would like to express my gratitude to my mother and father-in-law for their support.

TABLE OF CONTENTS

LIST OF TABLES

LIST OF FIGURES

LIST OF SCHEMES

LIST OF ABBREVIATIONS

3D	Three-Dimensional
AIMD	*ab initio* Molecular Dynamics
BO	Born-Oppenheimer Approximation
BZ	Brillouin Zone
CMD	Centroid Molecular Dynamics
D	Diffusion Coefficient
DFT	Density Functional Theory
GGA	Generalized Gradient Approximation
HK	Hohenberg-Kohn
KS	Kohn-Sham
LDA	Local-Density Approximation
MD	Molecular Dynamics
MBPT	Many-Body Perturbation Theory
MSD	Mean Square Displacement
NPT	Constant-Pressure and Constant Temperature
NQE	Nuclear Quantum Effect
NVT	Constant Volume and Constant-Temperature
PAW	Projector Augmented Wave
PBE	Perdew-Burke-Ernzerhof
PBC	Periodic Boundary Conditions
PES	Potential Energy Surface
PIMD	Path Integral Molecular Dynamics
QP	Quasiparticle
RDF	Radial Distribution Function
vdW	*van der Waals*
VACF	Velocity Autocorrelation Function
VASP	Vienna *ab-initio* Simulation Package
XC	Exchange-Correlation

CHAPTER 1

INTRODUCTION

Pressure-induced phase transitions and chemical reactions of a material, due to its importance, has attracted many investigators in geophysics and geochemistry, as well as in materials science. High pressure and temperature provide large compression energy ($P\Delta V$) and thermal ($T\Delta S$) energies, which can break intermolecular or intramolecular interactions in most stable materials. Therefore, under extreme conditions, most ambient-pressure liquid and solid materials become unstable and transform into new phases with higher densities. Many new structures that were not observed in the past under normal conditions have now been discovered at extreme conditions by both experiment and theory. These new structures are often novel and possess unusual properties, such as optical nonlinearity, low compressibility, and high energy density. Hence, high pressure methods have been developed as new tools for the synthesis of advanced materials of technological interest. For example, a large number of novel highly energetic materials have been obtained under extreme conditions [1,2]. In addition, many unique phenomena have emerged under high pressure and temperature. For example, crystalline ice Ih was found to transform into amorphous phases under mild compression [3]. Some chemical compounds, which do not react with each other at ambient pressure, start to react and form new compounds at high pressure. For example, different -Si-O-C- based compounds were recently discovered from reactions between SiO_2 and CO_2 under extreme conditions [4,5]. These discoveries challenge the conventional concepts in chemistry on the formation and stability of chemical bonds, how the atoms and molecules re-organize at short and long-range, and how kinetics and thermodynamics govern material stability.

High pressure research, however, still presents some challenges. In experiments, high pressure and high temperature conditions, are often mimicked by laser-heated Diamond Anvil Cell (DAC) which can generate static pressures up to 640 GPa [6,7] and temperatures up to 7000 K [8]. However, it is not often easy to reach and control the temperature and pressure in a DAC. On the other hand, adjusting the pressure in a computer simulation can be easily accomplished by just varying the size of the unit cell. With the rapid development of computer hardware and accurate electronic structure software, computer simulations are becoming more reliable and highly efficient. As a result, high pressure research can benefit substantially from computer simulations. In addition, computer simulations can explore regions of the phase diagram that are not directly accessible by experiments.

In principle, most properties of the liquid or solid materials can be understood by examining their structures and the nature of chemical bonding. Since all materials are composed of atomic nuclei and electrons, we only need to study the motions of both nuclei and electrons that govern the structures and bonding. Accordingly, theories that are required for computer simulations of liquid and solid materials can be divided into two main areas: *i.e.* those concerning mainly the electronic structures and those relating to the nuclear motions.

The focus of this thesis is to study phase transitions and chemical reactions of selected solids and liquids subject to high pressure and high temperature. There are three main objectives: (i) the exploration and design of new energetically dense materials based on high-pressure-induced chemical reactions, (ii) the study of the potential reaction between silica with common gas under deep Earth mantle conditions, and (iii) the study of the anomalous properties of ice and water. First-principles calculations were used in the first project. In the second and third projects, both ab inito molecular dynamics (AIMD) and empirical molecular dynamics (MD) were used due to the

larger system sizes. In addition, path integral molecular dynamics (PIMD) was performed using a centroid molecular dynamics (CMD) code, parallelized in this thesis using the open source Open MPI. This chapter presents the background of all the theories used in this study.

1.1 Schrödinger equation and Born-Oppenheimer approximation

The classical motions of macroscopic particles obey the laws of Newtonian mechanics. Therefore, once the initial conditions (positions) and momenta are defined, we can precisely predict the dynamical evolution. However, for a microscopic (quantum) system, based on the Heisenberg uncertainty principle, we cannot determine the exact position and velocity of a particle simultaneously. Hence, classical mechanics cannot predict the evolution of the electron. A new form of mechanics called quantum mechanicals has been introduced to explain and predict the behaviour of microscopic particles, for example, the poly-atomic nature of materials. In quantum mechanics, a wave function Ψ, which is a function of the particles' coordinates, is used to describe the state of a system. The motion of a poly-atomic system composed of N electrons and M nuclei is described by the many-body Schrödinger Equation, (1.1), which was proposed in 1926 by the Austrian physicist Erwin Schrödinger:

$$H\Psi(\vec{r}_1,\vec{r}_2,\cdots\vec{r}_N,\vec{R}_1,\vec{R}_2,\cdots\vec{R}_M) = E\,\Psi(\vec{r}_1,\vec{r}_2,\cdots\vec{r}_N,\vec{R}_1,\vec{R}_2,\cdots\vec{R}_M)\,, \qquad 1.1$$

where r_i are the Cartesian coordinates of the *i*th electron and R_i is the coordinate of the *i*th nucleus. The Hamiltonian operator is expressed as:

$$H = -\sum_{i=1}^{N}\frac{1}{2}\nabla_i^2 + \frac{1}{2}\sum_{i\neq i'}V(\vec{r}_i-\vec{r}_{i'}) - \sum_{j}^{M}\frac{1}{2M_j}\nabla_j^2 + \frac{1}{2}\sum_{j\neq j'}V(\vec{R}_j-\vec{R}_{j'}) + \sum_{i,j}V(\vec{r}_i-\vec{R}_j)\,. \qquad 1.2$$

This equation is expressed in atomic units (*a.u.*) (Hartree is the unit of the energy and $\hbar = 1$, $e = 1$, and $m_e = 1$). The first two terms in Eq. (1.2) correspond to the kinetic energy and Coulomb interaction potential of the electrons, respectively. The third and fourth terms are the kinetic energy

and Coulomb interaction potential of the nuclei. The fifth term represents the Coulomb interaction between the electrons and nuclei.

In principle, all properties of a system can be obtained from the solution of the many-body Schrödinger equation. In practice, a full quantum mechanical treatment is only solvable for the simplest systems, such as the H atom. In liquids or crystals, the total number of electrons and nuclei is on the order of 10^{23}. As one particle moves, the other particles will feel its Coulomb potential and experience a force and therefore have to move in order to maintain equilibrium in the structure. Hence, in a poly-atomic system, the motions of all the particles are correlated. Such correlations increase exponentially with the degrees of freedom of the system. To study such systems, the motions of the electrons are separated from that of the nuclei following the Born-Oppenheimer (BO) approximation which was introduced by Born and J.R. Oppenheimer in 1927 [9]. The BO approximation is also known as the "adiabatic approximation" in describing electronic structures. This approximation makes use of the fact that the mass of the electrons is less than that of the nuclei and their velocities are consequently much larger that of the nuclei. Using this concept, the movement of the electrons and nuclei can be decoupled. For a given arrangement of the nuclei, we can then describe the electronic structure separately and allow the electrons to relax to optimal eigenstates before the nuclei move to the next configuration. Mathematically, the Schrödinger Eq. (1.1) becomes:

$$H_e \Psi(\vec{r}_1, \vec{r}_2, \cdots \vec{r}_N) = E \Psi(\vec{r}_1, \vec{r}_2, \cdots \vec{r}_N), \tag{1.3}$$

and the Hamiltonian is

$$H_e = -\sum_{i=1}^{N} \frac{1}{2} \nabla_i^2 + \frac{1}{2} \sum_{i \neq i'} V(\vec{r}_i - \vec{r}_{i'}) + \sum_{i,j} V_{ext}(\vec{r}_i - \vec{R}_j). \tag{1.4}$$

With the BO approximation, the kinetic energy of the nuclear Coulomb potential can be considered as constant for a given nuclear configuration. The electrons can be considered as moving in an external potential (V_{ext}) due to Coulomb interactions between the electrons and the

nuclei. This simplified Hamiltonian depends only parametrically on the coordinates of the nuclei. The total energy of a poly-atomic system at a given spatial configuration is the sum of the total energy of the electronic many-body system as described in Eq. (1.3) and the classical inter-nuclei Coulomb repulsion:

$$E_{total} = E_e + E_{ion} . \quad 1.5$$

In other words, the total energy is a function of the nuclear geometry, and it has discrete eigenvalues corresponding to different electronic quantum mechanical states.

The lowest energy state is known as the ground state, and the higher energy states are known as excited states. The relationship of the total energy as a function of geometrical parameters is called a potential energy surface (PES). With a small variation in the nuclei's geometry, the total energy also changes. By continuous and gradual changes in the geometrical parameters, we trace the profile of the PES. At finite temperatures, the nuclei fluctuate about minima on the PES. The purpose of the dynamic simulation is to reproduce such patterns of fluctuations. The concepts of the BO approximation and the PES have enabled us to separate the tasks into: i) electronic structure calculations and ii) the motions of the nuclei. All the calculations in this thesis were performed within the BO approximation.

1.2 Electronic structure theory

For a static spatial arrangement of the nuclei in condensed matter, we need to solve Eq. (1.3) to obtain the wave functions and then compute the material properties. However, the solution to the many-body Eq. (1.3) is difficult to obtain. Besides the BO approximation, further approximations are needed. Density Functional Theory (DFT), which uses the electron density of the system as the basic variable, transforms the problem into an independent particle problem.

Furthermore, the periodic boundary conditions based on Bloch's theorem reduce the treatment of a large number of electrons in crystalline solids to that of the primitive cell. For liquids or disordered solids without periodicity, large supercells are often used to mimic the system. Pseudopotential methods or an all-electron projector-augmented potential replaces the strong nuclear potential, the core contribution to the Hartree and exchange-correlation potential into an ionic potential. Plane wave basis sets are used to represent the electronic orbitals with simple and adjustable mathematical functions.

1.2.1 Density functional theory

In DFT, the total electronic energy of a system is only a functional of the electron density. The application of DFT in electronic structure calculations has achieved great success in atoms, molecules and condensed matter since the 1980s. The concept of DFT originated from the Thomas-Fermi theory in 1927, which formulated the equation of the total energy of a many-electron system into a density-based expression [10-12]. But not until the 1960s was DFT formalized and proven by Kohn and Hohenberg [13,14].

Kohn-Sham formulation of DFT

In 1964, Hohenberg and Kohn introduced two theorems [13] which formally justified the use of electron density as the primary variable in calculating the total energy of an interacting, many-electron system. The first Hohenberg-Kohn (HK) theorem states that there is a one-to-one correspondence between the external potential $V_{ext}(r)$ and the ground state density $n(r)$. A universal functional of the total energy as a function of density must exist. The second HK theorem proves that the exact ground state density minimizes this functional and the corresponding energy is the

exact ground state energy. Unfortunately, the exact form of the energy functional for a many-body system is still unknown. In 1965, Kohn and Sham [14] proposed a practical scheme to calculate the total energy. This approach provided the basic recipe for DFT. They proposed to use a model of *non-interacting* electrons moving in an effective local potential to reproduce the *interacting* electrons in the external potential. Note that, in these two models, the electron densities at the electron coordinates need to be identical.

Based on the first HK theorem, the electrons' total energy can be written as:

$$E_e[n(\vec{r})] = \int V_{ext}(\vec{r}) \cdot n(\vec{r}) \cdot d\vec{r} + F[n], \tag{1.6}$$

where the functional F[n] is the sum of the potential energies of the electronic interactions and the electronic kinetic energy. However, the exact form of F[n] is unknown. Since it is easy to separate the contribution of the electronic Coulomb interaction from the total electronic interactions, F[n] can be further decomposed into:

$$F[n] = \frac{1}{2} \iint \frac{n(\vec{r}) \cdot n(\vec{r}')}{|\vec{r} - \vec{r}'|} d(\vec{r}) d(\vec{r}') + G[n], \tag{1.7}$$

where G[n] is an unknown functional that contains the kinetic energy term T[n] and other electronic interaction terms, known as exchange-correlation (XC) term $E_{xc}[n]$:

$$G[n] = T[n] + E_{xc}[n]. \tag{1.8}$$

The ground state total energy is obtained by minimizing $E_e[n]$ under the constraint of particle conservation through:

$$\int_V n(\vec{r}) d\vec{r} = N, \tag{1.9}$$

and according to the Variational Theorem

$$\int \delta n(\vec{r}) \left\{ V_{ext}(\vec{r}) + \int_V \frac{n(\vec{r}')}{|\vec{r} - \vec{r}'|} + \frac{\delta E_{xc}[n]}{\delta n(\vec{r})} + \frac{\delta T[n]}{\delta n(\vec{r})} - \mu \right\} d\vec{r} = 0. \tag{1.10}$$

Here, N is the number of electrons and μ is the chemical potential of a uniform gas of density n. The XC potential (V_{xc}) is derived from the E_{xc} term in Eq. (1.10):

$$V_{xc}(\vec{r}) = \frac{\delta E_{xc}[n]}{\delta n(\vec{r})}. \qquad 1.11$$

Since the kinetic energy functional T[n] in Eq. (1.10) is unknown, one needs to find an alternative way to solve Eq. (1.10). One way is to make use of the approximation that the many-body wave function is simply a product of the one-electron wave functions. The kinetic energy term can then be represented when computed with the electronic wave functions. The electron density of N non-interacting electrons can be written as:

$$n(\vec{r}) = \sum_{i=1}^{N} \left|\varphi_i(\vec{r})\right|^2 , \qquad 1.12$$

where $\varphi_i(\vec{r})$ is the *i*th electron wave function in the *non-interacting* system. Each $\varphi_i(\vec{r})$ obeys the one-particle Schrödinger equation:

$$\left\{-\frac{1}{2}\nabla^2 + V_{ext}(\vec{r})\right\}\varphi_i(\vec{r}) = \varepsilon_i\varphi_i(\vec{r}). \qquad 1.13$$

Eq. (1.13) was generalized to the case of *interacting* electrons by Kohn-Sham (KS). The external potential, the electronic Coulomb potential and the XC potential are the effective potential V_{eff}:

$$V_{eff}(\vec{r}) = V_{ext}(\vec{r}) + \int_V \frac{n(\vec{r}')}{\left|\vec{r} - \vec{r}'\right|} + V_{xc}(\vec{r}). \qquad 1.14$$

Each electron in the *interacting* electronic system satisfies the one-electron Schrödinger equation:

$$\left\{-\frac{1}{2}\nabla^2 + V_{eff}(\vec{r})\right\}\varphi_i(\vec{r}) = \varepsilon_i\varphi_i(\vec{r}). \qquad 1.15$$

Eq. (1.15) is known as the Kohn-Sham (KS) equation. V_{eff} depends only on the density, Eq. (1.14), Eq. (1.12), and Eq. (1.15) can only be solved self-consistently. After convergence, the eigenstates and eigenvalues obtained are referred to as the KS orbitals and KS energies, respectively. The ground-state electron density can then be calculated with KS orbitals via Eq. (1.12). The total energy in KS scheme is then a sum of the kinetic energy, exchange-correlation energy, Hartree energy and energy due to the potential of the nuclei. The total energy is given as:

$$E_e[n(\vec{r})] = \sum_{occ} \varepsilon_i - \frac{1}{2}\iint \frac{n(\vec{r})n(\vec{r}')}{|\vec{r}-\vec{r}'|} d\vec{r}d\vec{r}' + E_{xc}[n(\vec{r})] - \int n(r)\, V_{xc}(\vec{r}) d\vec{r}\,. \quad 1.16$$

Another equivalent form of the total energy is given by:

$$E_e[n(\vec{r})] = \sum_{occ} \int dr \varphi_i^*(\vec{r})(-\frac{1}{2}\nabla^2)\varphi_i(\vec{r}) + \int n(\vec{r})\, V_{ext}(\vec{r})\, d\vec{r} + \frac{1}{2}\iint \frac{n(\vec{r})n(\vec{r}')}{|\vec{r}-\vec{r}'|} d\vec{r}d\vec{r}' + E_{xc}[n(\vec{r})] \quad . \quad 1.17$$

Functional forms of exchange correlations

The KS DFT provides a practical scheme for finding the ground-state energy of a many-body system by mapping the *interacting* electron problem to a *non-interacting* single-particle problem. In this scheme, electronic interaction, except the electron Coulomb interaction, as well as the difference in kinetic energy of the *interacting* and *non-interacting* electrons are collected into the XC-energy, $E_{xc}[n]$. However, the true form of the XC functional is unknown. To actually use the KS DFT for practical problems, useful approximations have been introduced for the XC functional $E_{xc}[n]$. The simplest, commonly used approximation is the local-density approximation (LDA). The concept of LDA comes from the fact that the electron density is constant at all points in space for a uniform electron gas. The XC potential at each point in the *non-uniform* real system is set to be the known exchange-correlation potential from the *uniform* electron gas at the electron density observed at the same point:

$$V_{xc}(\vec{r}) = V_{xc}^{uniform}[n(\vec{r})]\,. \quad 1.18$$

Therefore, the XC functional can be written as:

$$E_{xc}^{LDA}[n] = \int n(\vec{r})\varepsilon_{xc}[n(\vec{r})] d\vec{r}\,, \quad 1.19$$

with

$$\varepsilon_{xc}[n(\vec{r})] = \varepsilon_{xc}^{uniform}[n(\vec{r})]\,. \quad 1.20$$

ε_{xc} can be divided into two parts, the exchange ε_x and correlation ε_c energies. The exchange contribution to ε_x was calculated analytically [15] as:

$$\varepsilon_x = -\frac{3}{4}\left(\frac{3n}{\pi}\right)^{1/3}. \qquad 1.21$$

The correlation term ε_c is calculated numerically with Quantum Monte-Carlo calculations for the homogeneous electron gas at a variety of electron densities [16]. The application of LDA is often limited to systems with slowly varying densities since its derivation was based on the uniform electron gases model. Therefore, if there are rapid changes in the electron density in a many-body system, LDA will not be suitable. One such case is covalently bonded solids. To improve the local density approximation, another form of exchanged-correlation functional called the Generalized Gradient Approximation (GGA) has been developed [17,18]. The GGA functionals include the dependency of spatial variation in the density. Therefore, GGA functional considers both the local density and the gradient of the electron density. The general GGA exchange-correlation functional is written as:

$$E_{xc}^{GGA}[n] = \int_v \varepsilon_{xc}[n] F_{xc}[n, \vec{\nabla} n]\, n(\vec{r})\, d\vec{r}. \qquad 1.22$$

F_{xc}, which is known as the enhancement factor, modifies the energy density by including the exchange (F_x) and correlation (E_c) terms. F_x is a function of the reduced density which is represented by:

$$s(r) = \frac{\left|\vec{\nabla} n(\vec{r})\right|}{2k_f\, n(\vec{r})}. \qquad 1.23$$

Here, the k_f is the Fermi wave vector. The correlation term is given as:

$$E_c = \int n(\vec{r}) \left\{ \varepsilon_c^{uniform}[n] + H(r_s, t, \varsigma) \right\} d\vec{r}, \qquad 1.24$$

where $\varepsilon_c^{uniform}[n]$ is the correlation energy of the homogeneous gas, $H(t,r_s,\zeta)$ is the correction term, the r_s is the Seitz radius and is independent of F_x, and t is the dimensionless gradient term defined as:

$$t = \frac{\left|\vec{\nabla} n(\vec{r})\right|}{2 g k_s n(\vec{r})}, \tag{1.25}$$

$$g = \frac{[(1+\varsigma)^{2/3} + (1-\varsigma)^{2/3}]}{2}, \tag{1.26}$$

k_s is dependent on k_f with $k_s = (4k_f / \pi)^{1/2}$ and ζ is the degree of spin polarization.

Since then, there have been several improvements and the GGA has taken different forms. The most successful XC functional for electronic structure calculations is the Perdew–Burke–Ernzerh (PBE) [19] functional. For the PBE functional, the relevant expressions are

$$F_x^{PBE} = 1 + \kappa - \frac{\kappa}{1 + \mu s^2 / \kappa}, \tag{1.27}$$

and

$$E_c^{PBE} = \int n(\vec{r}) \cdot \left\{ \varepsilon_c^{uniform}[n] + H(t, r_s, \varsigma) \right\} d\vec{r}\,. \tag{1.28}$$

From fitting Eq. (1.27) to a set of test structures, the empirical parameters obtained are $\mu \sim 0.2195$ and $\kappa \sim 0.804$. In the exchange energy (Eq. (1.28)), the correction term $H(t,r_s,\zeta)$ is written as:

$$H(t, r_s, \varsigma) = \gamma g^3 \log\left(1 + \frac{\gamma}{\beta} t^2 \frac{1 + At^2}{1 + At^2 + A^2 t^4}\right). \tag{1.29}$$

Again from fitting $\beta \sim 0.0667$, $\gamma \sim 0.031$ and

$$A = \frac{\beta}{\gamma}\left[\exp\left(\frac{-1\varepsilon_c(r_s, \varsigma)}{r g^3}\right) - 1\right]^{-1}. \tag{1.30}$$

The implementation of PBE has been demonstrated to be highly successful in solid state calculations involving elements, such as Si, C, O, *etc*. [20]. The PBE functional has been able to reproduce most of the geometrical parameters and total energy. For example,the PBE functional was favoured to reproduce correctly the energy difference between α-quartz and stishovite [21].

***van der Waals* corrected functionals**

One of the problems with the conventional DFT functionals is that they are unable to describe correctly the dispersive interactions resulting from dynamical correlations between fluctuating charge distributions. Such dispersive interactions, however, play an important role in determining the structure and properties of molecular crystals and biomolecules. In particular, they typically dominate in regions where little or no overlap of electron density occurs. To tackle this problem, *van der Waals* (*vdW*) corrected DFT functionals were developed. There are several methods of including the *vdW* correction in DFT [22], but in this study we only considered two types of correction: Grimme's [23] *local* and Dion's [24] *non-local vdW* correction. These two methods are referred to as "DFT-DT" and "*vdW*-DF", respectively.

The leading term in the *vdW* interaction is the dipole-induced dipole interaction described by the $-1/r^6$ decay of the interaction energy. Grimme proposed to add an additional energy term which accounted for the missing long range *vdW* interaction to the total energy. Thus the new total energy is denoted as:

$$E_{tot} = E_{DFT} + E_{disp}, \tag{1.31}$$

where E_{DFT} is the total energy calculated with a given XC functional. The pairwise additive dispersive energy E_{disp} is calculated according to:

$$E_{disp} = -\sum_{A,B} C_6^{AB} / r_{AB}^6, \tag{1.32}$$

where the C_6^{AB} is the dispersion coefficient determined by the elemental pair A and B. The dispersion coefficients are pre-calculated and tabulated. This method, known as DFT-D2 is widely used due to its simplicity and low computational cost. The main shortcoming of this method is the neglect of many-body dispersion effects and faster decaying terms such as C_8/r^8 or C_{10}/r^{10} interactions. Attempts have been made by including the faster decaying terms or correction to the

C_6 term [25,26], for example DFT-D3 [25] and DFT-D3 with Becke-Jonson [27]. Furthermore, Grimme's method relies on the reliability of the predetermined dispersive coefficients, which severely limits its accuracy. Dion *et al*. [24] introduced a non-empirical *vdW* corrected functional by including the *non-local* correlations to the local or seminal-local correlation functional. Therefore, the exchange-correlation energy becomes:

$$E_{xc} = E_x^{GGA} + E_c^{LDA} + E_c^{nl}. \quad 1.33$$

This non-local energy E_c^{nl} functional has the form:

$$E_c^{nl} = \frac{1}{2}\int\int n(\vec{r}_1)\varphi(\vec{r}_1,\vec{r}_2)\,n(\vec{r}_2)\,dr_1 dr_2 . \quad 1.34$$

$\varphi(\vec{r}_1,\vec{r}_2) = \varphi(n(\vec{r}_1), n(\vec{r}_2)), |\nabla n(\vec{r}_1)|, |\nabla n(\vec{r}_2)|, |\vec{r} - \vec{r}_2|)$ is similar to the classical Coulomb integration kernel. The *vdW* corrected XC functionals were used only in the study of water and ice; the *non-local vdw*-DF shows greater improvements in yielding the structure and properties of water and ice than the local DFT-D2/3 methods over the PBE functional. Similar trends have been reported previously [28].

The periodic boundary conditions

Although KS DFT transformed the interacting many-body problem into a *non-interacting* single-particle problem, to solve the Schrödinger equation of a solid or other condensed matter is still a challenge due to the very large number of *non-interacting* electrons (on order of Avogadro's number 6.022×10^{23}). Fortunately, crystalline solids possess periodicity since they are composed of repeating unique unit cells. Therefore, both the V_{eff} and electron have translational symmetry. This leads to the introduction of periodic boundary conditions (PBC) based on Bloch's Theorem [29], which states that the total wave function ψ can be represented as the wave function in a unit cell modulated with a periodic function. This wave is called the Bloch wave and can be written as:

$$\psi_i(\vec{k},\vec{r}) = e^{i\vec{k}\cdot\vec{r}} \cdot u_i(\vec{k},\vec{r}), \quad 1.35$$

where $\vec{r}$ is the position, $\vec{k}$ corresponds to a crystal wave vector in the first Brillouin Zone (BZ), $e^{i\vec{k}\cdot\vec{r}}$ is the phase of the wave, and *u* is a function with the same periodicity as the crystal such that $u_i(\vec{k},\vec{r}) = u_i(\vec{k},\vec{r}+\vec{R})$ for all lattice vectors $\vec{R}$. Thus, the translational invariance in wave function is represented as:

$$\psi_i(\vec{k},\vec{r}+\vec{R}) = e^{i\vec{k}\cdot\vec{r}} \cdot \psi_i(\vec{k},\vec{r}). \quad 1.36$$

Substituting Eq. (1.36) into KS equation, Eq. (1.15), the solutions form a new set of eigenequations, each for a given $\vec{k}$. Each $\vec{k}$ describes an electronic state of a wave. Therefore, instead of dealing with a large number of electrons in the extended system, one can solve the problem for a finite number of electronic bands at chosen k-points restricted to a single unit cell. In other words, the use of PBC enables the calculation of the electronic structure of a solid confined to the unit cell or conversely, reciprocal space in the first BZ. In practice, only a finite number of *k*-points are sufficient to give the correct ground state. This is because, for a dense *k*-point set, small variations in the *k*-points make little difference in the electronic wave functions between the interval of those points. One can use the electronic wave function at one *k*-point to represent the wave functions over a small region in the reciprocal space. Hence, the integration of the wave functions can be replaced by a summation over a collection of *k*-points. Observables, such as density, are calculated as integrals over all *k*-points within the first BZ. Hence, *k*-point sampling is an integral part of the calculation. Several efficient schemes have been developed for *k*-point sampling. The main idea is to represent integrals over the first BZ by the weighted summation over special *k*-points on a *k*-points mesh:

$$\frac{\Omega}{(2\pi)^3}\int_{BZ} d\vec{k} f(\vec{k}) \sim \sum_i f(\vec{k}_i)\omega_i . \quad 1.37$$

where Ω is the volume of the first BZ and ω_i is the weight factor of the *k*-point. The most commonly used scheme was proposed by Monkhorst and Pack in 1976 [30] and is known as MP mesh. The idea is simple: The MP mesh is simply generating equally spaced *k*-points in the first BZ but takes advantage of the space group symmetries of the lattice in the irreducible wedge of the first BZ. *k*-points in the first BZ are then selected according to their point group symmetry, which in turn determines the weight ω_i. Therefore, a few *k*-points allows a sufficiently accurate sampling and reduces the computational cost. One must be aware that in order to reduce the computational error one must use a dense *k*-points mesh.

Plane wave basis set

As has been shown above, with a proper exchange-correlation term and employing PBC it is feasible to solve the many-body KS equation for liquid or solid materials. The next step is to find a proper basis set to represent the KS orbitals. There are several possible choices of basis sets [31-33], each with its own advantages and disadvantages. For a system with periodic boundary conditions where the reciprocal space representation is more efficient, a plane wave (PW) basis set is a natural choice. Plane waves are exact eigenfunctions of the homogenous electron gas. A PW basis set is independent of the atom type or positions. The PW basis set is also easy to transform from real to reciprocal space through fast Fourier transform (FFT). It forms a complete basis set of simple mathematical functions. The completeness of the basis set can be controlled easily by adjusting only one parameter: the kinetic energy cut-off, E_{cut}.

Using the PW basis set, the single particle KS orbital $\psi_i(\vec{k},\vec{r})$ in Eq. (1.35) can be expanded as:

$$\psi_i(\vec{k},\vec{r}) = \sum_{\vec{G}} c_{i,\vec{G}+\vec{k}}(\vec{k}) \frac{1}{\sqrt{V}} e^{i(\vec{k}+\vec{G})\cdot\vec{r}}\ , \qquad 1.38$$

where $\vec{G}$ is the reciprocal lattice vector and $c_{i,\vec{k}+\vec{G}}$ is the coefficient of the PW basis set. The sum is the overall wave vectors (spatial frequencies) with the correct periodicity. Each wave vector represents a point in the reciprocal-space, and each Fourier basis function $e^{i\vec{G}\cdot\vec{r}}$ is a plane wave propagating in that space. In principle, an infinite number of plane waves are needed for the expansion. However, with $\left|\vec{G}\right|^2$ becoming larger, $c_{i,\vec{k}+\vec{G}}$ becomes smaller. Thus, only PWs with kinetic energies less than $\left|\vec{k}+\vec{G}\right|^2$ are more important. In practice, the PW basis set is truncated to include only PWs that have kinetic energies smaller than E_{cut}:

$$E_{cut} = \frac{1}{2}\left|\vec{k}+\vec{G}\right|^2 . \qquad 1.39$$

The pseudopotential approximation

Solving the many-body KS DFT equation for condensed matter relies on the use of the proper exchange-correlation term, PBC, and PWs basis sets. In the practical numerical implementation of the KS scheme of a real system, one has to deal with two distinct regimes: the core and the valences regions. The core states present difficulties in using the PWs basis sets to represent the orbitals. However, the core electrons are tightly bound to the nucleus and rarely affected by the chemical environment. Therefore, core electron wavefunctions are atomic in character and therefore highly localized and the expansion for such localized wavefunctions in the core region requires a large number of plane waves. In contrast, the valence states oscillate rapidly in the core region due to the orthogonality with the core electrons. These rapid oscillations result in a large kinetic energy and require more PW component in expanding the oscillatory wave functions. Since the physical properties of most matter depend more on the valence electrons, the

concept of a pseudopotential was introduced. The idea of a pseudopotential is to replace the strong Coulomb potential acting on the core electrons by an effective pseudopotential and to remove the oscillating part of valence electron wave functions in the core region by node-less pseudo wave functions. The (pseudo)potential and pseudo-wave function and the all-electron counterpart must be identical outside a radius, r_c. These requirements are shown schematically in Figure 1.1. With the pseudopotential approximation, only valence electrons outside r_c are considered explicitly. The pseudo-wave functions in the core region are node-less. Therefore, fewer PWs will be needed to construct the KS orbitals and thus reduce the computational cost. The cut-off radius must be properly chosen such that there is no overlap between the neighbouring atoms in the core regions.

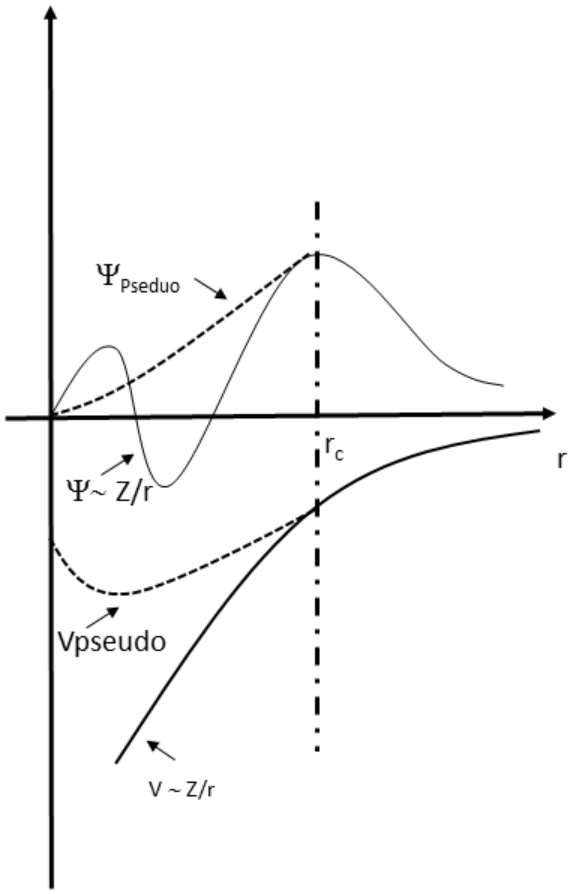

Figure 1.1 An all-electron valence wave function and electronic potential (solid lines) plotted against distance, r, from the atomic nucleus. The corresponding pseudo-wave function and

potential is plotted (dashed line). Outside a given radius, r_c, the all-electron and pseudo-electron values are identical. This figure is adopted from Ref. [34].

In 1994 [35], Blöchl developed an all electron scheme called Projector Augmented Waves (PAW). It has the numerical advantages of pseudopotential methods while it retains the physics of all-electron calculations. It also includes the correct nodal behaviour of the valence-electron wave function [36]. Figure 1.2 illustrates the general scheme to construct the PAW wave function, which is a composition of three wave functions. When the all-electron partial waves $\sum_{\alpha}\psi_n^{\alpha}(\vec{r})$ are added to the total wave functions, the corresponding pseudo-waves $\sum_{\alpha}\tilde{\psi}_n^{\alpha}(\vec{r})$ have to be subtracted. Hence, numerically, the reconstructed all electron wave function is a sum of the pseudo-wave function outside core region and the all electron partial wave function inside the core region with the corresponding pseudo partial wave function in the core region subtracted. The reconstructed KS wave function can be written as:

$$\psi_n(\vec{r}) = \tilde{\psi}_n(\vec{r}) - \sum_{\alpha}\tilde{\psi}_n^{\alpha}(\vec{r}) + \sum_{\alpha}\psi_n^{\alpha}(\vec{r})\,. \qquad 1.40$$

The PAW method is used in this thesis for electronic structure calculations.

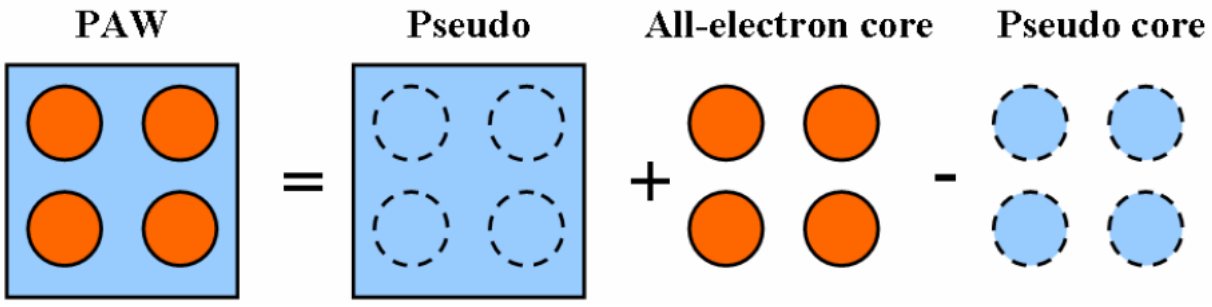

Figure 1.2 A simplified depiction of reconstructed PAW wave function that contains onsite and out-of-site contributions from all-electron and pseudo wave functions. This figure is taken from Ref. [34].

Self-consistency and ground-state total energy

Using the theories and numerical schemes described above, we are now able to solve the many-body electronic problem for any materials. In practice, the KS DFT equations need to be solved self-consistently to determine the electron density. The procedure which was used in this thesis for calculation of electronic structure is shown in Figure 1.3. A self-consistent calculation begins by constructing an initial guess density, $n[0]$, usually from the given atomic densities of a real system. The effective potential $V_{eff}(n)$ is then constructed from $n[0]$. The next step is to construct the KS equations with the initial density and the effective potential. This set of KS equations is then solved at each *k-point*, producing a set of pseudo wave functions expanded by the PW basis set. A new density will then be generated from the resulting KS orbitals. If the new density differs from the previous beyond a certain tolerance, the calculation needs to be repeated with the new density and reconstructed potential. The procedure is then repeated until the difference in the density is less than a given tolerance; then the calculation is converged. Once convergence is achieved, the ground-state total energy and density, KS orbitals and energies, as well as the force on each atom can be calculated. Other physical properties can also be derived from the ground-state wave function.

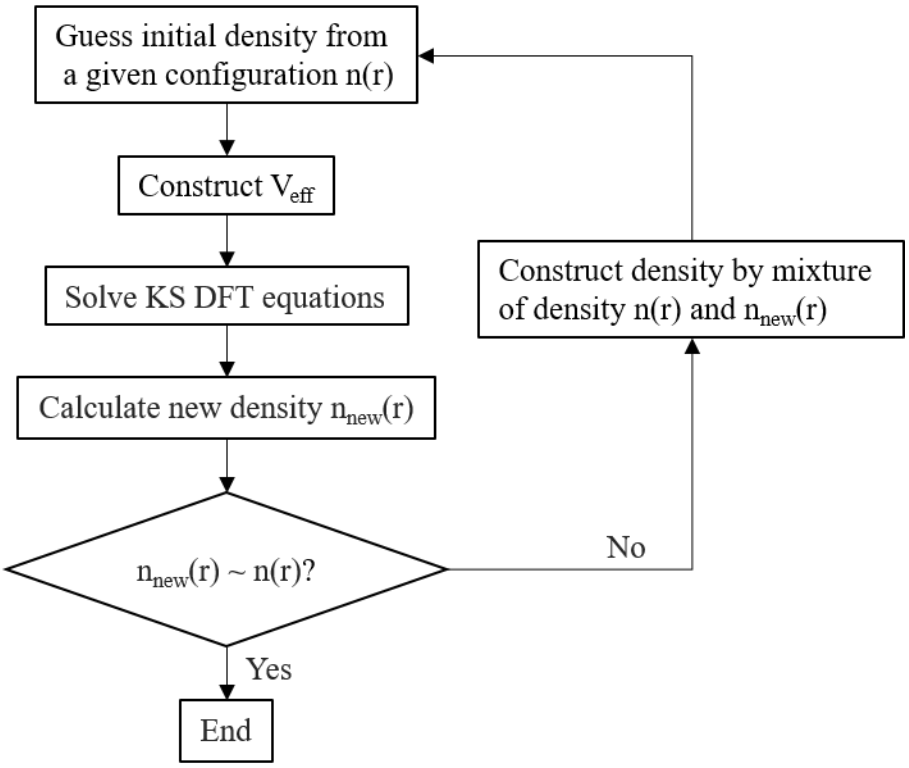

Figure 1.3 A flowchart illustrating the procedure in the self-consistent calculations using DFT with PW basis set.

1.3 Molecular dynamics

The electronic structure calculation described above is focused mainly on the behaviour of electrons in a many-body system with a fixed spatial configuration of the nuclei. The next problem in the material simulation is to describe the motion of the nuclei on the PES. All molecules or condensed matters are collections of nuclei with electrons. A different atomic configuration corresponds to a different point on the PES. The configuration with the lowest energy is called the ground state and is the global minimum. Due to energy barriers between different atomic configurations, some local minimum energy points also exist. The structural evolution between different states is of great importance in materials science. In real chemical environments, structural evolution is affected by the dynamical effect of the nuclei originating from temperature,

thermal and quantum effects. The method of molecular dynamics (MD) [37-40] was used to study the atomic propagation on the PES under finite temperature. This method treats each of the nuclei as classical particles, and the motions are determined by Newtonian mechanics driven by a force field. MD simulations are widely used to investigate the structure, dynamics, and thermodynamics in materials science.

MD simulations provide the temporal atomic positions and velocities of the system. To compare the MD results to experiment, one employs the theory of statistical mechanics, which provide rigorous mathematical expressions relating macroscopic properties to the distributions and motions of the atoms. The *thermodynamic state* of a system is defined by parameters such as the temperature T, pressure P, and the number of particles, N. Using the fundamental thermodynamic equations, *i.e.* Euler relationships, one can derive other thermodynamic properties, such as density or chemical potential. The thermodynamic *state* forms a phase space. Mechanical or macroscopic states are described by the positions and velocities or momenta, abbreviated as Γ. The property Λ of the system, such as potential energy, is a function of Γ described as $\Lambda(\Gamma)$. The system evolves with time and so do Γ and $\Lambda(\Gamma)$. A collection of points in the phase space is called an ensemble, which has different microscopic states but an identical thermodynamic state. The macroscopic thermodynamic properties are defined as an ensemble average, which is an average over a large number of micro states of the ensemble. Thus, an MD simulation generates a set of points in the phase space as a function of time according to the ensemble. Assuming ergodicity, properties generated from the MD simulations are the time average, which is the average taken over a period of time. The ergodic hypothesis states that the time average is equal to the ensemble average. Therefore, sampling over a sufficient amount of phase space and time, the experimentally relevant information concerning structural dynamics and thermodynamic properties can be calculated. To

represent the real experimental conditions, any MD simulation needs to be performed under a certain ensemble. There are three commonly known ensembles: microcanonical or *NVE* ensemble, canonical or *NVT* ensemble, and isothermal–isobaric or *NPT* ensemble. For each ensemble, the corresponding aforementioned thermodynamic variables are fixed during the MD simulation. Other thermodynamic quantities can be captured from within averages over the ensemble.

1.3.1 A simple MD program

An MD calculation proceeds mainly in four steps: initialization, force calculation, integration of equation of motion and data sampling. These steps are illustrated schematically in Figure 1.4. In the first step, one assigns the initial positions $\vec{r}_i(t_0)$ and define the velocities $\vec{v}_i(t_0)$ at time t_0. *i* is the index of the atoms in the system with N atoms. The initial velocities were set according to the Maxwellian distribution of equipartition relationship:

$$k_B T(t_0) = \sum_i^N \frac{m v^2_{\alpha,i}(t_0)}{N_f}, \tag{1.41}$$

where k_B is the Boltzmann constant, $T(t_0)$ is the temperature at time t_0. $v_{\alpha,i}(t)$ is the α=(x,y,z) component of velocity for atom i at time t_0, and N_f is the number of degrees of freedom. The forces on each atom are calculated from the gradient of the electronic potential energy. With this information, we can integrate Newton's equation of motion. There are two commonly used algorithms for integration: the Velocity Verlet (VV) algorithm and the Verlet Leapfrog (VF) algorithm. Both schemes can simultaneously evolve both the velocity and position. The VV algorithm is represented as:

$$\vec{v}_{n+1/2} = \vec{v}_n + \frac{\vec{f}_n \cdot \Delta t}{2m}, \tag{1.42}$$

$$\vec{r}_{n+1} = \vec{r}_n + \vec{v}_{n+1/2} \cdot \Delta t, \tag{1.43}$$

$$\vec{v}_{n+1} = \vec{v}_{n+1/2} + \frac{\vec{f}_{n+1} \cdot \Delta t}{2m}. \quad 1.44$$

The idea of this algorithm is to calculate the half-step velocity from the n^{th} step. This half-step velocity is used as the mean velocity between steps n and n+1 to update the velocity and position. The VF algorithm also makes use of the half-step velocities. The velocity can be seen to "leapfrog" over the current time n as described by,

$$\vec{v}_{n+1/2} = \vec{v}_{n-1/2} + \frac{\vec{f}_{n} \cdot \Delta t}{2m}. \quad 1.45$$

Then the new position and velocity at n+1 step will be calculated as:

$$\vec{r}_{n+1} = \vec{r}_{n} + \vec{v}_{n+1/2} \cdot \Delta t, \quad 1.46$$

and

$$\vec{v}_{n+1} = \vec{v}_{n+1/2} + \vec{v}_{n-1/2}. \quad 1.47$$

A trajectory storing the information of the positions and velocities as a function of time will be generated in the successive integration of the equation of motions. From the trajectory, time average properties can be calculated. The MD loop is repeated until the decided total time for the simulation is reached.

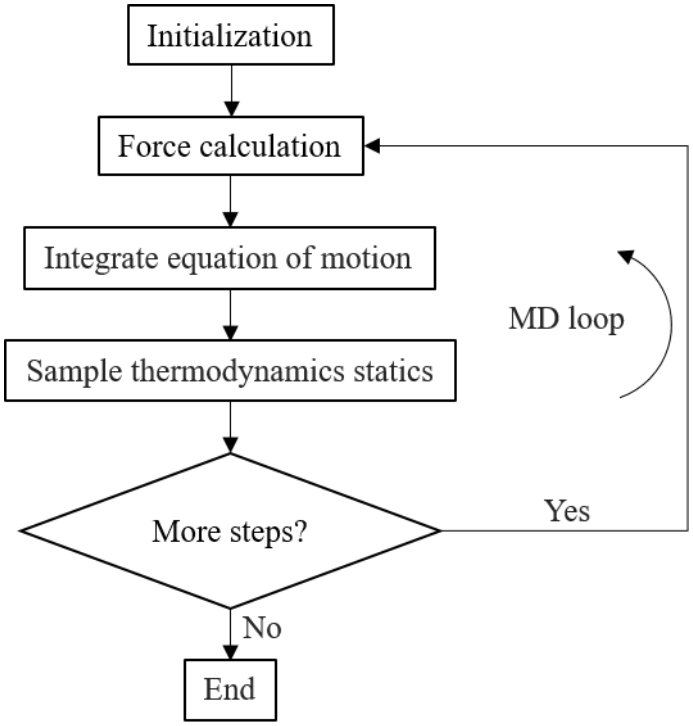

Figure 1.4 Schematic diagram of a basic MD code.

For most atoms, the nuclei can be treated as classical point-like particles, and their motions can be treated by Newton's laws; this forms the basis for classical MD. The forces on the atoms can be calculated quantum mechanically using the Hellmann-Feynman theorem, and this method is known as *ab initio* MD (AIMD). However, the forces can also be approximated with empirical potentials, and this method is herein referred to as empirical MD. Due to the use of parameterized empirical potentials, empirical MD is much faster and can be applied to much larger systems (millions of particles) than that of AIMD. For light elements, such as H, the nuclear quantum effects (NQEs) on their motion must be considered. Path integral molecular dynamics (PIMD) is a scheme used to investigate the NQEs.

1.3.2 Classical molecular dynamics based on Newtonian mechanics

For most elements, except perhaps the light atoms such H and He, the motion of the nuclei obeys Newton's laws. The motion of the atoms can be simulated with classical MD. The equation of motions is derived from Newton's second law:

$$\vec{F}_I = m\vec{a}_I, \tag{1.48}$$

and

$$\vec{F}_I = -\vec{\nabla}_I U(\vec{R}_I), \tag{1.49}$$

where $\vec{F}_I$ is the force exerted on the atom *I*, $\vec{a}_I$ is the acceleration vector, and m is the mass. Eq. (1.48) also shows that the force can also be calculated as the gradient of the potential energy $U(\vec{R}_I)$. With the forces calculated, the velocities will be easy to obtain. AIMD calculates the forces on the particles explicitly using the electronic wave functions. Empirical MD calculates the forces by using a given parameterized force field.

1.3.2.1 *Ab initio* molecular dynamics

In AIMD the forces are calculated from the Hellmann-Feynman Theorem. The force in Eq. (1.48) can be written as:

$$\vec{F} = -\frac{dE}{d\vec{R}}, \tag{1.50}$$

where the E can be obtained from solving the KS equations:

$$E = \langle \psi | H_e | \psi \rangle. \tag{1.51}$$

Substituting Eq. (1.50) into Eq. (1.48), the force becomes:

$$F = -\left\langle \psi \left| \frac{\partial H}{\partial \vec{R}_I} \right| \psi \right\rangle - \left\langle \frac{\partial \psi}{\partial \vec{R}_I} | H | \psi \right\rangle - \left\langle \psi | H | \frac{\partial \psi}{\partial \vec{R}_I} \right\rangle. \tag{1.52}$$

Since the ground state is the lowest energy state, it is the minimum point with respect to any variation of the wave function and thus the second and third terms vanish. This leads to an

expression of the force on an ion, which is given by the expectation value of the gradient of the electronic Hamiltonian in the ground state, (Hellmann-Feynman Theorem) [41,42].

AIMD simulations were performed by using VASP, the Vienna Ab-initio Simulation Package. [23,25,27,43-47], using the PAW potentials. The valence one-electron orbitals are expanded as PWs. The forces and full stress tensors can also be calculated. Both LDA and GGA exchange-correlation approximations are available. The DFT-DT and vdW-DF methods were also implemented in VASP.

1.3.2.2 Empirical force field molecular dynamics

In empirical MD, forces on the particles are evaluated from pre-defined parameterized potentials. These potentials are either fitted to empirical data or derived from first principles calculations of the PES. The motions of the nuclei are determined by Newtonian mechanics. At present, the largest system simulated by AIMD can be hundreds of atoms (in practice, around 500 atom) [48]. In comparison, there is considerable literature on empirical force filed potential calculations with millions to billions of atoms [49]. Hence it is possible to simulate interface, structural changes in bulk liquids, *etc*. For moderate system sizes, very long simulation times can be achieved. For example, processes that require relatively long times to occur can be simulated, *e.g*. a melting phenomenon from studying the interface. The main disadvantage of the empirical MD is that the fitted potential will never be as reliable as the exact quantum mechanical potential. Parameterized potentials often have poor transferability as the parameters are determined by parameterisation against selected properties. Thus, one has to be careful in choosing the proper potentials for different simulations.

Empirical force fields

An empirical force field is a function parameterized to represent the potential energy surface of a system. The functional form is often divided into different terms: the bonded terms for *intramolecular* interactions of atoms that are linked by covalent bonds, and non-bonded terms that refer to the *intermolecular* long-range electrostatic and *vdW* interactions. The total configuration energy can be written as:

$$U_{total} = U_{bonded} + U_{nonbonded}, \quad 1.53$$

$$U_{bonded} = U_{bond} + U_{angle} + U_{dihedral}, \quad 1.54$$

$$E_{nonbonded} = U_{electrostatic} + U_{vanderWaals}. \quad 1.55$$

There are many different forms of the potentials used to model the interactions' potential energy surfaces. Here, we only describe the potentials employed in this study.

Lennard-Jones potential

Lennard-Jones (L-J) potential [50] is a common model that describes the interaction between a pair of neutral atoms or molecules. The L-J potential is expressed as:

$$U(R_{IJ}) = 4\varepsilon\left[\left(\frac{\sigma}{R_{IJ}}\right)^{12} - \left(\frac{\sigma}{R_{IJ}}\right)^{6}\right], \quad 1.56$$

where ε is the depth of the potential well, R_{IJ} is the distance between two particles, and σ the finite distance at which the pair potential is zero. *VdW* interactions, including dispersion and repulsion forces between two molecules, are often modelled using L–J potential.

Ewald sum correction for long-range interaction

The Ewald sum [39,40] is the technique for evaluating the long-range Coulomb interactions between point charges and their periodic images in periodic systems. In periodic systems

composed of point charges of opposite signs with $\sum_i^N q_i = 0$, the Coulomb contribution to the potential energy is a direct summation, written as:

$$U_{Coul} = \frac{1}{2}\sum_{\vec{n}}\left(\sum_{i=1}^{N}\sum_{j=1}^{N} q_i q_j \left|\vec{R}_{ij} + \vec{n}\right|^{-1}\right), \qquad 1.57$$

where q_i and q_j are the point charges and N is the total number of particles. The sum over n is the sum over all the periodic points/images, $\vec{n} = (n_x L_x, n_y L_y, n_z L_z)$ where n_x, n_y, and n_z are integers. The particle i interacts with all other particles and periodic images but not itself. Therefore, in the summation, $i \neq j$, if n=0. Since there is always a finite contribution as the number of cells grow, the result depends on the order of summation. Hence, the direct sum over n is poor and poses a large drawback in the implementation.

To overcome this drawback, Ewald sum was introduced. The basic idea is to separate the interaction into short-range and long-range interactions through modifying the way of representation of the charge distribution. In Eq. (1.57), the point charge is a sum of δ-functions. In the Ewald sum, the point charge is represented by a Gaussian charge distribution of equal magnitude to the point charge, but opposite sign (Figure 1.5) with charge density $\rho_i(r) = q_i \alpha^3 \exp(-\alpha^2 r^2)/\sqrt{\pi^3}$, where α is the width of the distribution and r is the position of the centre of the distribution. The added charge cloud cancels q_i and thus screens out the interaction between neighbouring charges. The potential due to the screened charge falls to zero rapidly at large distances. In this fashion, the screened interactions are limited to a short range and can be calculated by direct summation over all the molecules constituting the *real space* short-range part of the Ewald sum. To represent potential due to the original point charges, a second compensating Gaussian charge distribution with the same sign and magnitude as the original one and with the same shape as that of the first Gaussian distribution is added for each point charge, correcting the

screening effect. The relationship between the original, the screened charge, and the compensating charge is given in Figure 1.5. The original charge is equal to the screened charge minus the compensating charge. The compensating charge cloud is a smoothly varied periodic function and can be calculated in reciprocal space. The total Coulomb potential is divided into two regions: short-range and long-range interaction, and is calculated separately in both real and Fourier space in Ewald sum. This potential is the *reciprocal space*/long-range part of the Ewald sum.

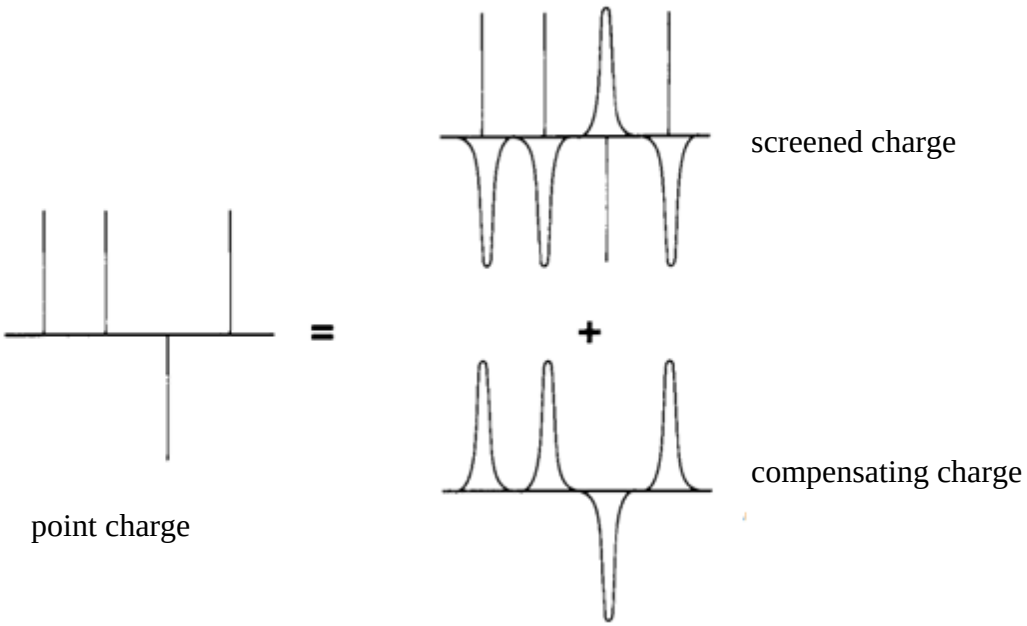

Figure 1.5 Representation of the original point charge by the screened charge minus the smoothly varying screening background. The vertical lines indicate the (+/-) charges. This figure is adopted from Ref. [40].

The introduction of the Gaussian charge distribution included the interaction of each ion with the surrounding charge cloud, the self-interaction. This self-interaction must be subtracted from the sums. Therefore, the Coulomb potential composed of three parts, the real (direct) sum, U^{sr}, the reciprocal (Fourier) sum, U^{lr}, and the constant (self-term), U^{0}:

$$U^{sr} = \frac{1}{2}\sum_{i,j}^{N'}\sum_{n} q_i q_j \frac{\mathrm{erfc}(\alpha r_{ij,n})}{r_{ij,n}}, \quad 1.58$$

$$U^{lr} = \frac{1}{2\pi V}\sum_{ij}^{N} q_i q_j \sum_{m\neq 0} \frac{\exp(-(\pi \vec{m}/\alpha)^2 + 2\pi i \vec{m}\bullet(\vec{r}_i - \vec{r}_j)}{\vec{m}^2}, \quad 1.59$$

$$U^{0} = \frac{-\alpha}{\sqrt{\pi}}\sum_{i}^{N} q_i^2, \quad 1.60$$

where V is the volume of the lattice, $\vec{m} = (l, j, k)$ is a reciprocal space vector, and *erfc* represents the complimentary error function. The self-term is a correction term that cancels out the interaction of each of the introduced screening charges with itself [51].

Water models

In this thesis, empirical MD was performed for water-based systems. Over the years, many water force fields have been developed. These models vary in the number of interaction sites, flexibility, and the treatment of polarizability. The water models can be classified into three main types: rigid, flexible, and polarizable models. Rigid models consider only non-bonded interactions with fixed atom positions for the O and H in the molecule. TIP4P/2005 and SPC/E are the two most commonly used models and have been shown to be successful in the prediction of many water properties. Flexible models connect the oxygen and hydrogen atoms with springs adding flexibility to describe bond stretching and angle bending. These models can provide internal vibration information. Polarizable models include explicit polarization terms to improve the ability to model water in different environments. SPC/FQ and Tip4p/FQ are the two common polarizable models. Detailed information on different models can be found in Ref. [52].

In this work, the TIP4P/ice [53] model (Figure 1.6) was chosen to investigate the phase changes of ice Ih. This model belongs to the four-point-site water model family. The O – H bonds are rigid. The four sites are the O atom, two H atoms and a “ghost” negative point. The H atoms

have positive charges. The modified version of the TIP4P/ice model has been shown to reproduce the solid phases of water, in particular, the improvement on the melting curve. The total potential energy of the system is the sum of the intermolecular *vdW* pair potential represented by the LJ function and the electrostatic interactions evaluated by Ewald sum.

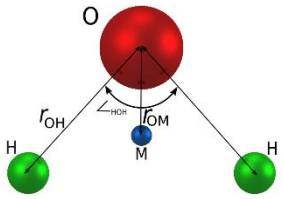

Figure 1.6 A schematic representation of the four-site TIP4P/ice model. This figure is taken from Ref. [54].

For the simulations performed with TIP4P/ice potential, DL_POLY [55], a parallel molecular dynamics package was used. DL_POLY is designed to facilitate MD simulation of macromolecules, polymers, ionic systems and solutions using empirical force fields. There are two versions of DL_POLY with the main difference being the implementation of the parallel algorithms. The DL_POLY classic is limited to systems with up to 30000 atoms. The DL_POLY_4 is able to deal with systems up to 10^9 atoms. The code used in this thesis is DL_POLY_4. The long-range electrostatic interactions treated were calculated with the Ewald summation method. Both the VV and VF algorithms for the integrations of the equation of motions were implemented. However, this package can only be used with the rigid water models.

Recently, a new flexible polarizable Thole-type (TTM2.1-F) water model (Figure 1.7), parameterized from accurate quantum calculations was proposed [56-59]. This model is also a four-site model. Instead of using static charge points, the positive and negative charges are modeled with smeared charges and allow the charge to vary with the environment. This flexible

version TTM2.1-F model is a modification of the rigid version TTM2-R model. In the TTM2-R model, the total potential energy includes the pair, polarization, and electrostatic terms:

$$U^{total} = U^{pair} + U^{pol} + U^{elec}. \quad 1.61$$

U^{pair} is a sum over all the oxygen sites by using the LJ potential,

$$U_{pair} = \sum_{I=1}^{N>1} \sum_{J>I}^{N} \left(\frac{A}{r^{12}} + \frac{B}{r^{10}} + \frac{C}{r^{6}}\right). \quad 1.62$$

The coefficients A, B, and C are fitted against the PES of the water dimer obtained from high-level quantum mechanical calculation. $U_{pol} = \sum_{I=1}^{K} \frac{\mu_I^{\,2}}{2\alpha_I}$ is a sum over all the induced dipole sites and represents the interaction of induced dipoles. The electronic contribution, U^{elec}, contains charge-charge, charge-dipole, and dipole-dipole interactions.

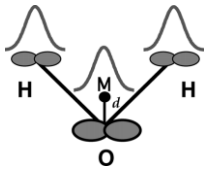

Figure 1.7 A schematic representation of the Thole-type water model. This figure is taken from Ref. [58].

The intramolecular flexibility of TTM2.1-F is achieved by coupling the Partridge-Schwenke (PS) [60] water monomer potential energy and dipole moment surfaces (DMS) to the intermolecular part of the 4-site all-atom polarizable TTM2-R model *via* a charge redistribution scheme [59]. The charge redistribution represents the change of static molecular dipole moment associated with geometry changes. PS obtained the most accurate PES and DMS available for the monomer from high-level *ab initio* calculation by using a 245-term and an 84-term to fit to the PES and DMS, respectively. The DMS of the isolated water monomer was given in terms of the geometry-dependent charges:

$$\begin{aligned}\vec{P}^{g} &= q(r_{H_1-O}, r_{H_2-O}, \theta_{HOH})\,\vec{r}_{H_1-O} + q(r_{H_2-O}, r_{H_1-O}, \theta_{HOH})\,\vec{r}_{H_2-O} \\ &= q^{O}\vec{r}_{O} + q^{H_1}\vec{r}_{H_1} + q^{H_2}\vec{r}_{H_2}\end{aligned} . \quad 1.63$$

Here, Pg is the dipole moment of a water monomer in gas-phase, and $\vec{r}_{H_1-O} = \vec{r}_{H1} - \vec{r}_{O}$ and $\vec{r}_{H_2-O} = \vec{r}_{H2} - \vec{r}_{O}$ are the distance vectors. The charges on atomic sites are defined as functions of the intramolecular geometry: $q(r_{H_1-O}, r_{H_2-O}, \theta_{HOH}) = q^{H_1}$, $q(r_{H_2-O}, r_{H_1-O}, \theta_{HOH}) = q^{H_2}$, and $q^{O} = -(q^{H_2} + q^{H_2})$. Here the superscripts denote the charges on the atomic sites, that is H_1, H_2, and O, while the subscripts indicate the charge sites, that is H_1, H_2, and the ghost M-site. The ghost massless charge M-site, which is located along the bisector of the HOH angle, is determined by [61-63]:

$$\vec{r}_{M} = \vec{r}_{O} + \frac{\gamma}{2}(\vec{r}_{H_1-O} + \vec{r}_{H_2-O}), \quad 1.64$$

with $\gamma = 0.4267$. The charges on the charge sites were derived from the atomic site charges in DMS according to the relationships:

$$\begin{aligned} q_{H_1} &= \frac{q^{H_1}}{(1-\gamma)} \\ q_{H_2} &= \frac{q^{H_2}}{(1-\gamma)} \\ q_{M} &= -(q_{H_1} + q_{H_2}) \end{aligned} . \quad 1.65$$

ReaxFF reactive force field

Traditional force fields described above were developed to represent physical interactions of a system with predetermined interaction sites and therefore did not consider the chemical reactivity. Hence, such models are not appropriate to model chemical reactions where the atom connectivity changes due to bond breaking and forming. To improve the modelling capability, researchers has been motivated to develop the ReaxFF reactive force fields [64,65] that are able to

describe such atomic and molecular interactions of the model system dynamically. The dynamic description is achieved by calculating the bond orders and atom valences dynamically, based on the evaluation of many-body potential terms. Detailed parameterization of atomic, bonding, angle and torsion properties of each particle and interaction within the same system are needed for a proper ReaxFF force field [65]. The total energy of a system is expressed as a sum of connectivity-dependent terms (the bond, over-coordination penalty and under-coordination stability, lone pair, valence angle energies and torsion energies), and non-bonding terms (*vdW* dispersion and Coulomb energies), and is written as:

$$E_{system} = E_{bond} + E_{over} + E_{lp} + E_{angle} + E_{tor} + E_{vdw} + E_{coulomb}. \quad 1.66$$

The over-coordination penalty is employed to prevent unrealistically over coordination of atoms, which is based on atomic valence rules. The forces are calculated as the gradient of the total energy.

Figure 1.8 illustrates a general scheme of a ReaxFF iteration in a computer simulation. In each iteration, the non-bonded interactions are calculated between every atom pair. The connectivity-dependent terms are evaluated as bond-order dependent to ensure their energy contributions vary upon bond dissociation or formation. In each iteration, the first step is to compute the bond orders, which is a function of interatomic distance and given as:

$$\begin{aligned} BO_{ij} &= BO_{ij}^{\sigma} + BO_{ij}^{\pi} + BO_{ij}^{\pi\pi} \\ &= \exp\left[P_{bo,1} \bullet \left(\frac{r_{ij}}{r_O^{\sigma}}\right)^{P_{bo,2}} \right] + \exp\left[P_{bo,3} \bullet \left(\frac{r_{ij}}{r_O^{\pi}}\right)^{P_{bo,4}} \right] + \exp\left[P_{bo,5} \bullet \left(\frac{r_{ij}}{r_O^{\pi\pi}}\right)^{P_{bo,6}} \right]. \end{aligned} \quad 1.67$$

Here, BO is the bond order between atom i and j. r_o are the equilibrium distances, and *P* are the parameterized bonding terms. The first, second, and third terms in Eq. (1.67) represent the single (σ), double (π), and triple bond ($\pi\pi$) order contributions, respectively. Since Eq. (1.67) includes the long-range interaction, it is possible to overestimate the bond order. Therefore, the bond order is modified by the degree of deviation to the valence of the atom. After the bond orders are

determined, the connective-dependent energy can be calculated. Finally, the atomic charges are calculated from the charge equilibration (QEq) algorithm [66]. The QEq atomic charges are assigned based on the ionization potentials, electron affinities, and atomic radii, and optimized by minimizing the electrostatic energies with the constraints that total changes must be constant and the all atomic chemical potentials must remain equal [66,67]. The non-bonding interactions are calculated from these charge distributions. In this thesis, ReaxFF force field was used to investigate the chemical reaction between quartz and H_2. The good performance of reactive force fields for the silica/water interface has been demonstrated by Fogarty et al. [67].

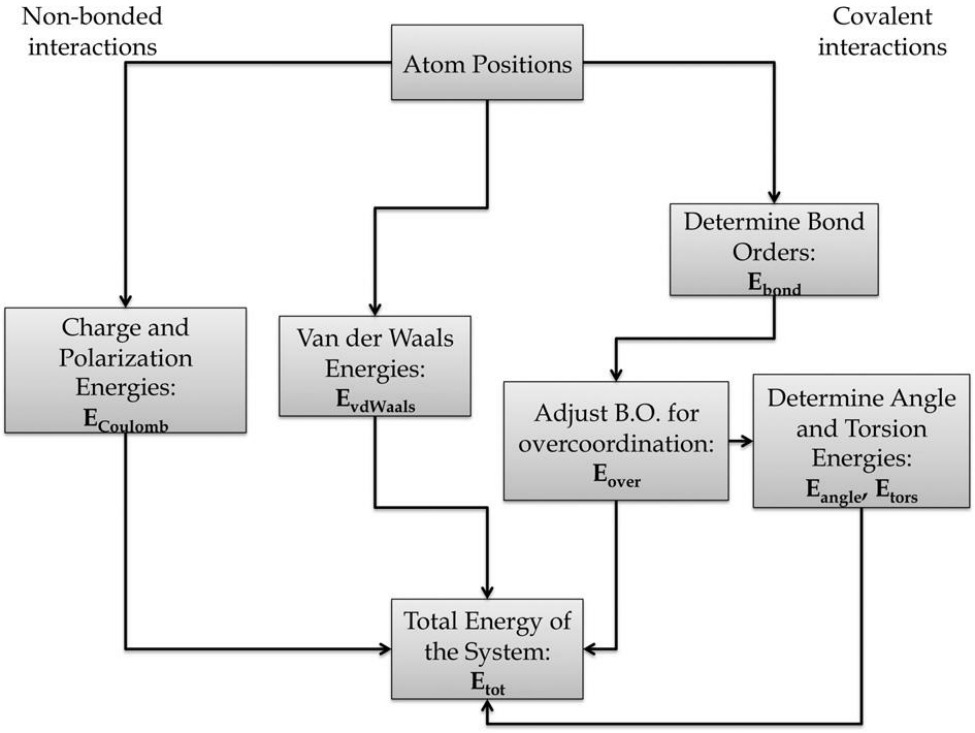

Figure 1.8 Illustration of the ReaxFF iteration in an MD simulation. The non-bonded interactions are on the left, and the covalent/connectivity-dependent interactions are on the right. This figure is taken from Ref. [65].

1.3.3 Meta-dynamics

In the study of chemical reactions, first-order phase transitions or protein folding, large energy barriers must first be overcome. Standard MD is not efficient enough to simulate such processes. The meta-dynamics method [68,69] provides a means to cross high free-energy barriers. The idea is to separate the simulation of the activated process into two parts regarding the microscopic degrees of freedom: the fast process, which can equilibrate on the simulation time scale, for example, the atomic configuration in a given lattice; and a slow process, which requires excessive time. The faster degrees of freedom can be treated by a standard MD while the latter is treated by meta-dynamics. The meta-dynamics employs the additional bias potentials to the original free energy to lower the energy barrier and promote crossing. The biased potential is constructed from a few order parameters (or degree of freedom) called collective variables (CVs). The underlying principle of the meta-dynamics is illustrated in Figure 1.9. In the illustration, only one order parameter is considered, and the PES of the system is represented by the black curve. To cross the energy barrier between A and B, additional “biased” potentials are added. Once a potential valley is filled, the other valleys can be explored.

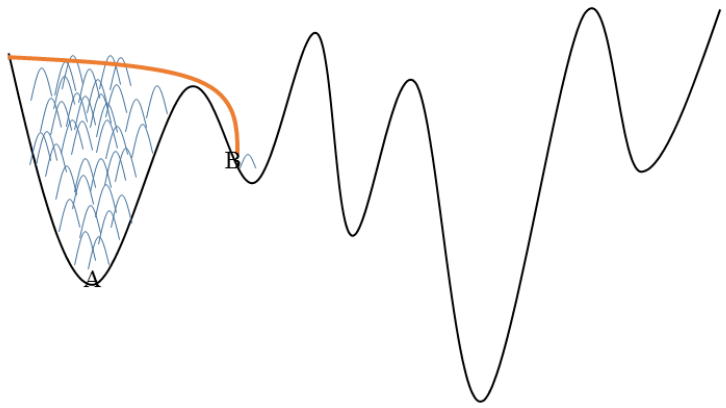

Figure 1.9 Illustration of the principles underlying the meta-dynamics method.

Different order parameters are chosen for specific properties. The set of order parameters used in simulations of structural transitions is the matrix of the model box edges, $\vec{h} = (\vec{a}, \vec{b}, \vec{c})$. The h matrix contains the freedom of the cell parameters, the 3 cell lengths, 3 angles and 3 global rotations. The 3 global rotations are removed by constructing an upper triangular form of the h matrix. The remaining six-dimensional order parameters are defined by a vector: $\vec{h} = (h_{11}, h_{22}, h_{33}, h_{12}, h_{13}, h_{23})^T$. The dynamics of this set of order parameters are written as:

$$\vec{h}^{t+1} = \vec{h}^{t} + \delta h \frac{\vec{\phi}^{t}}{\left|\vec{\phi}^{t}\right|}. \qquad 1.68$$

$\vec{\phi}^{t} = -\frac{\partial G^{t}}{\partial h}$ is the driving force, which is defined by using the history-dependent Gibbs potential, g^{t}. A Gaussian function g(h) is added to the point $\vec{h}^{t'}$ already passed. Hence the g^{t} is written as:

$$g^{t}(h) = g(h) + \sum_{t'<t} We^{-\frac{\left|\vec{h}-\vec{h}^{t'}\right|^2}{2\delta h^2}}. \qquad 1.69$$

The force $\vec{\phi}^{t}$ is then a sum of the thermodynamic forces. With proceeding time, this history-dependent potential fills up the valley and pushes the system out of the local minimum.

1.3.4 Path integral molecular dynamics

In the standard classical MD method discussed above, the quantum nature of the nuclei is neglected. However, for systems such as water and ice, in which the main component is dominated by the light element, H, nuclear quantum effects, NQEs, significantly affect the vibrational behaviors. A solution to describe the NQEs is the PIMD method in which the NQE is incorporated using Feynman path integral quantum statistical mechanics [70]. Due to the uncertainty of a quantum particle, PIMD samples the probability of the occurrence of motions. The quantum nature of the nuclei is mimicked by mapping the system of N particles onto an equivalent classical system

consisting of N_P particles (Figure 1.10). Each nucleus is mapped to *p* fictitious particles (beads) connected by springs. All the *p* particles share the same action and form a "path" in PIMD. The particles connected by springs are described by an effective Hamiltonian. The momentum p and position q for each ring path are expressed as a function of the constituting beads:

$$p = (p_i, \ldots, p_p), \tag{1.70}$$

$$q = (q_1, \ldots q_p), \tag{1.71}$$

The partition function Z of a single quantum particle is the sum over all the possible occupations corresponding to all the available energy states. In PIMD, Z is represented as a summation over the P beads:

$$Z = \lim_{P\to\infty}\left(\frac{mP}{2\pi\hbar^2\beta}\right)^{P/2}\int dq_1 \ldots \int dq_p \exp[-\beta V_p(q)], \tag{1.72}$$

where m is the particle mass, $\beta = \frac{1}{k_B T}$ is the inverse of the temperature, *p* is the number of beads and V_p is the ring potential. V_p is given by:

$$V_p(q) = \sum_{i=1}^{P}\left[\frac{mP}{2\hbar^2\beta^2}(q_i - q_{i+1})^2 + \frac{V(q_i)}{P}\right]. \tag{1.73}$$

$V_p(q)$ is approximated as a pair-wise additive potential, which is similar to that in a classical system. Since each bead is linked to its two nearest neighbours, it also feels the interaction potential through $V(q_i)/P$. Each "polymer chain" forms a closed path and obeys the condition $q_{i+p} = q_i$.

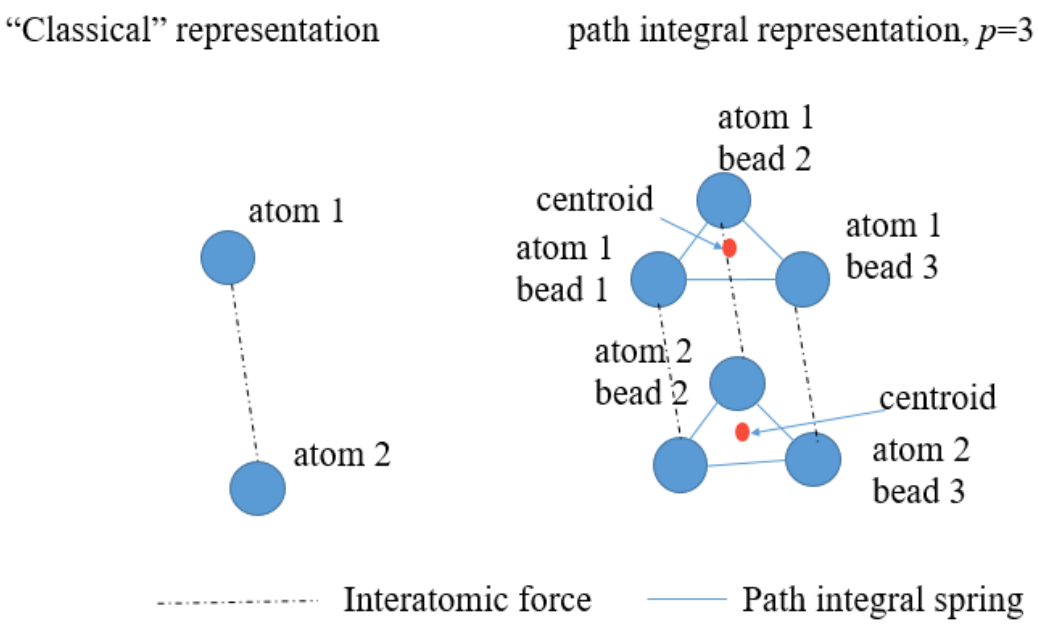

Figure 1.10 Schematic diagram of two interacting atoms with (left) a classical and (right) quantum path integral representation.

There are several practical schemes for the study of the dynamics of quantum systems. Ring-polymer path integral molecule dynamics (RPMD) and the central molecular dynamics (CMD) are the two most common methods, but they are conceptually distinct path integral molecular dynamics methods. RPMD is an exact/full PIMD method, which propagates the system using Hamilton's equations of motion in real time [71,72]. The method we employ in this thesis is CMD, which uses the centre mass (centroid) of the ring polymer as the primary dynamical variable [73-77]. CMD evolves the centroid under the effective quantum potential using the classical equation of motions. The RPMD and CMD were shown to approximate similar quantum behaviour in condensed phases. The advantage of CMD is that dynamical properties, such as the diffusion coefficient, can be calculated directly from the temporal evolution of the centroids [75,76]. The main formulation of CMD is presented below. The centroid variable is defined as:

$$x_0 = \frac{1}{P}\sum_{i=1}^{P} x_i \,, \tag{1.74}$$

The partition function then becomes the function in terms of equilibrium distribution of the centroid positions:

$$Z = \int dx_c \rho_c(x_c) \,, \tag{1.75}$$

with the centroid distribution being defined as:

$$\rho_c(x_c) = (\frac{mP}{2\pi\hbar^2\beta})^{P/2} \int dx_1 \ldots dx_P \delta(x_c - x_0) \exp(-\sum_{i=1}^{P} \left\{ \frac{mP}{2\hbar^2\beta}(x_i - x_{i+1})^2 + \frac{\beta}{P} V(x_i) \right\}. \tag{1.76}$$

The potential acting on the centroid is introduced as:

$$V_c(x_c) = -\frac{1}{\beta} \ln\left\{\rho_c(x_c)\right\}, \tag{1.77}$$

and the corresponding force is calculated as:

$$\begin{aligned} f_c(x_c) &= -\frac{dV_c(x_c)}{dx_c} = -\frac{1}{\rho_c}(\frac{mP}{2\pi\hbar^2\beta})^{J/2} \times \\ &\int dx_1 \cdots dx_P \delta(x_c - x_0) \left\{ \frac{1}{P}\sum_{j=1}^{P} \left.\frac{dV(x)}{dx}\right|_{x_j} \right\} \times \exp(-\sum_{i=1}^{P} \left[\frac{mP}{2\hbar^2\beta}(x_i - x_{i+1})^2 + \frac{\beta}{P} V(x_i) \right]) \end{aligned}. \tag{1.78}$$

The equations of motion for this centroid are written as:

$$\frac{dx_c(t)}{dt} = \frac{p_c(t)}{m}, \tag{1.79}$$

$$\frac{dp_c(t)}{dt} = f_c(x_c(t)) \,, \tag{1.80}$$

where p_c is the momentum of the center of mass. By integrating Eq. (1.72) and Eq. (1.73), the centroid coordinate and momentum can be obtained. However, the force in Eq. (1.78) is a function of an imaginary-time path integral and the sum over all the paths is needed at each time step. Hence, CMD calculations require significantly more computational effort than classical MD simulations. An improvement was made [75] to propagate only the higher normal-modes (NM) of the ring polymer along with the centroid and is called NM- CMD. The mass of the non-centroids normal modes needs to be very small so that their dynamics are far shorter than that of the centroid.

Path-integral CMD in the normal mode representation employing the TTM2.1-F water intermolecular model was implemented by Christen J Burnham in an in house code [78]. Each quantum particle is replaced by a *p*-harmonic-beads ring-polymer. The equation of motions is formulated with the centroid of the harmonic ring. The classical MD corresponds to a single bead (p=1) CMD. The Nosé–Hoover chain thermostat was implemented, which couples a system to a thermoset (*i.e.* a heat bath), to control the temperature. The Ewald sum method was used to compute the long-range interactions.

1.3.5 Post-processing methods

Besides static properties, the goal of an MD simulation is to study the dynamical properties of the system. Such dynamical properties can be extracted from a trajectory that contains the instantaneous positions and velocities of the particles accumulated in the simulation. This analysis is always performed after the MD simulation has completed. Autocorrelation functions, mean squared displacement functions, and pair correlation function can be calculated from the trajectory while other properties such as diffusion coefficient, and vibrational spectrum can be further computed from the autocorrelation functions.

Time-correlation functions

Time-correlation function is a powerful way to represent the dynamics of a system. Time correlation function is a statistical description of the time-evolution of a variable, describing the cause-and-effect relationship between two time-dependent properties, A(t) and B(t). A time-correlation function is invariant under translation of the time origin and is defined as:

$$C(t) \equiv \lim_{\tau\to\infty} \frac{1}{\tau} \int_0^{\tau} A(t_0)\, B(t_0 + t) = \left\langle A(t_0)\, B(t_0 + t) \right\rangle, \qquad 1.81$$

where $\langle \cdots \rangle$ stands for an ensemble average, and A and B are the dynamic variables of interest (*e.g.*, velocity, bond fluctuation, *etc.*). When A and B are different properties, C is a cross-correlation. If A and B are the same properties, then C is called an auto-correlation. The auto-correlation function is a measure of how the value of $A(t_0+t)$ is correlated to the initial value $A(t_0)$. It contains information of the decay due to interactions with the surroundings. If the two properties are highly correlated, the decay of the time correlation function is very short (eg. in the solid Figure 1.11). Conversely, if the properties are not correlated, the decay of the time correlation function is very fast (eg. in liquid, Figure 1.11). The level of correlation, C, plotted against time often starts at a certain value and then decays to a lower value.

The velocity autocorrelation function (VACF) is an example of a time-dependent correlation function since the atomic velocities are direct manifestations of the dynamics. In the VACF, the A(t) is replaced with velocity. It is constructed as follows: At a chosen time origin t_0, the velocity is $v_i = v_x(t_0), v_y(t_0), v_z(t_0)$, for atom i in the system of N atoms. The C(0) is calculated as an average over the N atoms:

$$C(t=0) = \frac{1}{N}\sum_{i=1}^{N} v_i(t_0) \bullet v_i(t_0). \qquad 1.82$$

At the next time step in the simulation $t_0+\Delta t$, VACF becomes:

$$Cv(t=\Delta t) = \frac{1}{N}\sum_{i=1}^{N} v_i(t_0) \bullet v_i(t_0+\Delta t). \qquad 1.83$$

This procedure is repeated at each subsequent time step to obtain a sequence of points; the VACF is then generalized as:

$$Cv(t=n\Delta t) = \frac{1}{N}\sum_{i=1}^{N} v_i(t_0) \bullet v_i(t_0+n\Delta t). \qquad 1.84$$

Since the velocities of the atoms in an equilibrium system exhibit periodic oscillations, the correlation Eq. (1.82) often expanded over a time range. Then the process is restarted to calculate

another VACF, beginning at a new time origin. Many time origins can be used provided they are sufficiently far apart in time that there are no correlations between them. In this way, we compute a series of time frames and will remove the erroneous dependence on the time origins. Typical results of VACFs for liquid and solid are shown in Figure 1.11.

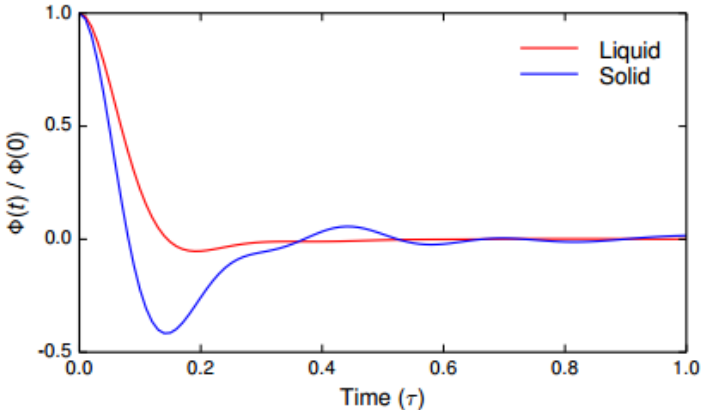

Figure 1.11 A typical velocity auto-correlation function for liquid (red) and solid (blue). This figure is taken from Ref [34]

Since the atom's velocity is related to the force, the study of VACF can reveal interactions in a system. In a solid, there are short-range interatomic forces and the atoms cannot displace freely from the equilibrium position. The atomic motions then oscillate around the mean position. The corresponding VACF often shows oscillations as illustrated in Figure 1.11. In the case of liquids, due to the diffusive nature, after a long time the atoms do not have fixed positions. Therefore, the VACF for a liquid normally shows an exponential decay from the starting value to zero often without oscillation indicating the loss of correlation with the time origin.

From VACF we can obtain other important dynamical properties of the system. Assuming that the VACF decays to zero, we can calculate the diffusion coefficient D from numerical integration:

$$D = \frac{1}{3}\int_{t=0}^{\infty} \left\langle v_i(t_0) v_i(t_0 + n\Delta t) \right\rangle dt \,. \qquad 1.85$$

The VACF can be Fourier-transformed to project out the underlying frequencies of the atomic vibrations according to the Wiener-Khinchin theorem [79]:

$$I(\omega) = \frac{1}{\sqrt{2\pi}} \int C(t) \exp^{-i\omega t} dt \,. \qquad 1.86$$

Mean-square displacement

In liquids, atoms (or molecules) do not stay in the same place but move continuously. From the atomic coordinates stored in the MD trajectory, we can obtain information on how far an individual particle has moved from the mean square displacement (MSD). MSD is defined as the square of the distance a particle has moved from its starting point within a time interval, Δt:

$$MSD = \left\langle \left| r(t) - r(0) \right|^2 \right\rangle . \qquad 1.87$$

Since it is the sum of squares, MSD is always positive. For a liquid, a plot of MSD against time should be a linear line with a finite slope. As discovered by Albert Einstein, the MSD is related to the diffusion coefficient as follows:

$$D = \frac{1}{6}\frac{d}{dt}\left\langle \left| r(t) - r(t_0) \right|^2 \right\rangle . \qquad 1.88$$

In general, if the simulated time is short, the MSD formalism is preferred. However, for long simulation time, it is expected that the velocity correlation function and Einstein diffusion equation should give identical results [80].

Pair correlation function

In an MD simulation, pair-correlation functions extracted from the trajectory provide an insight to the structure, which can be compared to experimental data. Pair correlation function,

also called radial distribution function (RDF), *g(r)* describes how density varies as a function of the distance from a reference particle. Therefore, it represents how atoms are radially packed around each other. g(r) is defined as:

$$g(r) = \frac{gn(r)}{\rho \cdot 4\pi \cdot r^2 \cdot \Delta r}. \qquad 1.89$$

Here gn(r) is the number of particles in the shell of width Δr at distance r, and ρ is the density of the system. RDFs are computed as histograms of two-particle distances. Such histograms are constructed as follows: First, a particle i with position r_i is chosen as the reference point. Then we define a spherical shell with thickness Δr, and count the number of particles, which are included in this shell. The *g(r)* is obtained by dividing the number of particles within the volume and averaging over the total number reference particles. We plot *g(r)* normalized by the density of the system against the distance r. An example of the *g(r)* is illustrated in Figure 1.12. Within a short distance from r, the *g(r)* is zero. This indicates the 'hard sphere "radius"' of the atom, as the pair of atoms cannot approach closely. Then a number of peaks might appear. The position of the first peak corresponds to the nearest neighbour's distance. Peaks at longer distance indicate long-range ordering. A solid always has sharper peaks while for a liquid, they are much broader due to the randomness.

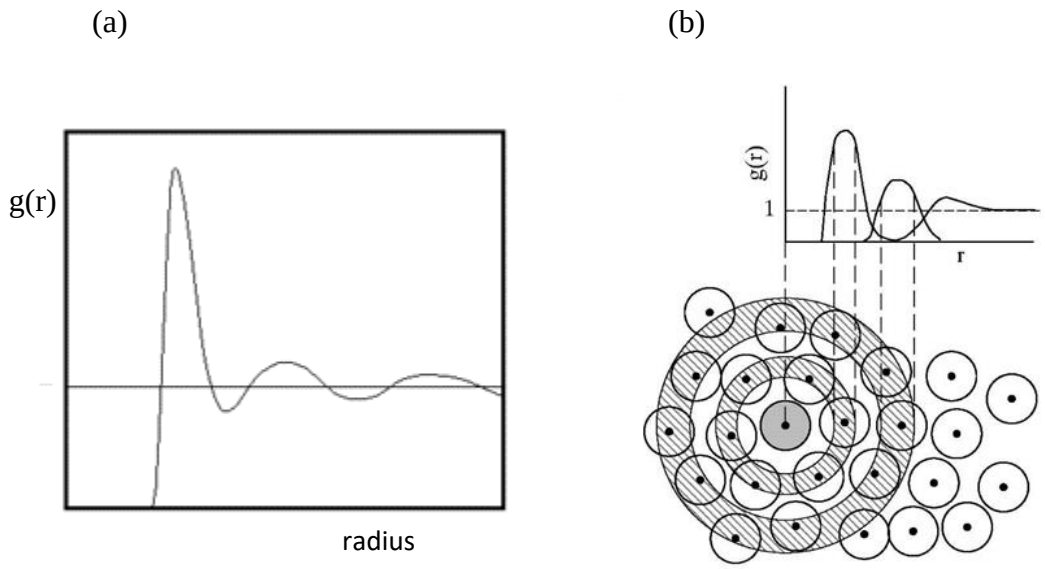

Figure 1.12 (a) A typical RDF of liquid. (b) Scheme of a two-dimensional fluid and its RDF. The first peak in the RDF corresponds to the first shell (nearest neighbours).The shallow second peak is the result of the more loosely packed second nearest neighbours. This figure is adopted from Ref. [81].

1.3.6 First principles optical properties calculation (GW+BSE)

The optical properties were calculated by using the many-body perturbation theory (MBPT), which can describe quasiparticle (QP) excitations in solids [82]. A quasiparticle contains the effects of all other particles under the perturbation of the incoming photons and/or other electrons involved in the spectroscopic process. The quasiparticles interact *via* a weakly screened Coulomb potential. The MBPT calculations were performed in three steps: (i) a ground-state DFT calculation; (ii) a GW [83] calculation to obtain the dynamic screening and corrected QP energies; (iii) solving the electron-hole (*e-h*) interaction in the Bethe-Slapter (BSE) on top of GW routines and calculating the optical absorption spectra.

In the GW approximation, G is the one-particle Green's function and W is the screened Coulomb interaction. $W=\varepsilon^{-1}\upsilon$ is a product of the Coulomb kernel (υ) and the inverse dielectric matrix ε^{-1}. The one-particle Green's function is the dynamical one-particle density matrix, which gives information on the single-particle excitation spectrum. GW was developed for the calculation of self-energy using the perturbative treatment on the XC potential of the KS equations. The QP energies (E_{nk}^{QP}) can be calculated by solving the following nonlinear system QP equation:

$$(T + V_{ext}(r) + V_H(r))\psi_{nk}(r) + \int \sum(r, r', E_{nk}^{QP})\psi_{nk}(r')\,d^3r' = E_{nk}^{QP}\,\psi_{nk}(r), \quad 1.90$$

where T is the kinetic energy operator, V_{ext} is the potential of the nuclei and V_H is the Hartree potential. Σ is a self-energy operator, which describes the many-body effects due to the exchange and correlation. Σ is defined as:

$$\sum(r, r', \omega) = \frac{1}{4\pi}\int d\omega' e^{i\omega'\delta}\, G(r, r', \omega)W(r, r', \omega). \quad 1.91$$

The QP energies are complex quantities describing the positions (ReE_{nk}) and widths (ImE_{nk}) of the QP peaks. The QP energies can be obtained from non-self-consistent GW approximation (G_0W_0). In the G_0W_0 approximation, the self-energy of the system is calculated while the wave functions of the KS calculation are not updated. The screened Coulomb interaction W is computed with the dielectric function using DFT eigenvalues. Partially or fully self-consistent GW can improve the QP energies. In the partial self-consistent calculation, only the G term is updated with each iteration, while the functions of the KS calculations are from the initial DFT calculations. A full self-consistent GW scheme, updates both G and W and gives better results, but also requires more computational cost.

In the G_0W_0 scheme, the QP energy, E_{nk}^{QP}, is calculated from the diagonal matrix elements of the QP equation:

$$E_{nk}^{QP} = \mathrm{Re}\left[\left\langle \psi_{nk} \middle| T + V_{ext} + V_H + \sum(E_{nk}^{QP}) \middle| \psi_{nk} \right\rangle\right]. \quad 1.92$$

The eigenvalues of the QP excitation energy can be solved by iteration:

$$E_{nk}^{N+1} = E_{nk}^{N} + Z\,\mathrm{Re}\left[\left\langle \psi_{nk} \middle| T + V_{ext} + V_H + \sum(E_{nk}^{N+1}) \middle| \psi_{nk} \right\rangle - E_{nk}^{N}\right]. \quad 1.93$$

The interaction starts from the DFT eigenvalues ε_{nk}. The $N+1_{th}$ iteration is related to the N_{th} iteration through the linearized equation. Z, the normalization factor, is calculated as:

$$Z_{nk} = \left(1 - \mathrm{Re}\left\langle \psi_{nk} \middle| \frac{\partial \sum(\omega)}{\partial \omega}\bigg|_{E_{nk}^{QP}} \middle| \psi_{nk} \right\rangle\right)^{-1}. \quad 1.94$$

The BSE takes into account the electron-hole interaction and gives an accurate solution to the absorption spectrum. In the absorption, one has to deal with neutral excitations due to the simultaneous creation of a quasi-electron and a quasi-hole, which interact in the system. This process is described as:

$$|s> = \sum_{v}^{e} \sum_{v}^{h} A_{vc}^{S} a_v^* b_c^* |0>, \quad 1.95$$

where 0> is the ground state of the many-electron system, a_v^* and b_c^* create quasi-electrons and holes and A_{vc}^{S} is the coupling coefficient. The two-particle Hamiltonian associated with the BSE is defined as:

$$(\varepsilon_c^{Qp} - \varepsilon_v^{Qp}) A_{vc}^{S} + \sum_{v'c'} \left\langle vc \middle| K^{eh} \middle| v'c' \right\rangle A_{v'c'}^{S} = \Omega^{S} A_{vc}^{S}. \quad 1.96$$

All the valence bands and a sufficient number of conduction bands are needed to construct the two-particle Hamiltonian. ε_c^{QP} and ε_v^{QP} are the GW QP energies for the valence and conduction bands respectively. Ω^S is the excitation energy. K^{eh} is the electron-hole interaction kernel including the repulsive electron-hole exchange and attractive screened electron-hole interaction.

$$\left\langle vc \middle| K^{eh} \middle| v'c' \right\rangle = \int d^3r d^3r' \psi_c^*(r) \psi_v(r) v(r,r') \psi_{c'}(r) \psi_v^*(r) - \int d^3r d^3r' \psi_c^*(r) \psi_v(r)\, W(r,r') \psi_{c'}(r) \psi_v^*(r). \quad 1.97$$

1.4 Description of the thesis

The following is a synopsis of Chapters 2 to 5:

Chapter 2 reports the design strategies to lower the formation pressure for extended X-CO_2/X-CO composed of sp^3 C and O atoms. These methods include the addition of a catalyst (H_2 or O_2) to solid CO_2 and CO molecular solids and photochemical activation. Although additions of H_2 and O_2 are shown to successfully lower the formation pressure, the photo-excitation is the most efficient method and lowered the formation pressure to 15 GPa and 1200 K for the polymerization reaction of solid CO_2. All new forms of X-CO_2/X-CO obtained from the studies are quenched recoverable with favourable energy densities of 12.60 kJ/g (CO_2+H_2), 11.50 kJ/g (CO+H_2), and 8.63 kJ/g (photo exaction of CO_2). The experimental conditions referenced in chapter 2 were provided from our collaborator Choong Shik Yoo, Department of Chemistry, Washington State University, Pullman, WA 99164-2816, U.S.A.

Chapter 3 presents results on the study of possible reactions between silica with CO_2 and H_2 under Earth mantle conditions at pressures from 1 GPa to 30 GPa. Both crystalline and amorphous solids based on -Si-O-C- linkage were obtained from the reaction between CO_2 with SiO_2 zeolite, cristobalite, and stishovite. H_2 is shown to react with quartz under pressure to form highly ionized water, similar to the highly compressed liquid.

Chapter 4 reports the results of the investigation of the structural evolution of pressure-induced amorphization (PIA) ice Ih, at pressures from 0.1 GPa to 3 GPa. A new crystalline phase with a sheared ice Ih transition prior to amorphization was discovered. The existence of the intermediate crystalline structure is due to a shear instability. The results suggest that the PIA is primarily governed by kinetics. The experimental results on the new crystalline phase is given by our collaborators Chuanlong Lin and Guoyin Shen, HPCAT, Geophysical Laboratory, Carnegie

Institution of Washington, Argonne, Illinois 60439, USA. An *ab initio*-based flexible and polarizable Thole-type TTM2.1-F water model was examined for simulation of water properties with or without NQEs by classical molecular dynamics and path integral molecular dynamics. The inclusion of NQEs is shown to weaken the hydrogen as compared to classical MD calculations; thus a decrease of 20 K was observed in the melting point of ice from the TTM2.1-F water model.

In Chapter 5, the research projects and major conclusions are summarized, with discussions on future perspectives.

Most of the work presented in this thesis has now been accepted or submitted for publication. I only presented my contributions. The references are as follows:

(1) **X. Yong**, H. Liu, M. Wu, Y. Yao, J. S. Tse, R. Dias, and C. S. Yoo, Crystal structures and dynamical properties of dense CO_2, *Proc Natl Acad Sci U S A* 2016, **113**, 11110-11115.

(2) Y. Yao, **X. Yong,** J. S. Tse, and M. J. Greschner Dihydrogen bonding in compressed ammonia borane and its roles in structural stability, *J. Phys. Chem. C*, 2014, **118**, 29591-2 9598 (Not included in this thesis)

(3) **X. Yong**, J. S. Tse and C. S. Yoo Solid-state polymerization of co_2 from catalytic photoexcitation: an *ab initio* molecular dynamic study, *J. Phys. Chem. C*, (Revision under review, manuscript ID: jp-2016-101574)

(4) Z. Futera1, **X. Yong**, Y. Pan, J. S. Tse, and N. J. English, Formation and properties of water from quartz and hydrogen at high pressure and temperature, *Earth Planet. Sci. Lett* (accepted with minor revision, manuscript ID: EPSL-D-16-01218)

(5) **X. Yong**, Y. Pan, J. S. Tse, and N. J. English, Van der waals-corrected density functional theory study of liquid water, and pressure-induced structural evolution of ice ih, *J. Chem. Phys*. (Submitted, manuscript ID: A16.11.0320)

(6) Y.J. Ryu; C.S. Yoo, M. Kim, **X. Yong**, J. S. Tse, K. Sung, E.J. Kim, "Hydrogen-Doped Polymeric Carbon Monoxide at High Pressure, *Chem. Mater*, (Submitted, manuscript ID: cm-2016-05060c)

(7) C. Lin, G. Shen, **X. Yong**, J. S. Tse, and G. Shen, Kinetically-controlled structural transformations in H2O ice at high pressures and 96-160 K, Science (submitted: aal5213)

CHAPTER 2

THEORETICAL STUDY ON EXTENDED CARBON DIOXIDE: FROM GREENHOUSE GAS TO NOVEL SOLIDS

2.1 Introduction

2.1.1 High pressure and materials science

High pressure techniques are becoming a convenient and powerful tool for the synthesis and design of new materials with unusual properties. Pressure can significantly alter the interatomic/intermolecular interactions in fluids and solids because mechanical work (PΔV) is added to the system. The additional energy helps to overcome the nuclear repulsions, and the electrons localized in the intramolecular bonds become less stable as the kinetic energies are raised at high density. At high enough pressure, when this externally applied energy is close to the bond energy, significant physical and chemical changes, such as chemical reactions and structural transformations, may occur. At high pressure and high temperature, the compression (PΔV) always lead to novel electronic states and structures in materials.

2.1.2 Novel energetic materials based on extended solids

Energetic materials are compounds with a high amount of stored chemical energy that can be harvested upon stimulation by heat, impact, shock, and spark, *etc*. These energetic materials have been used extensively in civilian and military applications such as airbags, fireworks, mining, munitions, and anti-missile decoy flares. Conventional energetic materials, *e.g.*, gasoline and cyclo-tetramethylene tetranitramine (HMX), are often molecular solids with strong intramolecular covalent bonds and weak intermolecular *vdW* interactions. The large disparity between the inter- and intra-molecular distances results in relatively low densities and open structures. These

materials have large equilibrium volumes due to *vdW* intermolecular interactions between neighbouring molecules, and almost 90% of the space is empty, *e.g.*, the space in HMX (see Figure 2.1). The intermolecular bonds are weak and not efficient for energy storage. The energy stored in these conventional energetic materials depends primarily on the strong covalent bonds of the individual molecules. Therefore, conventional energetic materials suffer from low density, low material strength, and high shock sensitivity. To develop new materials with enhanced performance and greater predictability and functionality but without negative environmental impacts has become a new paradigm in the research field of energetic materials. An ideal advanced energetic material would completely replace the *vdW* interactions with strong covalent bonds, such as those in main group IV compounds and diamond-like extended solids in three-dimensional (3D) network structures. Such 3D-network structures should have higher density and can store more energy through strong covalent bonds.

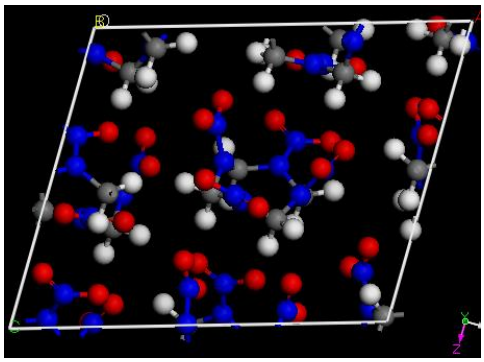

Figure 2.1 Structure of cyclo-tetramethylene tetranitramine (HMX) showing (~90%) empty space.

Low-Z elements are those in the first two rows of the periodic table. They are the most abundant components in the universe. The electronic and crystal structures formed from these elements are rather simple and well documented. However, studies have shown that most low-Z molecular solids, such as N_2, O_2, CO_2, and CO, are not stable under high pressure and high temperature and can be transformed to non-molecular extended solids by compression [1,84-87].

These extended solids are characterized by a 3D network of strong covalent bonds [2,20,86-92]. The high pressure phases are stabilized by the formation of chemical bonds between the elements at the expense of weakening the multiple bonds. The extended solids formed under extreme conditions may or may not transform back to the molecular phase at ambient pressure. Moreover, most of these extended phases are chemically inert and expected to exhibit novel thermal, mechanical, and optical properties. If the structure can be stabilized, they are chemically monolithic explosives containing both oxide (O) and fuel (C, N, H, *etc.*) atoms. Thus, pressure-induced extended solids offer new opportunities for the development of novel energetic materials [2].

Among the low-Z molecules, CO_2 is of vital importance because of its abundance in nature. CO_2 is a prototypical π bonded compound (C=O) with *sp* hybridized carbon σ orbitals. The orbital hybridization can be altered by pressure. Although the molecular structure of CO_2 is simple, in the condensed phase it can exist in several high pressure polymorphic forms, ranging from molecular solids to fully extended covalent solids (X-CO_2), the latter composed of sp^3 carbon and oxygen atoms [91]. These polymorphs have very different crystal structures. At present, the high pressure and high temperature phase diagram of CO_2 is still controversial [93,94]. A proposed phase diagram [94] is shown in Figure 2.2. At atmospheric pressure and temperature, the molecular solid phase I of CO_2, commonly known as dry ice, has a cubic structure with the space group, *Pa3* [95] and is a *vdW* crystal [91,96]. When compressed between 12 GPa and 22 GPa at room temperature, phase I transforms into a molecular orthorhombic phase (*Cmca*) III [97-100]. A second molecular phase (phase VII) [93] was found at high temperatures by heating CO_2-III to near the melting point. Above 40–60 GPa, molecular solids transform into non-molecular phases. Several non-molecular extended phases of CO_2 have also been reported, for example, tetrahedral bonded 3D

CO_2-V [85,101,102], distorted octahedral CO_2-VI, coesite-like *c*-CO_2 [103], and silica-like amorphous CO_2 [86]. X-CO_2 was first discovered by heating molecular solids of CO_2 (CO_2-III) to 1800 K at above 41 GPa. It was proposed to have a tridymite-like $P2_12_12_1$ structure [85,102]. However, following a different synthetic path, that is, from heating phase III at 20 GPa, then compressing the product to 41 GPa and then raising the temperature to ~1800 K, a different polymeric phase in a β-cristobalite-like *I*-42*d* structure was obtained [20,101]. In X-CO_2, the C=O bonds are completely broken to form C-O-C bonds with sp^3 hybridized C and O atoms. X-CO_2 is a fundamentally new material and is expected to possess novel properties, such as optical nonlinearity, low compressibility, and high energy density. However, the synthesis conditions [85,101,104] are too severe for practical industrial production. For the practical use of X-CO_2, it is important to find an effective approach to lowering the formation pressure and to recover it under ambient conditions.

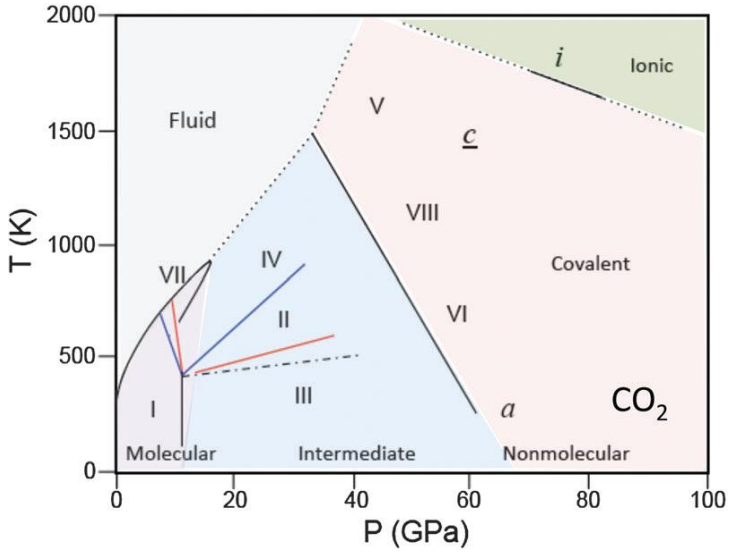

Figure 2.2 High pressure and high temperature phase diagram of CO_2 solid. This figure is taken from Ref. [94]. The phase boundaries are hypothetical.

Carbon monoxide (CO) is another important low-Z compound, where C and O are bonded through a triple bond. The C≡O bond, however, can be easily altered by pressure as it has been

shown that solid CO is more sensitive to pressure than CO_2. At ambient and low temperatures, condensed CO has a cubic $P2_13$ structure [105]. At 4 GPa, it transforms into a molecular solid with space group $Pm3n$ [106]. After further compression to 5 GPa and 300 K [84,107], the molecular phase transforms to an extended polymeric phase (X-CO). The onset of transition to a non-molecular phase increases to 12.0 GPa at a lower temperature (15 K) [108]. Therefore, solid CO is another promising candidate for the synthesis of fully extend solids composed of sp^3 hybridized C and O atoms.

Most of the high pressure X-CO_2 polymorphs can only be stabilized at high pressure and easily revert to the molecular state upon the release of pressure. In order to exploit the highly energetic X-CO_2 for practical applications, it is essential to (i) reduce the formation pressure and temperature (*i.e*. synthesis conditions) to be amenable to the current industrial capability (*e.g.*, a few GPa); (ii) enhance the stability of the product under ambient conditions. To achieve these objectives, it is essential to develop alternative synthetic pathways. Theoretical electronic structure calculation is an important tool for developing new strategies to understand the reaction mechanisms and the chemical bonding in the products. Computational modelling is now able to facilitate the study of chemical reactions under extreme conditions that are not accessible by experiments. The analysis of the trajectory of an MD simulation containing the temporal atomic positions can reveal the reaction pathway(s). This chapter reports several strategies that were investigated to lower the formation pressure for the synthesis of X-CO_2 and X-CO. We studied the effect of doping with small molecule (H_2 and O_2) and photo-excitation. In addition, the possibility of recovering CO_2-V at ambient conditions was investigated.

2.2 Solid-state polymerization of CO_2/CO from H_2/O_2-doping

To synthesize fully extended X-CO_2/CO solids composed of sp^3 hybridized C and O atoms at milder temperature and pressure, it is necessary to find a way to promote the chemical reactions by decreasing the contact between molecules in the solid. However, solid-state synthesis is often limited by the rate of atomic/molecular diffusion. Therefore, an alternative method is to increase the atomic diffusion rate which can be achieved by raising the temperature or by compression. It is also possible to enhance the chemical reaction rate through doping with small molecules as they can create defect sites with empty space. It has been shown that doping with impurity atoms is an effective way to change the electronic structure and bandgap of some molecular solids [109,110]. Furthermore, the compression of doped molecular solids has also been shown to produce novel compounds [110-112]. In some cases, polymeric compounds have been synthesized in the liquid and solid states without additional catalysts or solvents.

Hydrogen is a special element in the periodic table. It is the smallest and lightest element having the simplest electronic configuration. Furthermore, H_2 is a good reducing agent. Since X-CO_2 is expected to be a wide bandgap solid, this motivated the study of hydrogen activation on polymerization of CO_2. O_2 is another important small molecule and is a good oxidant. However, the mixture of molecular solids has reduced molecular mobility at high pressure, which may prevent the formation of thermodynamically stable products. These barriers can be overcome by heating the system at high pressure.

2.2.1 Polymerization of solid CO_2 from H_2 doping

Computational methodology

NPT AIMD calculations were performed. The VASP program was used for all the calculations. The PBE functional was employed, and the electron orbitals were expanded in the plane wave basis set. A plane wave basis set with an energy cutoff 400 eV was used. In view of the large supercell and that the system is a large gap insulator, only one *k*-point (Γ) was used to sample the Brillouin Zone. We started from a supercell consisting of 80 atoms ($16CO_2$:$16H_2$) constructed from the orthorhombic *Cmca* structure of CO_2-III. This CO_2-H_2 model was constructed by replacing randomly chosen CO_2 molecules with H_2. The stoichiometry was chosen to reproduce the experimental conditions of our collaborator. Simulations were performed at 41 GPa and 400 K, similar to the experimental conditions. A time step of 1.0 fs was used in the integration of the equation of motions. To study the possibility of recovering the product under ambient pressure, the simulated structure at high pressure and high temperature was quenched to 0 GPa and 300 K through an *NPT* simulation. To estimate the energy release of the quench-recovered product upon decomposition, the length of the longest axes of the CO_2-H_2 model system was doubled to create a vacuum/solid interface. The energy released was calculated from the difference in the total energies of the system at 80 K and 300 K at 0 GPa from *NPT* calculations. All AIMD simulations were performed for at least 10 ps.

Results and discussions

To study the H_2-activated synthesis of X-CO_2 from the polymerization of CO_2, AIMD simulations in the *NPT* ensemble were performed. The reaction between CO_2 and H_2 was found at 41 GPa and 400 K. To understand the reaction, we analyzed the structure of the product and the

atomic trajectories obtained from the simulation. The structure of the product is shown in Figure 2.3a–b. The product is a form of 3D connected X-CO_2 with a chemical formula $C_{15}O_{30}H_{15}$ consisted of a C-O single-bonded (C-O average bond length at 1.4 Å, Table 2.1) main chain (red chain in Figure 2.3a) and three side branches, S1, S2, and S3. S1 has a rather complicated structure composed of fused six-membered rings bridged through the etheric oxygen atom. S2 is *di*-carbonate (-O-(C=O)-O-(C=O)) and S3 is a formic acid ester (HO(C=O)-O-). The product has a clear 3D connected structure with most C tetrahedrally bonded to O and/or H atoms and/or hydroxyl group except for a few CO_3. In addition, hydrogen bonding between the O atom and the -OH group helps to stabilize the extended X-CO_2 (Table 2.1). The formation of X-CO_2 can also be identified from the calculated vibrational density of states (Figure 2.4) calculated from the Fourier transform of atomic velocity auto-correlation functions. The broad peaks at 1000–1050 cm^{-1} are the C-O-C bending vibrations. The peak at around 650 cm^{-1} is assigned to the CO_4 tetrahedral. The broad peak at 1300–1500 cm^{-1} is assigned to C-H bending modes. When the product was quenched to 300 K and 0 GPa, the extended structure obtained at high pressure was maintained (Figure 2.5), showing it is metastable under ambient conditions. To mimic the decomposition process, an *NPT* MD simulation at 0 GPa and 300 K was performed on the product constructed with the length of the longest axes of the original model system doubled to create a vacuum region above the solid surface. The decomposed product was found to be a mixture of CO_2, H_2, and other C-O small molecules (Figure 2.3c). The energy released was calculated to be 11.50 kJ/g.

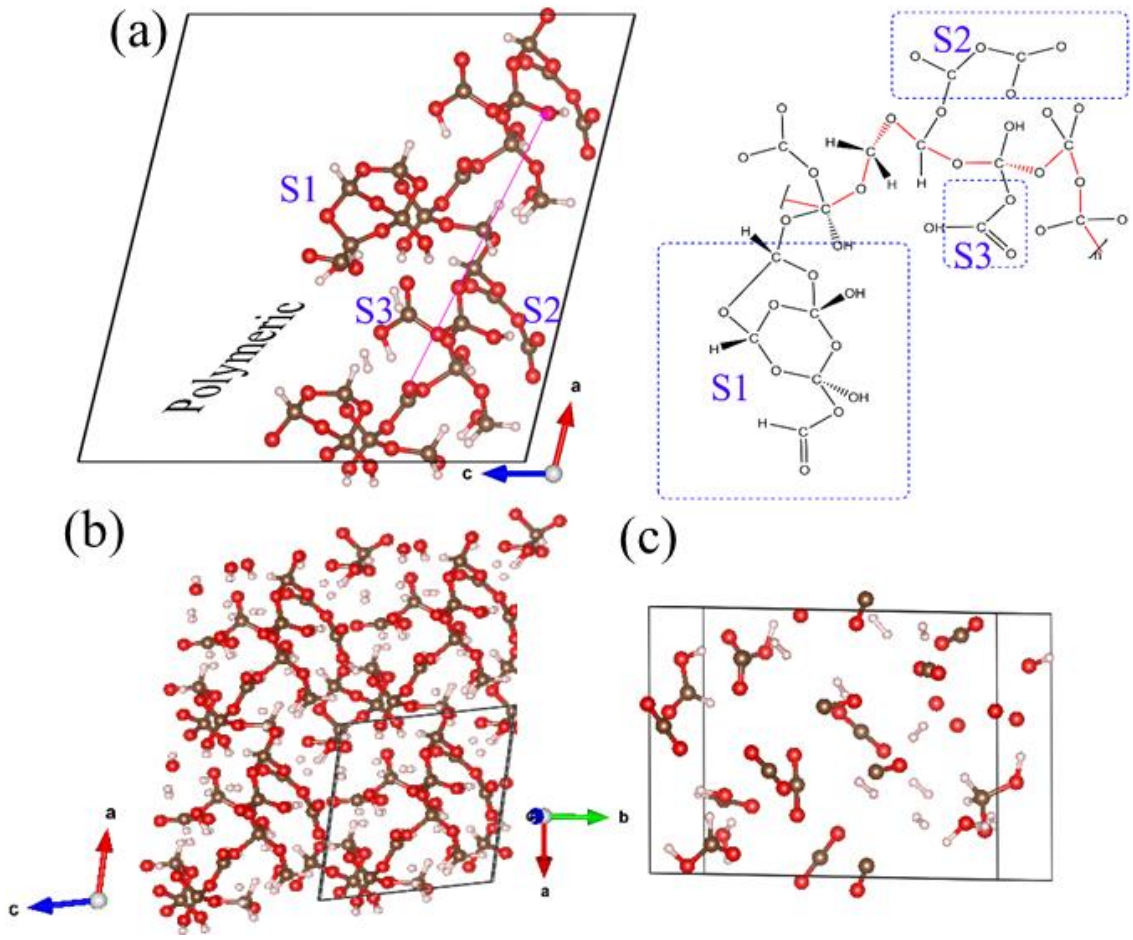

Figure 2.3 (a) Sketch of the extended X-CO_2 obtained from the CO_2 and H_2 polymeric reaction at 41 GPa and 400 K. (b) The projected structure of the same X-CO_2. (c) The decomposition products of X-CO_2. (C in grey, H in white, and O in red).

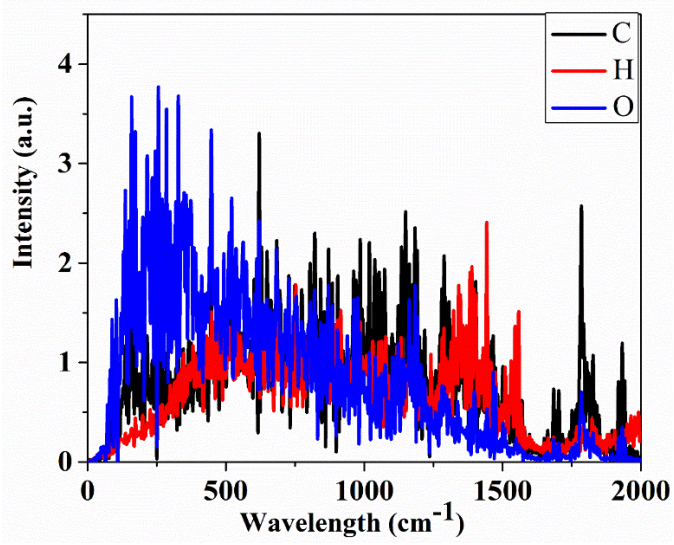

Figure 2.4 Vibrational density of states calculated from the Fourier transform of the atomic autocorrelation functions for the extended X-CO_2 obtained from the CO_2 and H_2 polymeric reaction at 41 GPa and 400 K.

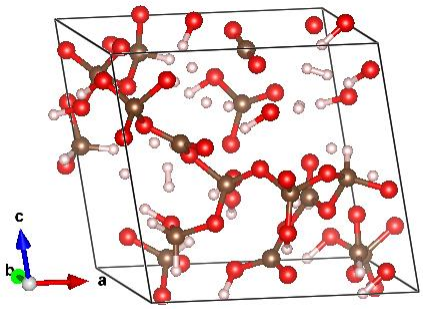

Figure 2.5 Quench-recovered structure of the extended X-CO_2 obtained from the CO_2 and H_2 polymeric reaction at 41 GPa and 400 K to ambient conditions. (C in grey, H in white, and O in red).

The MD trajectory was examined to reveal the reaction mechanism. The polymerization reaction was found to occur in six steps. Initially, the volume of the model system reduced gradually with compression (Figure 2.6a–b). Then, the reaction was initiated from a bent CO_2 molecule (Figure 2.7a) where the C orbitals changed from *sp* to sp^2 (P1 in Table 2.2). Upon further compression, the C=O distance elongated as the intermolecular separation was reduced. This

process was followed by the addition of H_2 to the C=O bond of the bent CO_2 (Figure 2.7b and P2 in Table 2.2). The H-addition increased the bent O-C-O angle to 103°. The H_2CO_2 and HCO_2 units were then available for further reactions. Subsequently, the HCO/H_2CO_2 groups reacted with another CO_2 through bonding between O atom of the HCO/H_2CO_2 and C atom of the CO_2 (Figure 2.7c–d and P3–P4 in Table 2.2). In this way, additional -O-C-O-C linkages were formed when more and more CO_2 molecules were involved in the reaction (Figure 2.8a and P5–P6 in Table 2.2). At around 5.4 ps, some of the CO_3 units were forced to twist (Figure 2.8a) thus breaking the π bonds. This resulted in the formation of the tetrahedral CO_4 (Figure 2.8b). Concomitantly, a sudden decrease in volume was observed (Figure 2.6b). From 5.4 ps to around 6.0 ps, more CO_4 units were formed. At 7.7 ps, the structural model was almost completely composed of CO_4, and no more significant changes were observed. The polymerization can be described as a reaction between O and C atoms from two neighbouring units arranged vertically with respect to each other. The orbital interaction diagrams in Scheme 2.1-2.3 indicate that the C orbital hybridization had changed from *sp* to sp^2 (P2) and then to sp^3 (in P3–P6). This change is consistent with the changes in the C-O bond length (Table 2.1) in which it increased from 1.15 Å in CO_2 to 1.40 Å in the product.

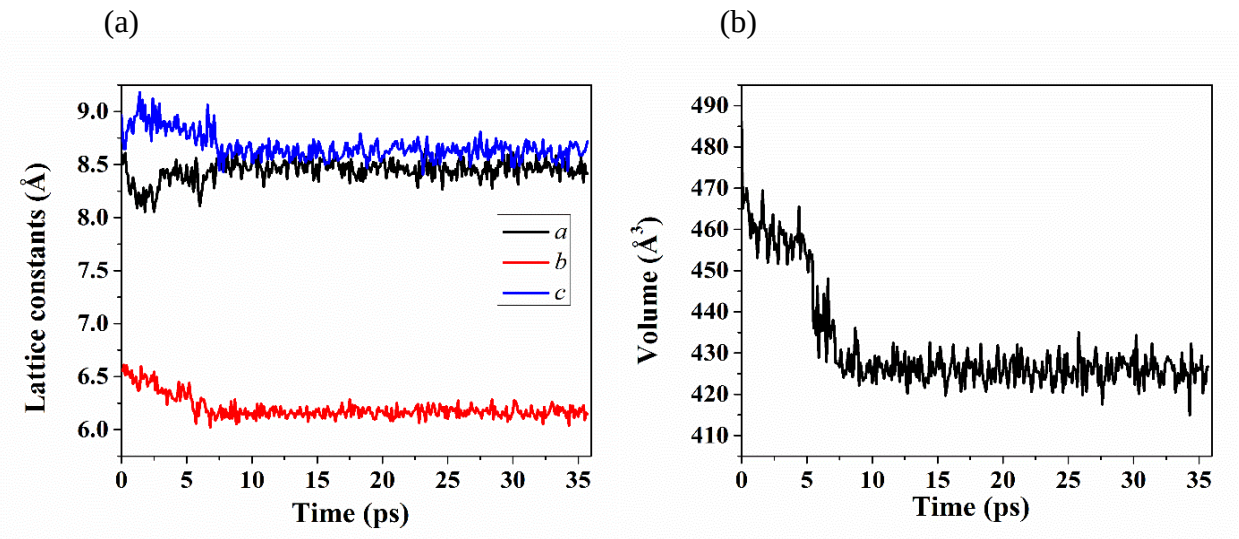

Figure 2.6 Evolution of the (a) lattice constants and (b) lattice volume of the CO_2-H_2 model with time in the *NPT* calculation at 41 GPa and 400 K.

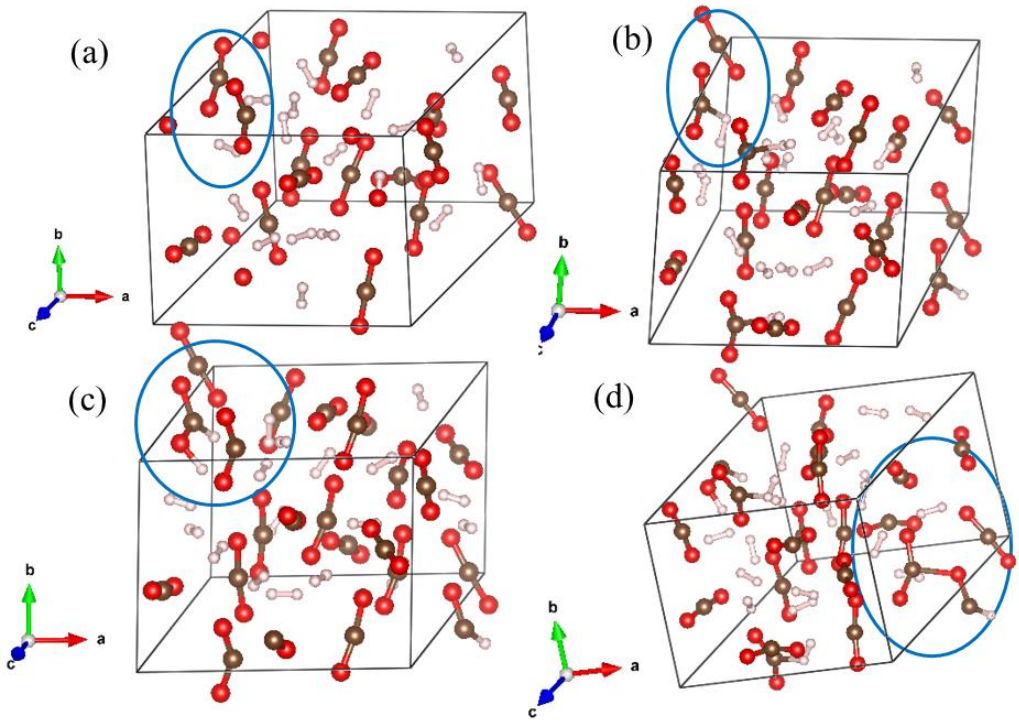

Figure 2.7 Snapshots of the CO_2-H_2 model from the *NPT* simulation at 41 GPa and 400 K at step (a) 20, (b) 108, (c) 148, and (d) 594. The blue circles highlight the structural changes as described in the text. (C in grey, H in white, and O in red).

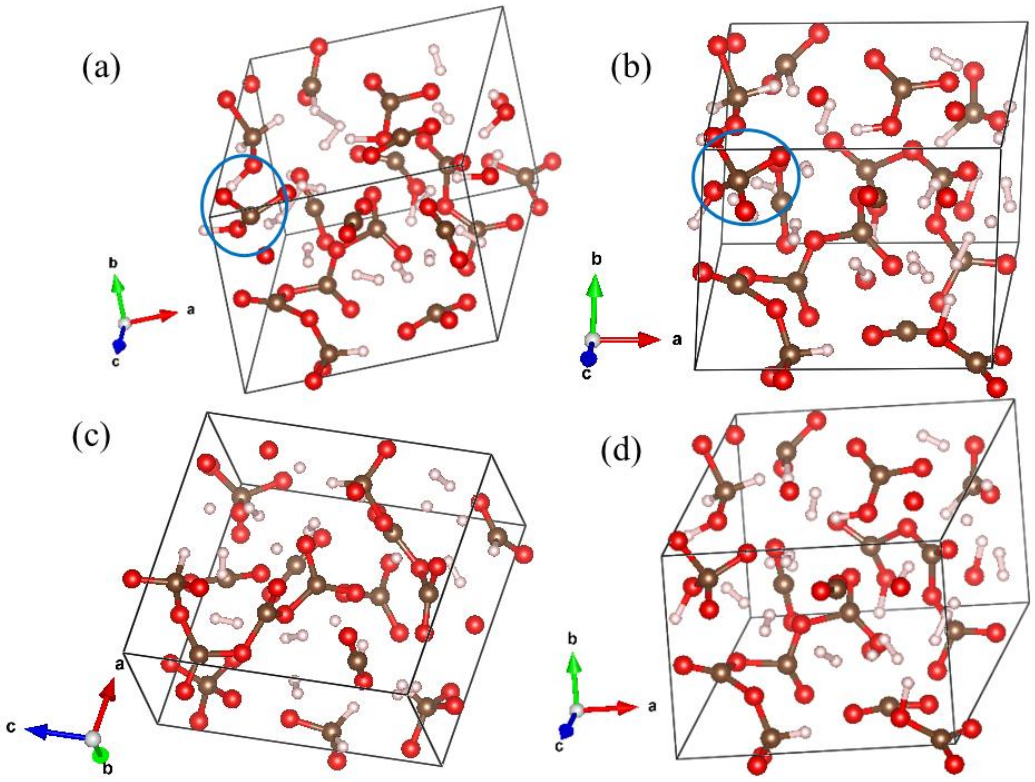

Figure 2.8 Snapshots of the CO_2-H_2 model from the *NPT* simulation at 41 GPa and 400 K at step (a) 5490, (b) 5570, (c) 5590, and (d) 7700. The blue circles highlight structural changes as described in the text. (C in grey, H in white, and O in red).

Table 2.1 Selected bond lengths in the X-CO_2 obtained from the CO_2 and H_2 polymeric reaction at 41 GPa and 400 K

	Bond length (Å)	notes
C-O	1.40	Single bonds
C-H	1.08	
O-H	0.96–1.38	Hydrogen bonding interactions exist

Table 2.2 The primary reactions of the CO_2 and H_2 polymeric reaction at 41 GP and 400 K: CO_2 re-hybridization and H_2 addition

Re-hybridization	P1	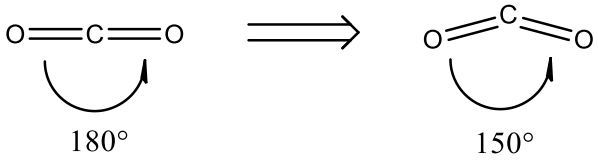

H_2-addition	P2	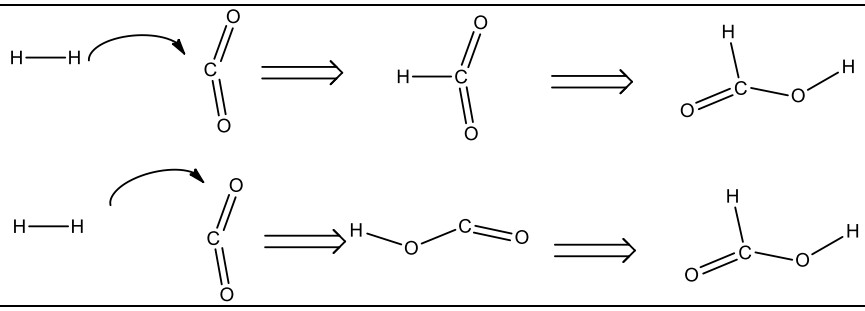

Table 2.3 Summary of the polymerization process in the CO_2 and H_2 polymeric reaction at 41 GP and 400 K

P3	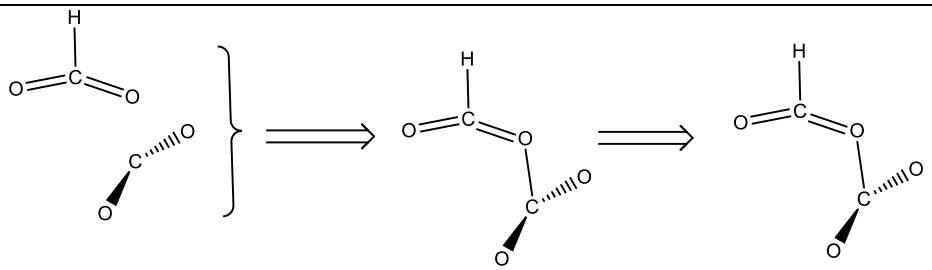
P4	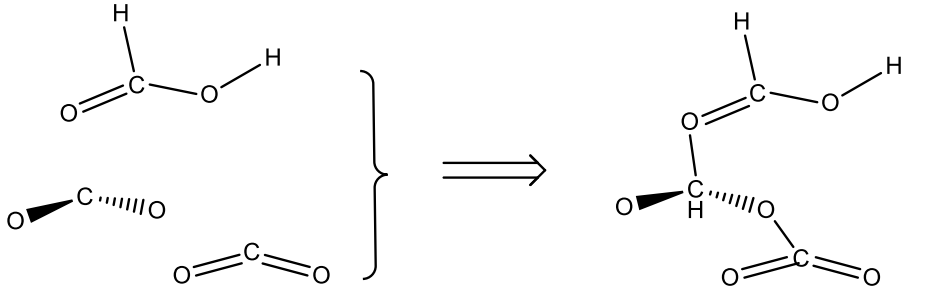
P5	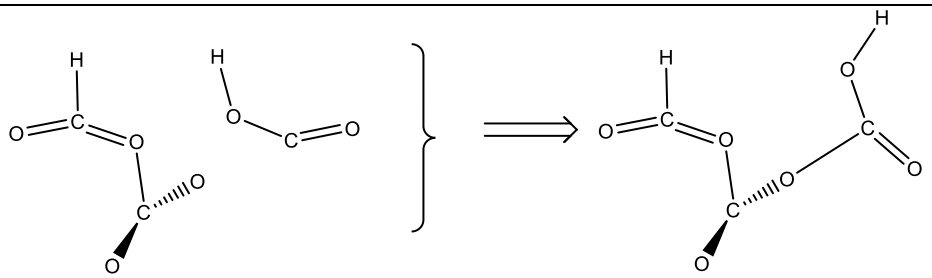
P6	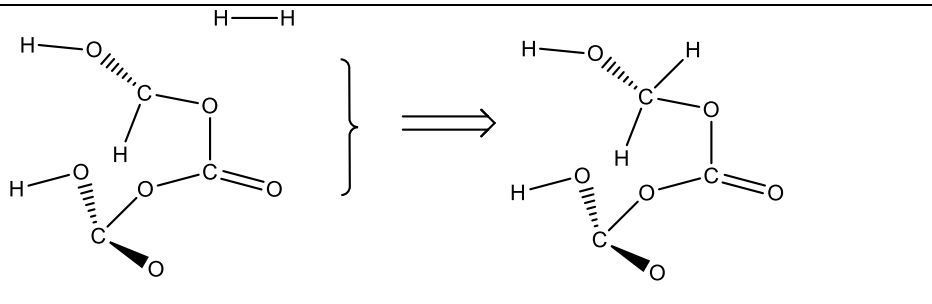

Scheme 2.1 Orbital interaction diagrams for the primary reactions 1 and 2 of the CO_2 and H_2 polymeric reaction at 41 GP and 400 K

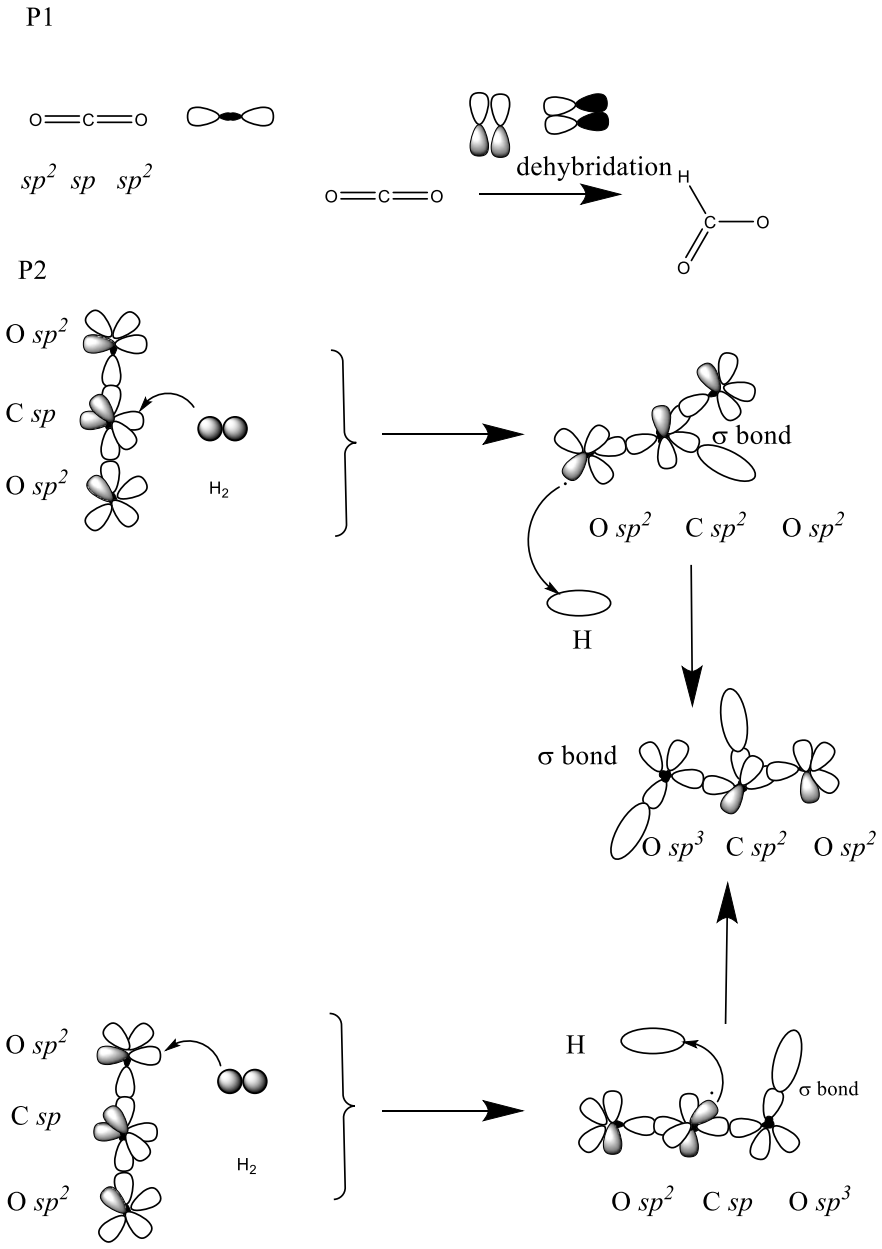

Scheme 2.2 Orbital interaction diagrams for the primary reaction 3 in the CO_2 and H_2 polymeric reaction at 41 GP and 400 K

P3

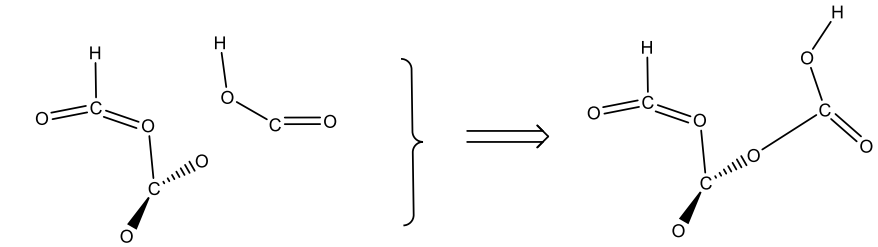

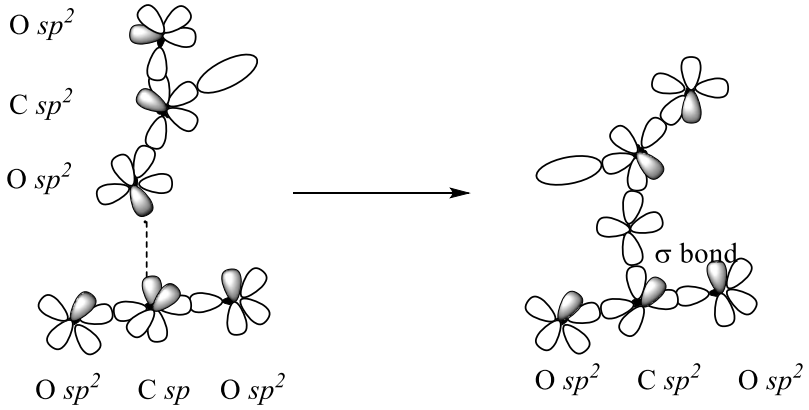

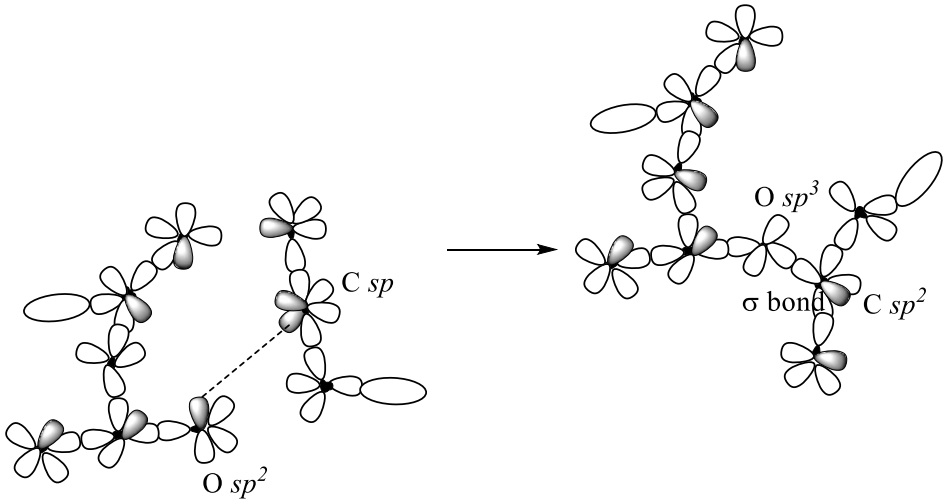

Scheme 2.3 Orbital interaction diagrams for the primary reaction 3 in the CO_2 and H_2 polymeric reaction at 41 GP and 400 K

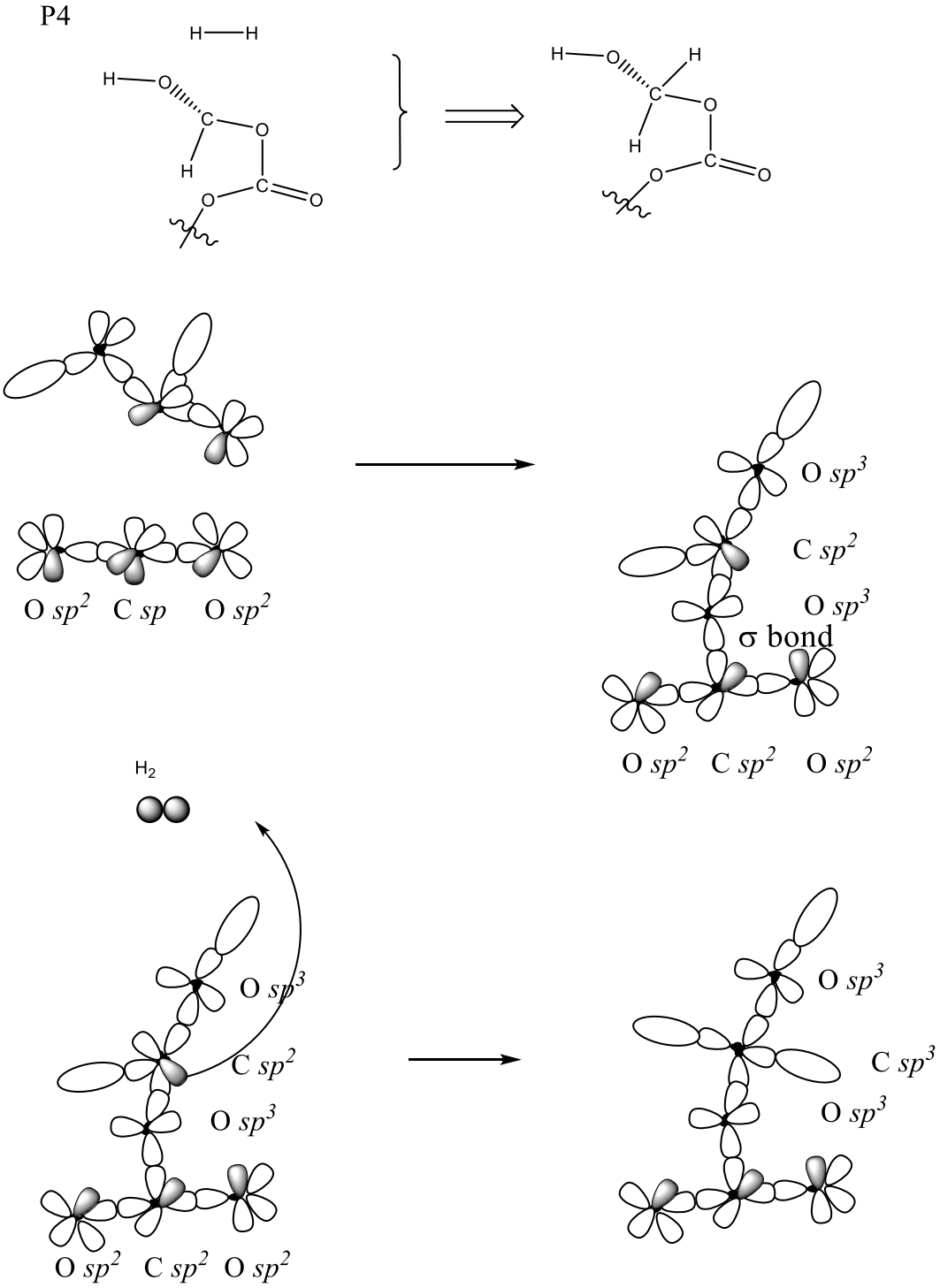

Conclusions

In summary, *NPT* AIMD calculations were used to investigate the synthesis of X-CO_2 from the H_2-activated polymerization of solid CO_2. An extended form of X-CO_2 was obtained. The extended structure is metastable and can be quench-recovered to ambient conditions. The estimated energy density is 11.50 kJ/g. The polymeric sequential reactions can be described as: (i) a reaction between the C s*p* and H 1s orbitals; (ii) a reaction between O sp^2 and H 1*s* orbitals; (iii) a reaction between C *sp* and O sp^2 orbitals, and (iv) a reaction between C sp^2 and H 1*s* orbitals.

2.2.2 Polymerization of solid CO from H_2 doping

From the study presented above, we have successfully demonstrated that the polymerization of solid CO_2 can be achieved by H_2 doping. However, the reaction conditions at 41 GPa and 400 K are still too high for practical purposes. An important detail obtained from the analysis is that the reaction was initiated by H_2-addition to the C=O π bonds that changed the hybridization of the C atom. Furthermore, it is shown that the smaller H_2 molecule creates more empty spaces to facilitate nearest neighbouring CO_2 to move closer. Solid CO is a simple molecular system with multiple π bonds and can easily be polymerized under very low pressure. Hence, H_2-doping may enhance the formation of an extended solid.

Computational methodology

The static geometry optimization method and AIMD simulations were both used in the study. Static structural relaxations at 0 GPa, 5 GPa, 8 GPa, 10 GPa, 15 GPa, and 18 GPa were performed on a CO-H_2 model consisting of a mixture of 30 CO and 3 H_2 molecules, which was constructed from the $P2_13$ ambient structure of solid CO (Figure 2.9), by using the FIRE method

[113] implemented in SIESTA [32]. FIRE stands for fast inertial relaxation engine, which is used for a structural relaxation-based MD scheme. In this scheme for structural minimization, the kinetic energy is removed from the system. The atomic positions are relaxed using an MD integrator and often to the steepest descent method. During the relaxation, temporal structural positions are accumulated in a trajectory file, which offers information on the structural changes and can be used to study the possible reaction pathway(s). To study the possibility of recovering the product at ambient pressure, the product formed at high pressure in the structural optimization was relaxed to 0 GPa, again using FIRE method. The PBE exchange-correlation functional and localized atomic double-zeta plus polarization (DZPD) basis sets are used to represent the electron orbitals in which the valence atomic orbitals are expanded with a polarized basis function with two exponents. In view of the large supercell and that the system is a large gap insulator, only one *k*-point (Γ) was used to sample the Brillouin Zone. To calculate the energy released from the quench-recovered product upon decomposition, once again length of the longest cell axes of the model was doubled to create a vacuum/solid interface. The energy released was calculated from the energy difference at 80 K and 300 K at 0 GPa from *NPT* AIMD calculations by the VASP code. To investigate whether the reaction product would undergo further structural changes at higher pressure, *NPT* AIMD simulations were performed at 20 GPa, 40 GPa, and 60 GPa and at different temperatures, (*i.e.* 300 K, 500 K, 1000 K, 1500 K, and 2000 K). In this case, the PBE exchange-correlation function was used, and the electron orbitals were expanded by PW basis sets. A time step of 1.0 fs was used in the integration of the equation of motions.

Results and discussions

To investigate the possibility of forming X-CO from the polymerization of CO using the H_2-catalyst, static geometry optimizations were performed. Calculations at pressures at 5 GPa and 8 GPa showed that no chemical reaction occurred (Figure 2.10a–b). The main effect of the pressure in this pressure range was to simply shorten the *b* and *c* cell axes (Figure 2.11a) of the solid. The change in the lattice parameters can be explained from the packing of CO. In the initial model, the CO molecules were mainly packed along the *b* (Figure 2.9a) and *c* (Figure 2.9c) axes through π–π interactions. Along the *a* direction (Figure 2.9b), neighbouring CO molecules were arranged in a head-to-tail fashion, *i.e.* the C atom of one CO is close to the O atom of the neighbouring CO. Hence initial compression broke the π–π interactions between the CO molecules in the *bc* plane. The π bonds of CO were broken and CO started to react with the neighbours forming a polymer structure (Figure 2.10c) at 10 GPa. The onset of the reaction was signaled by a sudden decrease in the lattice constants and volume (Figure 2.11a–b). For pure CO, the polymerization pressure was predicted to be 15 GPa at low temperature [114]. Therefore, the catalyst lowered the formation pressure by 5 GPa. However, even at 10 GPa, H_2 remained as a molecule and did not directly participate in the polymerization reaction. The product was a polycarbonyl polymer consisting of -(C=O)-(C=O)- groups, where the C-C and C=O distances were around 1.50 Å and 1.20 Å, respectively. This polycarbonyl polymer structure is similar to that formed in pure poly-CO found by X-ray diffraction [108] and from a previous theoretical prediction [114]. The C-C in the chain was single-bonded while the C=O was a π bond. At 15 GPa, one of the H_2 started to dissociate and C-H bonds were formed *via* the H-addition to the C=O bond (Figure 2.12a). The other two remaining H_2 did not react and remained in the molecular state. The final product was composed of two types of planar polymer chains (Figure 2.13): CO $(C_{15}O_{15})_n$ and a mixed CO-H_2 moiety

with formula $C_{11}O_{11}H_2$. The chains formed two distinct alternated molecular layers. Layer 1 was a polycarbonyl polymer composed of -(C=O)-(C=O)- (Figure 2.14a) and layer 2 was a hydroxyl-substituted polycarbonyl polymer (Figure 2.14b) arranged perpendicular to the *bc* plane along the crystallographic *a* direction. The -(C=O)- carbonyl groups had an average C=O bond length of 1.21 Å. The C-C contacts were all single bonded with an average length of 1.50 Å. Within layer 1 and layer 2, the chains were stacked through π-π interaction between the C=O double bonds (Figure 2.14a). Since only one H_2 was involved in the addition reaction to C=O (Figure 2.12a), there was no obvious change in the bond distances of C=O and C-C. In the polycarbonyl chains in layer 1 (Figure 2.14a), each C was bonded to 2 C and one O. In the hydroxyl-substituted polycarbonyl chains in layer 2 (Figure 2.14b), where the H-addition to C=O occurred, each C bonded to 2 C and one O, except that a four-coordinated C in the structure was bonded to one H, one O, and two C and the other four-coordinated C was bonded to 2 C, one O, and a hydroxyl group. These chains in layer 2 were bridged by C-O-C when the addition reaction occurred (Figure 2.14b). When the system was compressed further to 18 GPa, little change in the structure was observed (Figure 2.12b). The main effect was to bring the chains in the same layer closer. The spacing in the *c* direction between the two chains within the same layer decreased from 2.66 Å in layer 1 (2.64 Å in layer 2) at 15 GPa to 2.41 Å in layer 1 (2.51 Å in layer 2) at 18 GPa with a monotonic decrease in the volume (Figure 2.11a–b). When the high pressure X-CO was recovered to 0 GPa, the extended structure was maintained (Figure 2.15a). As described above the decomposition process was mimicked by *NPT* MD simulations at 0 GPa and 80 K and 300 K on a model where the length of the longest lattice was doubled. The decomposed product was found to be a mixture of CO, H_2, and HCO_3 (Figure 2.15b). The energy released was estimated to be 12.60 kJ/g.

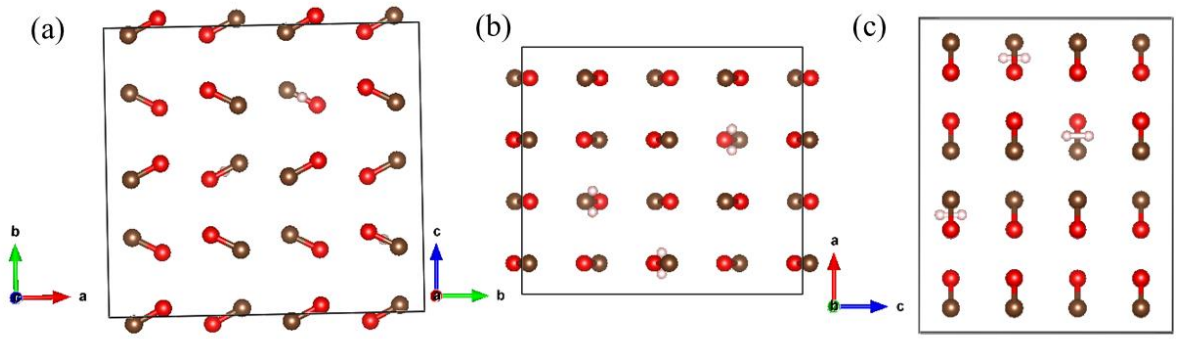

Figure 2.9 Projected structures of the CO-H_2 initial model in (a) *ab*, (b) *bc*, and (c) *ac* planes. (C in grey and O in red).

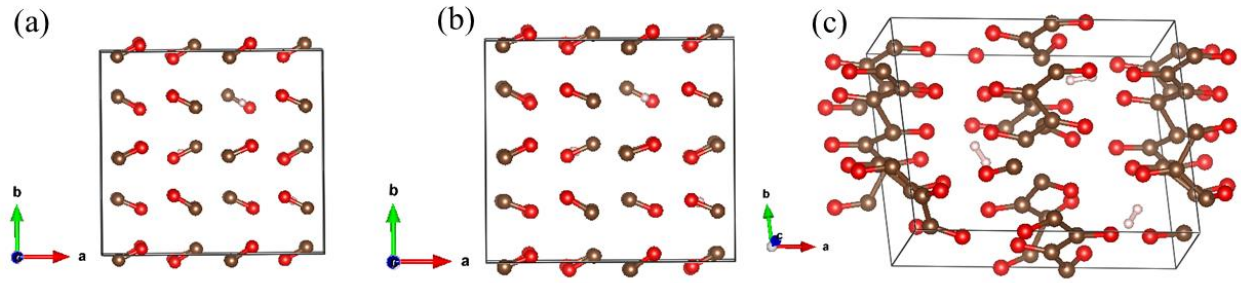

Figure 2.10 Structures of the CO-H_2 model optimized at (a) 5 GPa, (b) 8 GPa, and (c) 10 GPa. (C in grey and O in red).

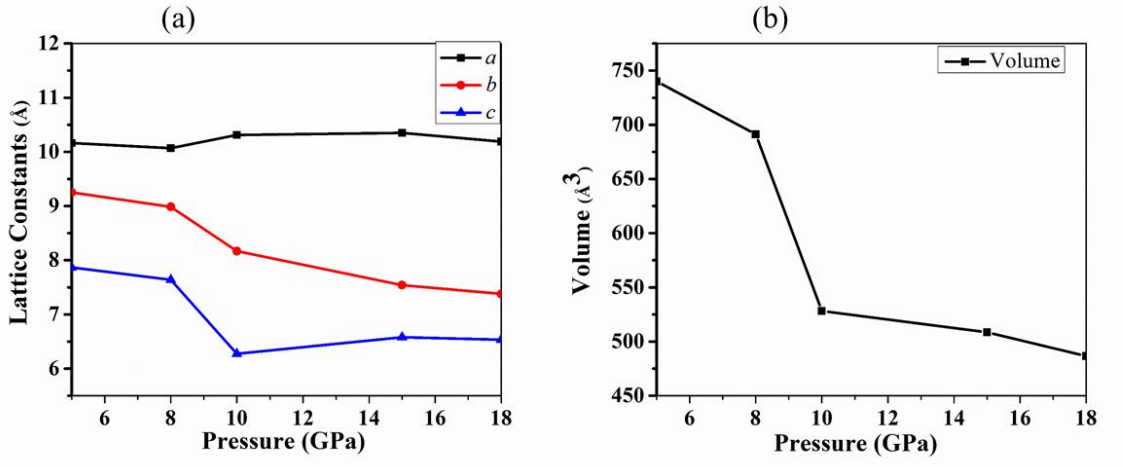

Figure 2.11 Plots of the lattice (a) constants and (b) volume of the optimized CO-H_2 model at 5 GPa, 8GPa, 10 GPa, 15 GPa, and 18 GPa.

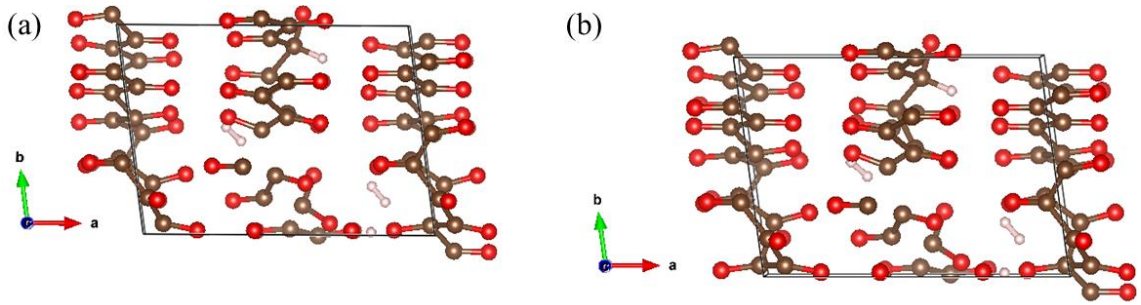

Figure 2.12 Structures of the CO-H_2 model optimized at (a) 15 GPa and (b) 18 GPa. (C in grey and O in red).

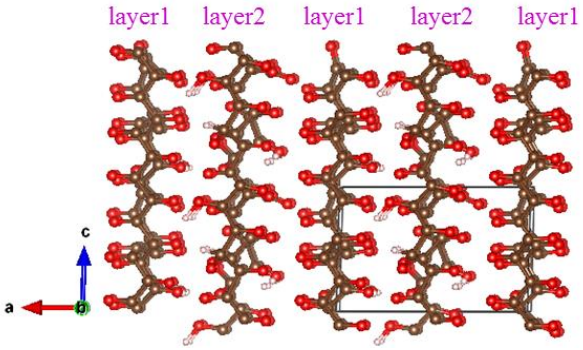

Figure 2.13 Structure of the CO-H_2 model optimized at 15 GPa composed of two distinct alternate polymer layers. (C in grey and O in red).

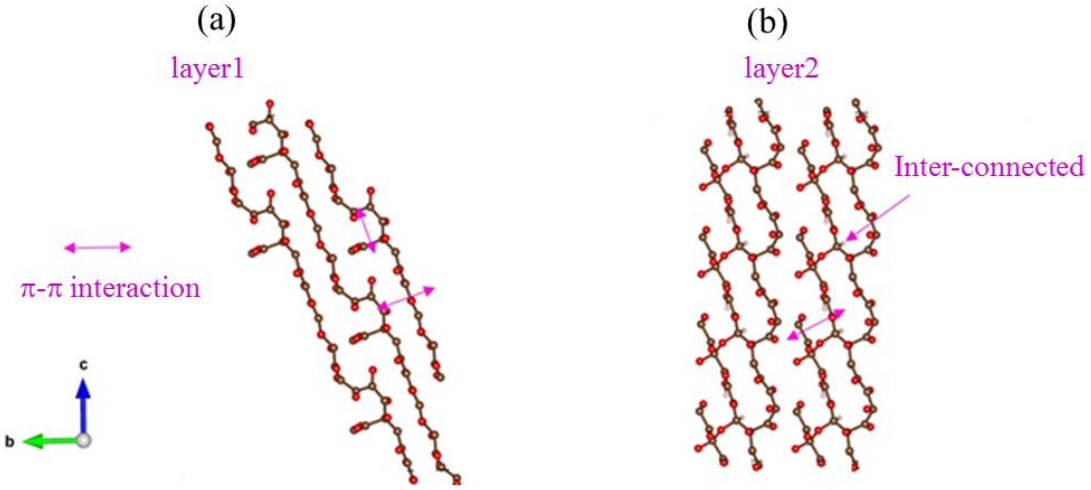

Figure 2.14 Depiction of (a) the π-π intermolecular interaction between to C=O double bonds in layer 1 (polycarbonyl), and (b) the π-π intermolecular interaction between two C=O double bonds and the O-bridged chain in layer 2 (hydroxyl-substituted polycarbonyl) of the X-CO obtained at 15 GPa. (C in grey and O in red).

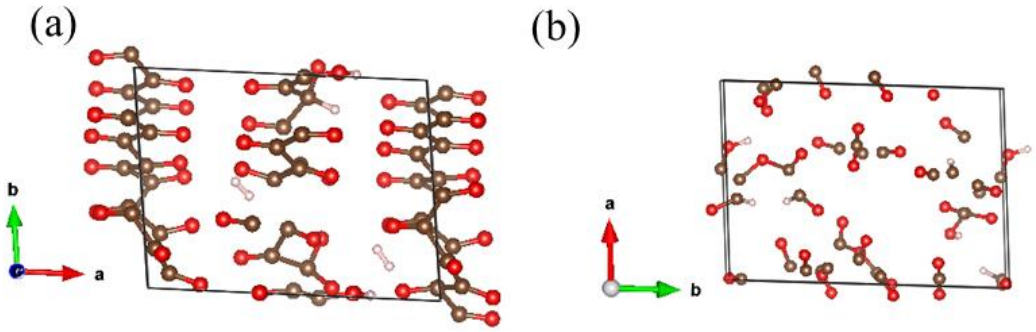

Figure 2.15 (a) Quench-recovered X-CO at ambient pressure. (b) The decomposition products of X-CO from geometry optimization. (C in grey and O in red).

To understand the reaction mechanisms, we analyzed the temporal atomic positions collected in the trajectories on the static compression. At low pressure from 5 GPa to 8 GPa, the main effect was the reduction of the unit cell volume (Figure 2.11a–b), and no reaction was observed. At 10 GPa (Figure 2.16a), neighbouring CO molecules were brought closer together and the C≡O triple bonds were broken. The CO molecules started to react through the orbital interaction between the C of two neighbouring CO forming a C-C σ bond. The smaller H_2 molecule provided empty space for this movement of CO. A *tri*-carbonyl (C=O)-(C=O)-(C=O) group was formed while other CO formed a *di*-carbonyl group at the same time (see Figure 2.16b). The space available for the sites created by H_2 in the CO-H_2 played an indirect but important role in promoting the chemical reactions. With time, more CO molecules were involved in the reaction, and long polycarbonyl chains were formed (Figure 2.16c). To study the addition of H_2, we analyzed the trajectory of the structure at 15 GPa (Figure 2.17). The H-addition to C=O bond in the chain in layer 2 changed the C hybridization from sp^2 to sp^3 (Figure 2.17a–d) while the layer 1 structure was not affected.

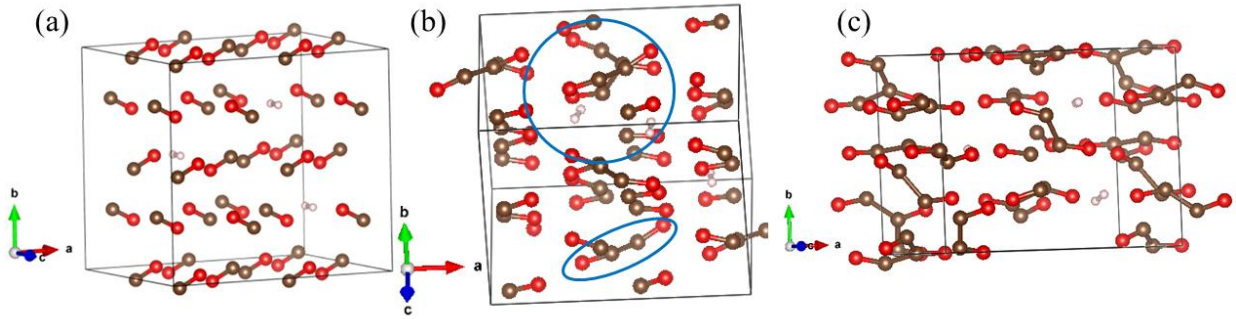

Figure 2.16 Snapshots of the CO-H_2 model from the trajectory of static compression at 10 GPa: (a) the initial structure, (b-c) at step 142 and 241. The blue circles highlight the structural changes described in the text. (C in grey and O in red).

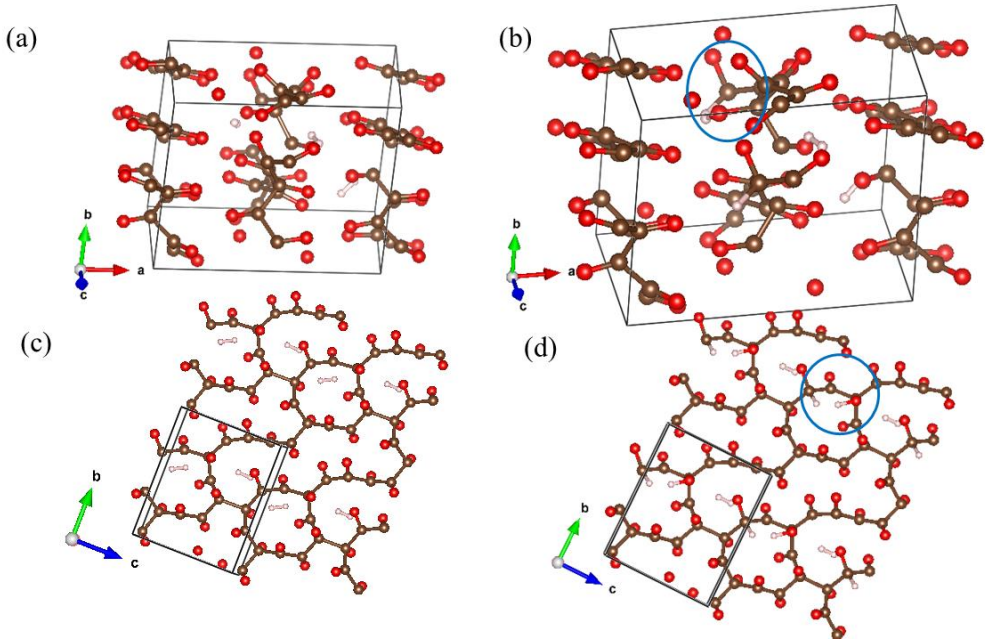

Figure 2.17 Snapshots of the CO-H_2 model from the trajectory of static compression at 15 GPa (a) before and (b) after H_2-addition. The projected structure for layer 2 (c) before and (d) after H_2-addition when looking along the *a* axes. The blue circles highlight the structural changes described in the text. (C in grey in O in red).

The polymerization reaction was found to proceed in three steps (Scheme 2.4): (i) The compression of the system brought the CO molecules closer together, breaking the C≡O triple bonds and forming new σ bonds; (ii) then the hybridization of C changed from *sp* to sp^2 in the

polycarbonyl chains, and (iii) in layer 2 where the H_2-addition to the C=O bond occurred. This reaction scheme suggests that adding more H_2 may be desirable to create more C-C and C-O single bonds.

Scheme 2.4 Orbital interaction diagrams for the formation of pure polycarbonyl and -OH substituted polycarbonyl chains in the polymerization of solid CO with H_2 doping

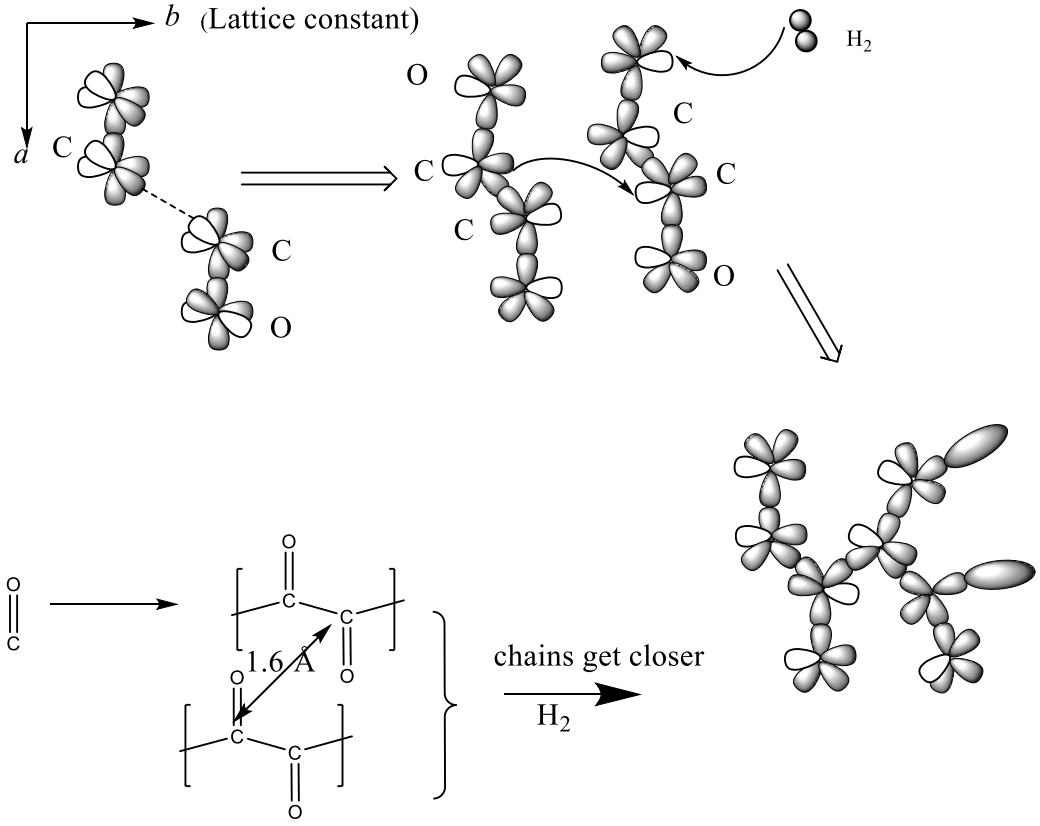

To investigate the possibility to obtain X-CO with higher carbon coordination, *i.e.* more sp^3 C and O, additional *NPT* AIMD calculations were performed at 300 K, 500 K, 1000 K, 1500 K, and 2000 K at 20.0 GPa and at 300 K and 1000 K at 40 GPa and 60 GPa. The calculation results at 300 K, and 20 GPa showed the remaining two H_2 molecules reacted with C=O in the polycarbonyl chains in layer 1 and layer 2 (Figure 2.18a), forming –OH substituted polycarbonyl chains and increasing the number of sp^3 C. Concomitantly, the π-π interactions between the chains

within the same layer became weakened, bringing polycarbonyl chains closer. Some of the broken C=O bonds reacted and formed tetrahedral sp^3 C bonded to the O atom and two other C atoms, as shown in (Figure 2.19a–b). Such changes were reflected in the decrease of *b* and *c* lattice constants (Figure 2.19c) since the polycarbonyl chains were perpendicular to the *bc* plane. Some small rings composed of sp^3 C also formed (Figure 2.18a). When the temperatures were increased to 500 K and 1000 K, the –OH substituted polycarbonyl chains in layer 1 and layer 2 started to react due to high atomic/molecular diffusion at the higher temperature. CO_4 units formed between the two layers (Figure 2.18b–c). Within the same layer, the π-π interaction disappeared completely, and most of the C atoms were sp^3 with a few remaining sp^2 C atoms in layer 1 (Figure 2.18b). Because of the formation of a C-C σ bond between –OH substituted polycarbonyl polymer chains within the same layer, the structure still had distinctive layered structures (Figure 2.18b–c). When the temperatures were increased to 1500 K and 2000 K, more reactions between layer 1 and layer 2 were observed (Figure 2.20a–b). However, instead of forming more sp^3 C bonded either with O or C, five-member lactone rings (Figure 2.20a) at 1500 K and fused six-member aromatic and five-member lactone rings (Figure 2.20b) at 2000 K were formed. We speculate that to obtain more CO_4 units, more C=O bonds need to be broken, and a higher pressure is needed.

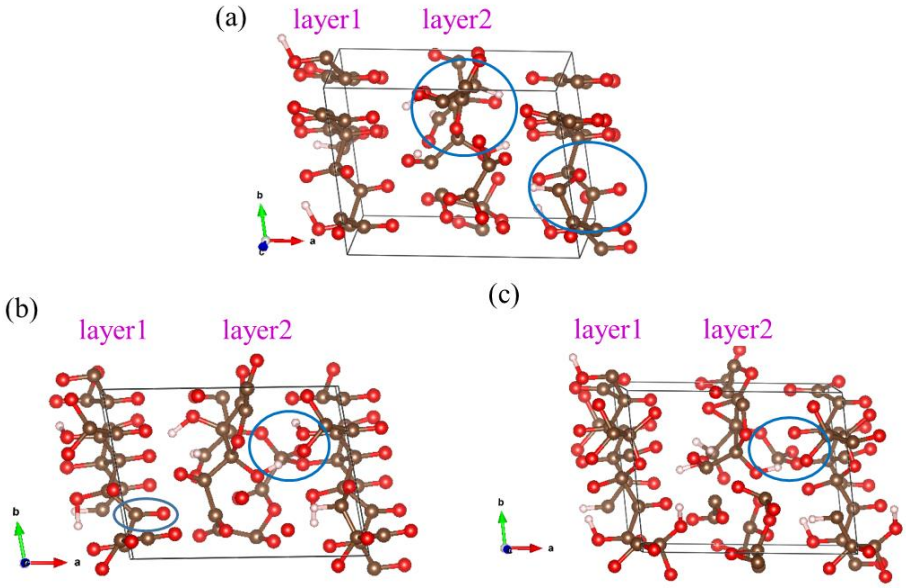

Figure 2.18 Final snapshots of the CO-H_2 model obtained from the *NPT* AIMD calculations at 20 GPa and (a) 300 K (b) 500 K, and (c) 1000 K. The blue circles highlight the structural changes in the simulation as described in the text. (C in grey and O in red).

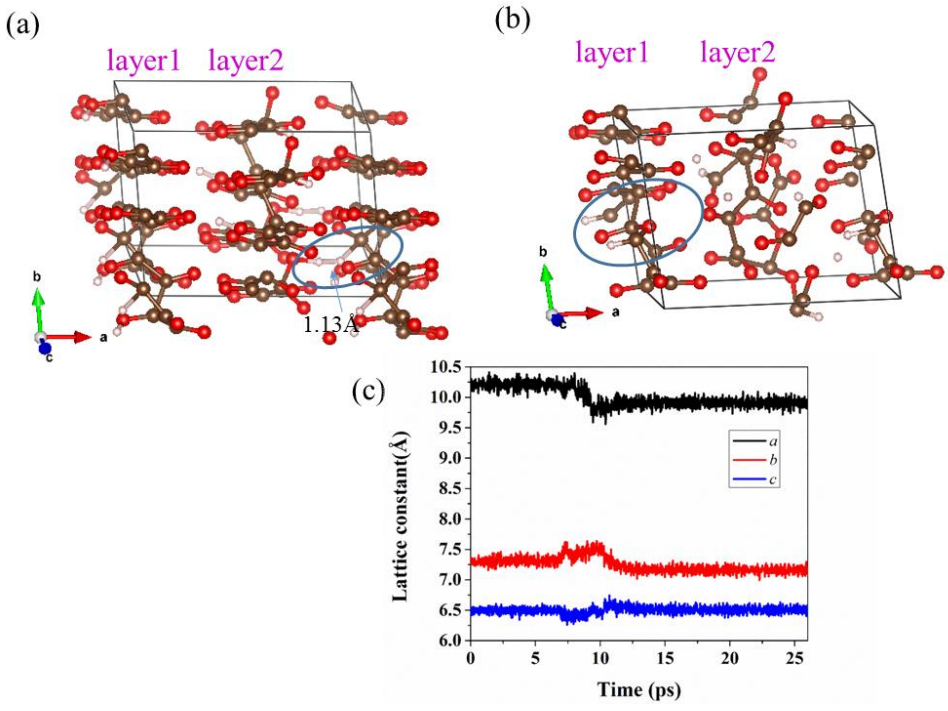

Figure 2.19 Structural evolution in the *NPT* simulation at 20 GPa and 300 K at (a) 7.0 ps and (b) 12.0 ps. (C in grey and O in red). (c) Evolution of corresponding lattice constants with time.

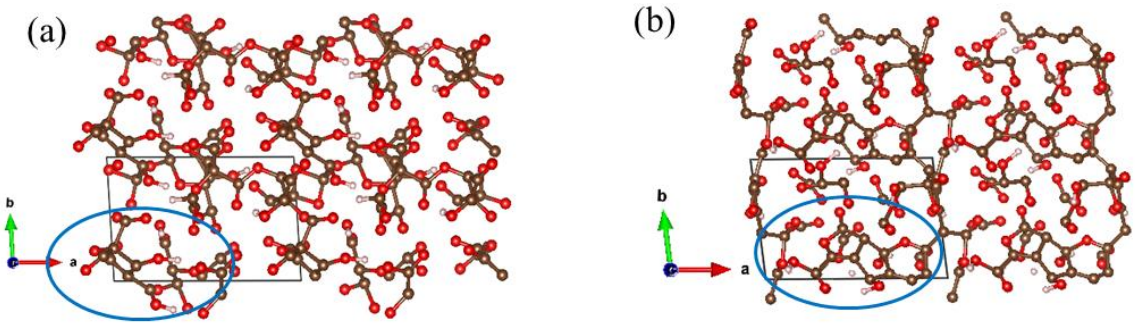

Figure 2.20 Final snapshots of the CO-H_2 model from the *NPT* AIMD calculations at 20 GPa and (a) 1500 K and (b) 2000 K. (C in grey and O in red).

To study whether higher pressure can affect the structure obtained at 15 GPa, we shock-compressed the product to 40 GPa and 60 GPa at 300 K. At 40 GPa, the –OH substituted polycarbonyl chains within the same layer were brought closer, and the chains started to link through the formation of C-C σ bonds leading to 4 coordinated C with C and O atoms within layer 1 and layer 2 (Figure 2.21a). Again, some sp^2 C still remained in layer 1. The polymer chains between layer 1 and layer 2 were pushed closer, forming CO_4. Compared to 20 GPa and 300 K, more C=O bonds were broken at 40 GP and 300 K. When the pressure was further increased to 60 GP, no significant change in the structure was found (Figure 2.21b). At 1000 K and 40 GPa (Figure 2.22a), there is no obvious change to the structure obtained at 300 K. In comparison, at 60 GPa and 1000 K, a fully sp^3 C polymer structure was obtained by connecting layer 1 and layer 2 (Figure 2.22b).

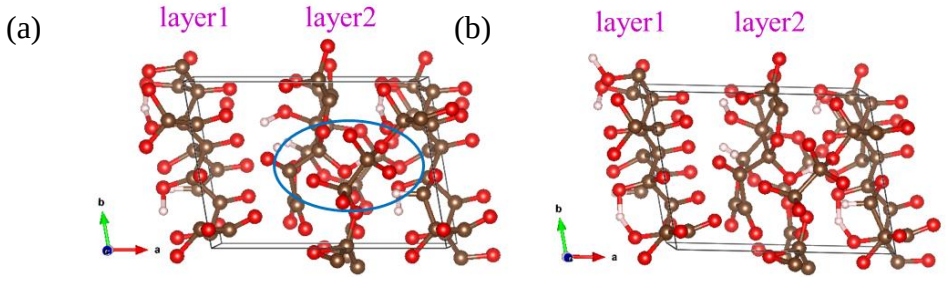

Figure 2.21 Final snapshots of the CO-H_2 model obtained from the *NPT* AIMD calculations at 300 K and (a) 40 GPa and (b) 60 GPa. (C in grey and O in red).

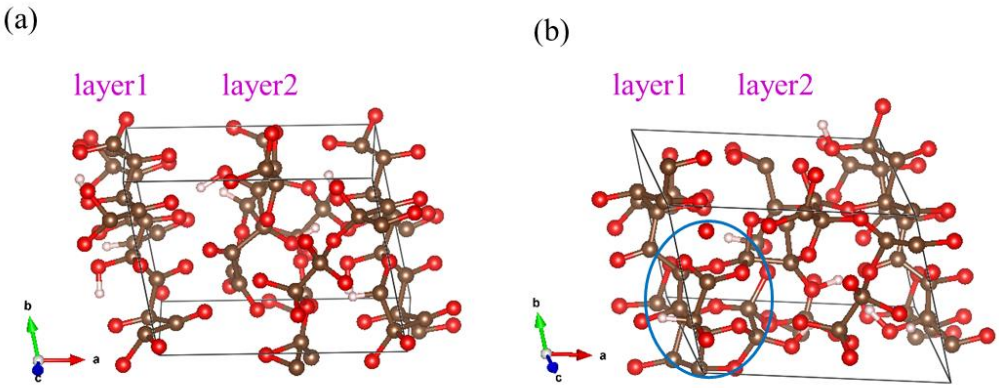

Figure 2.22 Final snapshots of the CO-H_2 model obtained from the *NPT* AIMD calculations at 40 GPa and 1000 K and (b) 60 GPa and 1000 K. (C in grey and O in red).

Conclusions

In summary, from static geometry optimization using the FIRE method and AIMD calculations at different pressures and temperatures, polymerization of solid CO catalyzed by H_2 was observed at pressure as low as 10 GPa. The X-CO formed is composed of polycarbonyl chains. However, a fully sp^3 C-extended solid can only be obtained at higher pressure and temperature. The effect of H_2 doping is shown to be the creation of empty space sites to allow CO to migrate and promote the reaction.

2.2.3 Polymerization of solid CO from O_2 doping

Although we have shown that new forms of X-CO_2 and X-CO can be formed by doping with H_2, the reaction conditions at 41 GPa and 400 K for solid CO_2 and at 10 GPa and low temperature for solid CO are still fairly demanding and not practical. Moreover, the products are still not composed solely of sp^3 carbon and oxygen atoms. The use of an oxygen-rich catalyst may be useful to form fully extend X-CO. O_2 is a common oxygen-rich oxidant. Doping with O_2 may not only provide space for CO migration but also oxidize C≡O and change the C completely to

sp^3. In addition, since the ground state of O_2 is a triplet, the *di*-radial nature is expected to be more reactive.

Computational methodology

AIMD simulations in the *NPT* ensemble on solid CO with an O_2 impurity were performed at 5 GPa and 400 K. The initial CO-O_2 model was constructed from the ambient *P2₁3* structure of solid CO by replacing a CO with an O_2. Since O_2 has a triplet ground state, open-shell spin-unrestricted calculations were performed. The PBE exchange functional was employed. A time step of 1.0 fs for the integration of the equation of motion was used. The simulation lasted for 15.0 ps. The AIMD calculations were performed using the VASP program.

Results and discussions

Theoretical results showed CO and O_2 started to polymerize at 5 GPa producing again a different form of X-CO product. The formation pressure was much lower than the predicted pressure of 10 GPa reported above on a polymerization of solid CO doping with 10% H_2. The final polymeric product features a 3D framework (Figure 2.23a). As shown in Figure 2.23b, there are three fundamental building blocks in the extended structure: polycarbonyl group composed of -(C=O)-(C=O)- with C=O of 1.34 Å and C-C of 1.54 Å, five-member lactone ring with C-O of 1.40 Å and C=C of 1.40 Å, and C-O chains with C-O of 1.41 Å. A few CO_2 molecules are also found. These species are identified by characteristic vibrational frequencies (Figure 2.24) calculated from the Fourier-transform of the velocity auto-correlation function. The peaks at 985 cm^{-1} are assigned to CO_3 carbonates; 688 cm^{-1} is O=C=O bending mode and the peak at 1776 cm^{-1} is assigned to stretch vibrations of the five-member lactone ring. The peaks in the range from 1660 cm^{-1} to 1685

cm^{-1} are assigned to C=C in the unsaturated lactone while the peaks in the range from 1150 cm^{-1} to 1280 cm^{-1} belong to -(C=O)-(C=O)- stretch modes. The peak at 1180 cm^{-1} is assigned to C-O-C stretch modes.

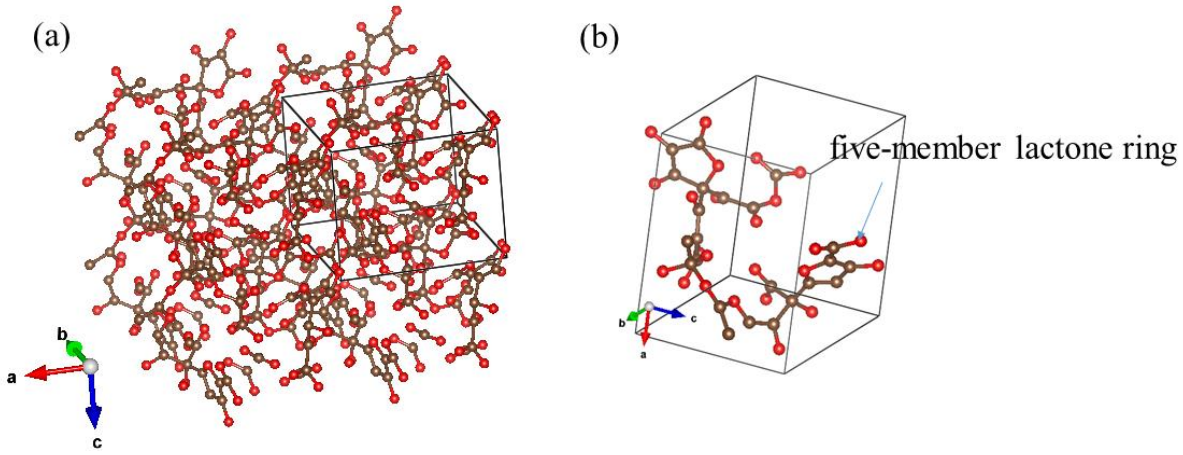

Figure 2.23 (a) Snapshots of the X-CO obtained from the *NPT* simulation at 5 GPa and 400 K. (b) The main building blocks of the X-CO: five-member lactone rings, polycarbonyl group composed of -(C=O)-(C=O), and C-O chains. (C in grey and O in red).

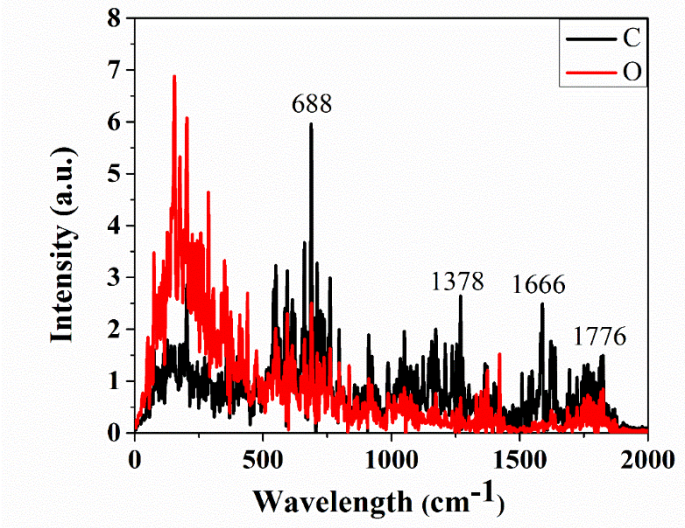

Figure 2.24 Vibrational density of states calculated from the Fourier transform of the atomic autocorrelation functions for the X-CO obtained at 5 GPa and 400 K.

To understand the reaction mechanism, the trajectory obtained from the *NPT* AIMD calculation was examined. The model was compressed (Figure 2.25a–b) and the reaction occurred

within the first 6 ps. The reaction was found to initiate from the formation of a C-C σ bond between two neighbouring CO molecules at step 107 (Figure 2.26b). Then the O_2 decomposed and reacted with two CO in the vicinity at step 144 (Figure 2.26c) forming CO_3 and CO_2. This indicated that O_2 oxidation can help to increase the coordination number of C-O. When the model system was compressed further, the carbonate species continued to react with neighbouring CO brought closer by pressure (Figure 2.26d). With more C≡O bonds being broken, five-member lactone rings were formed (Figure 2.26e–f). Eventually, lactone ring structures and longer chains appeared.

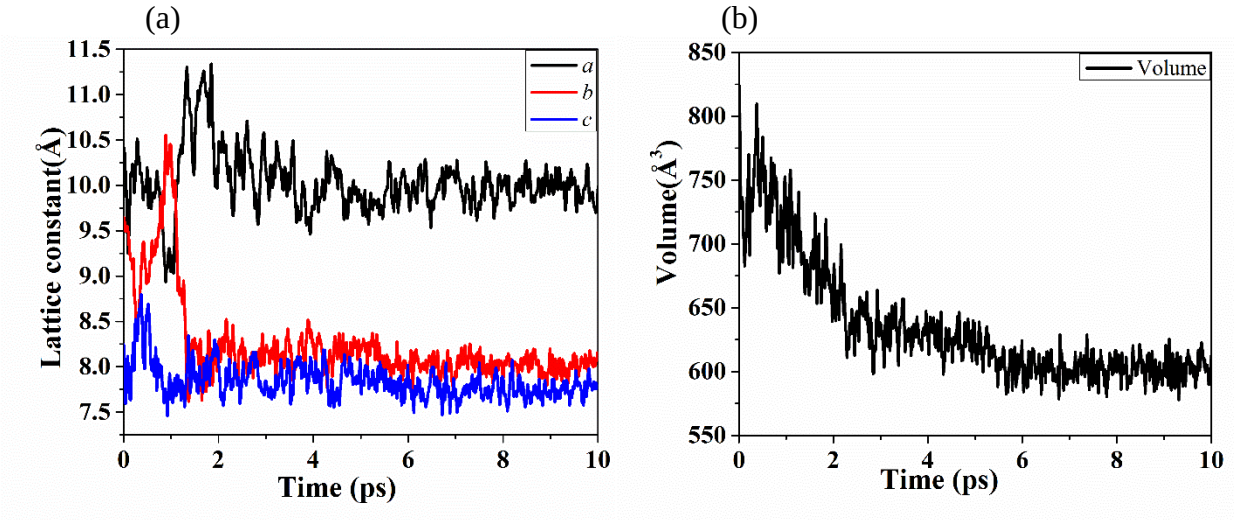

Figure 2.25 Evolution of lattice (a) constants and (b) volume of the CO-O_2 model with time in the *NPT* calculation at 5 GPa and 400 K.

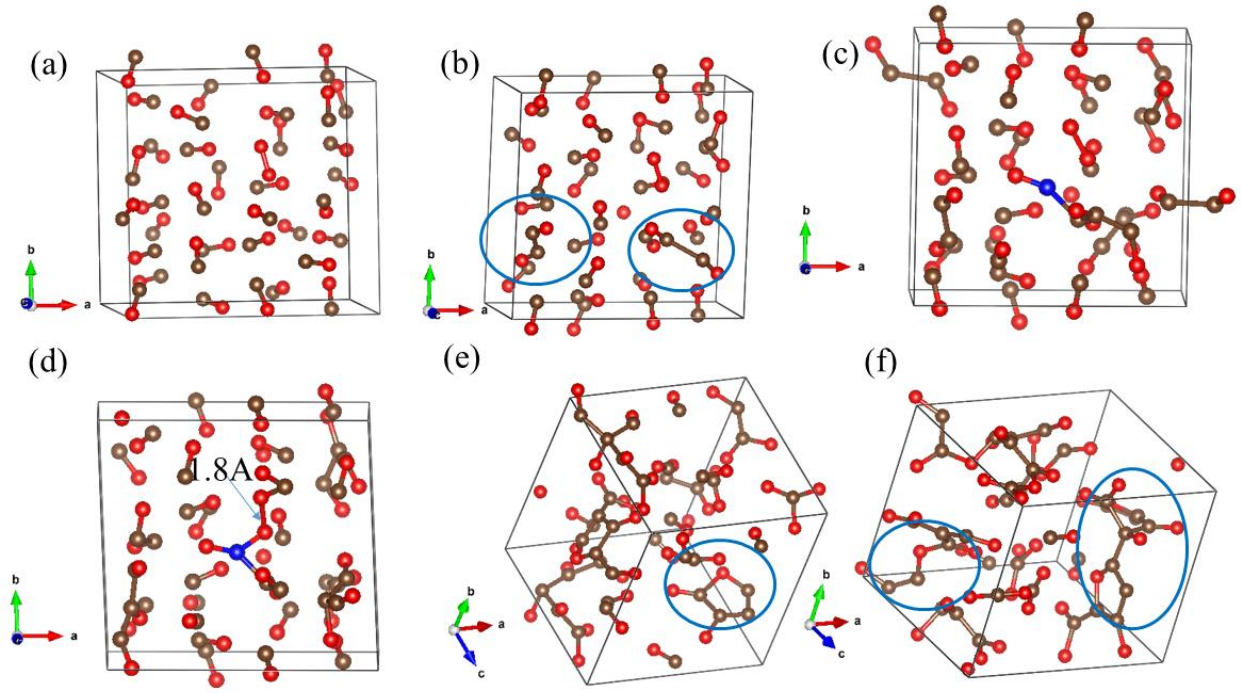

Figure 2.26 Snapshots of the CO-O_2 model during the AIMD calculation at step (a) 30, (b) 107, (c) 144, (d) 146, (c) 857, and (d) 3600. The C atoms that react with O are highlighted with blue in c. The blue circles highlight the structural changes described in the text. (C in grey and O in red).

Conclusions

In summary, we have obtained an extended 3D X-CO at 5 GPa and 400 K from O_2 catalyzed polymerization of solid CO. The onset of the reaction at 5 GPa is much lower than H_2-activation (10 GPa). O_2 helps to create more sp^3 C. The product is comparatively denser than that of H_2-activated X-CO and mainly composed of five-member lactone rings, polycarbonyl, and C-O chains.

2.3 Solid-state polymerization of CO_2 from photo-excitation

It is well-known that upon photolysis at 4.89 eV [115] the closed shell linear molecular CO_2 is excited to a bent triplet [116-118] *di*-radical. *Di*-radicals are chemically active and, in the

solid state, while the relative molecular positions are restricted, the radicals can be effective precursors for polymerization reactions. Furthermore, due to the high reactivity of the radical, it is expected that only a small number of photo-excited radicals are needed to initiate the process. To explore the feasibility and the conditions for the formation of extended X-CO_2 using photo-excitation, AIMD calculations in the *NPT* ensemble were performed. As shown below, we have found that photo-excitation significantly lowers the pressure and temperature required for the formation of X-CO_2. We have also found that the reaction product has a 3D framework structure formed from mostly sp^3 hybridized carbon and connected by oxygen atoms. The compound can be quench-recovered to ambient pressure. The recovered material has an energy content of 8.63 kJ/g upon thermal decomposition.

Computational methodology

NPT [43,119] AIMD simulation with Langevin thermostats was performed on *Cmca* phase (CO_2-III) [120], the experimentally observed stable phase at 300 K and pressure higher than 10 GPa. A model consisting of 96 atoms (32 CO_2) was used. Excited triplet CO_2 in the solid was generated by promoting an electron from the ground to the conduction band of a randomly selected molecule. Spin-polarized MD calculations were performed at a variety of temperature and pressure conditions, *viz.* 1200 K and 2000 K at 12 GPa, 500 K, 800 K and 1200 K at 15 GPa, 300 K, 350 K, 400 K, 500 K, and 800 K at 22 GPa, 800K at 25 GPa, and 800 K at 50 GPa. An integration time-step of 1.0 fs was used. Each MD trajectory was run for at least 10 ps and, in several cases, up to 150 ps. In most calculations, the fictitious mass for the crystal lattice was set to 10. To examine the effect of the box dynamics, additional calculations were performed with a heavier fictitious mass of 20. To investigate the effect of multiple excited CO_2, two randomly chosen CO_2

molecules were excited and calculations were performed at 12 GPa, 15 GPa and 22 GPa. To calculate the energy content upon thermal decomposition of the recovered product, a vacuum/solid interface region was constructed using the method described above in 2.2.1. The decomposition energy was estimated from the total energy difference calculated from micro-canonical *NVT* calculations of the recovered product at 80 K and after decomposition at 350K under ambient pressure. VASP [44-46,121], a plane-wave basis electronic structure code employing projected augmented wave potentials for the atoms was used for all calculations. The PBE functional was employed, and the electron orbitals were expanded in the plane wave basis set. A plane wave basis set with an energy cutoff 400 eV was used. In view of the large supercell and that the system is a large gap insulator, only one *k*-point (Γ) was used to sample the Brillouin Zone.

Results and discussions

A series of MD simulations at different temperatures and pressures were performed. At 12 GPa, with a single excited CO_2 molecule, no reaction was observed at 1200 K and 2000 K after 10 ps. Similarly, no reaction was observed at 22 GPa and 300 K even though the CO_2 molecules were brought closer to each other by higher pressure (Figure 2.27a). However, as will be explained in more detail later (*vide supra),* the delay in the reaction was simply a kinetic effect and not an indication that the reaction of CO_2 *di*-radical with neighbouring CO_2 molecules is not feasible at low pressure. At 22 GPa and 350 K, the formation of a dimer between the photo-excited CO_2 with a neighbour was observed (Figure 2.27b). Upon further heating to 500 K, CO_2 molecules started to react with each other and eventually formed polymeric chains (Figure 2.27c). It is obvious that high temperature facilitated the movements of CO_2 molecules and promoted reactions between the excited triplet CO_2 with its neighbours. Thus, to accelerate the reaction further, the model system

was heated to 800 K. At this temperature, chemical reactions proceeded almost immediately after a CO_2 molecule was excited by rapidly propagating to other CO_2 molecules through the formation of new chemical bonds. The X-CO_2 formed (Figure 2.28) was a mixture of sp^2 and sp^3 carbon. In this instance, out of the 32 CO_2 molecules in the model, 13 carbon became four-coordinated (sp^3), and 19 became three-coordinated (sp^2) to the oxygen atoms. When the temperature was raised to 2000 K, the number of four-coordinated C increased to 16, which accounted for half of the total number. If the pressure was increased to 25 GPa at 800 K, the number of four-coordinated C further increased to 19 with 13 three-coordinated C. The number of sp^2 and sp^3 C centres in the product was significantly affected both by the temperature and external pressure as the proportion of four-coordinated C continued to increase at 50 GPa. The mobility of CO_2 molecules in the solid increased with the temperature while the intermolecular distances decreased as the pressure rose. Consequently, the probability for contacts of the photo-excited CO_2 with its neighbours was increased, and this accelerated the reaction and increased the concentration of sp^3 carbons.

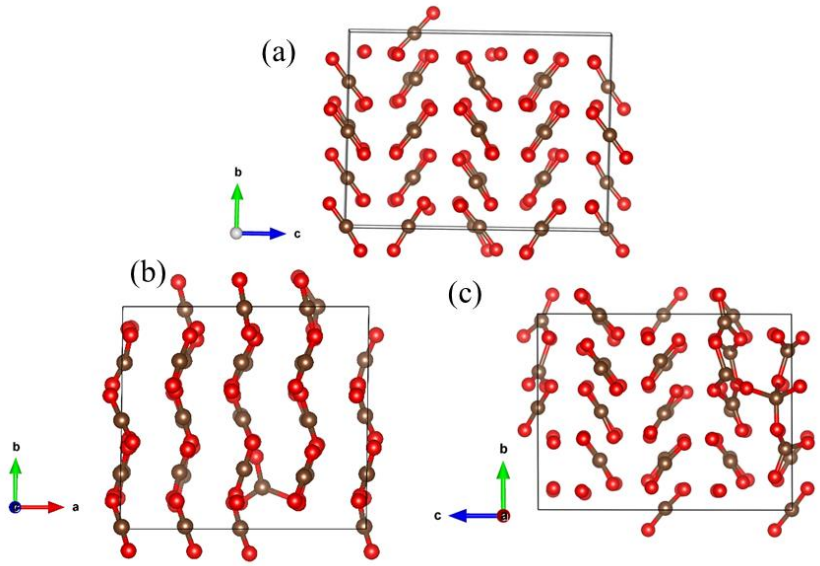

Figure 2.27 Final snapshots of the solid CO_2 model upon the single-molecule photo-excitation at 22 GPa and (a) 300 K (b), 350 K, and (c) 500 K. (C in grey and O in red).

The theoretical results show the combination of photo-excitation and high temperature is an effective way of promoting the polymerization process in the synthesis of X-CO_2. To confirm the kinetic nature of the reaction, we repeated the MD calculations using a heavier fictitious mass and a much longer simulation time. The heavier mass of the simulation box slowed down the fluctuations of the model box allowing more time for the CO_2 molecules to migrate and increasing the chance for the radical to interact with its nearest neighbours. Indeed, the reaction was observed even at 350 K and 15 GPa. This is strong evidence suggesting that, in the experimental time scale, the synthesis of X-CO_2 could be achieved even at much lower temperature and pressure conditions.

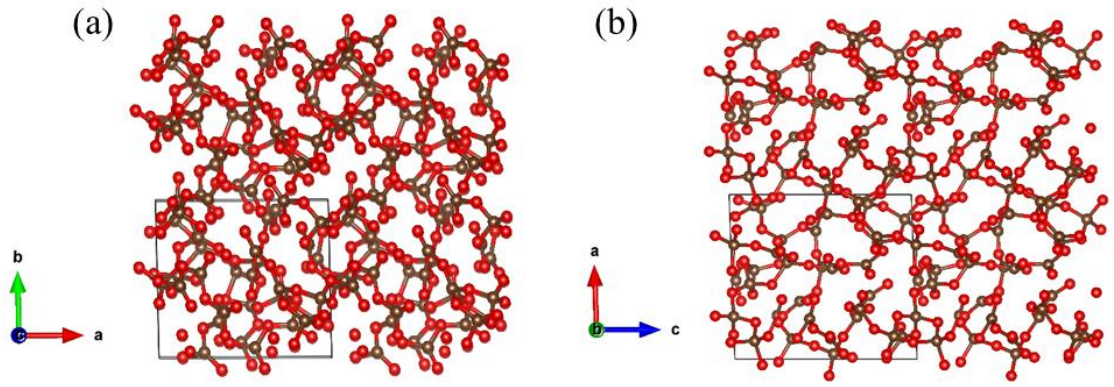

Figure 2.28 Projected final snapshots of the solid CO_2 model in (a) *ab*-plane and (b) *ac*-plane phase from the MD trajectory, showing the structural transformation upon single-molecule photo-excitation at 22 GPa and 800 K. (C in grey and O in red).

To examine the pathway leading to the reaction product, we analyzed the MD trajectory at 22 GPa and 800 K from a single excited CO_2 since the simulation resulted in a fully extended polymeric structure consisting of three and four-fold coordinated C atoms. A snapshot of extracted from the final structure from the 40 ps MD trajectory is depicted in Figure 2.28. The reaction product can be described as an extended 3D-network constructed from linked planar CO_3 and

tetrahedral CO_4 units. Among the four coordinated C, three of the C-O bond lengths are about 1.35 Å while the remaining one is usually longer, about 1.44 Å. The four oxygen atoms form a tetrahedron that links with other species *via* corner sharing. The three-coordinated CO_3 form a planar carbonate structure with one short C-O bond of 1.22 Å and two longer C-O bond lengths ranging from 1.35 Å to 1.40 Å. The hybridization of C changed from *sp* in CO_2 to the sp^2 in CO_3 and then to the sp^3 in the four-coordinated environment. The presence of CO_4 and CO_3 is revealed in the calculated vibrational density of states of the product shown in Figure 2.29. The peak at 1829 cm^{-1} can be assigned to the carbonyl stretch. The peaks at 985 cm^{-1}, 1185 cm^{-1}, and 1386 cm^{-1} are characteristic for the –O-(C=O)=O- vibrational modes of CO_3 carbonates, while the peak at 640 cm^{-1} is unique to the C-O-C stretching/bending mode in CO_4 tetrahedral.

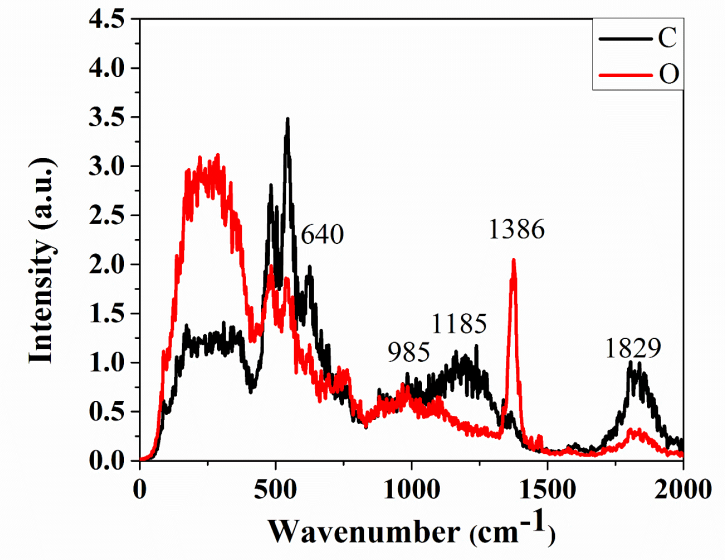

Figure 2.29 Vibrational density of states calculated from the Fourier transform of the atomic autocorrelation functions of the X-CO_2 obtained at 800 K and 22 GPa.

To examine the kinetic effect, we extended the *NPT* simulation at 22 GPa and 800 K to 134 ps. Salient features of the structural changes in the model with time are shown in Figure 2.30. In the first 120 ps after initial compression, apart from the shortening of *c* and *b* cell lengths, little

change in the *a* axes or the lattice angles was observed. In this initial stage, the external pressure led to compression of the (010) planes of the *Cmca* structure. After 120 ps, the crystal lattice was found to have sheared, and the length of the *a* axes started to contract. Figure 2.31 shows several snapshots taken from the MD trajectory. The reaction was initiated by the photo-excited bent CO_2 perpendicular (Figure 2.31a) to the (010) plane. This formed a reaction centre that helped to bring neighbouring CO_2 in the adjacent layer along the *a* direction closer together. The O atoms of the bent CO_2 then reacted with another molecule in the (010) plane (Figure 2.31b) producing CO_3. This resulted in the shortening of the *b* and *c* cell axes. When more CO_2 molecules were moved to the reactive CO_3, O-C-O- centres then chains and cages started to form. Upon further compression, the planar CO_3 were twisted, and the π bonds were broken. Subsequently, when another CO_2 situated perpendicularly to the planar CO_3 was brought closer, CO_4 (Figure 2.31d) was formed. This process led to a sudden decrease in the *c* axes at 58.1 ps (Figure 2.30). A closer examination found the structure to be composed of a mixture of CO_3 and CO_4 (Figure 2.32a–b) with the CO_3 located mostly in the (010) plane. In addition, the number of CO_4 had increased to 5 within 0.1 ps. The distortion of the lattice from orthorhombic symmetry (Figure 2.30) occurred at around 120 ps, due to the large length change of the *a* axes as more CO_3 reacted and increased the number of CO_4 units from 10 to 13. This analysis demonstrates the importance of kinetics as a longer MD run permitted the CO_2 to propagate, and the relaxation of the crystal lattice led to the formation of more CO_4 species. Scheme 2.5 depicts the schematic of the reactions. Since triplet CO_2 is a *di*-radical, the primary process was the insertion of the unpaired electron on the radical O atom into the C atom (σ^*) of a neighbouring CO_2. This initiated the subsequent polymerization reactions forming -O-C-O- chains.

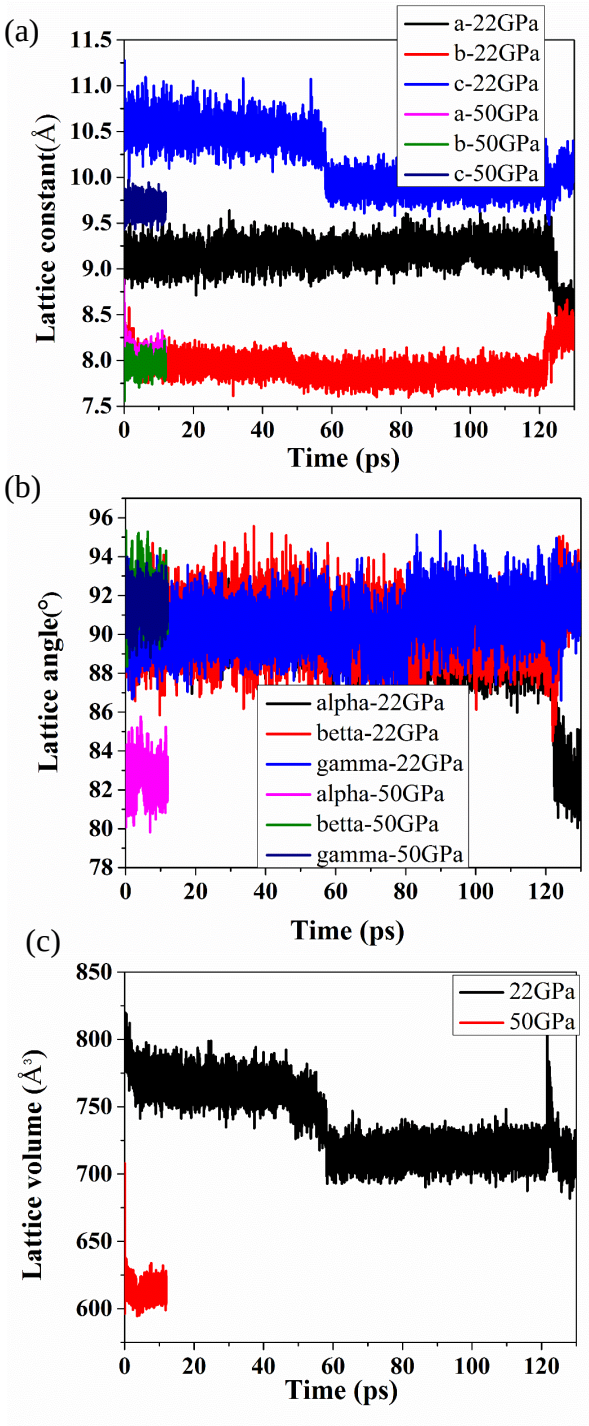

Figure 2.30 Evolution of (a) lattice constants, (b) lattice angles, and (c) lattice volume of the CO_2 structural model with time in the *NPT* AIMD simulations at 22 GPa and 800 K and 50 GPa and 800 K upon single-molecule photo-excitation.

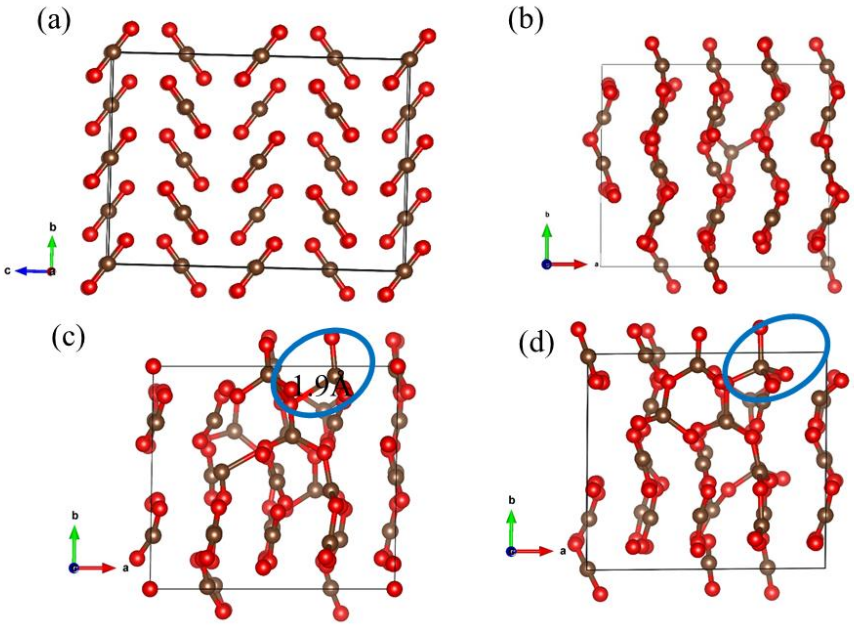

Figure 2.31 Snapshots of the solid CO_2 model from the *NPT* simulation at 22 GPa and 800 K at different stages: (a) initial (b) 2.0 ps, (c) 15.0 ps, and (d) 15.5 ps upon single-molecule photo-excitation. Blue circles highlight the structural changes described in the text. (C in grey and O in red).

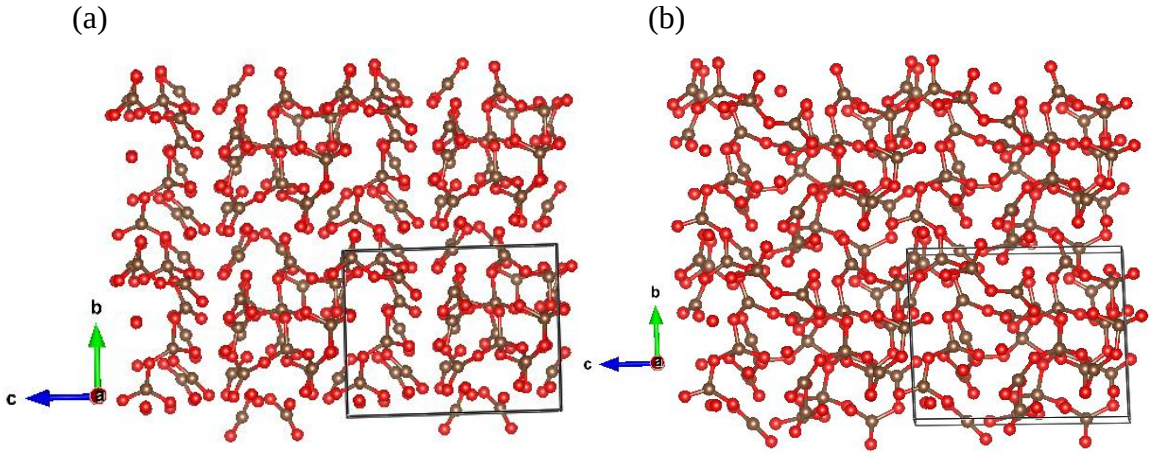

Figure 2.32 Snapshots of the solid CO_2 model from the *NPT* simulation at 22 GPa and 800 K at (a) 58.1 ps and (b) 58.2 ps upon single-molecule photo-excitation (C in grey and O in red).

Scheme 2.5 The primary reactions of the polymerization of solid CO_2 upon single-molecule photo-excitation

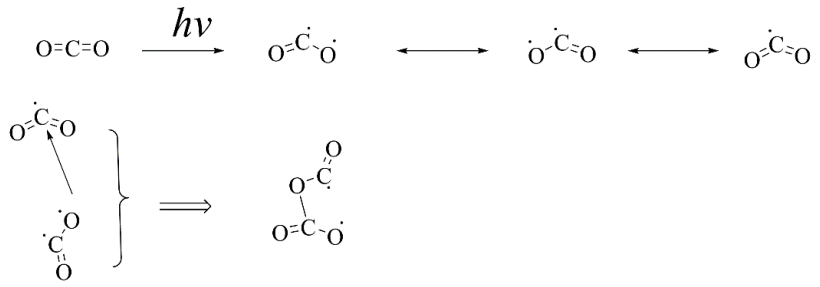

To explore how pressure can affect the carbon coordinations, we examined the trajectory (Figure 2.33) of the MD calculations performed at 50 GPa and 800 K, which was a continuation from the compression at 22 GPa and 800 K. We found that the CO_2 model system had sheared significantly with an obvious shortening of the *a* axes (Figure 2.30a). The Higher pressure helped to increase the number of distorted planar CO_3 species. We found two different reactions involving "twisted" CO_3 on the formation of sp^3 carbon atoms. The first one was *via* the formation of a C-O bond with a close-by CO_3 (Figure 2.33a–b). The interaction was facilitated by one of the O atoms of the second CO_3 located on top of the twisted CO_3. A second way was to react with yet another CO_3 through the formation of a C-C bond (Figure 2.33c–d). This reaction only occurred when the C atoms of the two CO_3 groups situated on top of each other. This configuration, however, was less energetically favourable due to the repulsion interaction between the CO_3 units. Consequently, at 50 GPa and 800 K, most of the sp^3 C centres were CO_4.

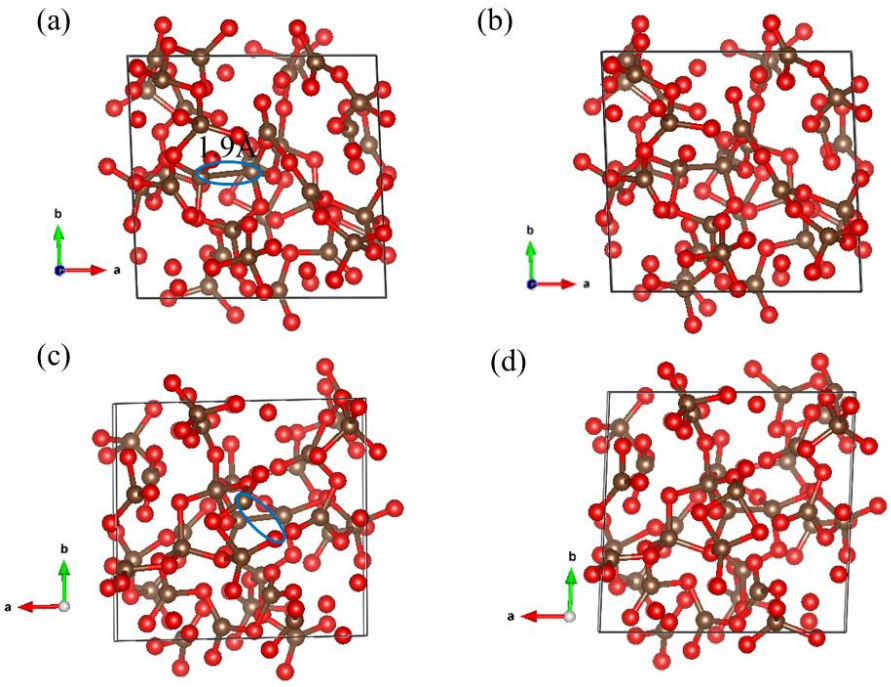

Figure 2.33 Snapshots of the solid CO_2 model from the *NPT* simulation at 50 GPa and 800 K at step (a) 90, (b) 100 (c) 394, and (d) 400 upon single-molecule photo-excitation. Blue circles highlight the structural changes described in the text. (C in grey and O in red).

Encouraged by the results from a single photo-excited CO_2, we expected that multiple excited CO_2 would further enhance the reaction kinetics and reduce the pressure and temperature required. To investigate this effect, two randomly selected CO_2 molecules were excited. At 12 GPa at 300 K and 500 K, two isolated dimers were formed immediately, but no further reaction was observed in the next 50 ps. When the temperature was increased to 1200 K, C-O chains with sp^2 C and sp^3 C centres (Figure 2.34a) were formed after 40 ps. Once again, the long molecular separation at low compression apparently limited the rate of the polymerization reaction. When the pressure was slightly increased to 15 GPa at 500 K, two CO_2 dimers were formed readily (Figure 2.34b). When raised to 800 K (Figure 2.34c), two tetramers were formed. At 1200 K, the migration of CO_2 increased rapidly and more CO_2 moved to the nascent CO_2 dimer, forming a

trimer and the polymerization reaction proceeded to form extended CO_2 with mixed sp^2 and sp^3 C-O coordinations (Figure 2.34d).

As above, we also examined the atomic trajectory from the simulation with two excited CO_2 at 15 GPa and 1200 K. Figure 2.35 shows selected snapshots from the *NPT* calculation. Similar to the case of the single excited CO_2 presented above (*vide supra*), the reaction started with a bent excited CO_2. In this case, both excited bent CO_2 reacted with their respective neighbours immediately, creating the dimer precursors for the subsequent polymerization reaction. Since there were two reaction centres, the polymerization reaction rate had accelerated, transforming solid CO_2 rapidly into connected CO_3 and CO_4 in just under 1 ps. The results showed the initial formation of the dimer and the subsequent polymerization process was similar to that of the single excited CO_2, but the reaction obviously had proceeded much faster. In experiments, since multiple CO_2 will be excited simultaneously, we expect the formation of X-CO_2 will occur readily. Therefore, multiple photo-excited CO_2 lower the energy barrier while high temperature increases the diffusion rate and fully extended X-CO_2 can be synthesized at lower temperature and pressure than static compression to 40 GPa and 1800 K.

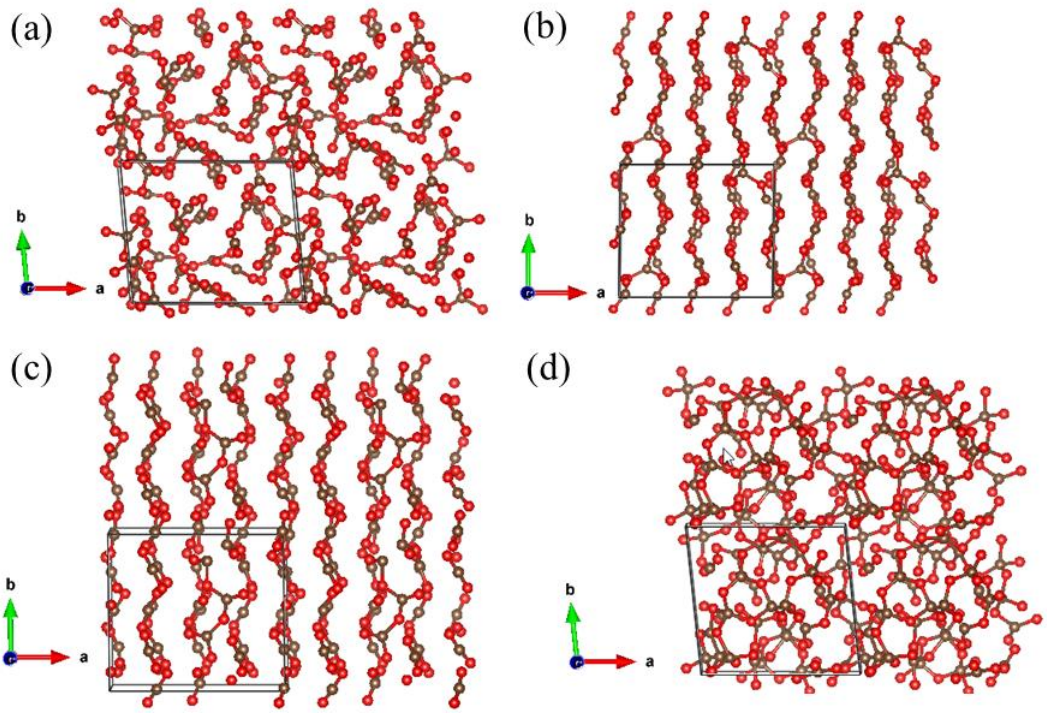

Figure 2.34 Final snapshots of the solid CO_2 model after two CO_2 molecules were photo-excited from the AIMD simulations at (a) 12 GPa and 2000 K, 15 GPa and (b) 500 K, (c) 800 K, and (d) 1200 K. (C in grey and O in red).

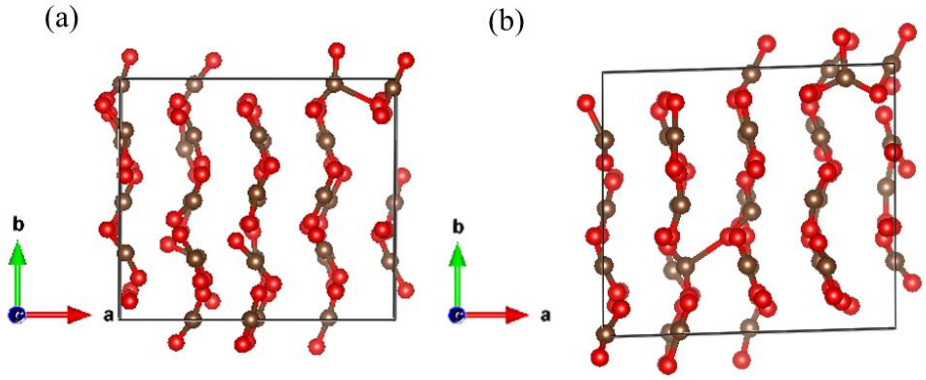

Figure 2.35 Structural evolution of the solid CO_2 model after two CO_2 molecules were photo-excited from *NPT* calculations at 15 GPa and 1200 K at step (a) 100 and (b) 105. (C in grey and O in red).

To investigate whether the predicted high pressure (22 GPa and 800 K) product can be quench-recovered, an *NPT* simulation at 0 GPa and 300 K was performed. MD results confirm the

X-CO_2 product is metastable, and the structure can be maintained at 300 K and 0 GPa (Figure 2.36a), suggesting it could be recovered under ambient pressure and temperature. We studied thermal decomposition of the product and the accompanying heat evolution. Again, the longest axes of the model was doubled to create a solid/vacuum interface. After a 10 ps *NVT* calculation at 0 GPa and 300 K, the X-CO_2 decomposed into CO_2, cyclic carbonate rings and a few short C-O chain molecules (Figure 2.36b). From the total energy difference between the initial X-CO_2 and the decomposed product, we found the reaction was exothermic with an energy release of about 8.63 kJ/g. It is noteworthy that the density of the recovered X-CO_2 produced by photo-excitation is 2.65 g/cm^3, which is about two-thirds of the recovered CO_2-V [122]. A lower density is because not all the C were converted to fully sp^3 bonds. Yet the theoretical results show the X-CO_2 generated by photo-excitation of solid *Cmca* CO_2 is stable at ambient pressure and low temperature and has a favourable heat of decomposition making it a promising high-energy material.

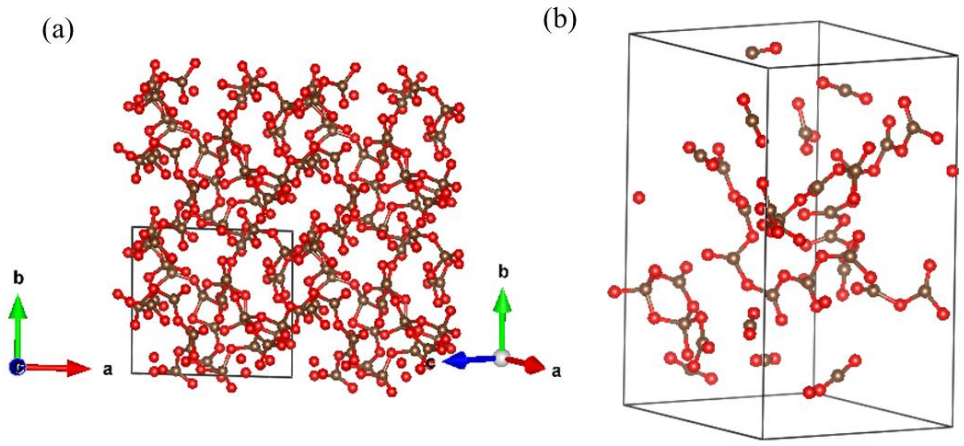

Figure 2.36 (a) Quench-recovered structure of the high pressure and high temperature (22 GPa and 800 K) form of X-CO_2 to ambient pressure and (b) The decomposed product of X-CO_2 obtained. (C in grey and O in red).

Conclusions

A new and efficient synthetic route for X-CO_2 through catalytic photo-excitation of molecular solid CO_2-III has been proposed. Results from AIMD simulations showed that a 3D extended X-CO_2 network with four- and three- coordinated C atoms connected by oxygen can be formed even at pressure as low as 15 GPa and 1200 K. These conditions are much lower than 41 GPa and 1800 K, which are required for static compression. Under a realistic experimental time-frame, the pressure and temperature required are expected to be significantly lower than the theoretical prediction. The mechanisms for the polymerization reaction are identical for single or multiple excited CO_2 molecules. Furthermore, the reaction is controlled by the freedom of CO_2 migration and therefore should proceed readily on a realistic experimental time scale at substantially lower pressure and temperature than the predicted conditions. The CO_2 singlet $\rightarrow$ triplet excitation energy of 4.89 eV is accessible with two-photon absorption. The energy is lower than that of materials usually used as anvils for high pressure experiments, *e.g.,* the indirect band gap energy of diamond of 5.5 eV [123] and cubic boron nitride (*c*-BN) of 6.36 eV [124] under ambient pressure. It is noteworthy that the band gap of diamond increases with pressure up to 370 GPa, as shown recently from X-ray energy loss spectroscopy [125]. Therefore, the laser photon will not be blocked, and the experimental condition for the proposed photo-excited reaction is achievable in a diamond anvil cell experiment [126]. The relatively mild synthetic conditions may even make it feasible to adopt the current technology for industrial-scale production.

2.4 Stability and recovery of CO_2 phase V at ambient pressure

The chemical stability of molecular CO_2 is due to the strong C=O π bonds. However, the synthesis of fully single-bonded extended CO_2-V with a β-cristobalite structure indicates that the

C = O π bond can be transformed to intermolecular σ-bonds from heating CO_2 at 21 GPa [93,101]. Besides the high energy-density, the CO_2-V [85,93,101,102] is predicted to exhibit intriguing properties such as optical nonlinearity and super-hardness, making it as an attractive energetic material. However, this structure is thermodynamically stable only at high pressures (above ~20-40 GPa), posing a significant challenge for its practical use. On the other hand, the metastability of the sp^3 bonding is expected to result in considerable kinetic barriers to the reverse transformation into molecular phase and can be sufficient for ambient-pressure recovery. To provide insight into the observed meta-stability and possible recovery of CO_2-V, we performed meta-dynamics [119,127,128] simulations to examine the structural evolution of CO_2-V upon pressure unloading. Theoretical details of the meta-dynamics method have been documented in many book chapters and reviews [119,127]. In essence, it is a conceptual extension of the idea of constant-pressure MD simulation. By filling energy minima with a series of history-dependent Gaussian potentials, depending on the collective variables (order parameters), the potential energy surface at finite temperature and pressure can be explored. In the case of structural phase transformation, the collective variables are the scaled lattice vectors of the supercell.

Computational methodology

Meta-dynamics [69] calculations employing the VASP program were performed to investigate the possibility to recover the extended CO_2–V phase under ambient pressure. The supercells employed in the simulations contained 48 atoms, and only a single *k*-point was used. In each meta-step, there were 400 MD steps for a total simulation time of 0.8 ps. Gaussian width and height parameters of 3 or 2 (kbar $Å^3)^{1/2}$ and 20 or 10 kbar·$Å^3$ were used, following the guidelines presented in Ref. [129]. The phonon band structure was used to characterize the stability of the

quench-recovered CO_2-V. Phonons were calculated using the supercell method implemented in the PHONOPY program [130]. The forces due to atomic displacements were calculated using the linear response method implemented in the VASP code.

Results and discussions

The calculation started with the β-cristobalite-like *I*-42*d* structure at 40 GPa and 300 K (Figure 2.37a). Within the first 120 meta-steps (Figure 2.37b), the free energy of the system dropped after reducing the pressure. Then the system stabilized at 0 GPa and there was little change in the enthalpy. After releasing the pressure from 40 GPa, the simulation cell expanded with the lattice volume increased from 297.5 $Å^3$ to 360.2 $Å^3$. The tetragonal lattice constant *a* and *b* also increased from 7.1 Å to 7.7 Å, but only very small change occurred in the ***c*** axis (Figure 2.38). Similar results were obtained using different Gaussian widths and heights (Figure 2.37b–c). The meta-dynamic calculations show that the *I*-42*d* structure of CO_2-V can be preserved at 0 GPa. The 3D network character of the structure is maintained at 0 GPa and the structure is mechanically stable as no imaginary frequency was found in the phonon band structure shown in Figure 2.39. This prediction was confirmed by a recent experiment [101] showing CO_2-V can be recovered at ambient pressure and stable up to 200 K.

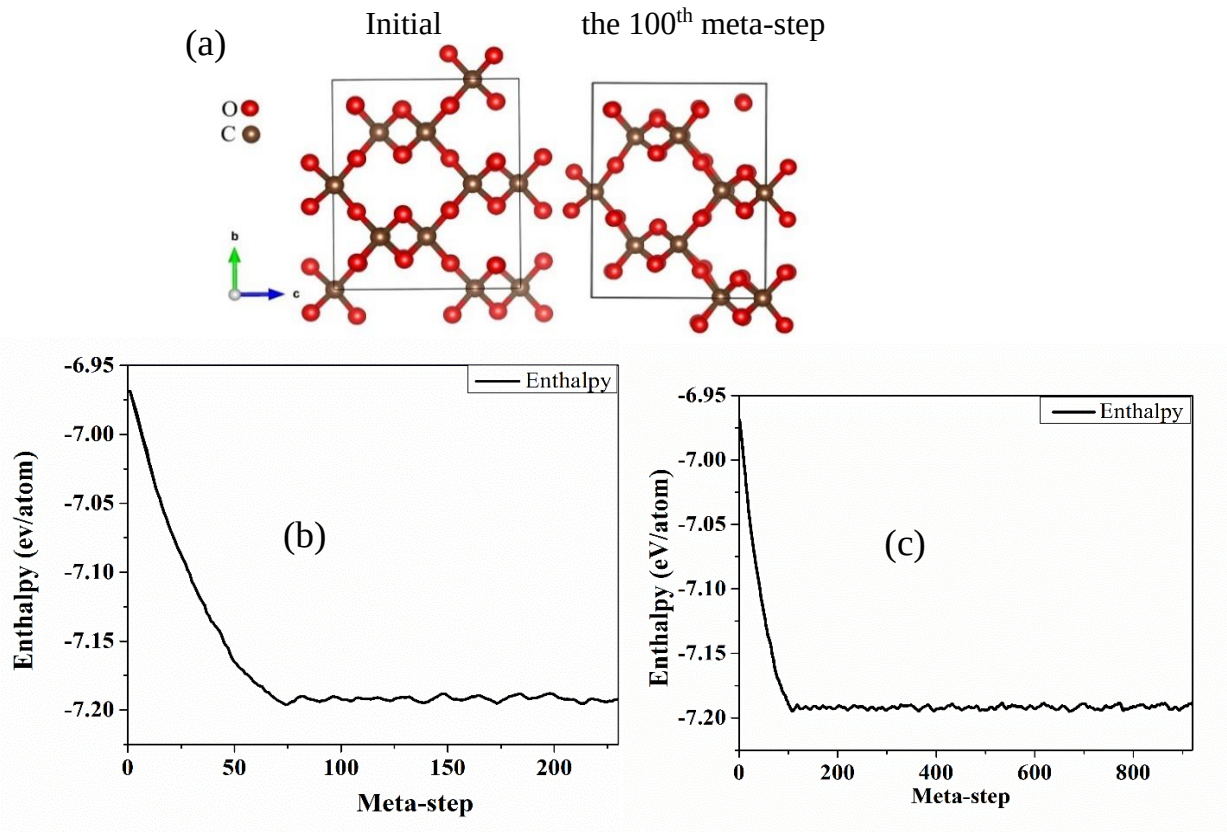

Figure 2.37 (a) Initial β-cristobalite like *I-42d* structure of CO_2-V and the obtained structure in the 100th meta-step. (C in grey and O in red). Plot of the evolution of the temporal total energy with (b) meta-step Gaussian width = 3.0 and height = 20.0 and (c) Gaussian width = 2.0 and height = 10.0. This figure is from Ref. [118].

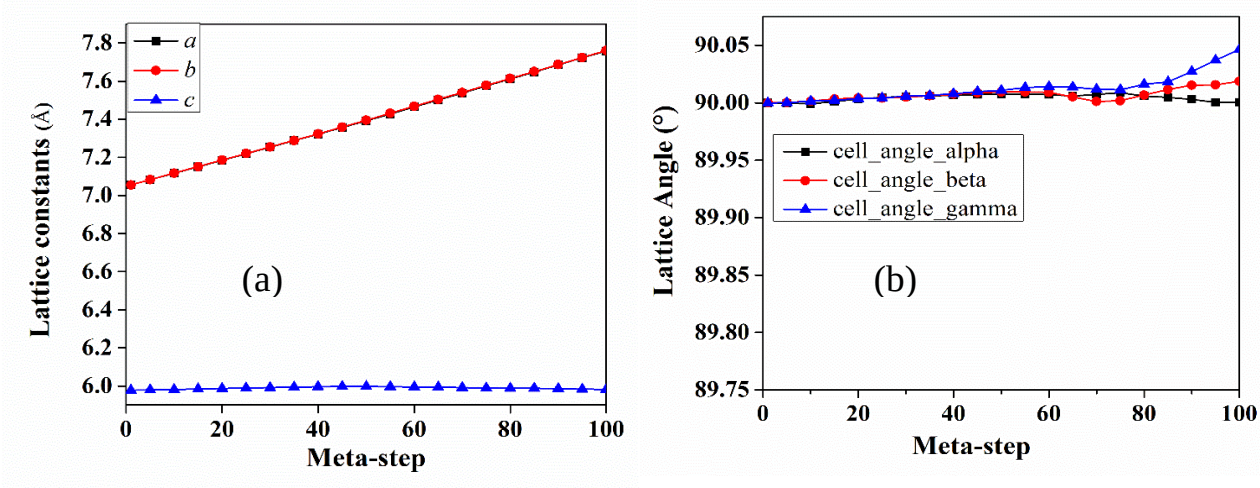

Figure 2.38 Evolution of lattice parameters of CO_2-V with meta-step: (a) lattice constants and (b) cell angles. This figure is from Ref. [118].

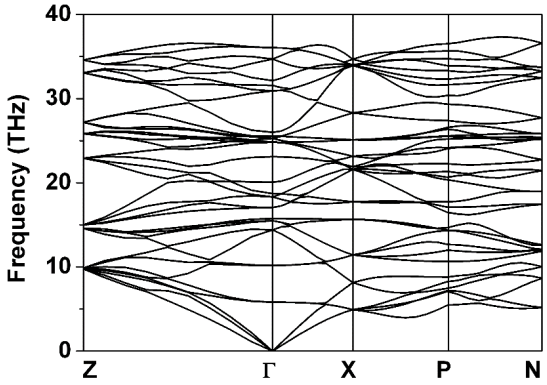

Figure 2.39 The calculated phonon band structure of *I*-42*d* recovered ambient pressure. This figure is from Ref. [118].

Conclusions

We have found that the β-cristobalite-like *I-42d* structure of CO_2-V is metastable at ambient pressure and can be recovered at low temperature. Therefore, the recovered CO_2-V may be used as a high energy-density material.

2.5 General discussion and summary

The reported non-molecular CO_2-V is a possible high-energetic material. However, the straightforward synthetic condition would require 41 GPa and 1800 K. Furthermore, these conditions hinder large-scale industrial production. In this chapter, we explore different strategies to lower the formation pressure for the synthesis of X-CO_2 and X-CO. These include doping with H_2 and O_2 and photo-excitation. We found doping was able to lower the formation pressure to 5 GPa for the polymerization of CO. However, the conversion to fully four-coordinated C and O were not completed. Photo-excitation of solid CO_2 offers the better results. It successfully lowered

the formation pressure to 15 GPa or even less for the synthesis of X-CO_2. This condition is within the current industrial capability. The obtained product is almost a fully sp^3 X-CO_2. Finally, we demonstrate CO_2-V obtained at high pressure and high temperature is quench-recoverable.

CHAPTER 3

NOVEL CHEMICAL REACTIONS OF SILICA UNDER PRESSURE

Silica (SiO_2) is one of the most globally abundant and useful materials. As silicate, it is the main component of the Earth's surface. Pure silica can exist in many polymorphic forms in both solid and liquid phases (Figure 3.1) [119,131-139] with Si in either four- or six-fold coordination with oxygen atoms. Under ambient conditions, Silica is covalent solid, and the most stable polymorph is α-quartz which can be found in nature. Quartz transforms successively into three different crystalline phases: β-quartz (quartz-II) [133], tridymite [137], and cristobalite [139] by heating before melting (phase diagram in Figure 3.1). Upon compression, at ~2.0 GPa, α-quartz transforms into coesite. At 9.0 GPa, stishovite becomes the most stable solid form up to 300 GPa. All the low-pressure forms of crystalline silica are constructed from corner-sharing four-coordinated Si-O tetrahedra. In the denser stishovite, the Si-O coordination increases to six. At even higher pressures, several polymorphic forms with higher coordination numbers are found. Apart from the common crystalline forms, many meta-stable structures have also been found [119]. SiO_2 is chemically inert and does not easily react with common gases, such as CO_2 and H_2, under ambient conditions. However, recently, chemical reactions of silica with CO_2 and H_2 under Earth's mantle conditions have been reported, though there is no detailed information on the structures or the underlying chemical reaction mechanisms. In this chapter, the reactions of silica with CO_2 and H_2 under high temperature and high pressure conditions at the Earth's mantle are investigated using MD calculations.

3.1 Chemical reactions between SiO_2 and CO_2

3.1.1 Introduction

Carbon dioxide and silica are two of the fundamental components of the Universe. Both are group IV oxides. Molecular CO_2 is the main greenhouse gas, the current amount in the atmosphere has become a severe challenge to human life. The presence of CO_2 in the Earth's mantle also plays an important role in volcanic and seismic activities. CO_2 is chemically inert at ambient conditions. Under high pressure and high temperature, CO_2-fluid becomes supercritical and can percolate into most materials. This is the reason it is often used as a solvent for chemical extraction. C is the only group IV element that forms a stable double π bond with oxygen—a strong double bond. However, this double bond can be affected by extreme pressure. As described in Chapter 2, under moderate pressures, CO_2 crystallizes into *vdW* molecular solids. Under high pressure and high temperature (above 41 GPa and 1800 K), molecular CO_2 can transform into an extended solid with single bonded C-O [94] and share a similar structure with the β-cristobalite polymorph of SiO_2. At ambient conditions, CO_2 and SiO_2 do not react with each other. However, their reactivity can be significantly altered under high pressure and high temperature. The analogy between CO_2 and SiO_2 at high pressure has stimulated several recent studies to investigate possible reactions between them [4,5,140-142]. Such reactions could have practical applications. For example, injection of the CO_2 underground has been proposed to be a new and efficient way of removing the extra CO_2 from the atmosphere [143-145]. The possibility of the formation of 3D extended covalent solids may help to stabilize the reaction products, which may even be potential candidates for high energy content materials. The exploration of the chemical reaction between CO_2 and SiO_2 under high pressure will help the development of new chemistry between these two

chemical species. However, present experimental and theoretical works on this subject are still limited [4,5,140,142,146].

In 2011, Santoro *et.al*. [4] reported the first observation of the formation of a disordered silicon carbonate by compressing CO_2 into the voids of a micro-porous silica (zeolite) at pressures at 18–26 GPa and temperatures between 600 K and 980 K. In 2014, the same group [5] identified a novel crystalline cristobalite-type SiO_2-CO_2 solid solution from the reaction of CO_2 and a silica melt at 16–22 GPa and temperatures higher than 4000 K. However, no information on the detailed structure or the reaction mechanism was presented. Here, we undertook a thorough theoretical investigation of the reaction between CO_2 and SiO_2 using both DFT-based AIMD simulations and total energy calculations. The theoretical information obtained will help reveal the nature of such novel SiO_2-CO_2 reactions and the pathways in forming stable compounds. As shown below, the calculations confirm that disordered or crystal compounds can be formed between SiO_2 and CO_2 under different thermodynamic conditions. In addition, the cristobalite-like SiO_2-CO_2 is found to possess interesting and useful properties for practical applications.

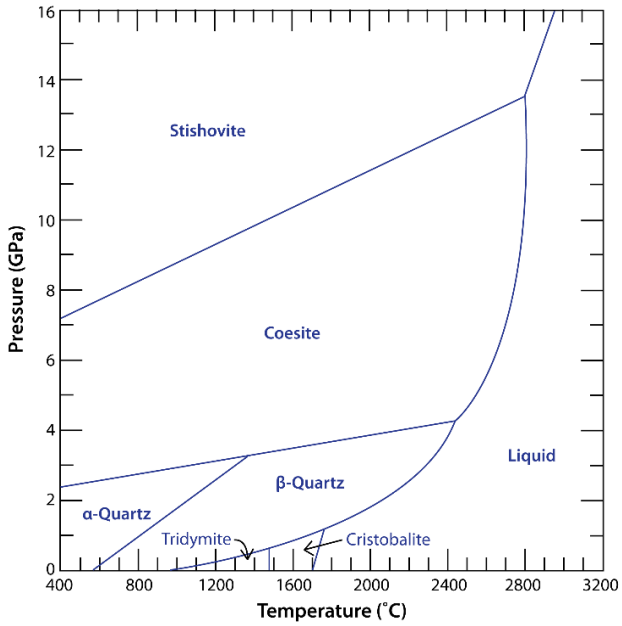

Figure 3.1 High pressure and high temperature phase diagram of SiO_2 (Adopted from Ref. [147])

3.1.2 Chemical reactions between porous quartz and CO_2—forming disordered compounds

Zeolites are microporous silica and can be synthesized with pores of different sizes formed from linkages of four-, five-, six-, and ten-membered rings of SiO_4 tetrahedra. A typical example is given in Figure 3.2. The porous framework structures have the ability to be filled with small molecules through physical absorption [148], and this unique property has been exploited industrially for gas separation and storage [149]. Therefore, microporous silica is suitable starting materials to investigate potential reactions between encaged CO_2 and zeolite under pressure. As such, a disordered silicon carbonate was successfully synthesized at 18–26 GPa and 600–980 K on zeolite SSZ-56 by filling the pores with CO_2 [4].

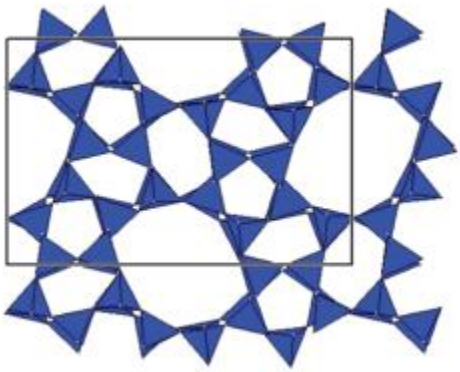

Figure 3.2 Microporous silica (zeolite SSZ-56) with four-, five-, six-, and ten-membered rings of SiO_4 tetrahedra. This figure is taken from Ref. [148].

Computational methodology

This novel finding prompted the theoretical study to investigate the chemical reaction of CO_2 in SSZ-56 with AIMD simulations. The calculations started from the optimization of the

structure of zeolite SSZ-56, a member of the family of SFS zeolites with a crystal structure consisting of 56 SiO_2 (Figure 3.3a) [4,150]. 40 CO_2 molecules were inserted into the channels (Figure 3.3b) to create the same chemical composition as the system used in the experiment. To follow the experimental conditions, the SiO_2-CO_2 model system was equilibrated for 3 ps to 500 K and then to 1000 K at 0 GPa with *NVT* MD calculations. This was followed by *NPT* MD simulation at 26 GPa and 1000 K and then a separate calculation at 30 GPa and 500 K. In each case, the MD calculation lasted for at least 13 ps. It is noteworthy that the pressures and temperatures are far below the transition pressure of molecular CO_2 to non-molecular CO_2 above 41 GPa and 1800 K. A time step of 1.0 fs was used in the integration of the equations of motion. The PBE exchange-correlation functional was employed. VASP [44-46,121], a plane wave basis electronic structure code using projected augmented wave potentials for the atoms was used for all the calculations. The PBE functional was employed, and the electron orbitals were expanded in the plane wave basis set. A plane wave basis set with an energy cutoff 400 eV was used. In view of the large supercell and that the system is a large gap insulator, only one *k*-point (Γ) was used to sample the Brillouin Zone. The MD trajectories were examined to identify the reaction mechanisms and products.

Results and discussions

During the temperature scaling stage, no reaction between SiO_2 and CO_2 (Figure 3.4) was observed. In this period, the microspore framework was maintained and the CO_2 distributed uniformly inside the channels. Upon compression to 26 GPa and 30 GPa, the lattice constants got shortened, most noticeably in the *b* axes (Figure 3.5a–b). This indicated that the porous SiO_2 framework had shrunk, and the SiO_2 framework started to distort. At 30 GPa, the *a* lattice constant

(*x*-direction) was shortened more than the *b*, as compared to 26 GPa. In both calculations, the compressed structure helped to bring the SiO_2 and CO_2 units closer, and chemical interaction was observed. The reactions between SiO_2 and CO_2 occurred on the surface (Figure 3.3c–d) of the channels forming unidentate, bidentate, and bridged carbonates (Figure 3.3e). This observation is exactly the same as suggested from the experimental vibrational spectra [111]. After 8 ps, the model system equilibrated and there was no more change in the lattice constants. Polycarbonate (CO_3) chains composed of (-O-(C=O)-O-) were formed in the large channel with some unreacted CO_2 molecules. The product consists of 3 coordinated carbonate (CO_3) groups with an average C-O bond length of 1.45 Å. Remarkably, even after the reaction, the SFS framework was only slightly distorted, and the gross zeolite structure was maintained (Figure 3.6). The reactions between the SiO_2 and CO_2 resulted in the increase of the local Si-O coordination number to five.

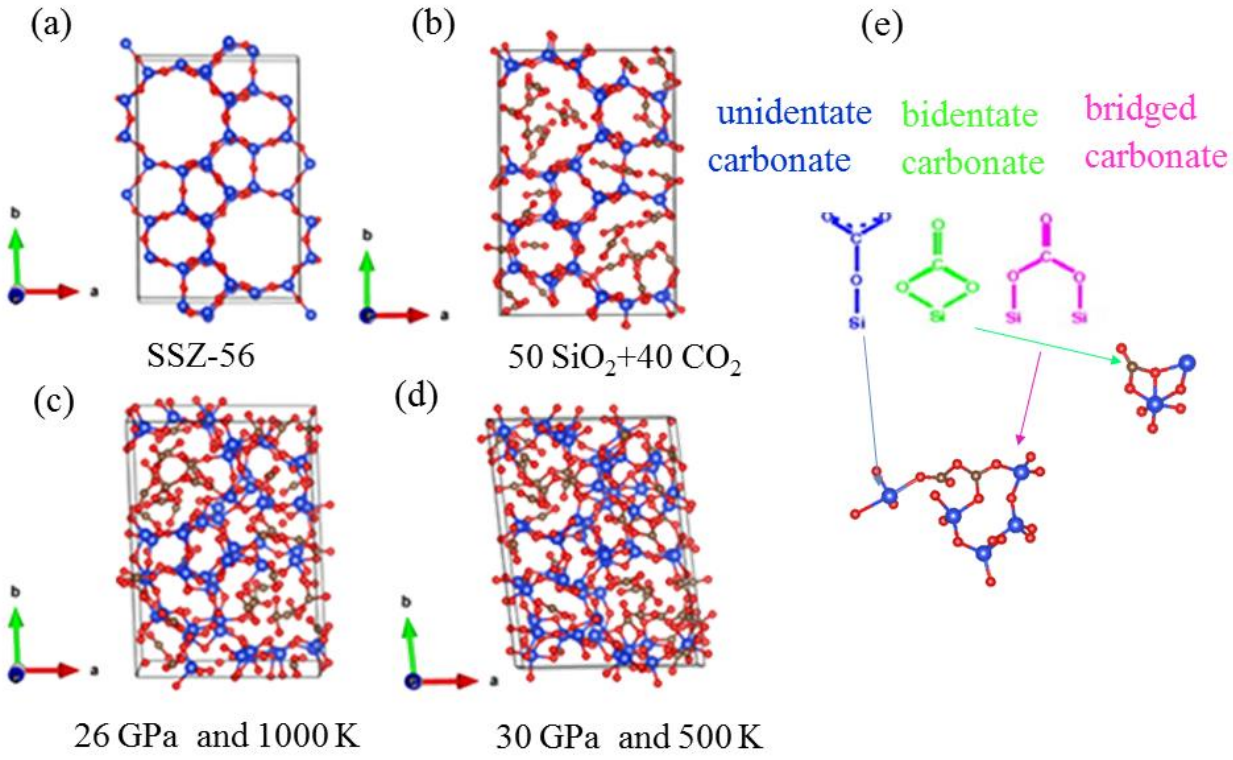

Figure 3.3 (a) The optimized SSZ-56. (b) The initial structure of the SiO_2-CO_2 model. Final snapshots of the SiO_2-CO_2 model from *NPT* calculations at (c) 26 GPa and 1000 K and (d) 30 GPa and 500 K. (e) Fragments extracted from the final snapshot at 26 GPa and 1000 K, showing the unidentate (blue), bidentate (green), and bridged carbonates (purple). The arrows in e point to the fragments associated with the distinctive species found in the experiment. (Si in blue, C in grey, and O in red).

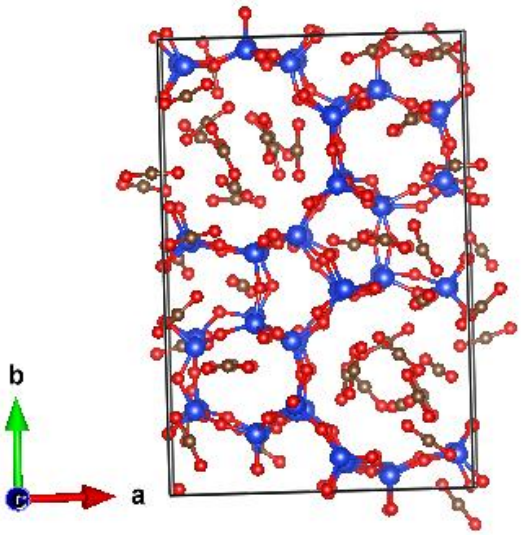

Figure 3.4 Final snapshot of the SiO_2-CO_2 model from the *NVT* simulation at 0 GPa and 1000 K. (Si in blue, C in grey, and O in red).

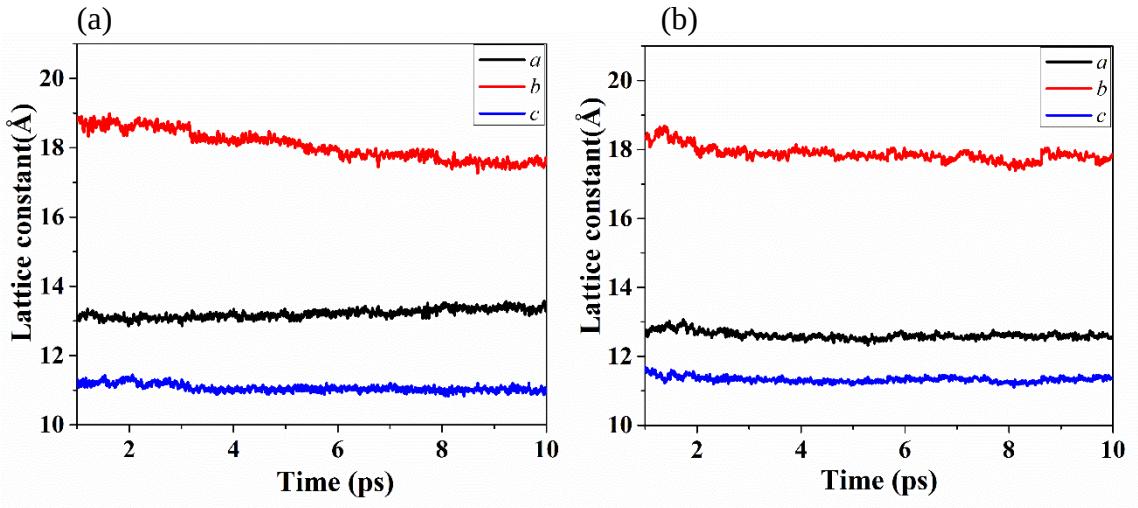

Figure 3.5 Temporal evolution of the lattice constants in the MD simulations performed at (a) 26 GPa and 1000 K and (b) 30 GPa and 500 K.

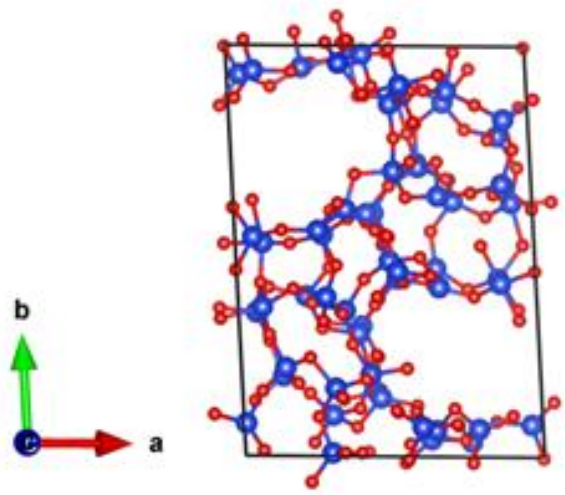

Figure 3.6 SiO_2-Framework of the final structure of the SiO_2-CO_2 model from the *NPT* MD calculation at 26 GPa and 1000 K with CO_2 molecules and polycarbonate chains removed. (Si in blue and O in red).

To explore the reaction mechanism, we analyzed the temporal atomic movements along the MD trajectory. For both simulations (i.e. 26 GPa at 1000 K and 30 GPa at 500 K), similar results were found. The temporal variation of the lattice constants plotted in Figure 3.5 shows a slowly decreasing trend indicating that the reaction between SiO_2 and CO_2 proceeded gradually. At high pressure and high temperature, some of the CO_2 exhibited large amplitude O-C-O bending motions. When the bent CO_2 moved close to the surface of the SiO_2 channels, the O of CO_2 started to bond with the Si forming a 5-Si-O coordinated Si centers (Figure 3.7a). The C hybridization changed from *sp* to sp^2. This initial reaction mainly occurred in the small pores. This is reasonable since the bent CO_2 only needed to migrate a short distance before reaching the channel surface. The reacted CO_2 was then trapped and immobilized in the channels. In the next step, the reaction between C with the bridging O of two corner-shared SiO_4 tetrahedra (Si-O-Si linkage) formed the bidentate carbonates (Figure 3.7b). The reaction proceeded at a very slow rate, and no further

reaction was observed for 3.5 ps although the lattice constants were further reduced. After 3.5 ps, a similar reaction between CO_2 and SiO_2 in the large channel was observed (Figure 3.7c). Since the large pores are more spacious, the reacted CO_2 can orient parallel to the channel. With more free CO_2 molecules were diffused into the channel, more reactions were observed (Figure 3.7d–e). Unidentate carbonates were formed if the CO_2 molecules were situated perpendicular to the channel surface (Figure 3.7d). Bidentate carbonates were also formed in the large pores (Figure 3.7d–e). Up to 6.1 ps, the CO_3/carbonates in the large channels continued to react further when additional CO_2 being brought closer by diffusion leading to the formation of polycarbonate chains attached to the channel surface (Figure 3.7f–h). A similar reaction mechanism was also observed at 30 GPa and 500 K.

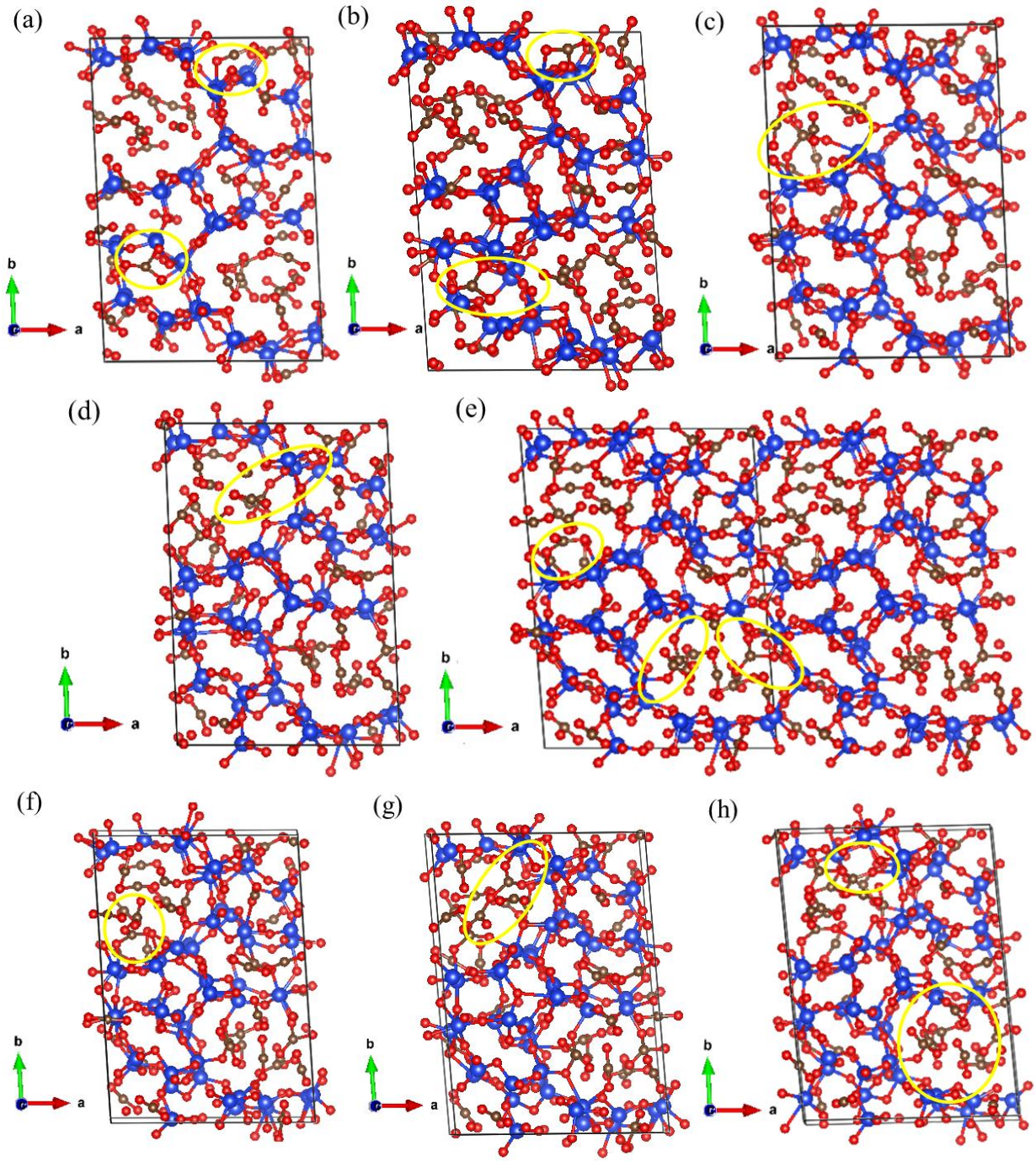

Figure 3.7 Snapshots of the SiO_2-CO_2 model system at different stages from the *NPT* calculation at 26 GPa and 1000 K: at step (a) 479, (b) 749, (c) 3501, (d) 3821, (e) 6101, (f) 6131, (g) 6201, and (h) 8000. The yellow circles highlight the structural changes described in the text. (Si in blue, C in grey, and O in red).

The reaction can be summarized into three primary stages (Scheme 3.1). (i) At high temperature the CO_2 molecule became bent. (ii) The initial reaction was between O of the CO2 and Si of the SiO_4 tetrahedra on the surface of the channels where the lone pair on the O interacted with the empty $\sigma*$ orbital of SiO_2 (see Scheme 3.2) and the C bonded to the bridging Si-O-Si forming CO_3. (iii) Finally, subsequent reactions with other free CO_2 produced the polymer structure.

Scheme 3.1 The three primary reactions: (i) The bending of CO_2 at high temperature and high pressure. (ii) The oxygen of the bent CO_2 bonded with Si of SiO_4 tetrahedra on the surface of the zeolite channel forming a five-coordination Si centers. And (iii) the other O atom of the CO_2 interacts with additional CO_2 molecules and initialized polymerization

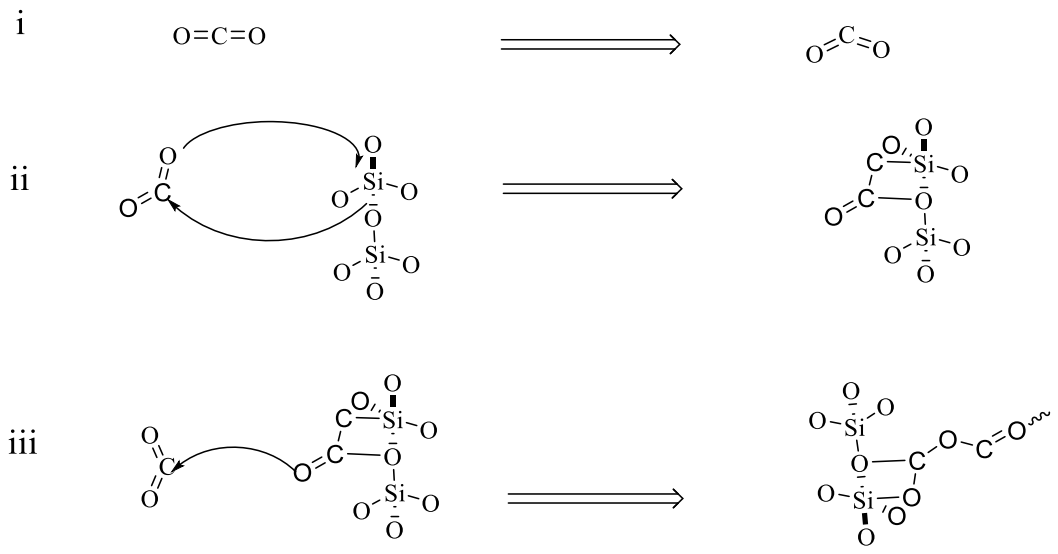

Scheme 3.2 Orbital interaction diagram of the initial chemical reaction between CO_2 and SiO_2

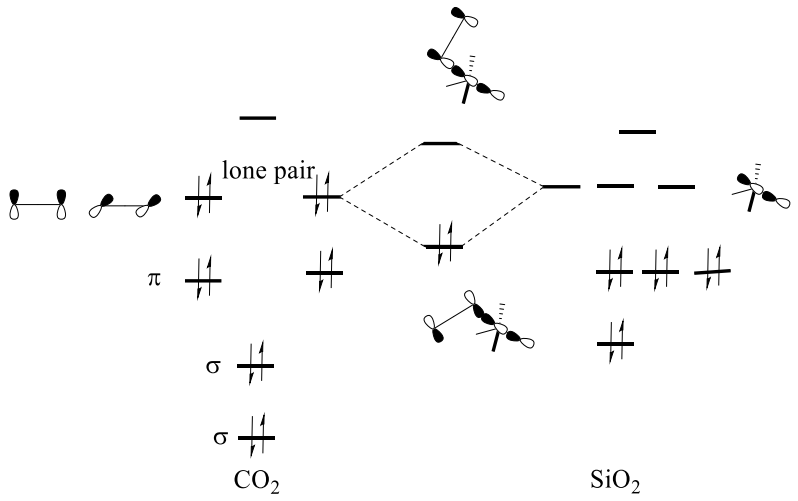

Conclusions

In this part, *NPT* MD simulations were performed and confirmed the chemical reactions between CO_2 in microporous SiO_2 (Zeolite SSZ-56). The theoretical results are in substantial agreement with experiment in which chemical reactions were observed at 26 GPa and 1000 K. The products inferred from infrared spectra are revealed in the calculations. The reaction occurred at the pore surface through the interaction between the Si and O with an excited, bent CO_2. Subsequent reactions eventually led to the formation of polycarbonate chains.

3.1.3 Formation of cristobalite-like SiO_2-CO_2 solid solution

The high pressure polymorphs of CO_2 and SiO_2 share several similar structures. However, due to the significant differences in the C-O and Si-O bond lengths, the formation of a SiO_2-CO_2 crystalline was not foreseen as a stable solid, which would require both C and Si to have compatible coordination environments. Therefore, it was totally unexpected a crystalline solid, composed of

similar stoichiometric amounts of CO_2 and SiO_2 to be synthesized from the reaction of CO_2 with melted zeolite SSZ-56 at 16–22 GPa and 4000 K. Even more remarkable, this new material can be recovered to ambient conditions and was found from X-ray diffraction to have an α-cristobalite structure with both C and Si fourfold coordinated to the oxygen atoms [5].

To study this unexpected experimental finding, the reaction product of CO_2 in zeolite SSZ-56 described above was melted at 10000 K using AIMD simulation in the *NVT* ensemble. Quenching of the molten structure was carried out by lowering the temperature slowly in steps of 100 K to 500 K. In the melt, both Si and C atoms diffused evenly (Figure 3.8a). Upon quenching, a structure composed of linked CO_4 and SiO_4 tetrahedra through corner-sharing, the basic structural feature of the cristobalite structure, and remaining of CO_3 were found (Figure 3.8b). It is not surprising and not unexpected that the calculations did not reproduce the observed crystal structure. However, the essential structural motif of the SiO_2-CO_2 solid solution, *i.e*. the occurrence of linked CO_4 and SiO_4 tetrahedra, was clearly observed. Therefore, it is indeed possible to form a crystalline linked CO_4 and SiO_4 tetrahedra solid.

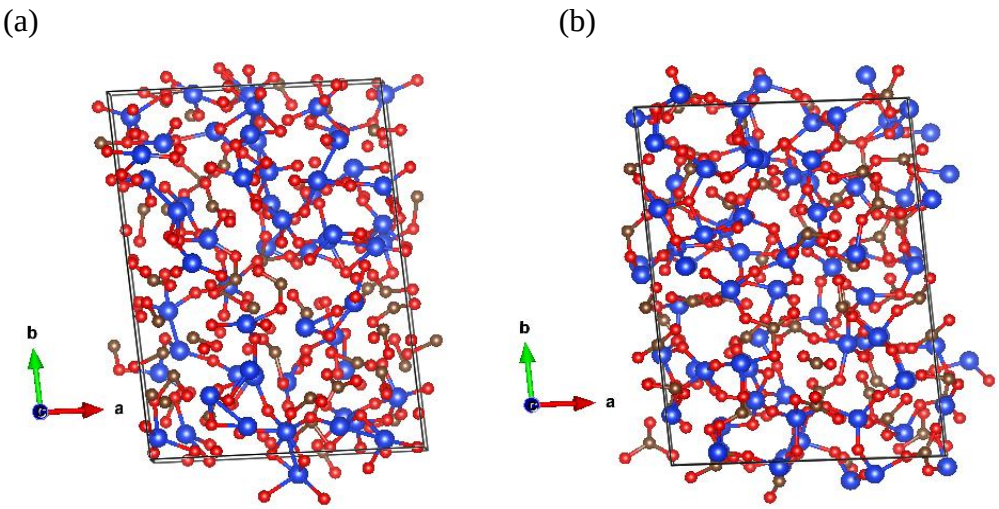

Figure 3.8 (a) Final snapshot of the SiO_2-CO_2 model from the *NVT* calculation at 10000 K and 26 GPa.(b) Quenched product of the SiO_2-CO_2 model from 10000 K and 26 GPa to 500 K and 26 GPa. (Si in blue, C in grey, and O in red).

To understand the stability of the experimentally observed α-cristobalite SiO_2-CO_2 solid solution, we constructed an α-cristobalite-type structure with equal amounts of CO_2 and SiO_2, *i.e*. $Si_2C_2O_8$. The model was constructed by replacing half of the Si atoms with C atoms randomly. The model structure was then fully optimized at selected pressures. The optimized model is monoclinic $P2_1$ space group (Figure 3.9a), but the unit cell angles are very close to 90°. The optimized lattice parameters at 9 GPa are a = 4.389 Å, b = 4.181 Å, and c = 5.983 Å. The theoretical structure, accounting for the distortion in the crystal structure due to disordered C and Si positions, is in fair agreement with the experimentally observed cristobalite-type tetragonal $P4_12_12$ structure with a (= b) = 4.594(1) and c = 5.938(3) Å at 7 GPa [5]. The predicted structure is dynamically stable and thermodynamically metastable relative to SiO_2 cristobalite and phase-III solid CO_2. It can be quenched recoverable as no soft mode was found in the calculated phonon band structure shown in Figure 3.10a. The calculated Raman and infrared spectra are in very good agreement with experimental results (Figure 3.9b). In the Raman spectrum, a single dominant sharp peak observed at around 540 cm^{-1} is clearly reproduced by the calculations.

The thermodynamic stability of the SiO_2-CO_2 solid solution with the α-cristobalite structure in the pressure range 2–25 GPa is determined from a comparison between the calculated enthalpies of the SiO_2-CO_2 model and the sum of CO_2-III and quartz and CO_2-III and α-cristobalite, shown in Figure 3.10b. Solid CO_2-III was chosen as the reference because it is the stable solid phase in this pressure range. The results show that the solid solution is thermodynamically unstable with respect to CO_2 and quartz, but it is thermodynamically stable with respect to CO_2-III and α-cristobalite SiO_2 at pressures higher than 10 GPa. Therefore, α-

cristobalite SiO_2-CO_2 can be formed at pressures higher than 10 GPa and high temperature and the material will become a metastable phase when recovered at ambient pressure.

To examine the electronic and physical properties of the novel SiO_2-CO_2 solid solution with the cristobalite-type structure, the electronic band structure, optical spectrum, elastic modulus, and hardness were calculated. The optical spectrum was computed by solving the Bethe-Salpeter equation (BSE) using *GW* corrected eigenvalues. Elastic constants were computed by the strain-stress method, and bulk modulus and shear modulus were derived from the Voigt-Reuss-Hill averaging scheme [151,152].

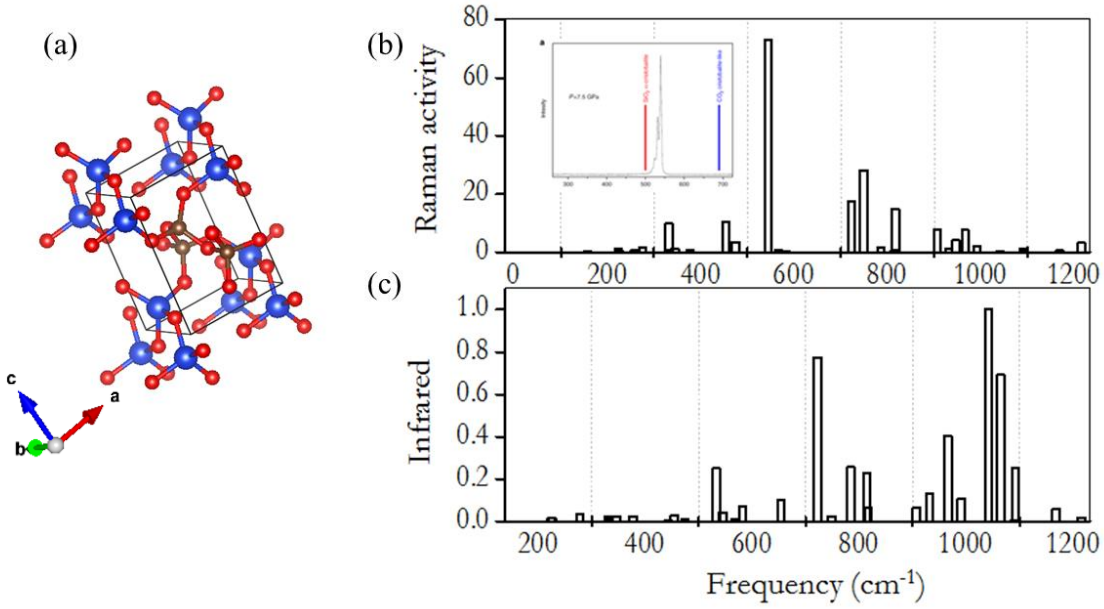

Figure 3.9 (a) The optimized α-cristobalite-like SiO_2-CO_2 solid solution. (Si in blue, C in grey, and O in red). (b) The calculated Raman and (c) IR spectrum of the α-cristobalite-like SiO_2-CO_2 solid solution.

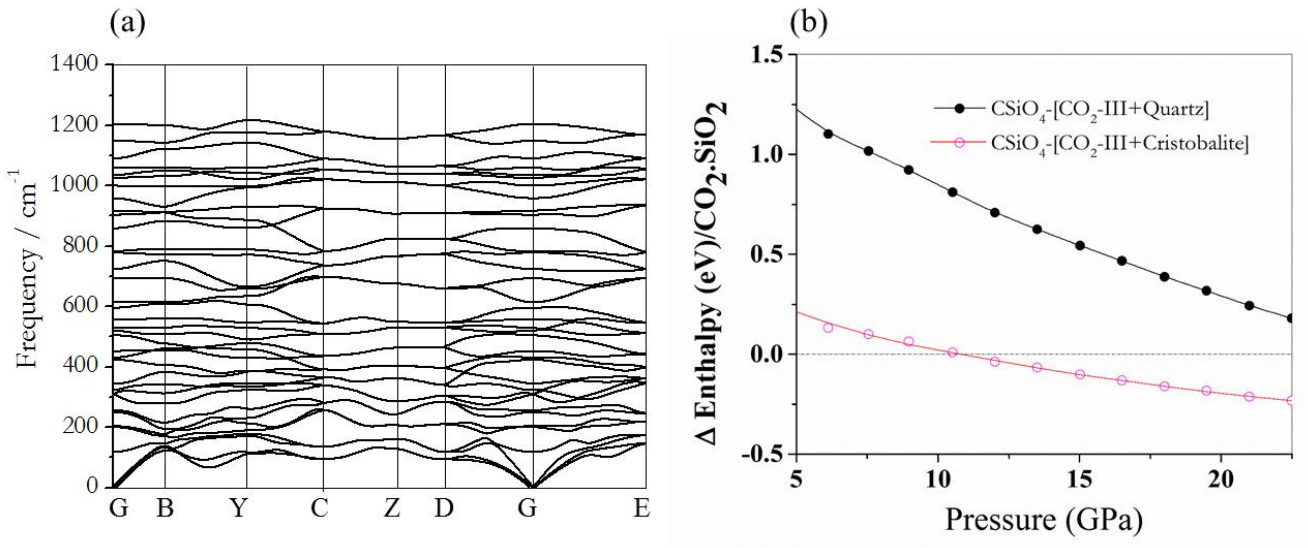

Figure 3.10 The calculated (a) phonon spectrum and (b) formation enthalpy for the α-cristobalite-like SiO_2-CO_2 solid solution with respect to phase III of CO_2 and quartz, and α-cristobalite, respectively.

The band structure shows SiO_2-CO_2 solid solution is an insulator with a direct band gap of 7.0 eV (Figure 3.11a). The band gap is less than that of the SiO_2 analogies (the band gap of polycrystalline is 8.9 ± 0.2 eV [153]; for the thermally grown amorphous SiO_2 film it is 9.3 eV [154]; for amorphous SiO_2 it is 9.7 eV [155]). Furthermore, crystalline silica: *a*-quartz, β-quartz, *a*-cristobalite, β-cristobalite, and β-tridymite are shown to have rather similar electronic band structures and band gaps [156-159]. In the SiO_2-CO_2 solid solution, the dispersions of the valence electronic bands are surprisingly flat throughout the entire Brillouin zone. The calculated absorption spectrum also shows a band-edge absorption around 7.0 eV with a broad main absorption at 12 eV. The reflectivity is quite small at low frequency as the compound is transparent. The calculated low-frequency refractivity is $n(\omega) = 1.17$, which is close to quartz (1.45). Thus, the SiO_2-CO_2 solid solution may also be a good glass material. The recovered SiO_2-CO_2 solid has a bulk modulus *B* of 55.62 GPa, which is higher than that of quartz (36.4 GPa) [160]. The calculated

Vickers hardness H_v is ca. 11.0 GPa, which is comparable to that of quartz at 9.81-11.3 GPa [161]. A larger bulk modulus and hardness as compared to quartz are due to the stronger C-O bonds in the structure.

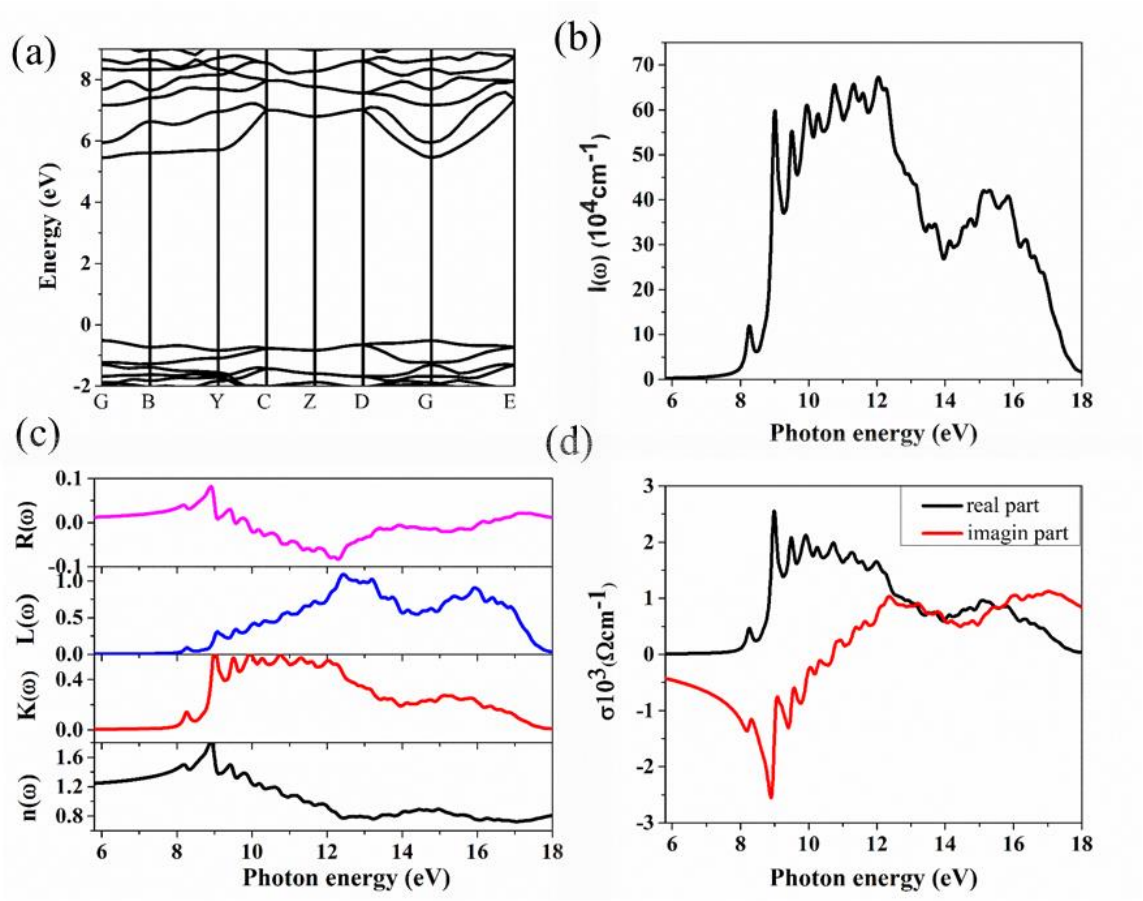

Figure 3.11 The calculated (a) electronic band structure, (b) absorption spectrum, (c) refractivity spectrum, energy-loss spectrum, extinction coefficient, and refractive index, and (d) optical conductivity for cristobalite-like SiO_2-CO_2 solid structure

In summary, MD simulations in the *NVT* ensembles and static optimization have been performed to investigate the formation of a SiO_2-CO_2 solid solution from the melt. Although the α-cristobalite-like SiO_2-CO_2 compound was not directly obtained nor expected to be obtained from the quenched product of the reaction between SiO_2 and porous SiO_2, examination of the local

structure strongly suggests possible formation of corner-shared CO_4-SiO_4 linkages. Electronic structure calculation on the model of the SiO_2-CO_2 solid solution shows a similar but slightly distorted α-cristobalite-like SiO_2-CO_2 structure. The stability of this solid solution over 10 GPa is established. Optical calculations on this new material show similar optical and physical characteristics, but superior properties to quartz.

3.1.4 Chemical reactions between CO_2 and stishovite-SiO_2

Silica together with $MgSiO_3$ and $CaSiO_3$ are three of the main oxide components of the terrestrial mantle of Earth. Stishovite is stable at pressures above 9 GPa [162]. It was first synthesized in 1961 [163] and was later found in nature at the impact site at Meteor Crater, AZ in 1962 [164]. Upon compression, stishovite undergoes further transformations to three dense phases with 6 oxygen-coordinated Si up to 300 GPa [165]. Therefore, it might be the dominant silica phase in the Earth's lower mantle. Recently, technology for pumping atmospheric CO_2 underground has been developed to remove CO_2 from the atmosphere. If CO_2 can react with the high pressure phase stishovite, this can increase the CO_2/silica stability and the method could even be used for CO_2 storage. In the following, we extended the study of the reaction between CO_2 and silica to the high pressure phase of SiO_2—stishovite.

Computational methodology

Initial exploration calculations were performed with a supercell model consisting of a slab of crystalline stishovite with two open surfaces (vacuum regions) constructed from geometry-optimized stishovite unit cells (Figure 3.12 a) comprised of four rows of SiO_6 and terminated with Si-O-Si bridged surfaces. 16 CO_2 molecules were introduced to the vacuum region above the slab

to generate a SiO_2-CO_2 model with SiO_2:CO_2 ~ 1:1 stoichiometry (Figure 3.12b). We studied two thermodynamic conditions: (i) at 25 GPa and temperatures up to 4000 K and (ii) at 50 GPa with temperatures up to 10000 K. *NVT* MD calculations were performed to equilibrate the system at each preset temperature. This was followed by isothermal-isobaric *NPT* MD simulations at the selected pressures. The time step used in all the MD simulations was 1 fs. The VASP code [44-46,121], a plane-wave basis electronic structure code employing projected, augmented wave potential [35,166] for the atoms, with the PBE [19] exchange–correlation functional was used for all calculations.

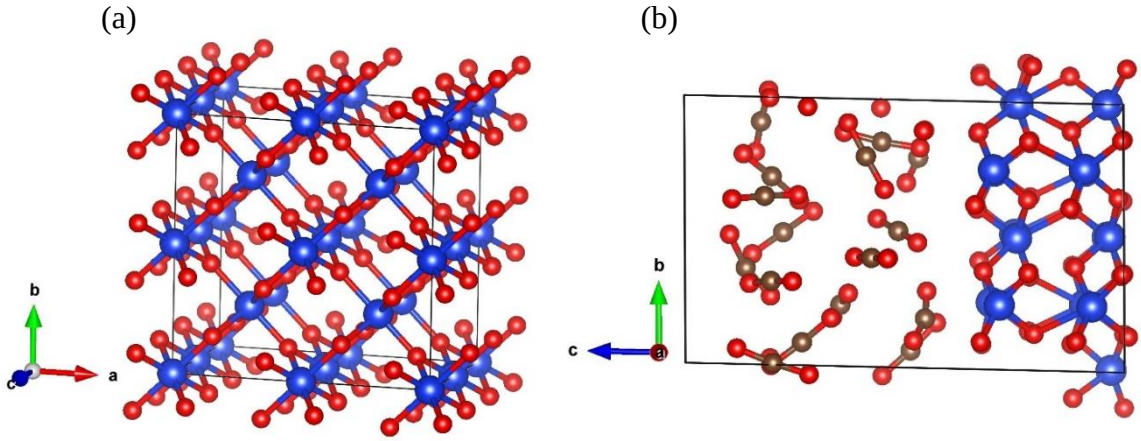

Figure 3.12 Structures of (a) stishovite and (b) the initial model of SiO_2-CO_2. (Si in blue, C in grey, and O in red).

Chemical reactions between stishovite and CO_2 at 25 GPa and high temperatures

We first performed a series of AIMD simulations at 25 GPa and different temperatures. The pressure was chosen in order to be comparable with the experimental conditions for the reaction of CO_2 with zeolite SSZ-56 [4]. At 1000 K, the reactions were initiated at the gas/solid interface while the bulk stishovite framework remained intact (in Figure 3.13a). The CO_2 was bonded to the stishovite surface forming carbonate CO_3 in that, the O of the CO_2 bonded to the Si

of the SiO_2 on the surface while the O of the Si-O-Si connected with the C of CO_2. Both the bidentate and bridged carbonates were observed (in Figure 3.13b). Some bent CO_2 only bonded to Si on the stishovite surface forming a Si-O bond (in Figure 3.13b). In the vacuum region, most of the CO_2 remained as free molecules. At 2000 K, a similar product was obtained (Figure 3.14). However, carbonate dimers on the surface of stishovite were found between the bent CO_2 attached to the surface and the carbonate (CO_3) (Figure 3.14). There were still CO_2 molecules between two slabs. Higher temperatures promoted faster diffusion, and more CO_2 was brought into contact with the surface. The stishovite slab was melted at 4000 K and then a disordered product was obtained (Figure 3.15a). Apart from the bidentate and bridged carbonates (CO_3), a few C-O chains consisting of either CO_3 and CO_3, or CO_3 and CO_4 attached to SiO_5 through Si-O-C- linkage (Figure 3.15b) were formed, but there was no Si-C bond. The local Si-O coordination was a mixture of four, five and six coordinated ions.

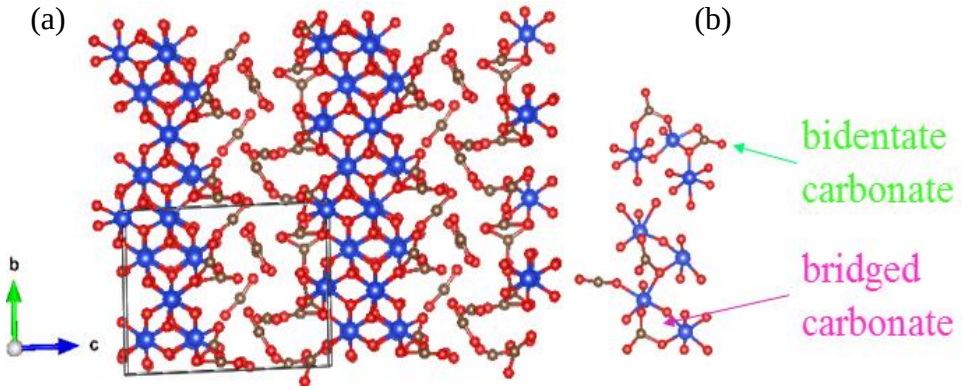

Figure 3.13 (a) Final structure of the SiO_2-CO_2 model from the *NPT* simulation at 1000 K and 25 GPa. (b) Fragments extracted from the final structure: the bidentate (green) and bridged (purple) carbonates. (Si in blue, C in grey, and O in red).

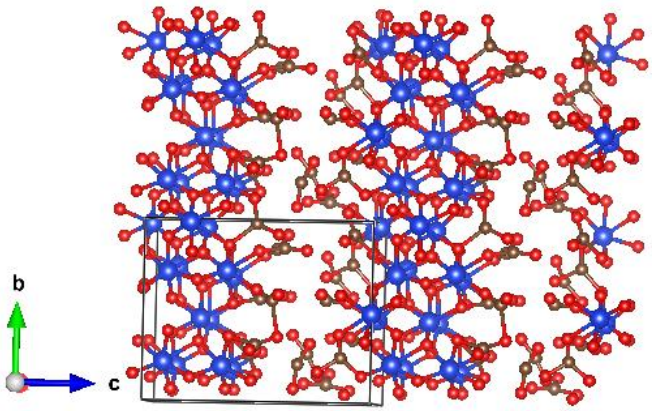

Figure 3.14 Final structure of the SiO_2-CO_2 model from the *NPT* simulation at 2000 K and 25 GPa. The black circle highlights the structural changes described in the text. (Si in blue, C in grey, and O in red)

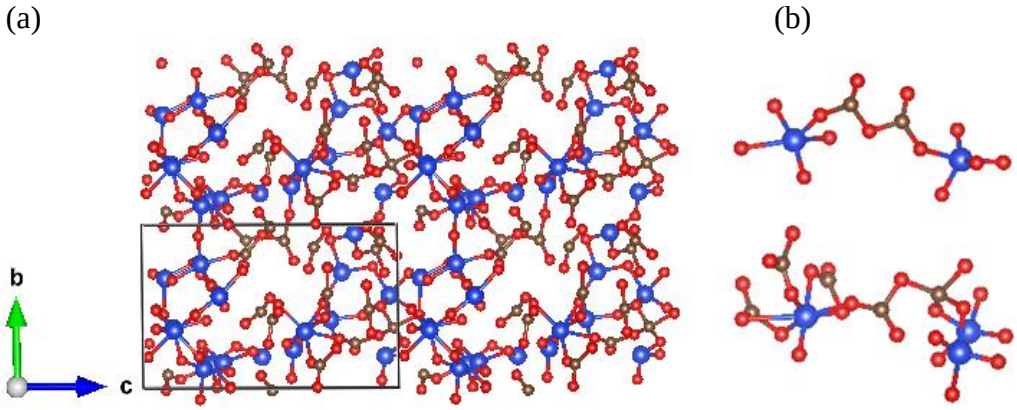

Figure 3.15 (a) Final structure of the SiO_2-CO_2 model from the *NPT* simulation at 4000 K and 25 GPa, (b) C-O chains consisting of either CO_3 and CO_3, or CO_3 and CO_4 attached to SiO_5 identified in the final structure. (Si in blue, C in grey, and O in red).

Chemical reaction stishovite and CO_2 at 50 GPa and high temperatures

To mimic the pressure and temperature conditions in the Earth's lower mantle, we increased the pressure to 50 GPa. Subsequently, significant chemical reactions between CO_2 and SiO_2 were observed readily at 2000 K leading to the formation of an extended solid with the bulk stishovite framework intact (Figure 3.16a). The bulk and surface Si atoms remained to be 6

coordinated to O. In the vacuum interface, C-O chains composed of CO_4 and CO_3 attached to the stishovite surfaces through the formation of C-O-Si linkages (Figure 3.16b). Corner-shared CO_4 and SiO_6, unidentate, bidentate, and bridged carbonates were formed on the surface. There were also a few CO_3 units bridging two SiO_6 units and no formation of C-O chains (Figure 3.16b). When the temperature was increased to 4000 K and 6000 K, the Si framework collapsed (Figure 3.17 and Figure 3.18), and the diffusion of the Si atoms indicated the system was in a molten state. Si-O-C linkages, similar to those in the product from 4000 K and 25 GPa, were observed. However at that point, most Si–O was 6 coordinated. At 10000 K the SiO_2 framework completely melted and there was almost uniform distribution of Si and C atoms through the model box. The reaction product had become a mixture of Si and C clusters with some Si-O-C bonds formed (Figure 3.19).

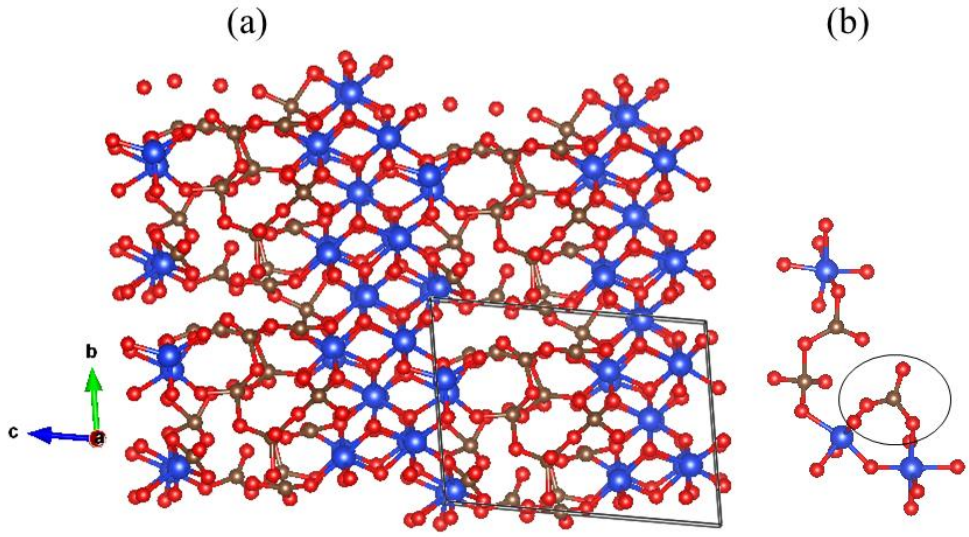

Figure 3.16 (a) Final structure of the SiO_2-CO_2 model from the *NPT* simulation at 2000 K and 50 GPa. (Si in blue, C in grey, and O in red). (b) C-O chains consisting of CO_4 and CO_3 attached to the stishovite surface and the bridged CO_3 bridging two SiO_6 units. The black circle highlights the structural changes described in the text.

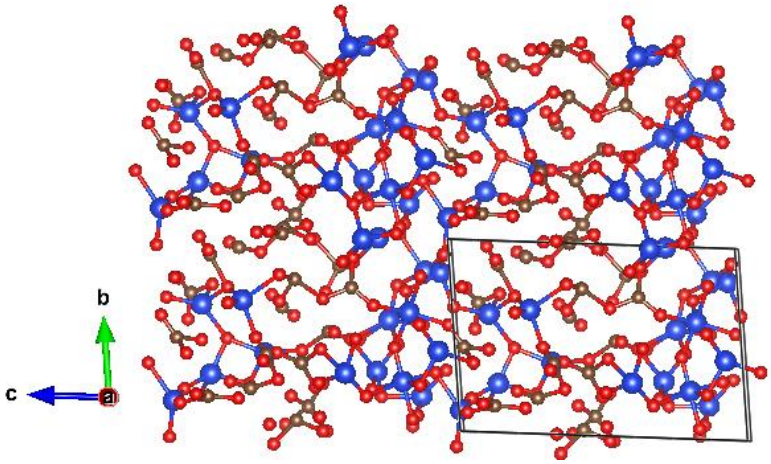

Figure 3.17 Final structure of the SiO_2-CO_2 model from the *NPT* simulation at 4000 K and 50 GPa. (Si in blue, C in grey, and O in red).

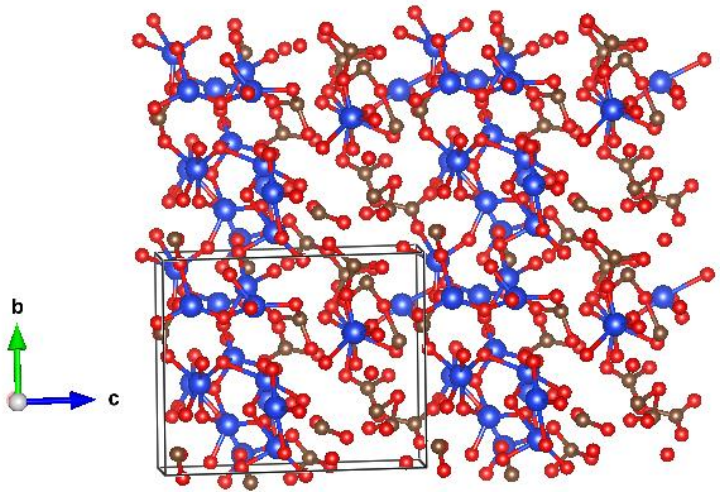

Figure 3.18 Final structure of the SiO_2-CO_2 model from the *NPT* simulation at 6000K and 50 GPa. (Si in blue, C in grey, and O in red).

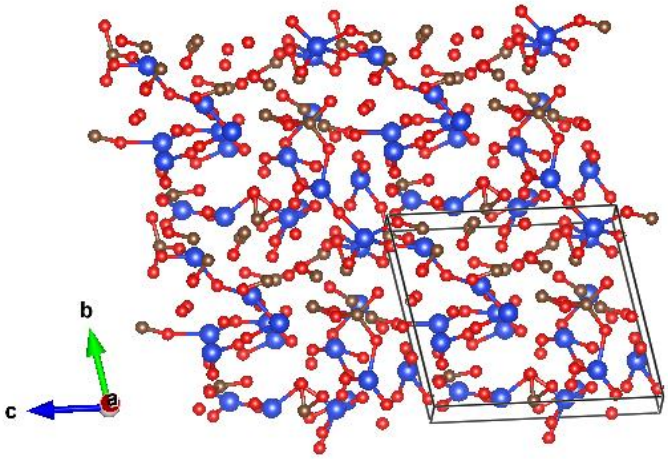

Figure 3.19 Final structure of the SiO_2-CO_2 model from the *NPT* simulation at 10000 K and 50 GPa. (Si in blue, C in grey, and O in red).

Quenched products

To investigate the reaction products, the system was quenched from the melted SiO_2-CO_2 model at 10000 K and 50 GPa to 500 K and 25 GPa (Figure 3.20). The quenched product was a Si-O-C-O interconnected compound. It was a mixture of 4, 5 and 6 Si-O coordinations in the ratio 3:7:6. The appearance of five-coordinated, intermediate Si atoms agrees with other simulations [167,168]. The C atoms were either three- or four-coordinated to O and roughly in the ratio 11:2. Compounds of similar structure were obtained by quenching the system at 50 GPa from 6000 K to 500 K, and the number of 4, 5 and 6 coordinated Si changed to 4:5:6. Now, the number of 3 coordinated C atoms was dominant and the ratio of 3- to 4- coordinated C atoms was 11:1. In comparison, the quenched product obtained at 25 GPa had more 5 coordinated Si atoms (Figure 3.21).

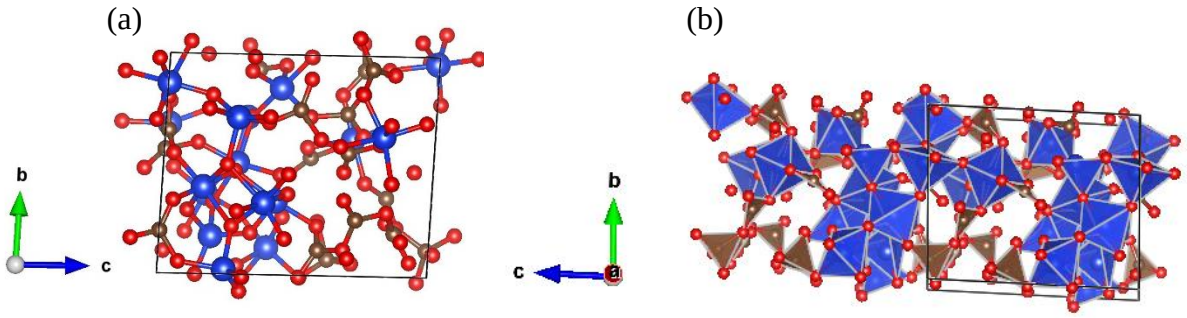

Figure 3.20 Final structure of the SiO_2-CO_2 model from the *NPT* simulation at 500 K and 25 GPa quenched from 10000 K and 50 GPa: (a) the atoms and bonds are presented by balls and sticks; and (b) polyhedral representation of the C-O and Si-O. (Si in blue, C in grey, and O in red).

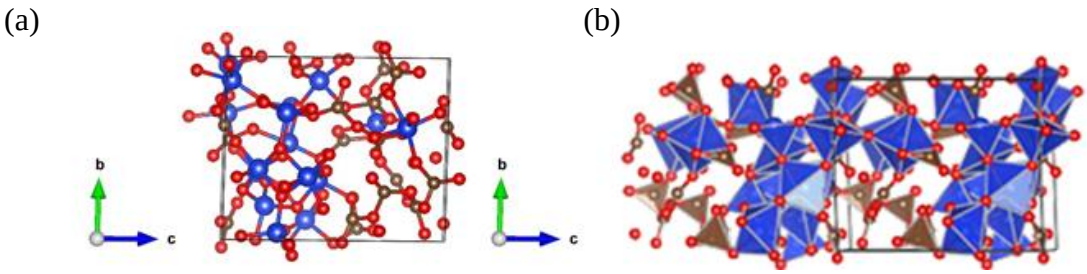

Figure 3.21 Final structure of SiO_2-CO_2 model from the *NVT* simulation at 500 K and 50 GPa quenched from 6000 K and 50 GPa: (a) the atoms and bonds are presented by balls and sticks; and (b) polyhedral representation of the C-O and Si-O. (Si in blue, C in grey, and O in red).

Reaction Mechanisms

The MD trajectories were analyzed to trace the reaction path. At a low pressure (25 GPa), before the stishovite structure melted (at 4000 K), the reaction was initiated from the surface of the stishovite. Unlike the bulk, due to the truncation of the unit cell, the Si atoms on the surface were four-coordinated to O. The reaction started from the bonding of two O atoms from two different CO_2 molecules (marked as C1 and C2 see Scheme 3.3) to the site of four-coordinated Si. Then the C2 started to react with the bridging O atom of corner-shared, surface SiO_4 and bulk SiO_6 and formed CO_3. At 4000 K, the stishovite solid framework melted. At 50 GPa and 2000 K, the

same mechanism was observed. However, upon further compression, the C2 continued to bond with another bridging O atom of the corner-shared surface SiO_4 and bulk SiO_6 and the O of CO_2 reacted with free CO_2 molecules to form CO_4. Then one of the π bonds of CO_2 (C1) broke and continued to bond with other free CO_2. With more free CO_2 molecules involved in the reaction, corner-sharing CO_4 with bridging O atoms were formed on the surface of the stishovite slab (Scheme 3.3).

Scheme 3.3 Reaction scheme of CO_2 with stishovite; C1 and C2 are used to mark two different types of reacting CO_2

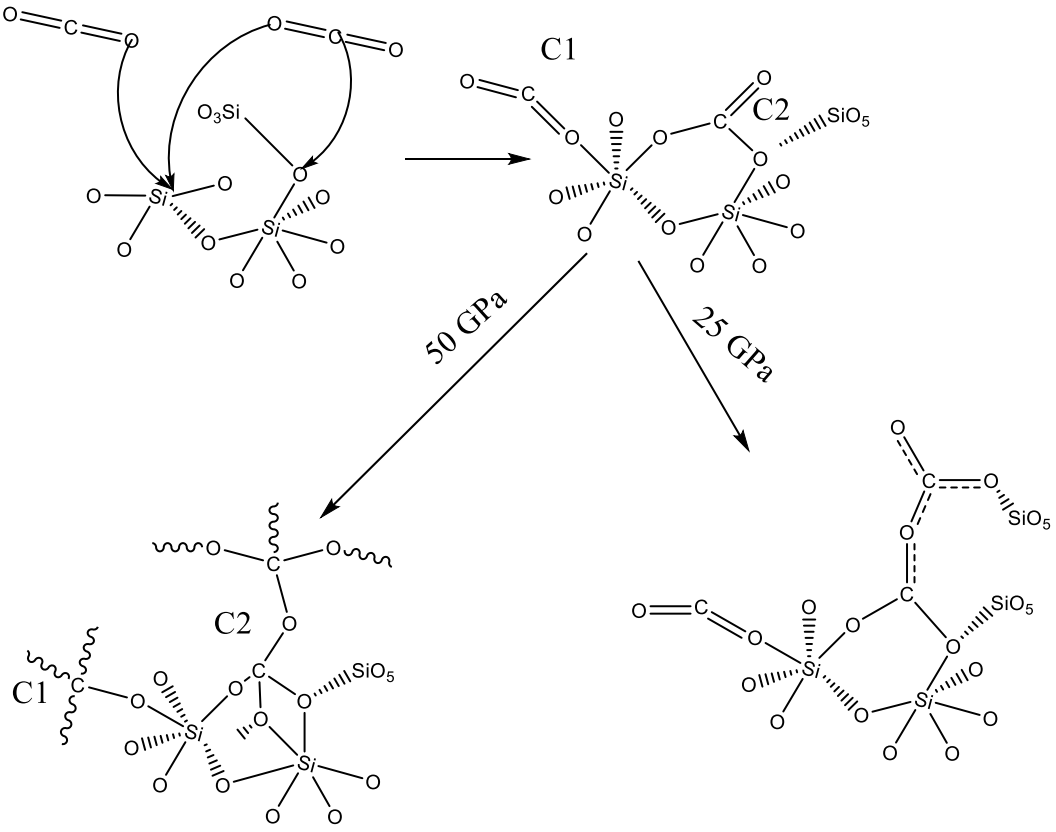

Conclusions

In summary, the *NPT* AIMD simulations showed that SiO_2-CO_2 compounds can be formed from chemical reactions between CO_2 and stishovite under high pressure and high temperature. At 50 GPa and 2000 K, an extended solid structure was obtained in which the bulk stishovite was intact and C-O chains consisting of CO_3 and CO_4 were formed and grew on the surface. Disordered SiO_2-CO_2 compounds were obtained at 25 GPa and 50 GPa and at temperatures above the melting point of stishovite.

3.2 Chemical reactions between quartz and H_2

Introduction

Silicon dioxide, known as silica, with its rich tapestry of various polymorphs and forms, is one of the most abundant materials found on Earth and other terrestrial planets. The stability and chemical reactivity of silica under ambient as well as high temperature and pressure conditions are therefore of critical interest not only to geoscience but also for wide industrial and technological applications. The phase diagram of silica, exhibiting polymorphism and assessing its thermodynamic stability, was completed relatively recently by Swamy and Saxena [169] for temperatures up to 3200 K and pressures up to 15 GPa. In this high temperature and pressure phase diagram region, silica can metamorphose from quartz, the most stable form of SiO_2 at ambient conditions, to tridymite, cristobalite, coesite, and stishovite. The first three polymorphs are well known for their low-temperature (α) and high temperature (β) forms [131,170].

Because of its ubiquitous presence and technological importance, properties of quartz have been widely studied both experimentally [171-174] as well as by computer simulations [175-177]. Except for pH-dependent proton ad/desorption on the silica surface in aqueous environments

[178,179], and low solubility in water [180,181], quartz is chemically a very stable material at ambient conditions, and generally does not interact with other species. Recently, Shinozaki *et al*. [182] used Raman and infrared spectroscopy to study the dissolution of SiO_2 in H_2 gas under high pressure and temperature conditions close to Earth's upper mantle. In contrast to aqueous dissolution, which leads to silicon species containing hydroxyl groups such as H_4SiO_4 or $H_6Si_2O_7$, dissolution in hydrogen gas at high pressure and temperature yields SiH_4 and H_2O. Here, in an effort to elucidate the underlying mechanisms of this interesting process, we carried out MD simulations to capture the essential underlying features, which are shown to have important implications for the origin of water on Earth, the nature of mantle dynamics, and the trigger for nucleating deep earthquakes in the continental mantle lithosphere.

Computational methodology

We created a bulk model of α-quartz with a trigonal supercell ($a = b = 29.460$ Å, $c = 64.824$ Å, $\alpha = \beta = 90.0°$, $\gamma = 120.0°$) containing 1296 SiO_2 units. We relaxed this model by slow, gradual heating to 100 K and to a pressure of 1 GPa by *NPT* MD simulation using the reactive force field ReaxFF, developed by van Duin *et al.* [183,184], as implemented in the LAMMPS software package [185-187]. The time step for all MD used throughout this study was 0.2 fs. Analogously, we prepared a trigonal supercell of identical dimensions filled by 3294 hydrogen molecules (H_2), and this model was equilibrated to the same state (100 K, 1 GPa) as the first one. The density of H_2 gas was selected to conform to a pressure of 1 GPa at 100 K, using the virial definition in a single-phase calculation [39], prior to incorporation into this solid-gas interfacial system. These two structures were merged to form an initial SiO_2-H_2 interfacial model—the quartz slab was separated by 1.5 Å from hydrogen gas at both sides, resulting in an initial *z* cell dimension of 147.0

Å. This system was then brought very carefully to a target temperature of 1700 K and a pressure of 2 GPa (corresponding to experimental conditions of Ref. [182]), by a sequence of 20 ps *NPT*-MD runs. To avoid any artificial structural changes, this sequence of *NPT* equilibration runs was divided into 10 stages. At each stage, the temperature was raised linearly by 160 K and the pressure by 100 MPa during each 20 ps simulation, where the thermal bath was coupled by a five-chain Nosé-Hoover thermostat-barostat [188,189]. We equilibrated the system by at least another 20 ps of MD at each stage until thermodynamic quantities had converged. The system was successfully equilibrated at each stage, which was confirmed by subsequent short *NVE* simulations featuring excellent energy conservation; no unexpected structural changes or sudden potential-energy jumps occurred.

Results and discussions

Silica, in its α-quartz polymorph, is very stable at ambient pressure and room temperature when no interaction with molecular hydrogen can be expected. Therefore, we first performed MD of the SiO_2/H_2 interface under these conditions to confirm the stability of our model and performance of the reactive force field. Hydrogen gas at this temperature and pressure is very dilute, with an experimental density of 0.0899 g/cm^3, behaving practically as an ideal gas; its contact with the silica surface is minimal. Naturally, silica undergoes structural relaxation near the surface, while the bulk region of the slab model maintains the regular crystal structure. As the surface model was created by cutting bulk quartz crystal, dangling bonds can be found on the surface atoms, the valence of which is not saturated chemically. This high-energy structure underwent reconstruction when the surface layer was relaxed, and a fraction of the surface oxygen atoms interacts with hydrogen (a). This process was expected, and proceeded to the simulation's

equilibration phase, after which the structure remained stable. This physically realistic behaviour at ambient conditions is reassuring, serving to lend confidence to these ReaxFF potentials.

Afterwards, we conducted the system carefully to the target temperature of 1700 K and a pressure of 2 GPa by the stage-by-stage procedure described in the previous section. With increasing pressure and temperature, molecular hydrogen diffused into the sub-surface region of the quartz slab (by Fick's Law), as can be seen in Figure 3.22. As the pores in quartz are relatively spacious vis-à-vis comparatively small H_2 molecules, H_2 molecules penetrated deeper and deeper into the crystal structure; finally, hydrogen was found in the whole silica slab in a semi-uniform concentration profile (Figure 3.22b–d). During this step-by-step equilibration, hydrogen maintained its molecular structure initially, although the H-H bond was considerably elongated and strained to 1.0–1.1 Å (Figure 3.22b–d). These weakened hydrogen molecules subsequently underwent dissociation once 1700 K and 2 GPa conditions were approached (Figure 3.22e). The resulting atomic hydrogen interacts chemically with the oxygen atoms of silica. Finally, oxygen's interaction with hydrogen weakened its original binding to silicon atoms, resulting in the formation of water molecules inside the slab. Analysis of the atomic trajectory revealed the following three-step process (see Scheme 3.4): Initially, H_2 penetrated into the porous channels of quartz. Then the H_2 interacted with one of the corner sharing O atoms and a Si atom. The interaction led to the dissociation of H_2 forming an O-H and a Si-H bond. A second H_2 then reacted with Si of the neighbouring SiO_4 in a similar manner. This led to the formation of H_2O and breaking the SiO_4 tetrahedra linkage. This process continues at 1700 K and 2 GPa until a complete layer of water has evolved below the slab's surface, as is clearly visible in Figure 3.22e. The silica itself was transformed into an amorphous structure of SiO_xH_y.

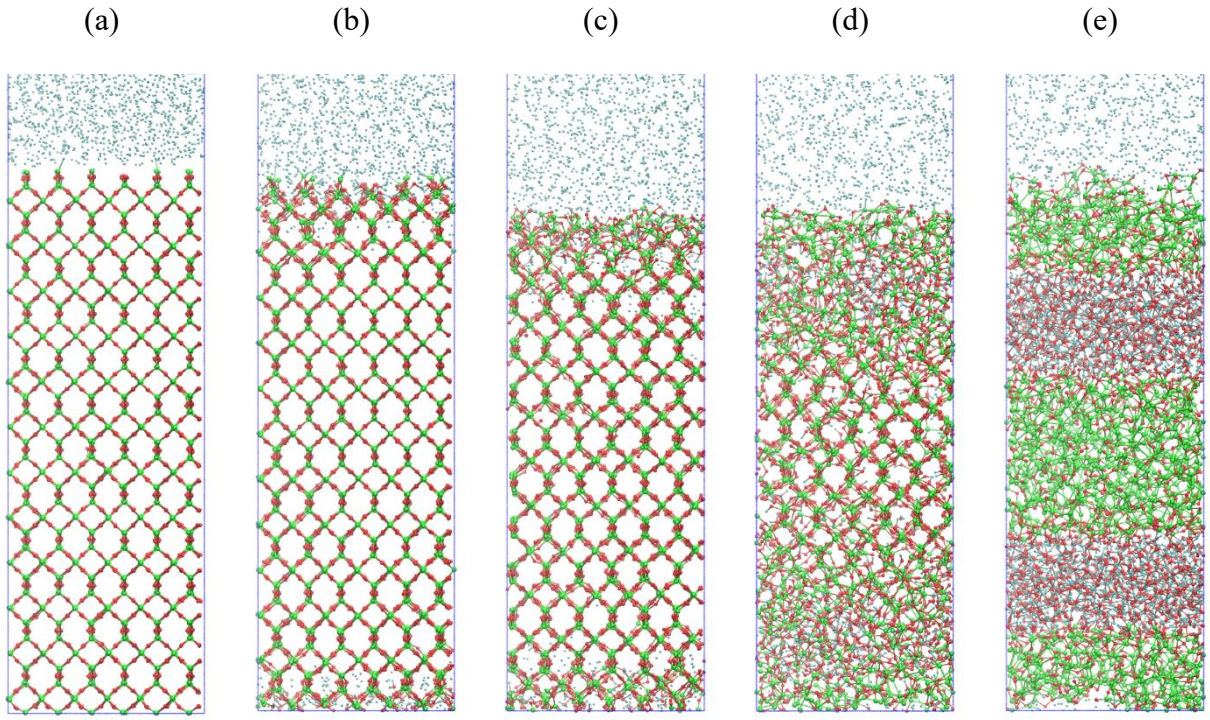

Figure 3.22 Snapshots of the silica slab in different stages of the performed MD simulation: (a) initial structure; (b) initial model equilibrated to 100 K and 1 GPa; (c) structure at 580 K and 1.3 GPa; (d) structure at 1220 K and 1.7 GPa; (e) final structure at 1700 K and 2 GPa. All structures are oriented to (100) direction. Silicon atoms are shown in green, oxygen in red and hydrogen in light blue color. (These five figures were produced by our collaborators, Zdenek Futera and Nail J English, School of Chemical and Bioprocess Engineering, University College Dublin, Belfield, Dublin 4, Ireland)

Scheme 3.4 Evolution of water by reaction of hydrogen gas with the silica. From left to right: H_2 molecule adsorbs to Si-O pair in the crystal lattice, dissociated to atomic hydrogen and forms the water molecule while the remaining hydrogen atoms are attached to Si

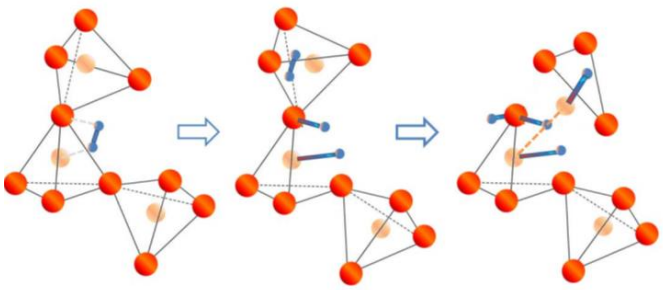

The oxygen density distribution along the *z*-axis (Figure 3.23a) of the water/silica interface (Figure 3.23b) clearly shows three distinct regions, *viz*. the H_2, quartz and water layers. Since there is no O in the H_2 layer, the corresponding density is zero. The density of O in the quartz layer is less than that of the water layer. A "water box" can be extracted in the region sandwiched between 15.0 Å and 26 Å along the z-axis. The density of water confined in this region is 1.99 g/cm^3, which is much higher than the ambient density but is surprisingly similar to water obtained at 23 GPa and 700 K in a shock experiment [190]. Hence, in addition to the external pressure, the two silica layers form a capsule encaging and exerting forces on the water layer to form a higher-pressure local environment. The O-O radial distribution function (RDF), $g_{OO}(r)$, of the confined water is calculated and shown in Figure 3.24. The RDF shows structural features remarkably similar to a previous molecular dynamics simulation study [191] on high pressure (26.8 GPa) water with a density of 1.95 g/cm^3. In both cases, the O atom distribution at the first minimum in the O-H radial distribution of 1.25 Å is nonzero. Following the interpretation provided earlier [191], this feature indicates the molecular dissociation. The $g_{OO}(r)$ shows that the first nearest neighbour separation is shifted to shorter distances compared to the RDF of water under ambient conditions. In addition, the distinctive two-peaks structure in $g_{HH}(r)$ in ambient water has merged into one broad peak. According to the previous study, these changes in the atomic RDFs are caused by the collapse of the nearest neighbour oxygen network due to significant intramolecular dissociation. On the basis of these similarities, we conclude that some of the water molecules in the water layer have been dissociated into ionic species. This conclusion is justified by visual inspection of the water structure and further substantiated from calculations of the O-H coordination number for each O atom in the water layer where the first minimum in $g_{OH}(r)$ was found to be nonzero. It is not accurate to use an arbitrary cutoff criterion for the O-H bond length to determine the coordination

number. Instead, we counted the coordination number by matching each hydrogen atom to the nearest oxygen atom. The results are graphically summarized in Figure 3.25, which clearly shows the presence of OH^-, H_2O, H_3O^+, and H_4O^{2+} species in the water-layer region. Incidentally, although we are not sure of the pressure of the the trapped water, results of the analysis show that the structure of the confined water is remarkably similar to that of the pure liquid at high pressure and high temperature (> 20 GPa, 3000 K) predicted from previous theoretical calculations [164]. This further supports our conclusion that, even with an external pressure of only 2 GPa, the water confined between silica behaves like high pressure water.

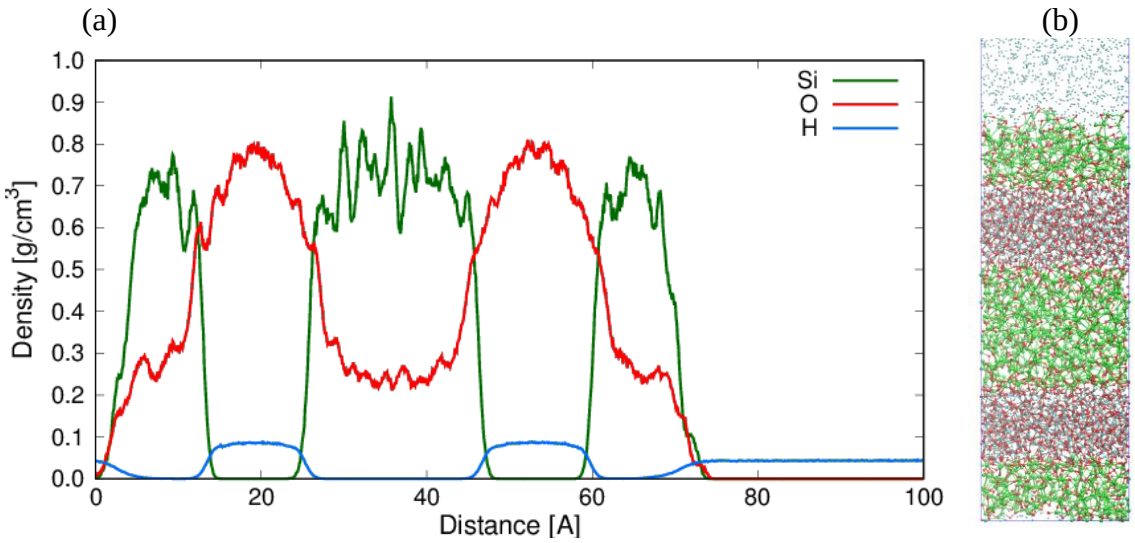

Figure 3.23 (a) Density distribution of individual chemical elements measured along the *z* direction—perpendicular to the interface. (b) Final snapshot of the MD simulation at 1700 K and 2 GPa on which the density distribution was analyzed. Silicon atoms are shown in green, oxygen in red and hydrogen in light blue colour.

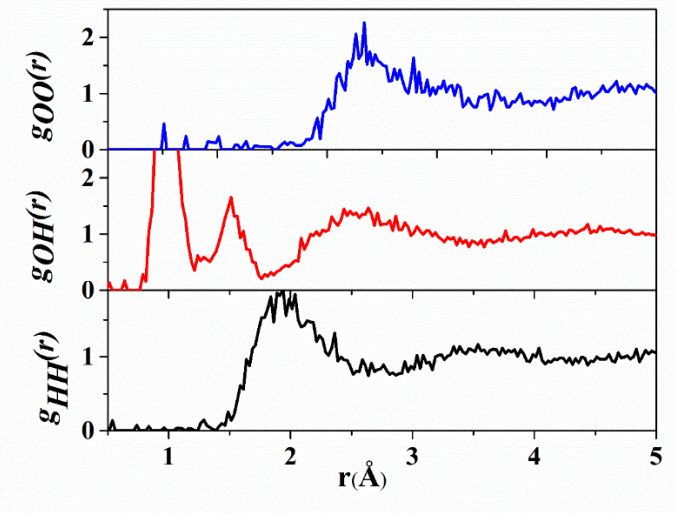

Figure 3.24 The oxygen-oxygen, $g_{OO}(r)$, oxygen-hydrogen, $g_{OH}(r)$, and hydrogen-hydrogen, $g_{HH}(r)$ RDF of the water extracted from the final structure at 1700 K and 2 GPa.

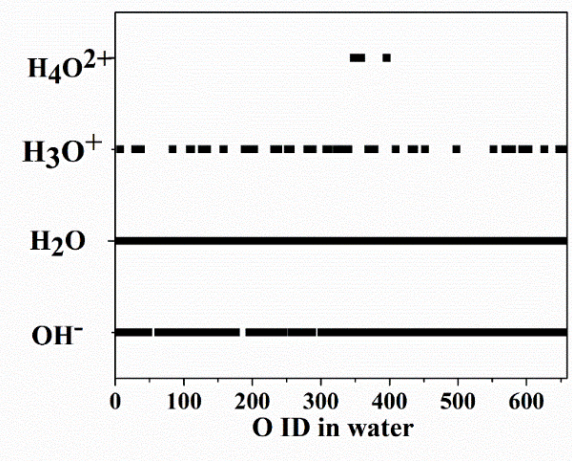

Figure 3.25 Number of hydrogen atoms (represented by OH^-, H_2O, H_3O^+, H_4O^{2+} compounds) associated with each oxygen atom in the water layer formed during the MD simulation at 1700 K and 2 GPa.

In the experimental study, it is suggested that gaseous SiH_4 was formed as a by-product of the reaction of H_2 with quartz. The argument is based on the assignment of a Si-H Raman mode to the stretching vibration of molecular SiH_4 under ambient pressure. Within the timescale of the computer simulation, we only observed the formation of different Si-H species but never molecular

SiH_4. To explain the experimental results, we computed the vibrational density of states of the system after the reaction. Once the Si-H bonds formed between the SiO_2 and H_2 reactions, they were stable throughout the MD simulation (Figure 3.26). This allowed the computation of the bond-length autocorrelation functions (ACFs). The Fourier transform of the ACF of a particular Si-H bond gives the corresponding vibrational spectrum. After careful analysis, we identified 5 distinct types of Si-H bonds, shown in Figure 3.27. These are: Si-H bonds in H-Si_4 (I), H-Si_3O with bridging Si-O-Si (II), H-Si_3 (III), H-Si_3-O, H located on the opposite side (*anti*) of the bridging O of Si-O-Si, (IV) and H-Si_3O, H-Si_3-O, H located on the same side (*syn*) of the bridging O of Si-O-Si, (V). The calculated characteristic vibrational frequencies for these species are 2159 cm^{-1}, 2389 cm^{-1}, 2450 cm^{-1}, 2450 cm^{-1}, and 2200 cm^{-1}, respectively. The calculated frequencies are within the range observed in the experimental Raman spectrum of a broadband from 2100-2300 cm^{-1}.

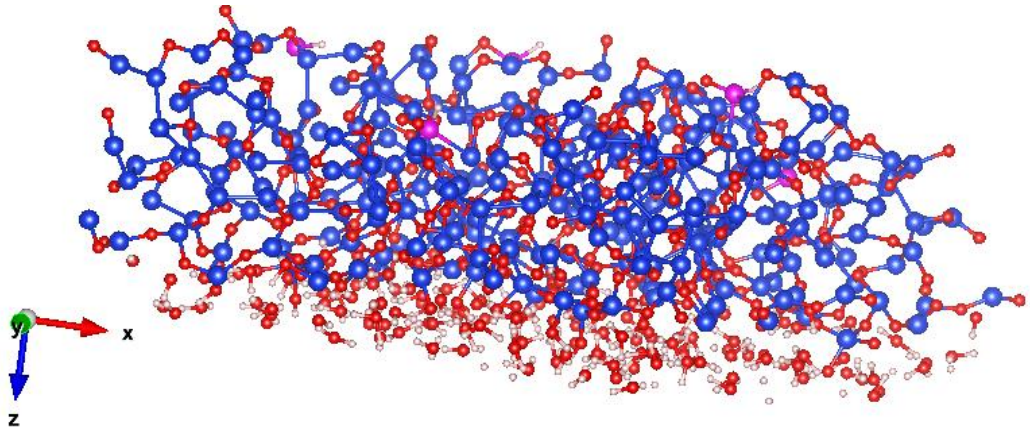

Figure 3.26 Amorphous SiO_xH_y layer extracted from the final step in the MD simulation. Silicon is shown in blue, oxygen in red, and hydrogen in white. Si-H bonds present in the structure are highlighted by magenta colour.

2159 cm^{-1} 2389 cm^{-1} 2450 cm^{-1} 2450 cm^{-1} 2200 cm^{-1}

Figure 3.27 Si-H bond types extracted from the final MD structure at 1700 K and 2 GPa and their corresponding vibrational frequencies. (Sil in blue, O in red, and H in white).

Conclusions

We performed MD simulation of the dissolution of quartz in molecular hydrogen fluid under high temperature and pressure. The simulations were performed using classical yet reactive force fields, allowing sufficiently large chemical changes in the system. We confirmed that at a temperature of 1700 K and pressure of 2 GPa, molecular hydrogen dissociates inside the silica, interacting with oxygen atoms, and this reaction process ends up with the formation of water molecules, as was observed experimentally by Shinozaki *et al.* [182]. Interestingly, the evolved water remains confined in the amorphous structure of silica, and its structure and properties resemble liquid water under substantially higher pressure (*ca.* 23 GPa). Analysis of the structure and Si-H vibrations showed no formation of molecular SiH_4. The H atoms are attached to the surface of Si clusters and the Si-O framework. Our results have implications for fundamental geoscience questions from the origin of water on Earth to the effects on mantle dynamics and the triggering mechanism for enigmatic deep earthquakes in the continental mantle lithosphere.

3.3 General discussion and summary

Novel reactions between different polymorphs of SiO_2 with CO_2 and H_2 were observed under different pressures and temperatures. Therefore, the Si-O bond and C=O bond are altered by the pressure and temperature. The formation of 5 coordinated Si atoms plays a critical role in promoting the reaction between CO_2 and SiO_2. This was also seen in the pressure-induced phase transitions of SiO_2 [167,168]. Porous quartz is spacious and easy to be compressed and distorted. The distorted four-coordinated Si centres attract the lone pair electron of the O in CO_2 forming five-coordinated Si atoms that initiate the whole reaction. For the denser stishovite consisting of SiO_6 units, the natural defects in the form of four-coordinated SiO_4 promote the reaction.

The porous structure is also essential for the unusual reaction between quartz and gases as it can be filled with small molecules. The large surface area of the channels also provides more SiO_2 and increases the chance to react with either H_2 or CO_2. In addition, there is a higher possibility of compression of the porous structure bringing the gas close to the surface, which is critical for the reactions. Hence, it might be possible for porous SiO_2 to react with other small gas or liquid molecules under different pressures and temperatures.

CHAPTER 4

THEORETICAL STUDY ON THE MELTING TEMPERATURE OF ICE IH AND STRUCTURAL EVOLUTION UNDER PRESSURE

Water, whether in the gas, liquid, or solid phase, is the most abundant compound on the surface of the Earth. Water is essential to all living things. It possesses anomalous properties that are different from those of most other liquids, *e.g.*, a maximum density at 4 °C and an expanded volume upon freezing. Ice under pressure also has many different crystalline forms. To date, at least sixteen different known crystalline ice structures have been identified [52,192,193]. Over the years, a significant number of experimental and theoretical studies have been devoted to the understanding of the structural complexity and anomalous properties of water and ice at the atomistic level [28,194-198]. However, several problems are still in hot debate [28,199,200]. This chapter addresses three of these problems: (i) the mechanism for pressure-induced amorphization of ice Ih, (ii) the nature of the amorphous ice, and (iii) the search for an *ab initio*-based intermolecular model for the simulation of water properties.

4.1 Pressure-induced crystal→crystal transition prior to amorphization

Under different temperature and pressure conditions, water can exist in as many as 16 crystalline forms [192,193] and several amorphous states [3,201-203]. The discovery of pressure-induced transformation from crystalline ice Ih to high-density amorphous (HDA) phase at 77 K and 1 GPa in 1984 [3] was a major milestone in the study of the physics and chemistry of ice. Following this discovery, several different amorphous states and transformations between them have been observed at different temperature and pressure regimes. For example, HDA ice was obtained through the compression of ice Ih at low temperature (80–100 K). When quench-recovered and heated under ambient pressure, the HDA phase transformed to a low density

amorphous (LDA) [3,201] form. However, when the HDA form was heated under pressure, it transformed to an even higher-density amorphous (VHDA) phase [202]. The amorphization of ice Ih and HDA→LDA transitions have become prototypical examples in the investigation of solid-state amorphization and amorphous→amorphous transitions of many materials, *e.g.*, α-quartz [204], α-GeO_2 [205], and $AlPO_4$ [206]. Pressure-induced amorphization (PIA) is the cornerstone of the hypothetical and controversial two-liquid model of water and currently is under intense scrutiny, despite that extensive efforts devoted to characterizing the amorphization process using volumetric, Raman, neutron, and ultrasonic measurements, as well as theoretical simulations [3,207-214].

PIA originally was believed to be related to thermodynamic melting [3], but it was later suggested that, at low temperatures (< 160 K), PIA resulted from a mechanical instability in the water lattice where one of the Born's stability conditions [215] violated [216]. This violation led to the collapse of the crystalline structure and resulted in the metastable HDA form [216]. In other words, the transformation process is not truly a thermodynamics process, since an amorphous phase is only metastable. Single-crystal neutron inelastic scattering and ultrasonic experiments have confirmed a softening of the shear elastic modulus under compression [209-212,217]. Refined X-ray diffraction experiments on α-quartz [204], α-GeO_2, and $AlPO_4$ [218] showed that amorphization was a multi-step process when the samples were compressed in qusai-hydrostatic media. For example, *in-situ* X-ray diffraction measurements on quartz have shown that there is a precursor crystal→crystal transition at ~21 GPa prior to PIA [219]. Furthermore, depending on the hydrostatic condition, several crystalline phases have been observed to bypass the crystal→amorphous transitions [220]. These results clearly show that deviatoric stress plays an important role in the PIA of α-quartz and other materials. However, for ice at low temperature, a

detailed investigation of the pressure-induced structural evolution near the onset of amorphization by diffraction methods or computational simulations is still lacking, despite that the information on the modifications of the hexagonal lattice under pressure which is the key to better understanding the nature of the amorphization. In this project, we investigate the structural evolution of the hexagonal lattice of ice Ih under pressure by performing both empirical and AIMD simulations.

4.1.1 Empirical MD simulations

Computational methodology

Classical molecular dynamic simulations were performed. Three proton-disordered ice Ih models comprising 96, 432, and 768 H_2O molecules were used as the initial structures. The orthorhombic unit cell for 96 and 432 H_2O molecules were taken from Ref. [221], while the 768 model is a 2×2×2 supercell expansion of the 96 molecule model. These models are labeled as Ice-Ih-96, Ice-Ih-432, and Ice-Ih-768, respectively (Figure 4.1). In the MD calculations, the model systems were first equilibrated to 80 K and 0 GPa in an *NVT* ensemble for 40 ps. In contrast to previous MD simulations [199,216,222,223], a series of *NPT* simulations were performed at 80 K with the pressure being increased slowly from 0.0 GPa to 0.7 GPa at a step of 0.1 GPa, and then from 0.8 GPa to 2.0 GPa at a step of 0.2 GPa. In order to fully relax the structure, each simulation was run for at least 100 ps. The TIP4P/ice model [53] was used since it was developed specifically to reproduce the melting temperature of hexagonal ice at 272.2 K. An integration time step of 1 fs was used. The long-range electrostatic interactions were computed by using the Ewald sum method [224], with real-space cutoff distances of 6.0 Å, 8.0 Å, and 8.0 Å for Ice-Ih-96, Ice-Ih-432, and Ice-Ih-768, respectively. All calculations were performed with the DL_POLY code [55]. To

validate the procedure, we first performed *NVT* and *NPT* simulations at 250 K and 0 GPa for Ice-Ih-96 with TIP4P/ice model. The calculated density of 0.905 g/cm^3 agreed well with a previous study [53].

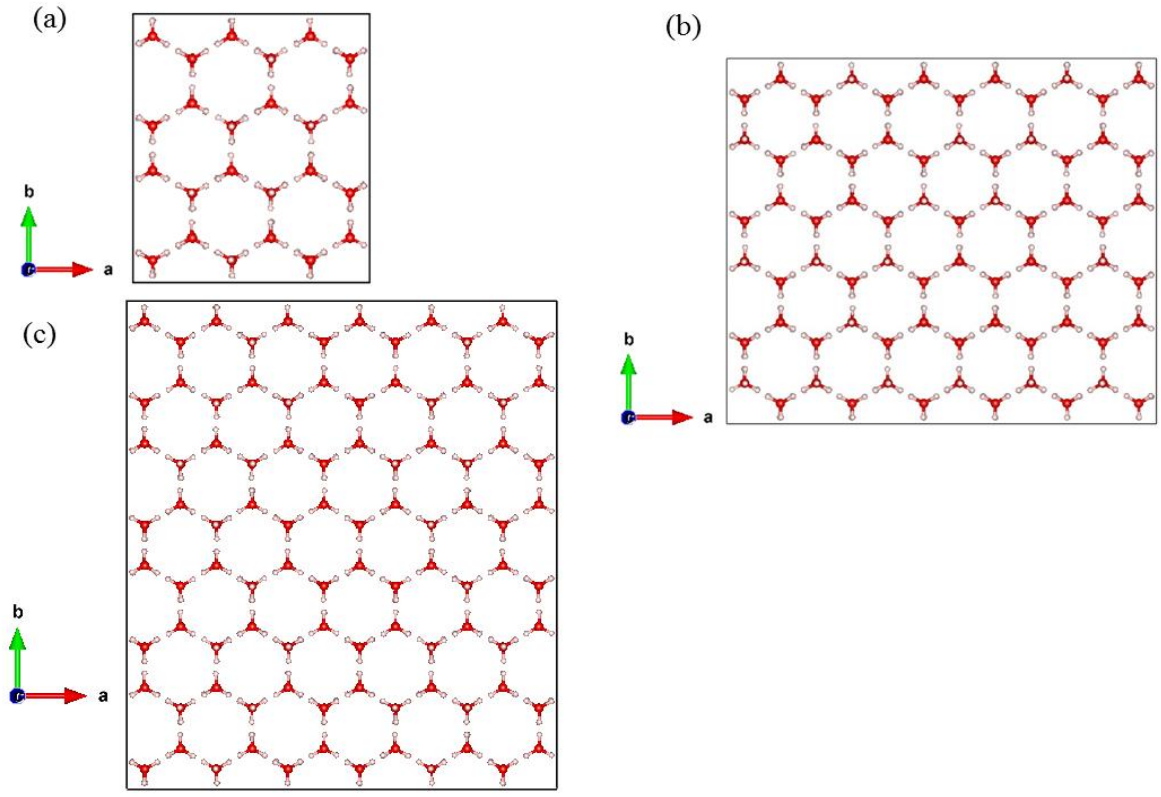

Figure 4.1 Structures of the (a) Ice-Ih-96, (b) Ice-Ih-432, and (c) Ice-Ih-768 models. (O in red and H in white).

Results and discussions

The densities of the three ice Ih models at 80 K are plotted in Figure 4.2. A phase transition at 80 K is observed from the evolution of the density. Although the calculated transition pressures are somewhat higher than the experimental results, the MD calculations produce a similar density-evolution trend. The calculated densities increase monotonically with pressure below 1.1 GPa.

This is in excellent agreement with experimental piston-cylinder measurements [3,210]. At ~1.2–1.6 GPa in the MD calculations and 1.05-1.2 GPa in the experiments, the density of ice Ih increase abruptly corresponding to a densification of ~4%. Within this pressure region, the ice Ih structure remains crystalline (see below), but transforms into another structure. Above 1.6 GPa in the MD calculations and 1.2 GPa in the experiments, the density increases further and the structure amorphized. In summary, the MD results show that at 80 K, ice Ih has undergone a crystal→crystal transition prior to amorphization. Therefore, PIA does not occur in a single step, but rather through a multi-stage procedure involving an intermediate crystalline state.

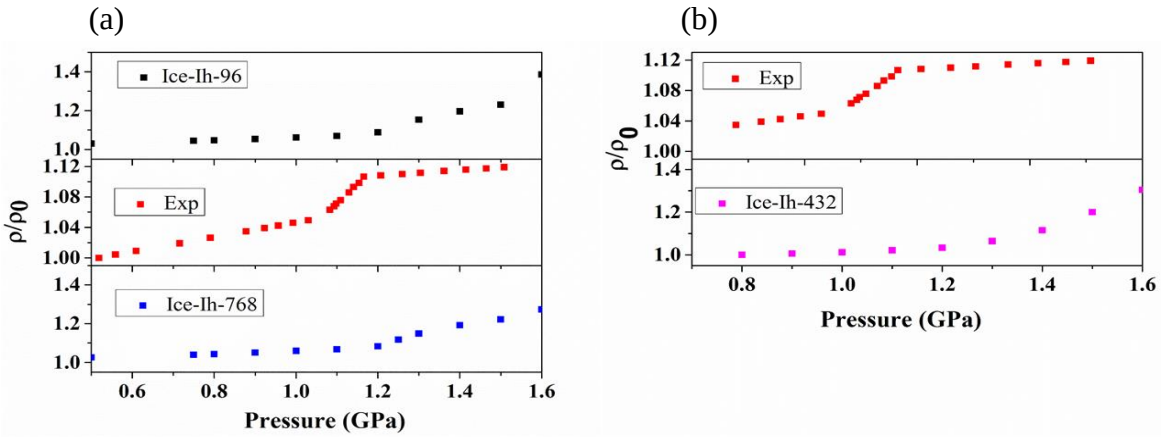

Figure 4.2 Comparison of the density evolution (ρ/ρ0) with pressure normalized to 0.5 GPa obtained from experiments (Exp) with MD calculations for the (a) Ice-Ih-96 and Ice-Ih-768 and (b) Ice-Ih-432.

The structural transformations are better illustrated by plotting the total energy of the system for each pressure increment, *i.e.*,

$$\Delta E = E_2 - E_1, \qquad 4.1$$

where E_1 and E_2 are the corresponding energies of two consecutive pressure points. The plot of ΔE against the corresponding pressure difference is shown in Figure 4.3. Up to 2 GPa, the plot can be divided into three regions. Below 1.2 GPa, the energy difference is small and increases only

slightly and gradually. A sudden increase in ΔE is observed between 1.2–1.5 GPa. Above 1.6 GPa, the values of Δ*E* are nearly identical to the values found below 1.2 GPa. This observation is in agreement with the calculated X-ray diffraction patterns (Figure 4.4 for Ice-Ih-96, Figure 4.5 for Ice-Ih-432, and Figure 4.6 for Ice-Ih-768). The results unambiguously show the existence of an intermediate crystalline phase between 1.3–1.5 GPa preceding complete amorphization at 1.6 GPa. The computed X-ray diffraction patterns for the three models are almost identical. From 0.8 to 1.2 GPa, there is little change as compared to ice Ih pattern. From 1.3 GPa and below 1.6 GPa (before amorphization), splittings of the Bragg reflection of ice Ih are observed. Eventually, the amorphous form is observed at a pressure higher than 1.6 GPa.

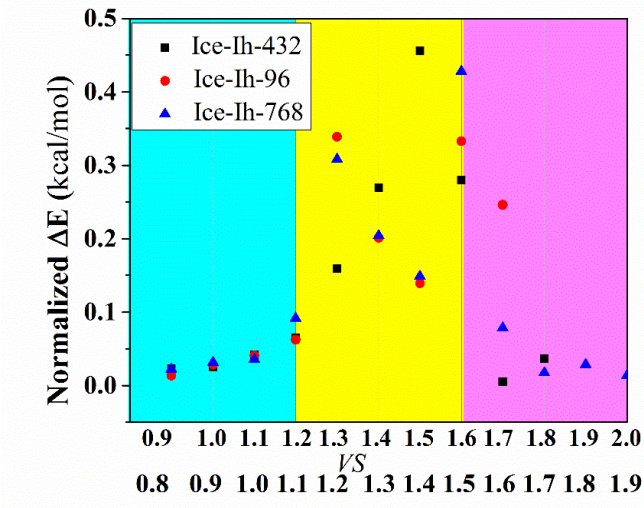

Figure 4.3 Normalized energy difference of the Ice-Ih-96, Ice-Ih-432, and Ice-Ih-768 models as a function of pressure increment. The *x*-axis is the pressure increment in GPa. The energy difference is taken by subtracting the total energy obtained between sequential pressures and normalized to the total number of H_2O in the model system.

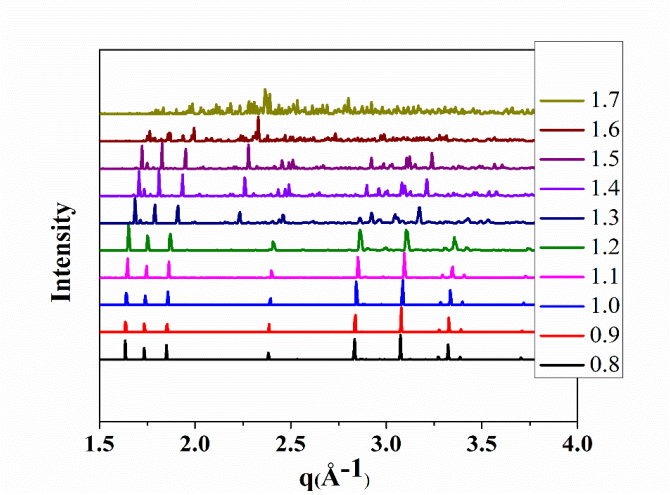

Figure 4.4 The calculated X-ray diffraction pattern for the Ice-Ih-96 under different pressures. Pressure unit is GPa.

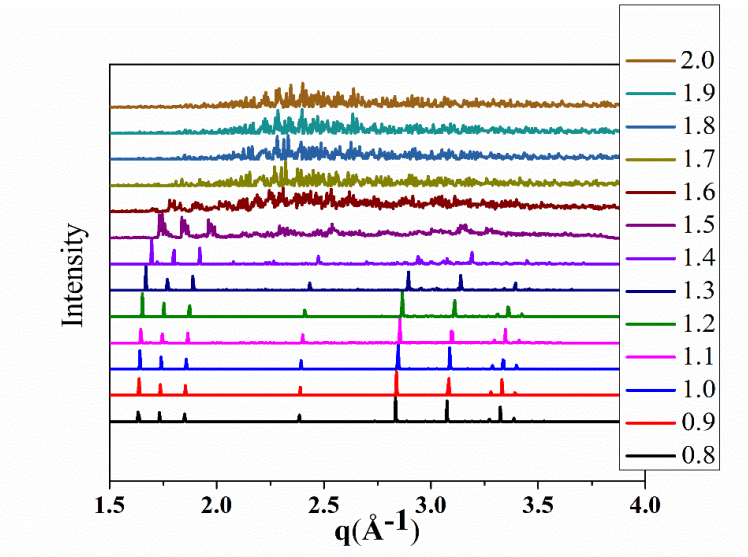

Figure 4.5 The calculated X-ray diffraction pattern for the Ice-Ih-432 under different pressures. Pressure unit is GPa.

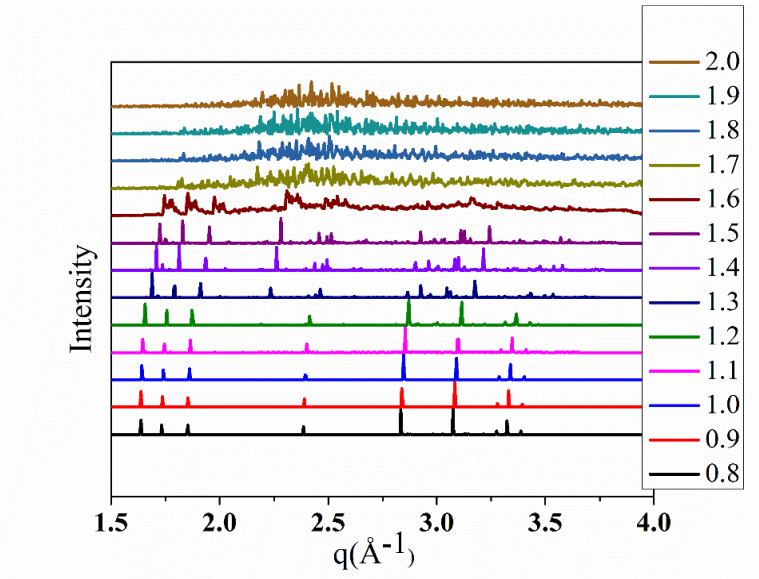

Figure 4.6 The calculated X-ray diffraction pattern for the Ice-Ih-768. Pressure unit is GPa.

The changes in the diffraction patterns between 1.2–1.5 GPa are due to a distortion of the ice Ih lattice. Figure 4.7 clearly shows that the hexagonal O-framework is sheared by compression. This sheared form of ice is metastable as the framework is maintained after geometry optimization at 1.3 GPa (Figure 4.8b). The optimized sheared intermediate phase has a similar X-ray diffraction pattern with that from MD simulations (Figure 4.9). To examine the structural change, we computed the O-O-O angle (θ, see Figure 4.10a) distribution function, P(θ), (Figure 4.10b) from the trajectories. Three types of distributions are observed. Before the transition, the O-O-O angle is distributed between 90° and 120° with the maximum at 109°, the expected tetrahedral angle. Above 1.3 GPa, the P(θ) suddenly broadened and spanned between 80–140 ° with the mean angle shifted to ~ 100°. Finally, in the amorphous state above 1.6 GPa, the P(θ) is very broad with a plateau region spread between 70° and 120° (Figure 4.10). The analysis shows that the main structural change (Figure 4.8) in the transition to the sheared form is the distortion of the O-O-O

angle from the ideal tetrahedral. The prediction of a crystal→crystal transition prior to amorphization motivated a careful experimental investigation. The experiment diffraction patterns as a function of pressure as shown in Figure 4.11 clearly show splitting of the Bragg reflections of ice Ih above 0.8 GPa and before the onset of amorphization at 1.5 GPa. We can conclude that PIA is not a simple first-order transition but one that involves a crystal→crystal transition prior to amorphization. The observations support an earlier suggestion that HDA is actually a frustrated disordered structure in which, at low temperature, the system does not possess sufficient energy to overcome the activation barrier for the re-orientation of the water hydrogen bonds into another crystalline phase (perhaps ice VIII [225]), upon further compression.

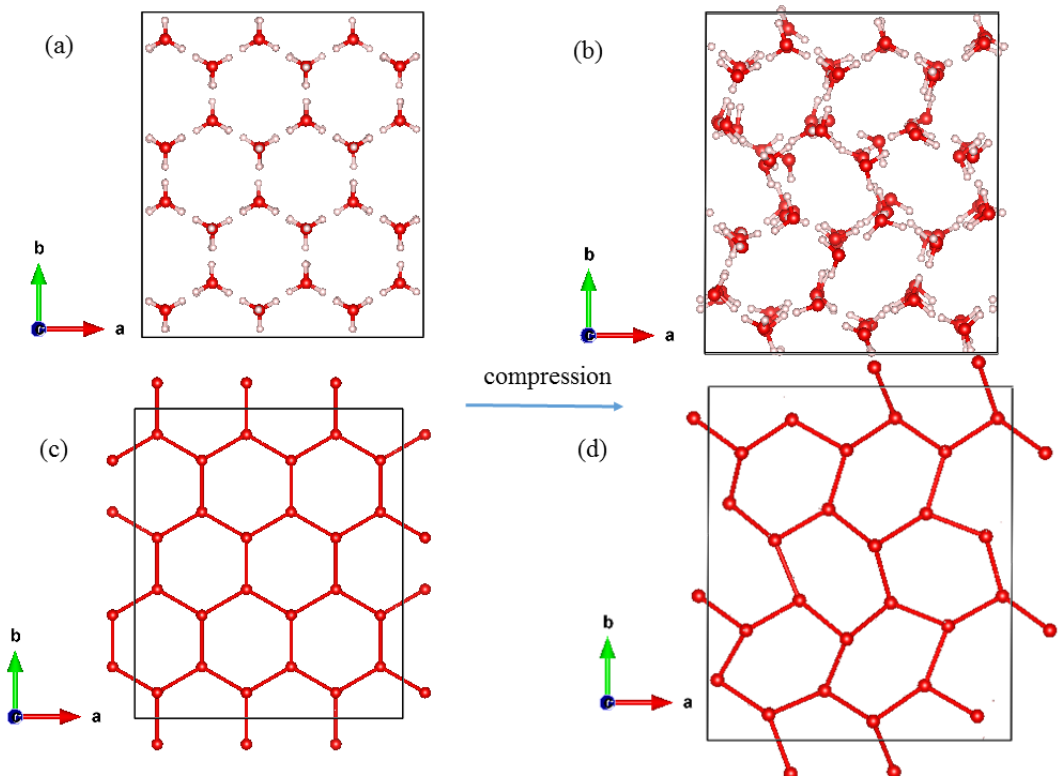

Figure 4.7 Projected structures of the (a) ice Ih and (b) intermediate sheared phase from *NPT* simulation at 1.3 GPa. One layer of oxygen framework extracted from (c) ice Ih and (d) the intermediate phase. (O in red and H in white).

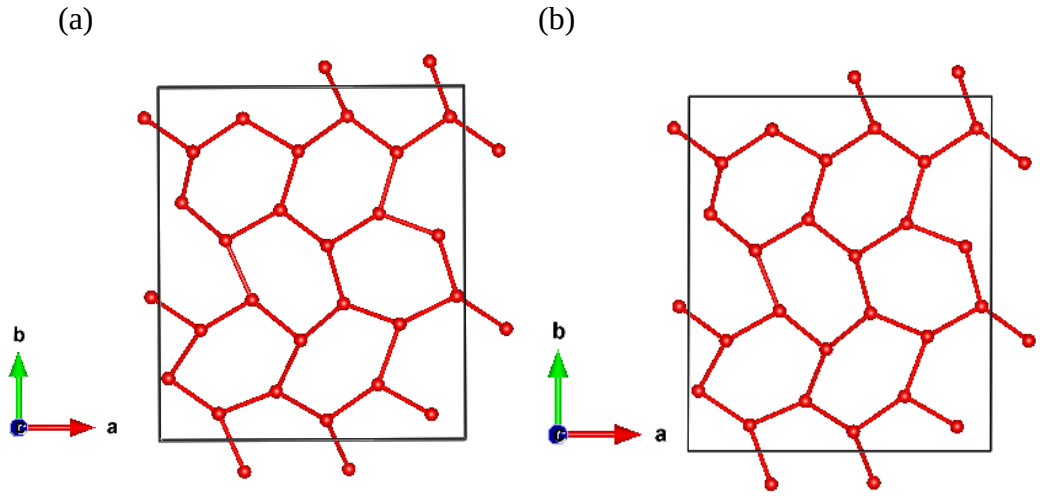

Figure 4.8 One layer of oxygen framework extracted from the sheared structure (a) before and (b) after optimization at 1.3 GPa. (O in red).

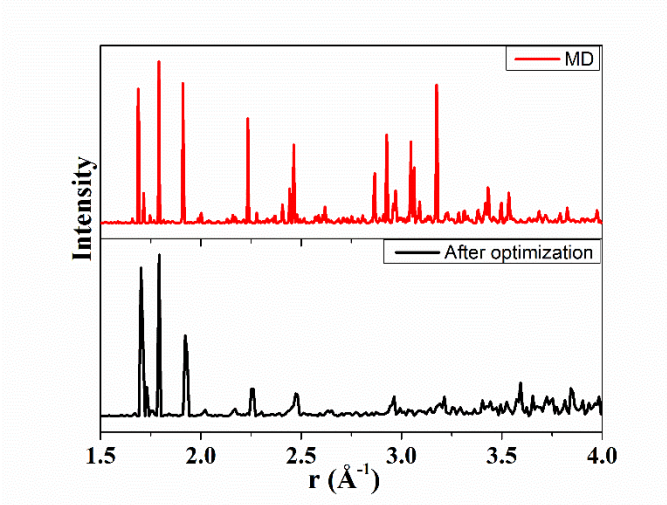

Figure 4.9 The calculated X-ray diffraction pattern for the sheared intermediate phase (top) from MD simulation and (bottom) after static geometry optimization.

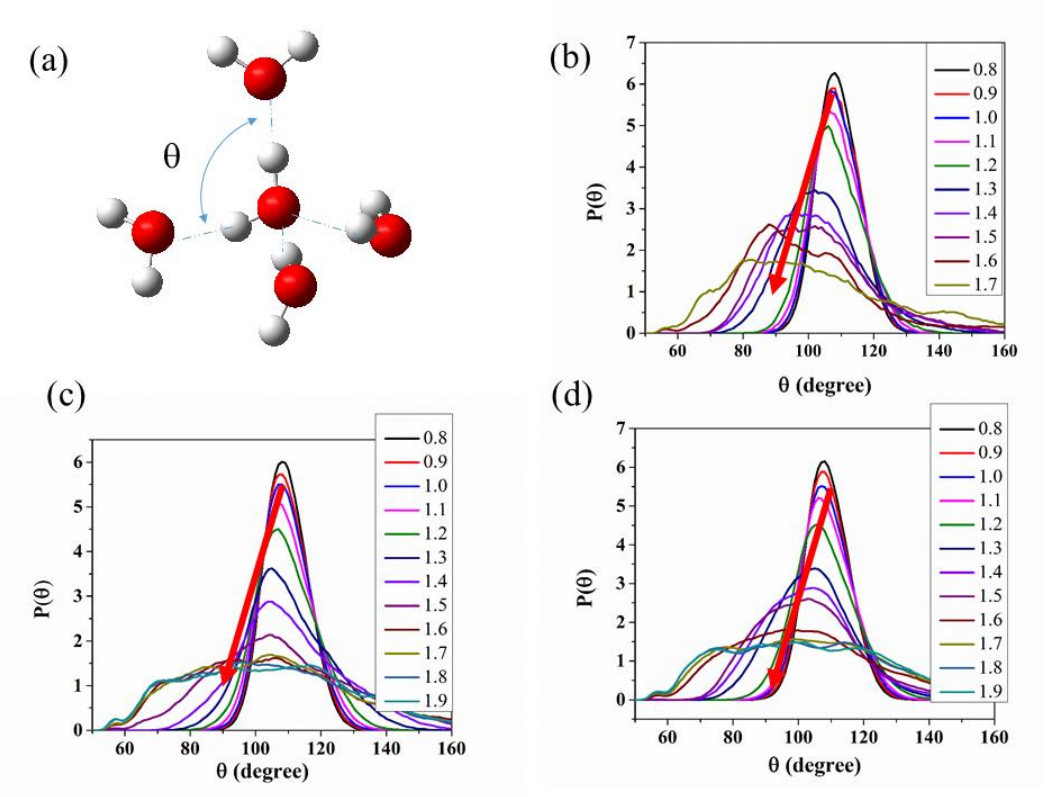

Figure 4.10 (a) Depiction of the O-O-O angle, θ, in ice. The θ-angle distribution function P(θ) at different pressures for the (b) Ice-Ih-96, (c) Ice-Ih-432, and (d) Ice-Ih-768. Pressure unit is GPa. The red arrows in b-c indicate the mean value-shifts of the peaks.

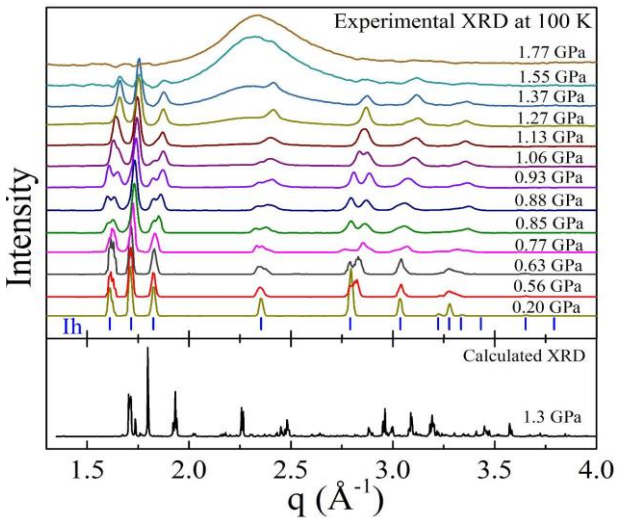

Figure 4.11 The calculated X-ray diffraction pattern for the sheared structure (bottom) at 1.3 GPa compared to experimental data at different pressures. The experimental X-ray diffraction pattern at 1.06 GPa correspond to that for the sheared structure.

4.1.2 AIMD simulations

The accuracy of computed water properties depends on the methodology used as well as on the quality of the intermolecular potential. The MD simulations described above employed the empirical TIP4P/ice water potential. MD calculations using empirical force fields have succeeded reasonably well in reproducing many experimental properties of ice and liquid water under a variety of thermodynamic conditions. Examples of properties include the site-site radial distribution functions, X-ray and neutral structure factors, the heat of vaporization, and the maximum density of liquid water [226,227]. The empirical force field method requires substantially less computational efforts than First-Principle-based methods and can be applied to large systems. DFT-based AIMD methods have also been used to study water and ice in a wide range of environments [28,228]. To validate the crystal→crystal transition found, we repeated the calculations using AIMD.

The currently available generalized gradient approximation, GGA, exchange-correlation functionals suffer from several known deficiencies. One of them is the neglect of *vdW* interactions, which has been shown to be the main reason for the failure of GGA functional in the prediction of the density of liquid water [194,197,229] (15–20% lower than experiment results). Thus, the predicted water configuration is often over-structured with a very low diffusion constant at room temperature. This observation is due to substantial underestimation of the fraction of broken H-bond. Recently, several *vdW* corrected exchange-correlation functionals have been developed and implemented in First-Principle-based electronic codes, *e.g.*, VASP. While this development has led to better-predicted properties of gas phase clusters, a similar understanding with regarding the properties of ice and liquid water has not been completed.

Recently, Angelos Michaelides [230] reported a study of *vdW* effects on the ice at ambient and high pressures. In that work, only the contribution of *vdW* interaction to the lattice energy and density was evaluated. More recently, DiStasio *et.al*., [218] studied the effects of exact exchange and dispersion interactions on the ab initio structure of liquid water. The inclusion of exact exchange is computationally demanding. This benchmark study was performed on a 128 water model and requited 1024 cores on a CRAY XE5 and took 5 days for 1 ps of simulation. The substantial computational requirements are currently out of reach for our applications. Here, we compared the performance of several different *vdW* corrected exchange-correlation functionals on the prediction of the structure of Ice Ih using both static geometry and AIMD calculations. The goal of these calculations was to select an optimal functional that may be useful for the study of the pressure effect on ice Ih.

Computational methodology

Selection of an optimal functional

A previously used 12 molecules model, labeled as Ice-Ih-12 (Figure 4.12a), was employed in this study. We used the DFT-D2 [23] and DFT-D3 methods of Grimme [25], the DFT-D3 method with Becke-Jonson damping [25,27], and the *non-local vdW*-DF proposed by Dion *et al.* [24] including the optPBE-*vdW* and rPW86-*vdW* functionals [195,231]. Only static geometry optimizations were performed. In addition, the DFT-D2 and *vdW*-DF functionals, specifically, the optPBE-*vdW* functional, were used to simulate the structure of liquid water by AIMD. In this case, a liquid water model containing 96 H_2O molecules (Figure 4.12b) with a density of 1.0 g/cm^3 was used. *NVT* MD simulations at 300 K and 330 K were performed for at least 10 ps.

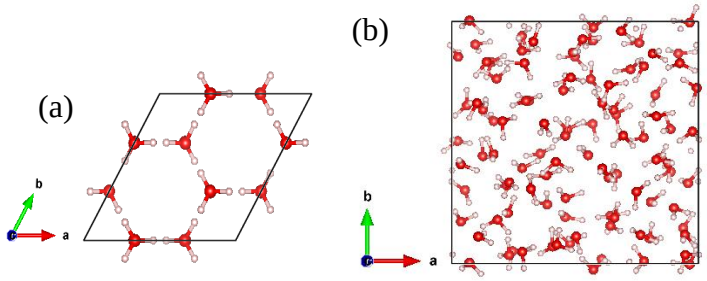

Figure 4.12 Structures of (a) Ice-Ih-12 and (b) a water box with 96 H_2O molecules

Table 4.1 compares the calculated and experimental [232] lattice constants and volume for the Ice-Ih-12 model. The lattice constants and volume obtained with the *non-local* optPBE-*vdW* functional show better agreements with the experimental data than the other functionals. Then we examined the performance of the empirically corrected (D2) and the optPBE-*vdW* functionals on the simulation of the liquid structure. The DFT-D2 calculated oxygen-oxygen ($g_{OO}(r)$), oxygen-hydrogen ($g_{OH}(r)$), and hydrogen-hydrogen ($g_{HH}(r)$) radial distribution functions [RDF, ($g(r)$)] at both temperatures are shown in Figure 4.13. Compared to the results obtained from the PBE functional alone, significant improvements in agreement with the experiment of the position and heights of the peaks of the ($g_{OO}(r)$), ($g_{OH}(r)$), and ($g_{HH}(r)$) are observed. Furthermore, the optPBE-*vdW* functional provided even better radial distribution functions of liquid water when compared to experiment. Compared to DFT-D2 and PBE, the first peak of ($g_{OO}(r)$) of 2.78 Å obtained from optPBE-*vdW* shifted by 0.02 Å to a longer distance (Figure 4.13a). Moreover, the height of the first peak is reduced in amplitude significantly. Hence, the optPBE-*vdW* functional produces a softer structure, which is in better agreement with the experiment. Thes results are consistent with previous investigations [218], where a similar systematic improvement over PBE functional in the ($g_{OH}(r)$) and ($g_{HH}(r)$) (Figure 4.13b-c) was observed from the inclusion of *non-local vdW* effects. In summary, the calculated structure properties from the optPBE-*vdW* functional for both liquid

and solid water are in better agreement with experimental data as compared to the results obtained with PBE and DFT-D2 functionals. In addition, the diffusion coefficient ($D = \frac{1}{6}\frac{d}{dt}\left\langle |r(t) - r(t\,0)|^2 \right\rangle$) calculated from optPBE-*vdW* is 0.15 Å^2/ps at 330 K and 0.14 Å^2/ps at 300 K, which are in reasonable agreement with the experiment values of 0.23 -0.24 Å^2/ps [233-235]. It is gratifying that we have obtained similar results on the static and dynamics properties as compared to the more elaborate exact exchange+*non-local vdW* calculations [218]. Therefore, this functional was used to investigate the pressure induced phase transitions of ice Ih. A time step of 1.0 fs was used for MD. Electron orbitals were expanded by PW basis sets with an energy cut-off of 1000 eV. Γ-point Brillouin-zone sampling was used.

Table 4.1 Comparison of the calculated and experimental lattice constants and volume

Functional	*a* (Å)	*b* (Å)	*c*(Å)	Volume (Å^3/H_2O)
PBE	7.64	7.64	7.19	30.32
DFT-D2	7.52	7.52	7.08	28.90
DFT-D3	7.55	7.55	7.09	29.18
DFT-BJ	7.55	7.55	7.09	29.15
optPBE-*vdW*	7.72	7.72	7.26	31.27
rPW86-*vdW*	7.90	7.90	7.43	33.45
Exp[a]	7.78	7.78	7.73	32.05

[a] Experimental results were taken from Ref [232]

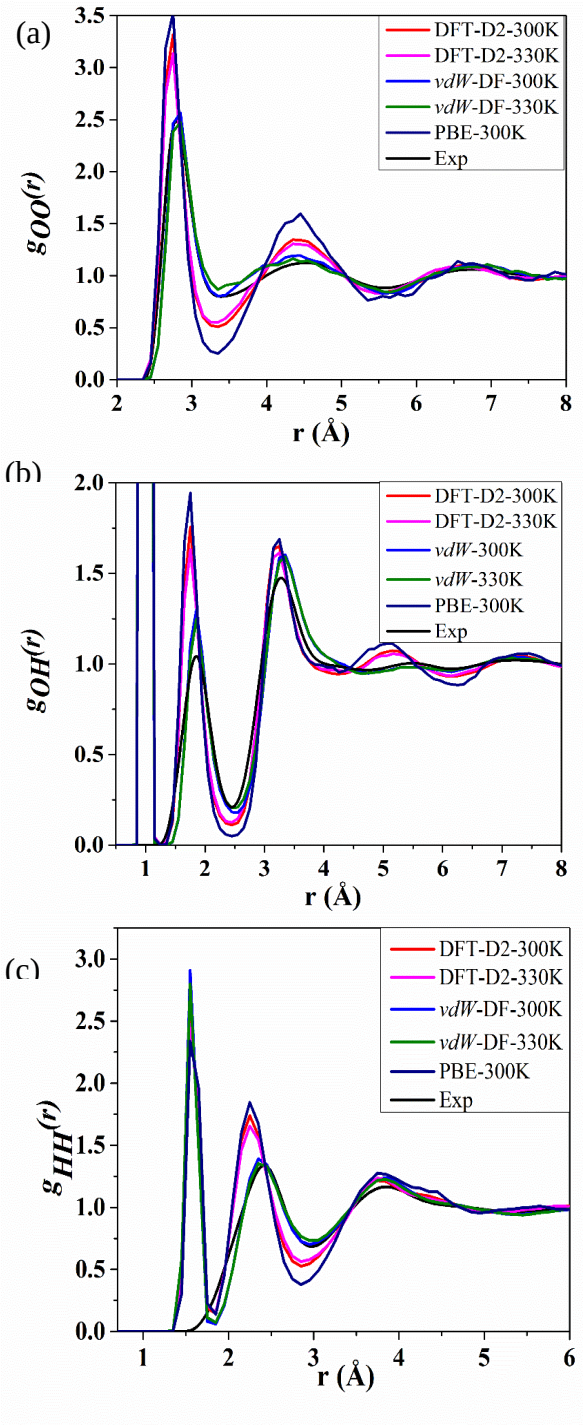

Figure 4.13 The (a) oxygen-oxygen ($g_{OO}(r)$), (b) oxygen-hydrogen ($g_{OH}(r)$), and (c) hydrogen - hydrogen ($g_{HH}(r)$) RDF of liquid water obtained from *NVT* MD simulations at 300 K and 330 K and 0.0 GPa using different exchange-correlation functionals compared with the experimental data [236] (the *vdW*-DF used is the optPBE-*vdW* functional).

AIMD simulations for the pressure induced crystal→crystal transition of Ice Ih

Since AIMD simulations are computationally more demanding than the empirical potential calculations, MD simulations were performed only on the small Ice-Ih-96 model (Figure 4.14a). Similar to the empirical potential calculations, we first scaled the temperature of the system to 80 K and 0.0 GPa. Then a series of AIMD calculations under *NPT* ensemble at pressures from 0.0 GPa to 0.9 GPa at the increment of 0.2 GPa were performed. From 1.0 GPa to 2.0 GPa, the pressure was increased at a step of 0.1 GPa and then simulations were performed at 2.2 GPa and 2.4 GPa. VASP program was employed.

Results and discussions

The evolution of the computed density with pressure is shown in Figure 4.14b. Below 1.0 GPa, the density increases monotonically. Similar to classical MD simulations, a sudden change in the density is found at 1.9 GPa. Snapshots of the structures taken from the AIMD trajectory at different pressures are shown in Figure 4.15 and Figure 4.16. Again, a clearly sheared oxygen lattice (Figure 4.16b) is observed prior to amorphization. The intermediate crystalline phase is confirmed by the calculated X-ray diffraction patterns (Figure 4.17a), which are very similar to the pattern obtained using MD calculations with TIP4P/ice water potential (Figure 4.4 for Ice-Ih-96, Figure 4.5 for Ice-Ih-432, and Figure 4.6 for Ice-Ih-768). The computed X-ray diffraction pattern for the sheared intermediate phase is similar to that of the experiment in terms of the splitting of the Bragg reflection (Figure 4.17b). Therefore, the structural transition found from MD calculations using the TIP4P/ice model is reproduced by AIMD. The two different computational approaches both predicted an intermediate crystalline before amorphization. The amorphization pressure of > 1.9 GPa by AIMD calculation is higher than the pressure predicted by both

experiments and MD calculations using empirical TIP4P/ice potential. A calculated higher transition pressure seems to be a common deficiency of the current *vdW*-functional as it also overestimated the crystal→crystal transition pressures in high pressure ices [28].

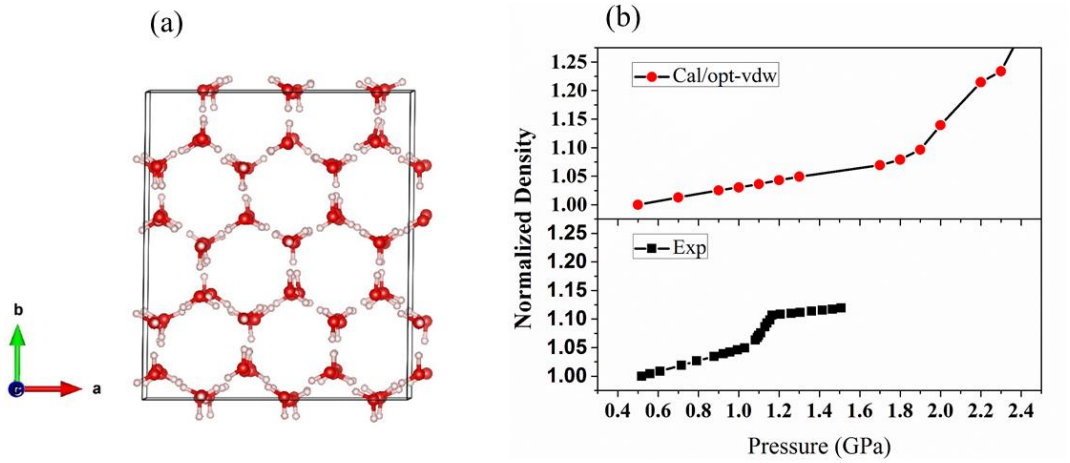

Figure 4.14 (a) Snapshot of the Ice-Ih-96 from the *NPT* AIMD simulation at 1.0 GPa and 80 K. and (b) Density changes (ρ/ρ0) with pressure normalized to 0.5 GPa for the Ice-Ih-96 from *NPT* AMID calculations at different pressures.

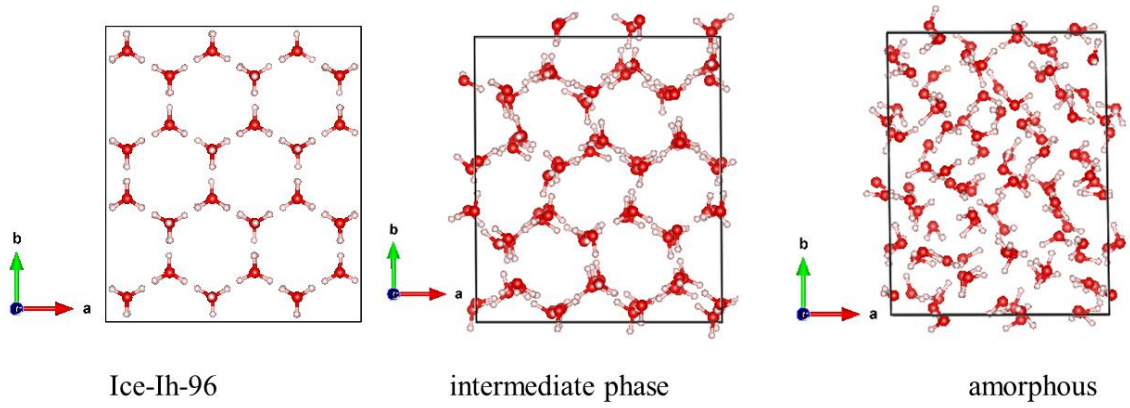

Figure 4.15 Structures of the Ice-Ih-96 at 0 GPa, the intermediate phase at 1.9 GPa, and amorphous ice at 2.2 GPa.

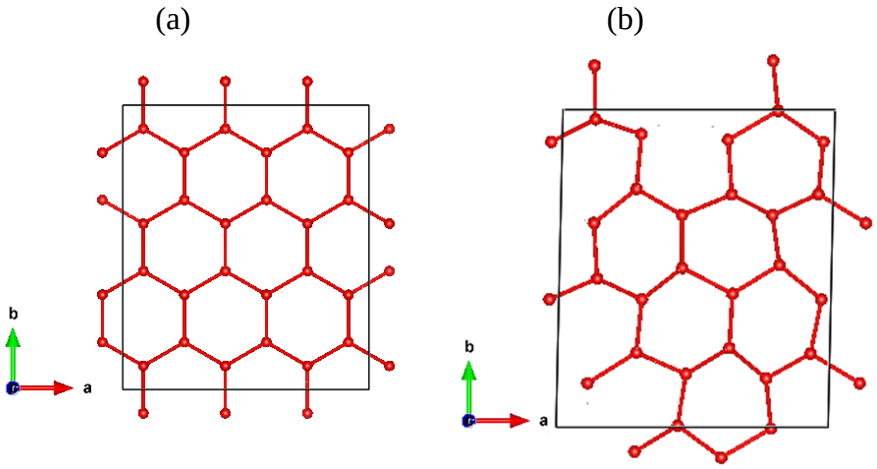

Figure 4.16 One layer of the oxygen framework extracted from the (a) Ice-Ih-96 and (b) intermediate phase. (O in red).

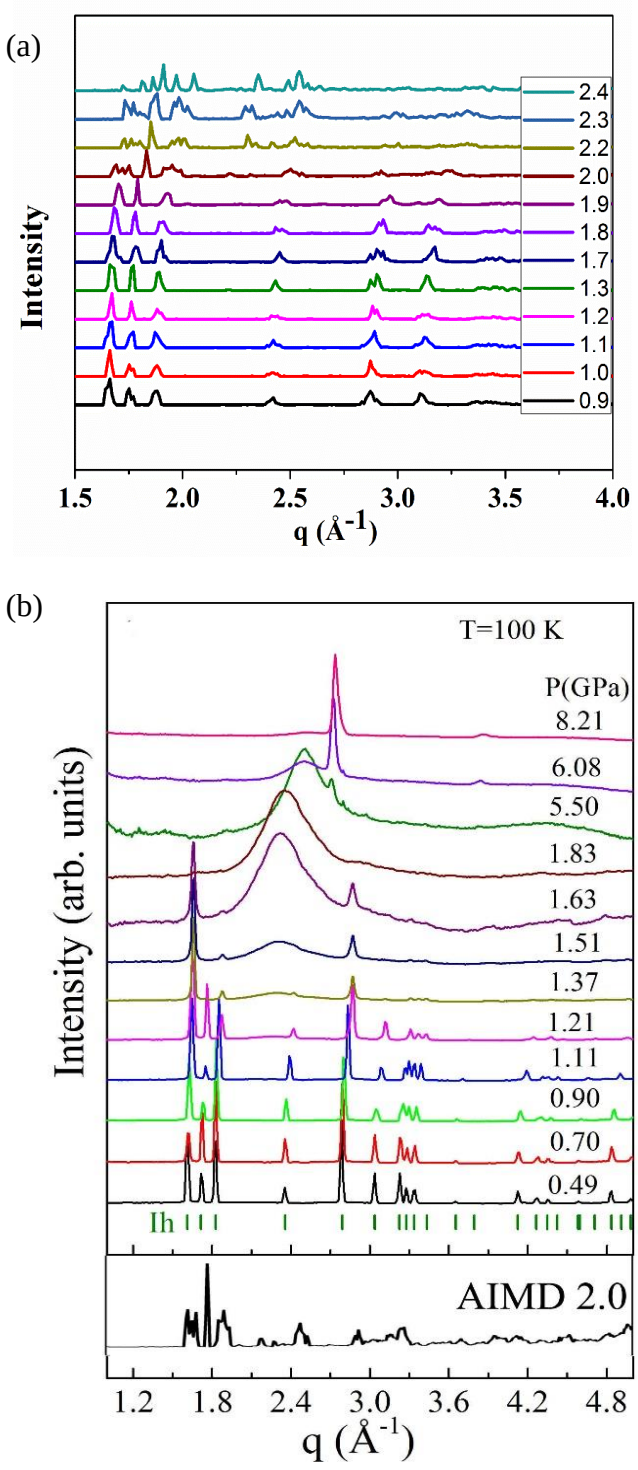

Figure 4.17 (a) The calculated X-ray diffraction pattern for the Ice-Ih-96 upon compression from AIMD calculations at different pressures. (b) X-ray diffraction patterns for the intermediate phase from AIMD calculations (bottom) at 2.0 GPa and experimental X-ray diffraction patterns at different pressures. The experimental result at 1.06 GPa correspond to that of the sheared structure.

4.1.3 General summary

The structural transformations of ice Ih compressed at 80 K have been characterized by MD calculations using empirical water potential and First-Principle density functional theory. A new intermediate crystalline phase occurring before amorphization was identified and also confirmed by experiment. The transformation from the ice Ih structure to the intermediate sheared lattice is no doubt due to a sheared instability, as was predicted in an earlier study [216]. The presented results suggest that, at 80 K, pressure-induced amorphization of ice Ih is not a one-step process as was previously believed but, rather occurs *via* an intermediate crystalline structure.

4.2 Melting temperature of ice Ih of the TTM2.1-F water model from ice/water two phases simulation

Over the years, significant experimental and theoretical efforts have been devoted to the understanding of the complexity of the properties of water and ice [28,196,197,200,237-239]. Classical MD using parametrized force field water intermolecular models have been successful in reproducing many observed properties such as the radial distribution functions [240,241], structure factors [242], and heat of vaporization [243]. However, to reproduce specific properties, many water models [52,244] such as TIP4P/2005, TIP4P/ice SPC/E, SPC/FQ, and Tip4p/FQ have been developed. These models are dependent on fitting parameters and therefore are not transferable. Another approach to developing unbiased water models is based on high-level electronic structure calculations on water clusters. Recently, a flexible, polarizable Thole-type water model was parameterized from highly accurate quantum calculations (TTM2.1-F) [58,59]. This model was obtained by fitting the water monomer potential energy and dipole surface computed by Partridge and Schwenke [60], using high level (Møller–Plesset perturbation theory-MP2-level of theory with

aug-cc-pVTZ basis sets, which expanded the atomic orbitals with diffused and polarized basis functions with three components) quantum chemistry calculations. This potential offers an alternative *ab initio* way to study water properties [245]. By considering intramolecular flexibility and polarizability, the TTM2.1-F model is able to produce an increase of the internal H–O–H bending angle with cluster size and the redshift of O-H stretching for water clusters (n = 2–6) as well as several structural and thermodynamics properties. In addition, TTM2.1-F is one of the polarizable water models able to reproduce the maximum density of water [200,245]. However, in most previous calculations, the nuclear quantum effects (NQEs) of the hydrogen atom are often neglected. Therefore, it is important to determine whether this Thole-type potential can also reproduce the melting temperature of the ice with or without NQEs. The NQEs of the TTM2.1-F model on the structure and thermodynamics of water [245] and the melting temperature of ice [246] have been investigated. It was shown that the TTM2.1-F model provides an accurate description of the properties of water. However, the predicted melting temperature of ice at 227.5 K (classical) and 242.5 K (quantum) are significantly lower than the experimental value of 273.16 K. Furthermore, the difference of the melting temperature between the classical and the quantum calculations of 16 K is lower than expectation [218,245,247,248]. The observations are surprising since if the potential energy and dipole surfaces computed by the quantum chemistry method are sufficiently accurate, one would expect the theoretical results should be in much closer agreement with experiment. For the benefit of future application of the potential for large-scale simulations, it is desirable to re-examine the Thole-type potential on the melting temperature of the ice with or without NQEs. For this purpose, we repeated the calculations on water and melting, employing larger models than have been used previously.

There are mainly two commonly used approaches for melting temperature determination using MD calculations: the free energy (FE) [249] and the two-phase methods (TPh) [198,250,251]. In the FE approach, the melting temperature (T_m) is defined by the condition of thermodynamic melting, that is, the Gibbs free energy difference between the liquid and solid phases is zero at melting, with $G_{liq}(P,T_m) = G_{solid}(P,T_m)$. Hence, to obtain a reliable melting point, accurate calculations are required, and the method is difficult to apply for complex systems. On the other hand, the TPh method is inspired by the natural process of melting. The melting temperature is defined as the temperature at which there is existing of a coexisting solid-liquid interface. Therefore, the TPh method can provide useful structural information on the melting process. In this work, the TPh method is used to investigate the melting temperature of ice with the TTM2.1-F Thole-type model. NQEs were included by path integral centroid molecular dynamics, PIMD.

Computational methodology

Path integral CMD in the normal mode representation employing the TTM2.1-F water models was implemented in an in-house code developed by our collaborator. In CMD, each quantum particle is replaced by a *p*-harmonic-beads ring-polymers ($p \geq 16$). The equation of motion is formulated with the centroid of the harmonic ring. In this work 16 beads were used to mimic the quantum nature of H and O. This choice has been shown to be sufficiently accurate to simulate the properties of water [20, 21]. The classical MD simulation corresponds to a single bead ($p = 1$) CMD. An integration time step of 0.1 fs was used in the simulation. A Nosé–Hoover chain thermostat was used to control the temperature. The Ewald sum was used to treat the long-range interaction potential. Only *NVT* ensemble is implemented in the current version of the code. The

original serial code was parallelized using the OpenMP libraries. Details can be found in the appendix of this thesis.

Validation of the method and computer codes

To validate our code, we first performed a classical *NVT* (p = 1) MD simulation on a liquid water model with 1000 molecules at 300 K. PIMD (p = 16) *NVT* simulations at 300 K were also performed to address the NQEs. The RDF for the liquid water computed from PIMD and classical MD calculations are compared to the experiment in Figure 4.18. The RDF is a measure of the probability that a particle will be located at a distance r from a reference particle in the system. The locations of the peaks indicate the center/reference atom has a stronger tendency to interact with other atoms at certain distances. The integrated area of the peak gives the number of neighbor atoms. The first peak of the oxygen-oxygen radial distribution function, $g_{OO}(r)$ (Figure 4.18a) is around 2.78 Å from both classical and PIMD calculations. However, the height of the peak from the PIMD calculation is much lower and is in better agreement with the experiment. For the oxygen-hydrogen radial distribution function, $g_{OH}(r)$ (Figure 4.18b), the first peak from the PIMD calculation is broader and also has a lower height (around 15.8) than the classical calculation. The trends agree well with previous work [245]. Improvement of PIMD over classical MD simulations is also observed for the hydrogen-hydrogen radial distribution function, $g_{HH}(r)$ (Figure 4.18c). In this case, the height of the first peak from the PIMD calculation is less than half of that from the classical MD simulation. Moreover, the second and third peak amplitudes and positions also agree well with experiments [236]. From the analysis of the radial distribution function, we can conclude that the structure obtained from the PIMD calculations is more representative of actual water than the structure obtained from the classical MD calculations. The broader distribution indicates that the water is less structured than that predicted from classical calculations.

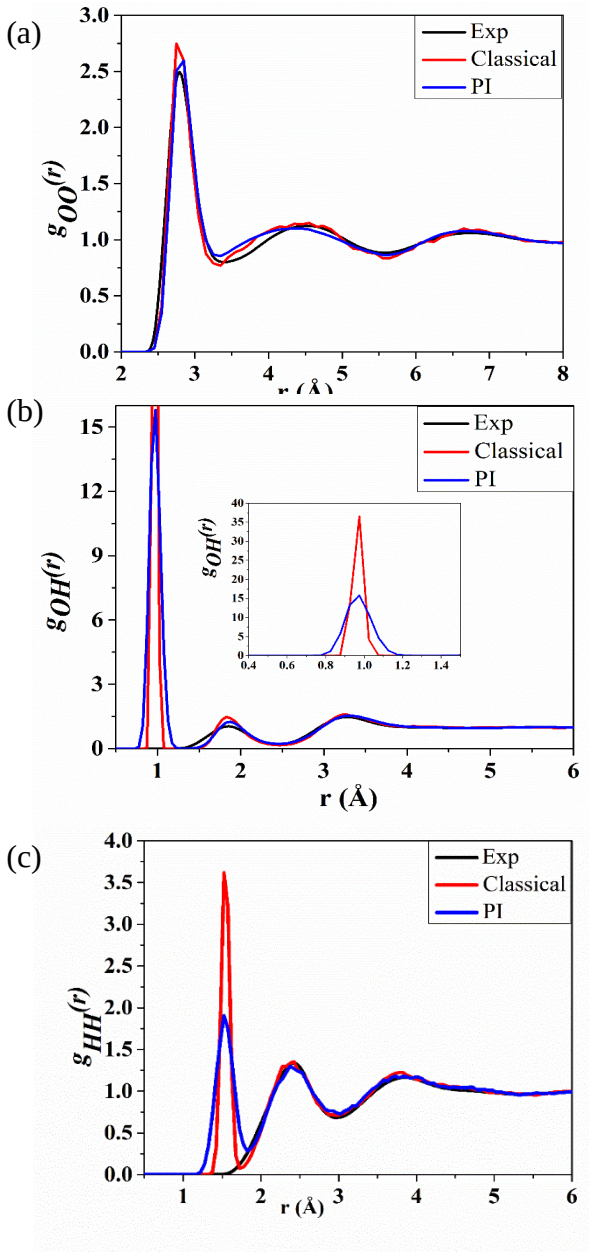

Figure 4.18 The (a) oxygen-oxygen ($g_{OO}(r)$), (b) oxygen-hydrogen ($g_{OH}(r)$), and (c) hydrogen-hydrogen ($g_{HH}(r)$) RDF of liquid water with density at 1.0 g/cm^3 at 300 K and ambient pressure from quantum (PI) and classical *NVT* simulation compared with the experimental RDF.

We further examined the NQEs on hydrogen bonds. We adopted the definition of a hydrogen bond as when the O-O distance is less than -0.0044*β^2+3.3 Å [245,252], where β is defined as the H_D-O_D-O_A angle (Figure 4.19). We computed the average number of intact hydrogen

bonds on one water molecule and decomposed them into H-bond-accepting-(A) and donating-(D) types. From classical simulations, most the H_2O (46%) molecules have an A2D2 type of hydrogen bond (Figure 4.19a). This is the traditional picture of a water molecule, which accepts and donates two hydrogen bonds. However, some water molecules have partially broken hydrogen bonds and therefore adopt A1D1, A1D2, A2D1 and A3D2 H-bonding. The general composition (*i.e*. the ratios between A1D1:A1D2:A2D1:A3D2) agrees well with previous *ab initio* calculations [218]. When NQEs are included, the A2D2 (46%) (Figure 4.19b) is still the most abundant form of hydrogen bond that water molecules adopted. However, the total number of double hydrogen-bond-donor decrease while that of the single-donor increase. These observations are in agreement with a previous report [245]. Furthermore, the A3D2 type of hydrogen bond disappears when NQEs are considered, while the A1D1 type of H-bond almost double. These results suggest the NQEs have softened the water structure. The diffusion coefficient of TTM2.1-F at 300 K and 0.0 GPa calculated from the velocity auto-correlation, $D = \frac{1}{3}\int dt \langle v(t) \cdot v(0) \rangle$ is 0.13 $Å^2$/ps (quantum) and 0.08 $Å^2$/ps (classical). These values are comparable to previous CMD calculations using TIP4P (0.543 $Å^2$/ps from the quantum calculation, 0.354 $Å^2$/ps from the classical calculation) [253] and SPC (0.42 $Å^2$/ps from the quantum calculation and 0.28 $Å^2$/ps from the classical calculation) [254] and the experimental values of 0.23 -0.24 $Å^2$/ps [233-235]. Overall, good agreements are found between the present calculations on a 1000 water model and 16 beads with the previous results [245] using a smaller model of 512 molecules and 32 beads. The favourable comparisons verified that our CMD code is correct.

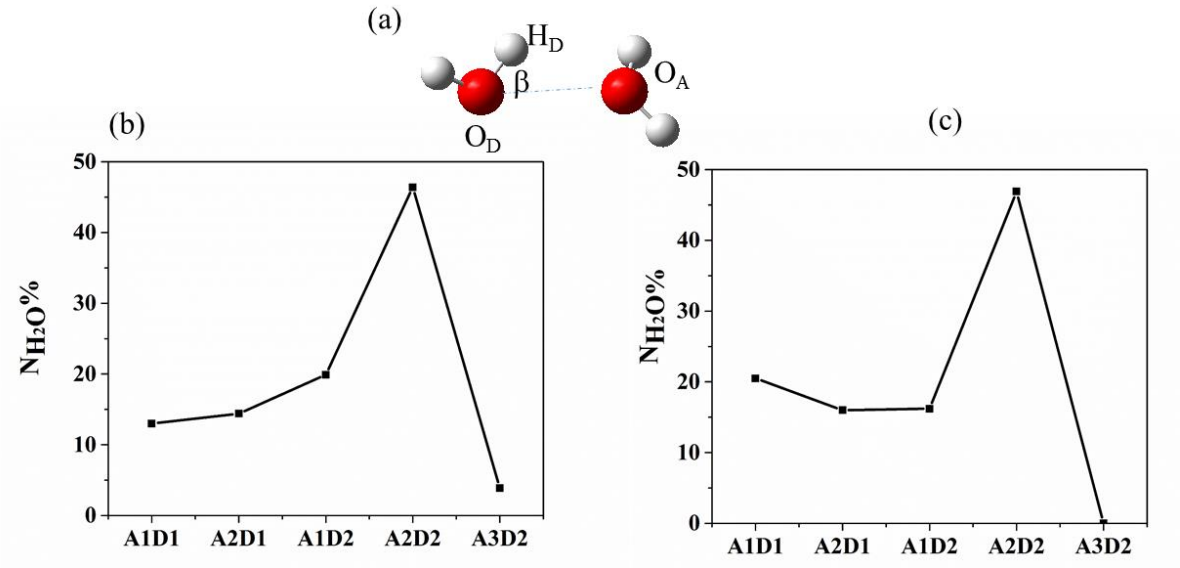

Figure 4.19 (a) Depiction of the H_D-O_D-O_A angel, β, in liquid water. Percentage-wise decomposition into H-bond-accepting-(A), and donating-(D) types of the intact hydrogen bonds per water molecules in liquid water from (b) classical and (c) quantum *NVT* MD simulations at 300 K.

Determination of the melting temperature of TTM2.1-F of ice Ih

We performed two-phase MD calculations with ice and liquid water in contact. To construct the ice/water interface, separately equilibrated samples of bulk ice Ih and water were needed. The initial ice Ih structure was taken from Ref. [221] with an orthorhombic cell, consisted of 96 H_2O molecules (Figure 4.20a). To obtain an approximate cubic ice/water box, a 2×2×1 supercell structure was constructed. The dimensions of the ice model were 27.04 Å × 31.22 Å × 14.72 Å with a density of 0.944 g/cm^3. A liquid water structure was obtained by melting the ice Ih model using TIP4P/ice water potential implemented in the DL_POLY program. Keeping the same *x* and *y* dimensions as ice Ih, the *z* box length was scaled to generate the correct liquid water density of 0.99g/cm^3. The oxygen-oxygen radial distribution function of the obtained liquid water (Figure 4.20b) showed good agreement with the experimental results [236,255]. The final dimensions of the liquid water box were 27.04 Å × 31.22 Å × 13.72 Å.

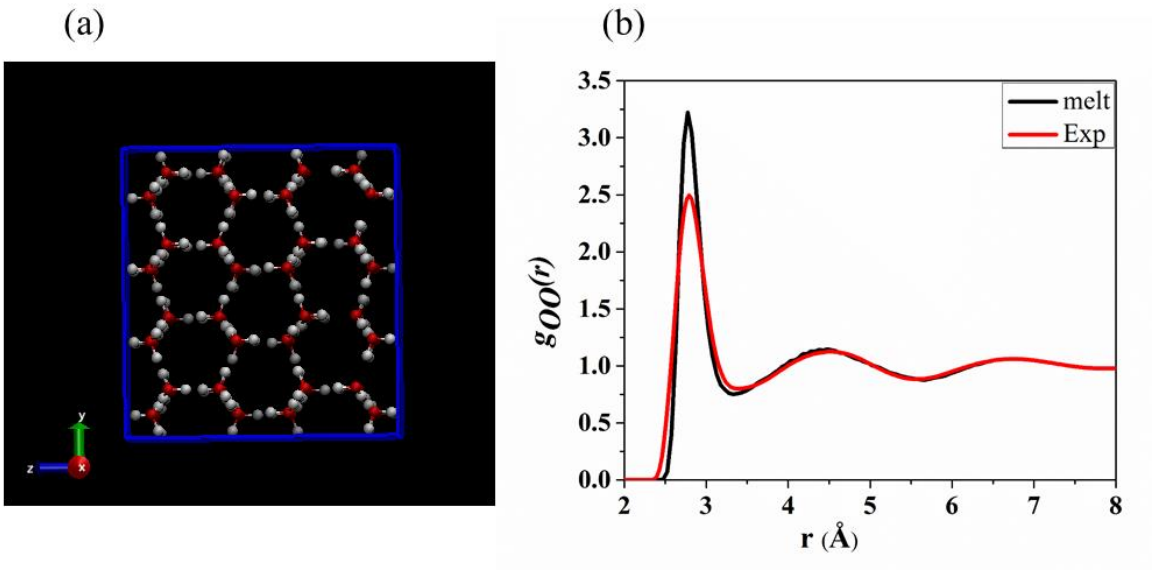

Figure 4.20 (a) Structure of ice Ih and (b) the oxygen-oxygen $g_{OO}(r)$ RDF of liquid water at 298 K and ambient pressure compared with experiment.

To relax the surface of the liquid and ice layers, first, we separated the two layers by 10 Å to remove any interaction. Then, we performed an *NVT* calculation at 80 K for 100 ps. After equilibration, the two layers were brought back into contact, and the box's dimensions were 27.04 Å x 31.22 Å x 28.49 Å. The system had a mean density of 0.956 g/cm^3. The two-phase model has a total number of 768 H_2O molecules (Figure 4.21b). To determine the melting temperature of the classical mode, first, *NVT* simulations were performed at 260 K, 270 K, 277 K, 280 K, 290 K, 300 K, and 320 K. In these calculations, the system was coupled to a thermostat. Hence, the energy absorbed or released during melting or freezing was immediately removed [256]. This accelerated the equilibration of the system [257,258]. Furthermore, coupling the system to a thermostat has been shown to facilitate higher crystallization rates [258], and this is an advantage for the simulation of melting. Subsequent to the classical calculations, the NQEs were considered by PIMD in the *NVT* ensembles at the same temperatures as used in the classical simulations.

Results and discussions

Classical MD simulations on the melting of ice Ih

The onset of melting can be determined visually from the inspection of structural changes. As shown in Figure 4.21a, at 280 K, the water starts to freeze into the ice region. In comparison at 320 K, the ice structure melts completely (Figure 4.21c). Hence the melting temperature should be between 280 K and 320 K. Melting, or freezing can also be determined from the change in the total energy (*i.e.*, the sum of potential and kinetic energies). In Figure 4.22 the evolution of total energies for *NVT* simulations at 260 K, 270 K, 277 K, 280 K, 290 K, 300 K, and 320 K are given. A continuous decrease in the total energies (Figure 4.22a) is observed at 260 K, 270 K, 277 K, and 280 K. This indicates that water is transforming into the ice phase. This feature is also reflected from the structural changes. An ice-like structure at the interface is shown in the snapshot taken from the simulation at 280 K (Figure 4.21a). Furthermore, new peaks appear at the interface in the oxygen density profiles along the *z*-axis of the two-phase model at 270 K (Figure 4.23a) and 280 K (Figure 4.23b).

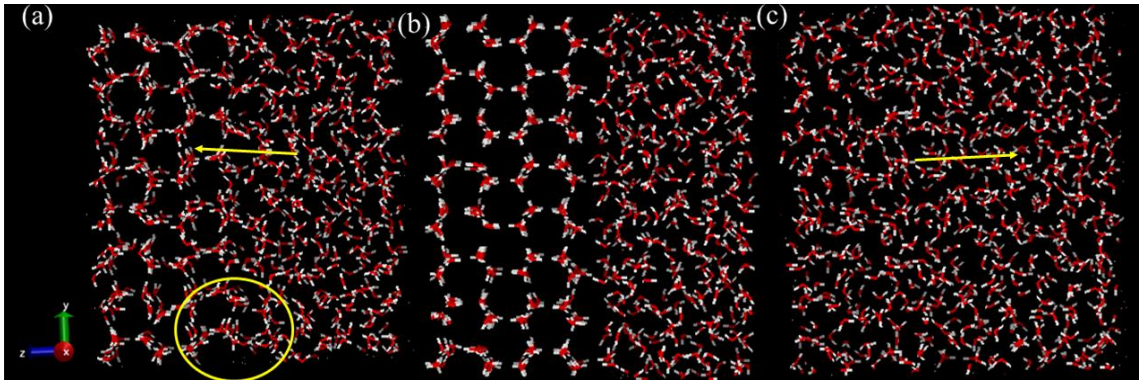

Figure 4.21 (a) Snapshots of the two-phase model from the classical MD calculation at 280 K (b) the initial configuration of the two-phase model, and (c) the two-phase model from the classical MD calculation at 320 K. The yellow circle indicates the forming of ice pattern, the arrows in a and c indicate water freezing into ice and ice melted, respectively.

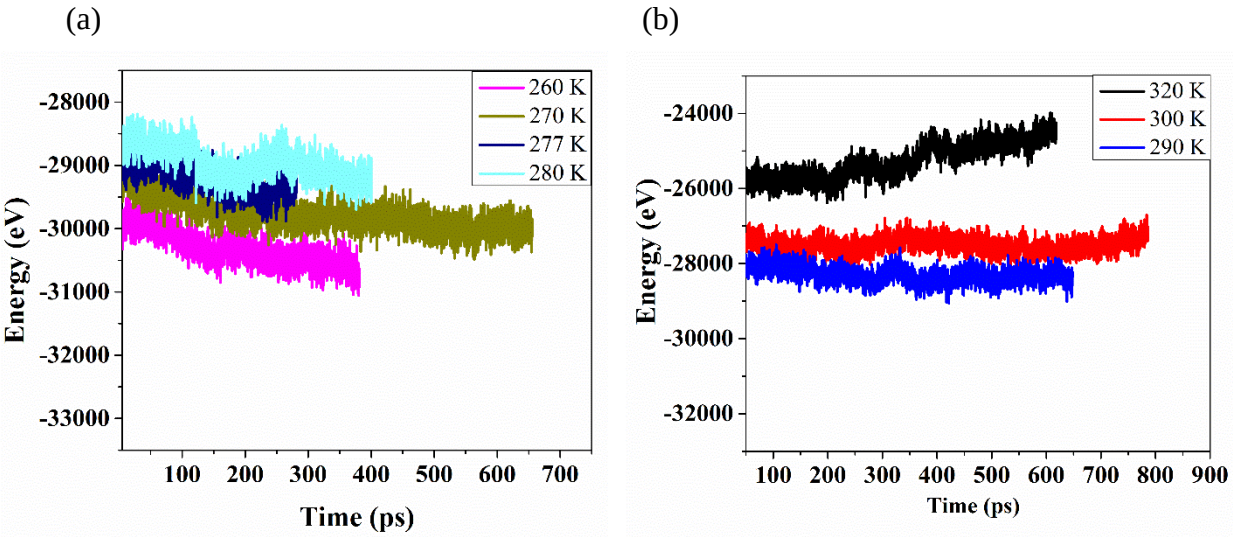

Figure 4.22 Evolution of the total energy in *NVT* classical MD simulations of the two-phase model at different temperatures: (a) from 260 K to 280 K and (b) from 290 K to 320 K.

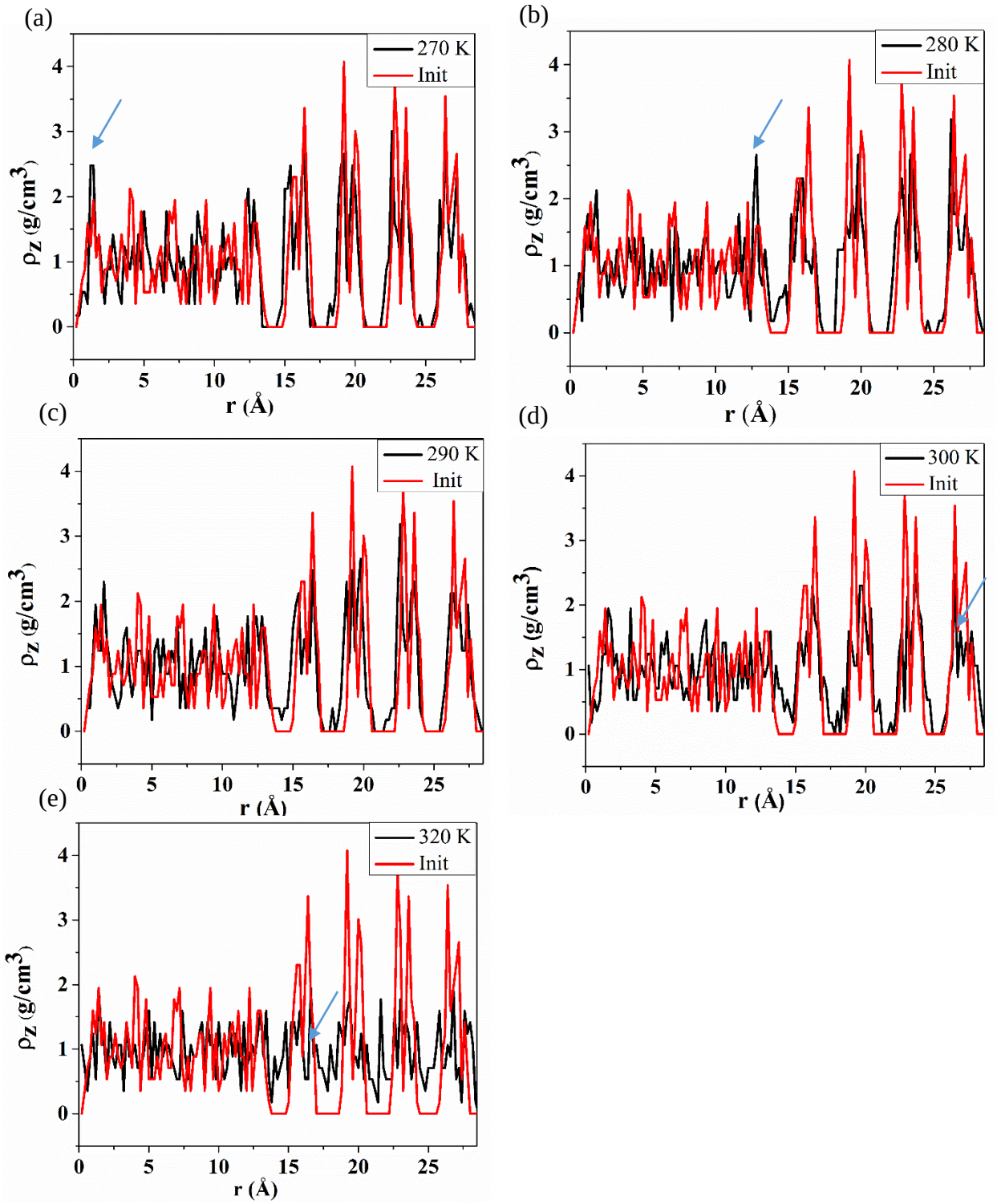

Figure 4.23 The oxygen density profiles along the *z*-axis for the two-phase model from *NVT* classical MD simulations at (a) 270 K, (b) 280K, (c) 290 K, (d) 300K, and (e) 320 K compared with that of the initial configuration. The arrows indicate the peaks, which change upon melting or freezing. In each figure, the *r* ~0.25–12.5 is the bulk water, ~12.5–15.6 is the interface, and ~15.6–27.5 is the bulk ice.

In Figure 4.22b, the total energy evolution in *NVT* classical MD simulations from 290 K to 320 K is shown. At 320 K, the total energy increases, indicating that ice has melted. The oxygen density profile (Figure 4.23e) near the interface also becomes continuous another sign of melting. The final structure of *NVT* calculation at 320 K (Figure 4.21c) is a fully melted structure. At 300 K, after 650 ps, there is a slow increase in the total energy. At 290 K, the total energy shows fluctuations around a mean value over 1000 ps. Furthermore, the oxygen density profile of ice layers at 300 K (Figure 4.23d) becomes broader, showing the onset of melting. In contrast, the oxygen density profile of the both ice and liquid layers at 290 K (Figure 4.23c) resembles that of the initial structures, indicating the chemical potentials of the ice and water are the same at 290 K leading to persistent coexistence within 650 ps, the length of the simulation. These observations lead us to conclude that the melting temperature of the TTM2.1-F model is around 290 K. It should be noted that even though *NVT* MD calculations were performed, the pressure over the temperature range studied here only fluctuates around 2.0 kbar (Figure 4.24), which is close to ambient conditions. Based on experimental data of the water solidus, we can estimate the error in melting temperature due to the uncertainty in pressure is ± 5 K [199,259].

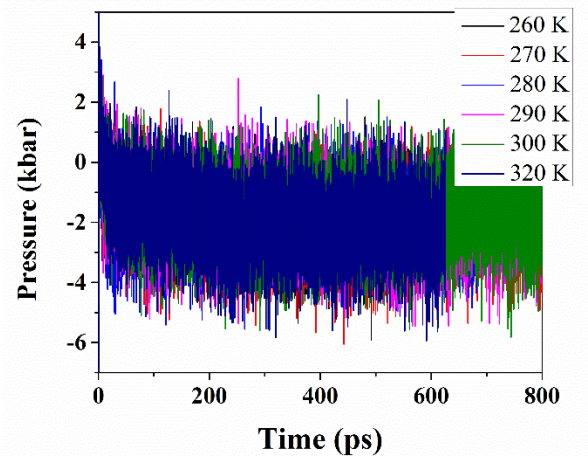

Figure 4.24 Evolution of pressure from *NVT* classical MD simulations at 260 K, 270 K, 280 K, 290 K, 300 K, and 320 K.

Nuclear quantum effects on the melting temperature of ice

To investigate NQEs on the melting of TTM2.1-F ice, we performed PIMD simulations at temperatures 260 K, 270 K, 280 K, 290 K, and 300 K in the *NVT* ensemble. Using similar analysis methods discussed above, we found that the melting temperature is between 270 K and 273 K. Subsequently, further PIMD calculations at these two temperatures were performed for a much longer time (1.2 ns). As shown in Figure 4.25a, the formation of the ice pattern at the interface is evident at 270 K while the melting of the ice layer into liquid is observed at 273 K (Figure 4.25c). Once again, the average pressure of the system in the PIMD simulations is small, around 1.0 kbar. Thus, we expected an error of ± 5 K in the predicted melting temperature [199,259]. We conclude the melting temperature of the quantum TTM2.1-F model including NQEs is between 270 K and 273K. Therefore, the NQEs lower the melting temperature by around 20 K. This temperature difference is quite reasonable, as it has been shown that a uniform temperature increase of ~30 K is expected when NQEs is neglected in both *ab initio*[247] and empirical potential MD simulations [218,245,248].

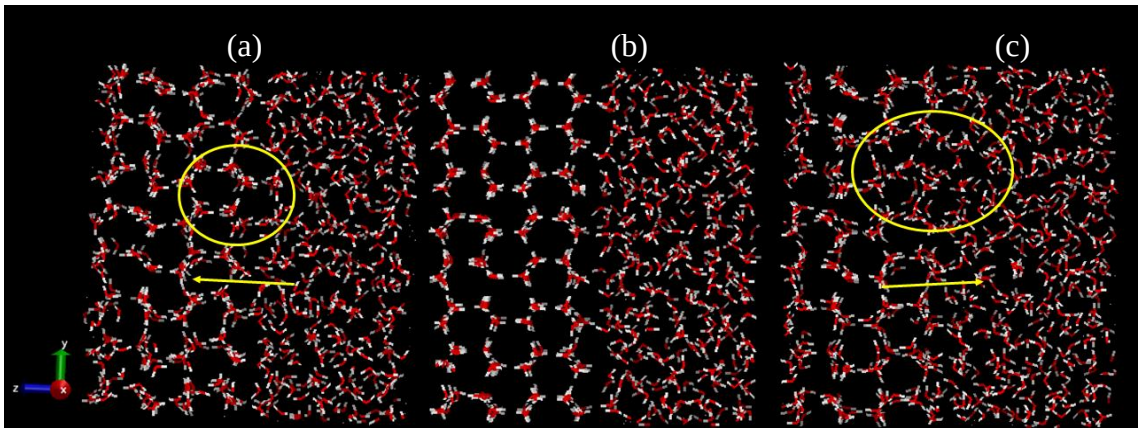

Figure 4.25 (a) Snapshots of the two-phase model from the *NVT* PIMD simulation at 270 K. (b) Initial configuration of the two-phase model. (c) Snapshot of the two-phase model from the *NVT* PIMD simulation at 273 K.

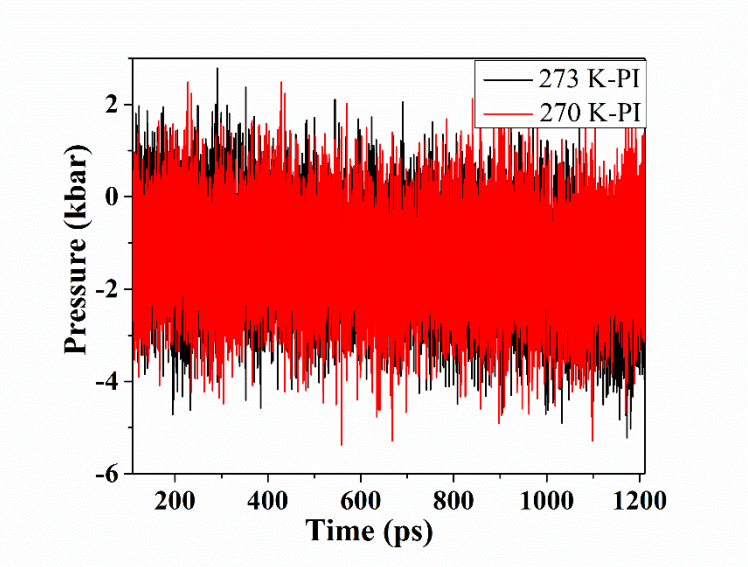

Figure 4.26 Evolution of the pressure for the two-phase model from *NVT* PIMD simulations at 270 K and 273 K.

It should be noted that PIMD simulation in an *NPT* ensemble has been previously performed to estimate the melting temperature of the TTM2.1-F water model [246]. Much lower melting temperatures of 238 K and 228 K were reported for the classical and PIMD models, respectively. These contrasting results can be explained by significant differences in the adopted approaches of the former and present work: (i) Thermodynamic ensembles: *NPT* ensemble was used in the earlier calculations, but *NVT* calculations were performed here; (ii) The size of the model system: a much smaller mode-192 H_2O model was used previously, compared to a 768 H_2O employed here; (iii) 32 beads were used in the earlier PIMD simulations and 16 beads were used in the present study; (iv) the NQEs of both O and H are included in the present work, and it is unclear whether NQEs of O were included. Furthermore, instead of using a hexagonal ice model, a cubic ice model was used in the earlier study. We believe that our structural model is more reasonable than the cubic model of the previous study. The structural model used here is substantially larger and has a larger interface. More water on the interface will help to dissipate

the heat associated with melting and freezing. On this point, the system-size effect is expected to be large due to the latent heat complications associated with the use of a thermostat. This was pointed out in a systematic study of water-ice [260] and in the nucleation of H_2S hydrate [261]. Since the equilibrium pressures of the current *NVT* calculations fluctuate by ±1 kbar, the effect of pressure on the computed melting temperature is expected to be small [199,259]. We believe that the *NPT* ensemble will have a minor effect. Moreover, in the *NPT* simulation on a small system, a large volume difference between ice and water (7-9%) for a wholesale change of phase will not be accurate or reasonable due to mechanical work of expansion/contraction being larger on a per-molecule basis. Furthermore, the aggressive sub-cooling necessary to produce wholesale freezing with a small system will lead to estimates of lower (colder) freezing points. In the *NVT* simulations for the prediction of melting temperature, errors in temperature are expected at temperatures above and below the melting point. As the ice is melted into water, the volume will decrease because water has a higher density. Hence, the pressure of the system will decrease. In the present *NVT* simulations, since the volume was kept fixed, this corresponds to the system being at too low pressure, and this will enhance the kinetics of melting and consequently the temperature is expected to be underestimated. Conversely, when liquid water is frozen into ice, the volume of the model will "increase", as well as the pressure, leading to an overestimated temperature. However, at the melting point, ice is in equilibrium with the liquid water at the interface, *i.e.* there are equal amounts of water changing into ice and vice versa. Since the current model was constructed with the correct densities for bulk ice and water, the error due to the volume change is expected to be small. Finally, it is not expected that the discrepancy in melting temperature can be attributed to the number of beads, as it was shown previously that 16 beads are already sufficiently accurate to mimic the NQEs of liquid water [20, 21]. We trust the present results are more reasonable.

Furthermore, we are not certain if the oxygen atoms were also treated as quantum particles in the previous study. We have computed the radius of gyration (rgy) to understand the significance of NQEs. The radius of gyration is the root mean square distance from each O/H atom of the 16 beads to their centroid. The results are summarized in Table 4.2. It is not surprising that hydrogen has a larger radius of gyration than oxygen for liquid water and an ice/water two-phase system. Perhaps surprisingly, the rgy of O is almost 1/4 that of H. Therefore, the NQEs of O is not negligible. To fully resolve the discrepancy between the previous *NPT* and present *NVT* calculations, it would be ideal to repeat the melting calculations using the TTM2.1-F potential in the *NPT* ensemble on a larger system and longer simulation. This will be pursued in the future.

Table 4.2 The calculated average radius of gyration (rgy) of O and two H atoms of H_2O from PIMD simulation for liquid water and ice/water two-phase model

	rgy-O(Å)	rgy-H1(Å)	rgy-H2(Å)
Liquid water	0.06	0.21	0.21
Ice/water	0.06	0.22	0.21

Melting dynamics and NQEs

To study the melting dynamics and the NQEs, we analyzed the trajectory and the hydrogen bond network. We present the analysis of the trajectory (Figure 4.27) from the *NVT* simulations using the classical model at 320 K, as the melting process was faster and a completely melted structure was obtained. Early in the simulation, H_2O molecules in the bulk ice and water layers did not diffuse into each other (Figure 4.27a). The main change occurred at the interface in which the H_2O in the liquid formed water cages with H_2O of the ice surface *via* hydrogen bonding (Figure 4.27b). Here, there are competitions between the formation and breaking of hydrogen bonds. Due to the higher kinetic energies at this temperature, H_2O in the liquid was found to diffuse into the

cages and this led to the melting of the ice layer (Figure 4.27c–d). Consequently, when more water was diffused into the ice (Figure 4.27 e–f), a completely melted structure was obtained.

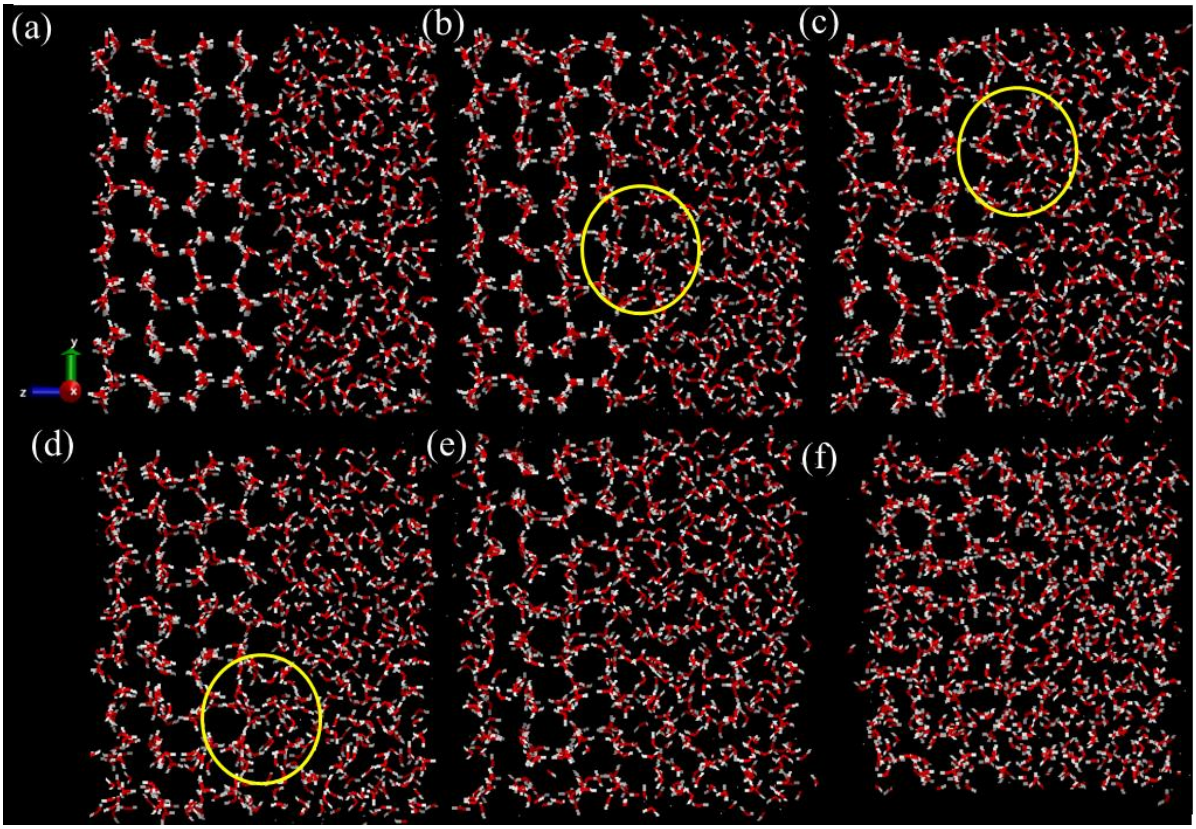

Figure 4.27 Structural evolution the ice/water two-phase model during the classical simulation at 320 K at different stages: (a) initial, (b) 50.0 ps, (c) 70.0 ps, (d) 100.0 ps, (e) 120.0 ps, (f) 400.0 ps. The yellow circle highlights the structural changes during the simulation as described in the text.

To study how the NQEs affect the melting process, we compared the hydrogen bond network in the classical simulation at 270 K with the PIMD simulation at 273 K. In the classical simulation, water is frozen into ice into the ice layer, while the PIMD simulation shows melting. Since the water molecules have similar classical kinetic thermal energies in both calculations, the difference comes from the NQEs. The hydrogen bond strength is related to the O-H band stretch and H-O-H bending as depicted in Scheme 4.1. To characterize the NQEs on the hydrogen bond, we analyzed the O-O (R_{OO}), O-H (R_{OH}) distance and the O-O-O angles (θ see Figure 4.29a), and

the hydrogen bond angle (β is HD-OD-OA in Figure 4.30) distribution functions. First, the distribution of H-O and O-O distances were computed. The results are plotted in Figure 4.28. The O-H distance is an indicator of the O-H stretching. The two peaks distribution in the H-O distance (Figure 4.28a) corresponds to the O-H covalent bond (short) and hydrogen bond interaction (longer). The covalent O-H bond length distribution become broader (0.9 ~ 1.2 Å) in the PIMD calculations. A flatter distribution of longer hydrogen bonding distances with a larger mean separation at 1.8 Å (Figure 4.28a) is found in the PIMD. These observations agree with an earlier study of NQEs on ice [262] in which the H atoms are also shown to be more delocalized, leading to weaker hydrogen bonds. In addition, the O-O distance (Figure 4.28b) also becomes longer when NQEs are included. The tetrahedrality of the system can be assessed from the O-O-O angle, θ distribution function, P(θ). The P(θ)s for the three distinct regions (ice bulk, water bulk, ice-water interface) of the system are illustrated in Figure 4.29b. The regions are defined based on the O-density distribution function along the z-axis. For the ice layer, there is little change in the P(θ) in the range from 60° to around 95°and from 120° to 160°. The P(θ) in the range from 95° to 160° becomes flatter, but the mean value is the same at 109°. This suggests that NQEs do not change the tetrahedrality of the ice layer. In both the interface and water layer, the P(θ) becomes flatter and broader. These changes are also observed from a simulation on bulk water [56,218]. Hence, the O-H stretching and H-O-H bending are more delocalized and weaken the hydrogen bonds. The broadening of the bend angle is also observed from H_D-O_D-O_A angle, β (see Figure 4.30) distribution function, the P(β) (Figure 4.30). Without NQEs, the β angles are distributed between 0°~40° with a mean value of 10°. When NQEs are considered, the distribution of β angles become broader and flatter. A larger bending (20° to 50°) angle again indicates a weakening of the hydrogen bonding network.

Scheme 4.1 Depiction of the motions of O-H in the water system

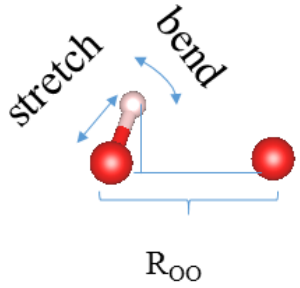

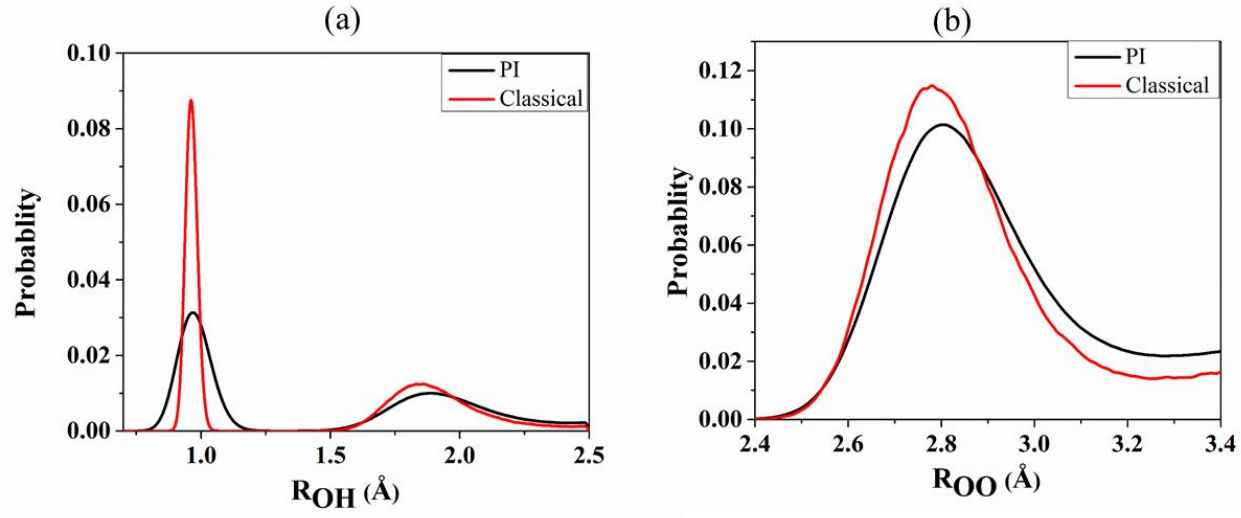

Figure 4.28 The (a) O-H and (b) O-O distance distribution functions in the classical (red) and PIMD (black) calculations.

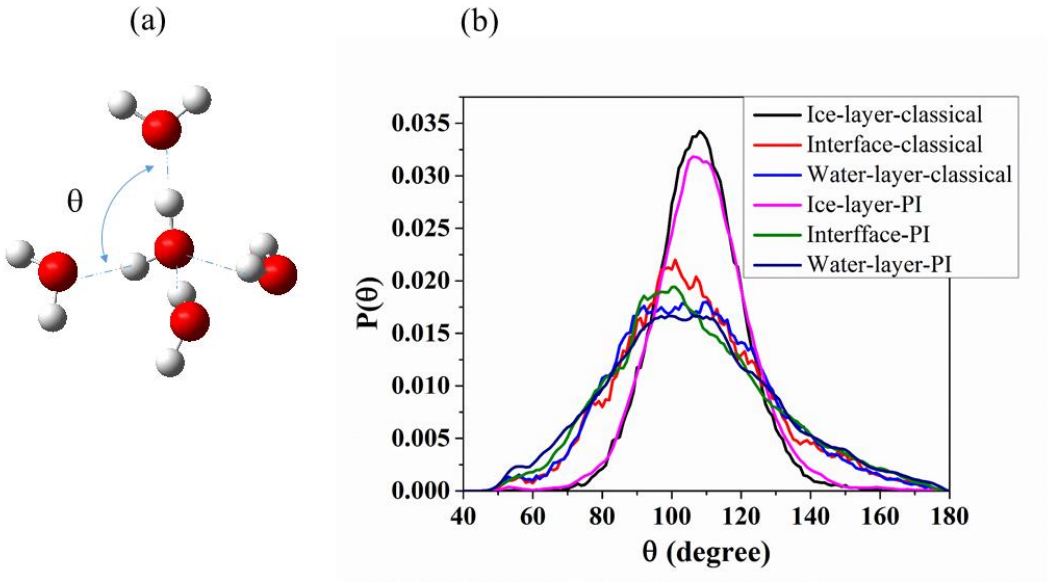

Figure 4.29 (a) Depiction of the O-O-O angle, θ, in the two-phase model and (b) the θ-angle distribution function, P(θ) in bulk water, ice, and ice-water interface from the PIMD calculation at 273 K and classical calculation at 270 K.

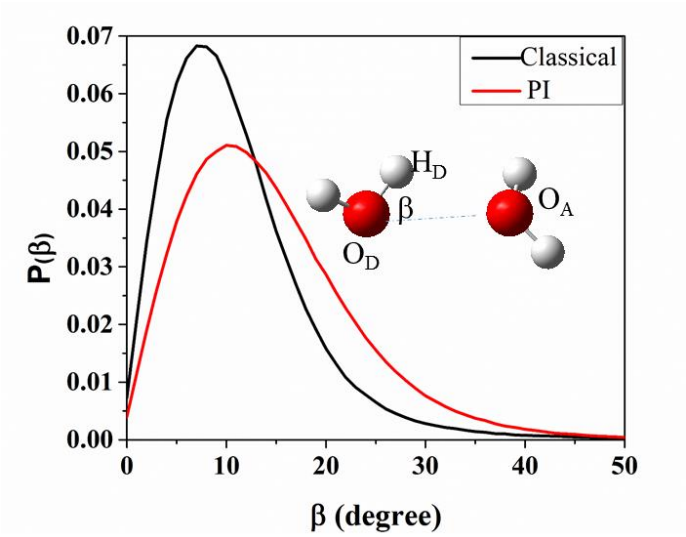

Figure 4.30 Depiction of the hydrogen bond angle, H_D-O_D-O_A, β, in the two-phase model and the normalized β-angle distribution function, P(β) from the PIMD calculation (red) at 273 K and classical (black) calculation at 270 K.

To evaluate the total effect of NQEs, we further analyzed the joint probability density P(δ, R_{OO}) as a function of the O-O distance and the proton transfer coordinate ($\delta = R_{HOD} - R_{HOA}$) of the hydrogen bond. A negative δ means that the H is bonded to one of the O atoms. If δ close to 0, it means that the H position is more symmetric and situated between the two O atoms. The strength of the hydrogen bond can be classified as strong, lower barrier, and weak based on the R_{OO} [263]. A hydrogen bond with a correlated R_{OO} less than 2.4 Å is defined as a strong bond. If R_{OO} is larger than 2.6 Å, then it is a weak bond. Those in the intermediate range are the low barrier bonds. The joint probability for the classical simulation is shown in Figure 4.31a. Most of the hydrogen bonds in the system have correlation R_{OO} in the range 2.6–3.0 Å with negative δ indicating the H atoms are bonded to one of the O atoms and can be regarded as weak hydrogen bonds. When NQEs are included, there is increased the probability of finding a hydrogen bond in a broader range of R_{OO} and δ. Compared to results from the classical simulation, the hydrogen bonds of the liquid structure obtained from PIMD are weaker. Therefore, the joint probability between R_{OO} and the negative δ suggest that NQEs, in general, weaken the hydrogen bonds and thus lower the melting temperature. It is noteworthy that some hydrogen bonds are found with a maximum δ close to -0.2 and a correlated R_{OO} at 2.4–2.6 Å, indicating that with NQEs, some of the H atoms started to share between the O atoms and become delocalized.

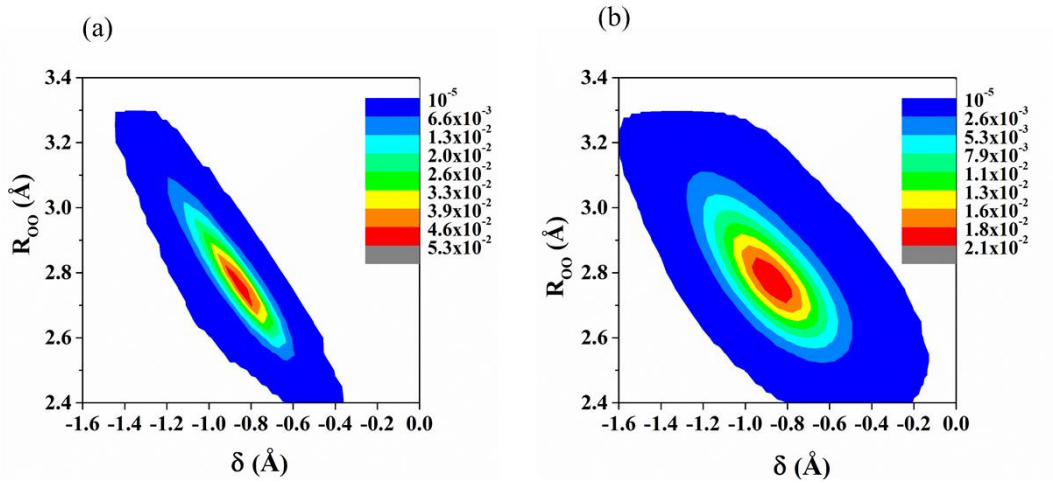

Figure 4.31 Joint probability P(δ, R_{OO}) to observe the hydrogen bond from the (a) classical MD calculation at 270 K and (b) PIMD calculation at 273 K.

Conclusions

In conclusion, using two-phase *NVT* simulations we found the ice/liquid melting temperature of the TTM2.1-F potential derived from *ab initio* calculation is around 290 K with classical MD calculations. The melting temperature decreased by 20 K and was close to 273 K when NQEs were included using PIMD. Detailed analyses of the radial distribution functions, angle distribution functions, and joint probability show that the temperature drop is due to the weakening of the hydrogen bonds.

CHAPTER 5

SUMMARY AND PERSPECTIVES

The objective of this thesis is to investigate pressure and temperature effects on structural phase transitions and chemical reactions in certain selected materials at an atomistic level using First-Principles electronic structure calculations and MD methods. In Chapter 1, the methodologies are introduced, including the theoretical background on DFT and various MD schemes used in the research. In Chapter 2, new strategies are proposed for the synthesis of high energetic materials at low pressure and low temperature based on extended X-CO_2 or X-CO with fully sp^3 hybridized C and O atoms at pressures within industrial capability. In Chapter 3, we report our investigations of possible chemical reactions of silica with CO_2 and H_2 under lower Earth mantle conditions. In Chapter 4, the structural evolution of ice Ih leading to PIA is presented. We also examined an *ab initio*-based TTM2.1-F water model in the prediction of the melting temperature of ice and structural properties of liquid water with and without NQEs.

5.1 Summary

Extended X-CO_2/X-CO is a highly energetic material but unfortunately can only be synthesized at high pressure and high temperature. If it could be quench-recovered, X-CO_2/X-CO could be used as an energetic material under ambient pressure. However, the synthesis conditions at 41 GPa and 1800 K were beyond the current industrial capability. To lower the formation pressure, we investigated several strategies by the addition of catalysts (H_2 and O_2) to solid CO_2 and CO and photochemical activation, as described in Chapter 2. AIMD calculations showed the addition of H_2 and O_2 successfully lowered the formation pressure and produced several forms of X-CO_2/X-CO. The products obtained from H_2-activated polymerization of CO_2 and CO were predicted to be recoverable under ambient pressure with estimated energy densities of 11.50 kJ/g

and 12.60 kJ/g for CO_2+H_2 and CO+H_2, respectively. The presence of H_2 or O_2 created large empty defect sites and promoted the migration of CO_2/CO molecules within the solids. Photo-excitation was found to be the most efficient method to lower the transition to 15 GPa and 1200 K for the polymerization of solid CO_2. It produced almost fully sp^3 hybridized C and O of X-CO_2 with an estimated energy density of 8.63 kJ/g.

Silica is the main component of the Earth's mantle and does not easily react with common gas under ambient conditions. Potential chemical reactions of silica with CO_2 and H_2 were investigated using AIMD and are described in Chapter 3. Both crystalline and amorphous SiO_2-CO_2 compounds were obtained from the reactions between CO_2 with SiO_2 zeolite and stishovite. The results are in agreement with recent experiments [4,5]. Using ReaxFF MD calculations, H_2 is shown to react with quartz under moderate pressure forming water confined by the SiO_2/SiH layers. The trapped molecules are highly ionized and have a structure similar to water obtained at 26.8 GPa and 700 K [191].

The structural evolution of ice Ih under compression was investigated by classical MD calculation using the TIP4P/ice water potential and AIMD with non-local *vdW*-corrected exchange-correlation functional. The amorphization is shown to be a multiple-step process. A new transition to a crystalline sheared ice Ih structure prior to amorphization was discovered. The results suggest that the formation of the high-density amorphous ice is governed by kinetics. The performance of an *ab initio*-based, flexible, polarizable Thole-type TTM2.1-F water model on the melting temperature of ice was examined with and without NQEs by using classical molecular dynamics and path integral molecular dynamics. Compared to the classical MD simulations, NQEs are shown to weaken the hydrogen bonds. Furthermore, a difference of 20 K is predicted in the

melting temperature of ice for the TTM2.1-F model with and without the consideration of the NQEs.

5.2 Perspectives

The results in Chapter 2 suggest that photo-excitation is the most efficient method to lower the formation pressure for X-CO_2. A rather low energy density of 8.63 kJ/g is estimated, as compared to those of the products from H_2-activated polymerization of CO_2 (12.60 kJ/g) /CO (11.50 kJ/g). The main reason is the existence of some small polycarbonate chains in the decomposition products. It is important to point out that *NVT* simulations were performed in the dissociated product calculation while *NPT* calculations were carried out for H_2-activated polymerization of CO_2/CO. Hence, it is desirable to perform *NPT* simulations, which allow the volume of the model to change during the simulation. This may lead to a more complete decomposition of the product into small fragments and therefore a higher energy density.

In Chapter 3, the results of the study of chemical reactions of silica with CO_2 and H_2 demonstrate that silica is chemically active under pressure and high temperature. CO and N_2 are two other common gas molecules and the breaking of triple C≡O and N≡N bonds is expected to be very sensitive to pressure [84,264]. Reactions of silica with CO or N_2 might be expected under Earth's mantle conditions. In particular, N_2 has lone electrons, which might help in forming new Si-N bonds through electron share/transfer between the atoms.

H_2O is a simple yet unique molecule. In the condensed phase, the environment affects the interactions between H_2O molecules through the hydrogen bonds, and this led to the complexity in the water phase diagram and many anomalous properties. H is the lightest element, and the behaviours of liquid water and ice are affected by NQEs. It is challenging to predict the properties

of water and ice from First-Principles calculations. The results in Chapter 4 suggest that in order to describe the properties of liquid water and ice correctly, three factors need to be considered: (i) a quantum instead of classical treatment of the H atoms; (ii) inclusion of *non-local vdw* effects; and (iii) for simulation of a large system, use of a proper *ab initio*-based water potential. The *ab initio*-based TTM2.1-F water model is reported to be able to produce several structural and thermodynamic properties of water clusters and liquid [58,246]. The results in Chapter 4 suggest an estimated melting temperature for ice of 290 K (273 K) using classical (quantum) TTM2.1-F. However, discrepancies with previously reported results [246] were found. We discussed the difference and explained possible reasons in Chapter 4. However, to fully resolve the discrepancy, we need to perform *NPT* classical and PIMD (with 32 beads) simulations and consider other effects, such as the system size and contact interfaces for ice/water beyond the [001] face of ice Ih described in Chapter 4. However, any different ice/water contact may present a different structural environment that might affect the melting temperature or melting rate. Therefore, it is important to investigate the melting of ice using a larger model and different bulk ice/water layers and interfaces. Water has many anomalous properties [227,265,266]. The compressibility of a normal liquid is expected to increase with temperature. In contrast, below 46 °C, the compressibility of liquid water increases when the temperature is lowered [265]. It has been suggested that the compressibility of water reduces the sea level by 40 m giving us 5% more land [52,267]. Therefore, it is important to know whether the *vdW* effects and NQEs with the TTM2.1-F can explain this anomalous compressibility.

APPENDIX—PARALLELIZATION OF THE CENTROID MOLECULAR DYNAMICS CODE

The original centroid molecular dynamics (CMD) code combined with the TTM2.1-F empirical water potential was written as a serial/sequential application, which was computationally slow for heavy and large systems. In my study, the code was parallelized to perform path integral centroid molecular (PIMD) using openMP (open multi-processing, available from Ref. [268]), which is one of the application programming interfaces (API). The parallelism in OpenMP, which works in conjunction with either C or FORTRAN languages, features with a multi-thread shared memory. OpenMP uses a collection of compiler directives that describe the parallelism in the source code. The compiler directives are statements that can be added in the FORTRAN or C code. Along with library functions and environmental variables, OpenMP generates a multi-thread version of the code [269]. In the thread model of parallel programming, a single process (program) can spawn multiple, concurrent "threads" (subprograms), as illustrated in Scheme A.1 (see below). One of the threads is a master thread, and the others are slave threads. The system divides a task among these threads which then run concurrently. By default, each thread is independent. The OpenMP directive forms two main kinds of constructs to control the parallelism by inserting compiler directives into the source code. First, it provides parallel directives, for example, "!$OMP PARALLEL" and "!$OMP END", to create multiple threads for the enclosed block of the code. Second, it provides directives to divide tasks among an existing set of parallel threads. For example, the "$OMP PARALLEL DO" can be used to divide the iterations of a loop among multiple threads.

Scheme A.1 Illustration of multithreading where the master thread forks off a number of threads which execute blocks of code in parallel, taken from Ref. [268]

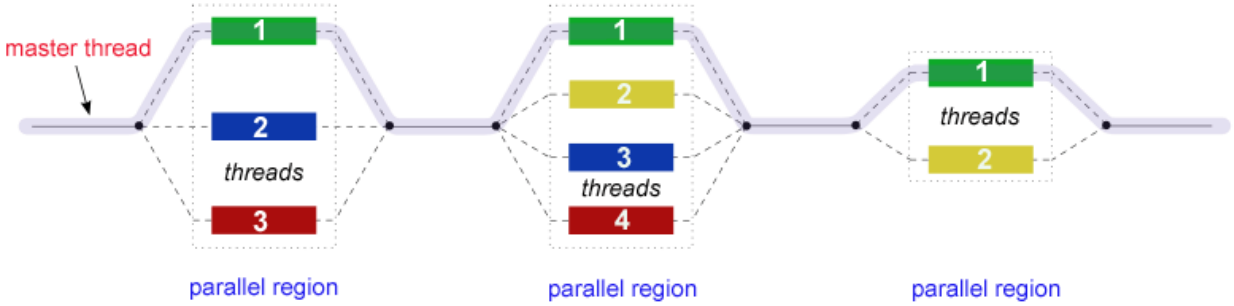

The following is an example of the paralleled part for the CMD code we have created. We parallelized only the loop over beads section.

```
########################################################################
!$OMP PARALLEL DO PRIVATE (n,ggg,ivec,rand,sigma)&
!$OMP
copyin(periodic,rigid_dudcvec,polar_model,pad3,natoms,pad4,ewald_eps,rcut,kcut,cvec,pi)&
!$OMPcopyin(rrr,force,dipole,phicc,phicd,efdc,efdd,efdd_real,efdd_rec,efext,mass,charge,alpha)
&
!$OMP copyin(diptensor,cgrad,alpha_ij,athird_cc,athird_cd,athird_dd,qrattle,constraint_index)&
$OMPcopyin(distance,inter_model,intra_model,intrahh_model,pad,dqdcvec,frac,rcom,drr,fracfo
rce,cveci)&
!$OMP copyin(atno,anchor,molec,moltype)&
!$OMP copyin(uqq,udq,udd,udspring,ulj,uintra,uext,utotal)
do m = 1,nbeads
      do n = 1,natoms


      end do
   end do
  !$OMP END PARALLEL DO
```

Figure A.1 displays the evolution of the total energy, *i.e.*, the sum of the potential energy and the kinetic energy of ice-Ih from PIMD calculation using 4 beads in the *NVT* ensemble at 80 K, from both sequential and parallel calculations with the same CPU time. The results suggest that the parallel code runs faster than the sequential code with identical results. Table A.1 compares the speeds of the parallel and serial/sequential version of the CMD code. Significant speed improvement was obtained when we parallelized the loop for the beads.

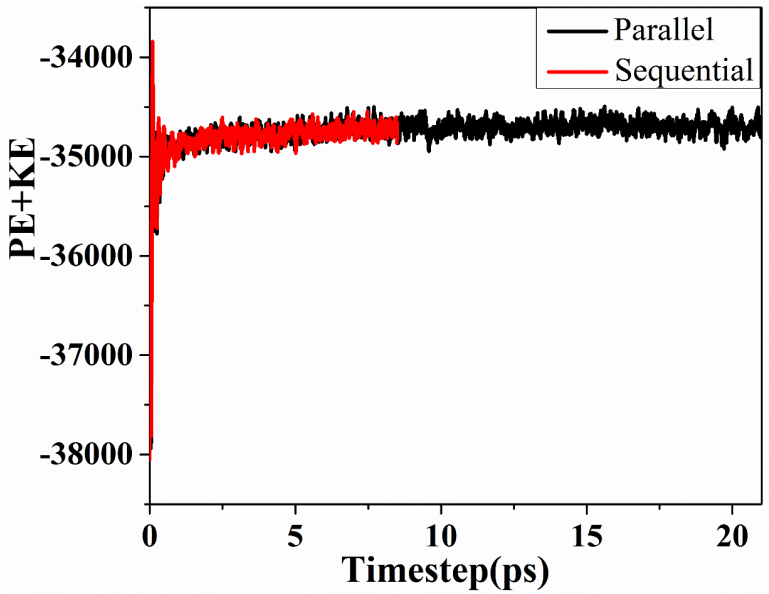

Figure A.1 Evolution of total (pe+ke) energy of ice Ih obtained from the parallel and serial code running the same time, from *NVT* PIMD simulations at 80 K and 0 GPa using 4 beads.

Table A.1 Comparison of the speeds of the parallel and sequential code for each *NVT* PIMD simulation for ice Ih at 80 K using the same number of beads and running within the same real time, 50 minutes

Number of beads used	Steps of Sequential code in 50 minutes	Steps of Parallel code in 50 minutes	Speeds up(parallel/sequential)
2	860	1514	1.74
4	396	1294	3.26
6	263	913	3.47
8	255	980	3.84
16	120	654	5.45

REFERENCES

[1] H. Y. Yu, D. F. Duan, F. B. Tian, H. Y. Liu, D. Li, X. L. Huang, Y. X. Liu, B. B. Liu, and T. Cui, *J. Phys. Chem. C* **119**, 25268 (2015).

[2] M. J. Lipp, W. J. Evans, B. J. Baer, and C.-S. Yoo, *Nat. Mater.* **4**, 211 (2005).

[3] O. Mishima, L. D. Calvert, and E. Whalley, *Nature* **310**, 393 (1984).

[4] M. Santoro, F. Gorelli, J. Haines, O. Cambon, C. Levelut, and G. Garbarino, *Proc. Natl. Acad. Sci. U S A* **108**, 7689 (2011).

[5] M. Santoro, F. A. Gorelli, R. Bini, A. Salamat, G. Garbarino, C. Levelut, O. Cambon, and J. Haines, *Nat. commun.* **5**, 3761 (2014).

[6] S. Block and G. Piermarini, *Phys. Today* **29**, 44 (1976).

[7] L. Dubrovinsky, N. Dubrovinskaia, V. B. Prakapenka, and A. M. Abakumov, *Nature commun.* **3**, 1163 (2012).

[8] A N.V.Ch, ra Shekar, P.Ch.Sahu, and K. G. Rajan, *J. Mater. Sci. Technol.* **19**, 518 (2003).

[9] M. Born and R. Oppenheimer, *Anna. Phys.* **389**, 457 (1927).

[10] L. H. Thomas, *Math. Proc. Cambridge Philos. Soc.* **23**, 542 (1927).

[11] E. Fermi, *Rend. Accad. Naz. Lincei* **6**, 602 (1927).

[12] E. Fermi, *Z. Phys.* **48**, 73 (1928).

[13] P. Hohenberg, *Phys. Rev. B* **136**, B864 (1964).

[14] W. Kohn and L. J. Sham, *Phys. Rev. B.* **140**, A1133 (1965).

[15] G. D. Mahan, *Many-Particle Physics* (Plenum Press, New York, 1990).

[16] D. M. Ceperley and B. J. Alder, *Phys. Rev. Lett.* **45**, 566 (1980).

[17] J. P. Perdew and W. Yue, *Phys. Rev. B* **33**, 8800 (1986).

[18] J. P. Perdew and W. Yue, *Phys. Rev. B* **40**, 3399 (1989).

[19] J. P. Perdew, K. Burke, and M. Ernzerhof, *Phys. Rev. Lett.* **77**, 3865 (1996).

[20] M. Santoro, F. A. Gorelli, R. Bini, J. Haines, O. Cambon, C. Levelut, J. A. Montoya, and S. Scandolo, *Proc. Natl. Acad. Sci. U S A* **109**, 5176 (2012).

[21] D. R. Hamann, *Phys. Rev. Lett.* **76**, 660 (1996).

[22] J. Klimeš and A. Michaelides, *J. Chem. Phys.* **137**, 120901 (2012).

[23] S. Grimme, *J. Comput. Chem.* **27**, 1787 (2006).

[24] M. Dion, H. Rydberg, E. Schroder, D. C. Langreth, and B. I. Lundqvist, *Phys. Rev. Lett.* **92**, 246401 (2004).

[25] S. Grimme, J. Antony, S. Ehrlich, and H. Krieg, *J. Chem. Phys.* **132**, 154104 (2010).

[26] A. Tkatchenko and M. Scheffler, *Phys. Rev. Lett.* **102**, 073005 (2009).

[27] S. Grimme, S. Ehrlich, and L. Goerigk, *J. Comput. Chem.* **32**, 1456 (2011).

[28] M. J. Gillan, D. Alfè, and A. Michaelides, *J. Chem. Phys.* **144**, 130901 (2016).

[29] A. Bloch, *Ann. Fac. Sci. Toulouse* **17**, 1 (1925).

[30] H. J. Monkhorst and J. D. Pack, *Phys. Rev. B* **13**, 5188 (1976).

[31] R. Orlando, R. Dovesi, C. Roetti, and V. R. Saunders, *J. Phys. Condens. Matter* **2**, 7769 (1990).

[32] M. S. José, A. Emilio, D. G. Julian, G. Alberto, J. Javier, O. Pablo, and S.-P. Daniel, *J. Phys. Condens. Matter* **14**, 2745 (2002).

[33] J. B. F. Æ. Frisch, in *Exploring Chemistry with Electronic Structure Methods* (Gaussian Inc, pp. 97.

[34] J. Yang, University of Saskatchewan, 2014.

[35] P. E. Blöchl, *Phys. Rev. B* **50**, 17953 (1994).
[36] C. J. Pickard, University of Cambridge, 1997.
[37] B. J. Alder and T. E. Wainwright, *J. Chem. Phys.* **27**, 1208 (1957).
[38] B. J. Alder and T. E. Wainwright, *J. Chem. Phys.* **31**, 459 (1959).
[39] M. P. Allen and D. J. Tildesley, *Computer simulation of liquids* (Clarendon Press, 1989).
[40] D. Frenkel and B. Smit, *Understanding Molecular Simulation* (Academic Press, Inc., 2001).
[41] R. P. Feynman, *Phys. Rev. B.* **56**, 340 (1939).
[42] H. Hellmann, *Einführung in die Quantenchemie von Hans Hellmann.* 1937), p.^pp. 285.
[43] M. Parrinello and A. Rahman, *J. Appl. Phys.* **52**, 7182 (1981).
[44] G. Kresse and J. Hafner, *Phys. Rev. B* **47**, 558 (1993).
[45] G. Kresse and J. Hafner, *Phys. Rev. B* **49**, 14251 (1994).
[46] G. Kresse and J. Furthmüller, *Computational Materials Science* **6**, 15 (1996).
[47] T. Bučko, J. Hafner, S. Lebègue, and J. G. Ángyán, *J. Phys. Chem. A* **114**, 11814 (2010).
[48] G. Lever, *Large-Scale Quantum-Mechanical Enzymology* (Springer Theses, 2015).
[49] V. Brazdova and D. R. Bowler, *Atomistic Computer Simulations: A Practical Guide* (wiely, 2013).
[50] J. E. Jones, *P. Roy. Soc. Lond. A: Mat.* **106**, 463 (1924).
[51] A. Y. Toukmaji and J. A. Board, *Comput. Phys. Commun.* **95**, 73 (1996).
[52] http://www1.lsbu.ac.uk/water/water_models.html (Accessed Aug 2001).
[53] J. L. F. Abascal, E. Sanz, R. García Fernández, and C. Vega, *J. Chem. Phys.* **122**, 234511 (2005).
[54] http://www.sklogwiki.org/SklogWiki/index.php/File:Four_site_water_model.png.
[55] W. Smith, C. W. Yong, and P. M. Rodger, *Mol. Simulation* **28**, 385 (2002).
[56] G. S. Fanourgakis and S. S. Xantheas, *J. Chem. Phys.* **128** (2008).
[57] C. J. Burnham, J. Li, S. S. Xantheas, and M. Leslie, *J. Chem. Phys.* **110**, 4566 (1999).
[58] G. S. Fanourgakis and S. S. Xantheas, *J. Phys. Chem. A* **110**, 4100 (2006).
[59] C. J. Burnham and S. S. Xantheas, *J. Chem. Phys.* **116**, 5115 (2002).
[60] H. Partridge and D. W. Schwenke, *J. Chem. Phys.* **106**, 4618 (1997).
[61] J. R. Reimers, R. O. Watts, and M. L. Klein, *Chem. Phys.* **64**, 95 (1982).
[62] J. R. Reimers and R. O. Watts, *Chem. Phys.* **85**, 83 (1984).
[63] M. A. Suhm and R. O. Watts, *Mol. Phys.* **73**, 463 (1991).
[64] T. P. Senftle *et al., npj Comput. Mater.* **2**, 15011 (2016).
[65] M. F. Russo and A. C. T. van Duin, *Nucl. Instrum. Met. B* **269**, 1549 (2011).
[66] A. K. Rappe and W. A. Goddard, *J. Phys. Chem.* **95**, 3358 (1991).
[67] J. C. Fogarty, H. M. Aktulga, A. Y. Grama, A. C. T. van Duin, and S. A. Pandit, *J. Chem. Phys.* **132**, 174704 (2010).
[68] R. Martonak, A. Laio, and M. Parrinello, *Phys. Rev. Lett.* **90**, 075503 (2003).
[69] R. Martonak, A. Laio, M. Bernasconi, C. Ceriani, P. Raiteri, F. Zipoli, and M. Parrinello, *Z Kristallogr* **220**, 489 (2005).
[70] R. P. Feynman and A. R. Hibbs, *Quantum Mechanics and Path Integrals* (McGraw-Hill Companies, 1965), pp. 365.
[71] A. Perez, M. E. Tuckerman, and M. H. Muser, *J. Chem. Phys.* **130**, 184105 (2009).
[72] I. R. Craig and D. E. Manolopoulos, *J. Chem. Phys.* **121**, 3368 (2004).
[73] S. Jang and G. A. Voth, *J. Chem. Phys.* **111**, 2371 (1999).

[74] E. A. Polyakov, A. P. Lyubartsev, and P. N. Vorontsov-Velyaminov, *J. Chem. Phys.* **133**, 194103 (2010).
[75] J. Cao and G. A. Voth, *J. Chem. Phys.* **100**, 5093 (1994).
[76] J. Cao and G. A. Voth, *J. Chem. Phys.* **100**, 5106 (1994).
[77] M. Pavese, S. Jang, and G. A. Voth, *Parallel Comput.* **26**, 1025 (2000).
[78] Privat communication
[79] N. Wiener, *Acta Math.* **55**, 117 (1930).
[80] http://www.compsoc.man.ac.uk/~lucky/Democritus/Theory/msd2.html.
[81] http://www.ccp5.ac.uk/DL_POLY/Democritus/Theory/rdf.html.
[82] G. Onida, L. Reining, and A. Rubio, *Rev. Modern Phys.* **74**, 601 (2002).
[83] L. Hedin, *Phys. Rev. B* **139**, A796 (1965).
[84] W. J. Evans, M. J. Lipp, C. S. Yoo, H. Cynn, J. L. Herberg, R. S. Maxwell, and M. F. Nicol, *Chem. Mater.* **18**, 2520 (2006).
[85] V. Iota, C. S. Yoo, and H. Cynn, *Science* **283**, 1510 (1999).
[86] M. Santoro, F. A. Gorelli, R. Bini, G. Ruocco, S. Scandolo, and W. A. Crichton, *Nature* **441**, 857 (2006).
[87] M. I. Eremets, A. G. Gavriliuk, I. A. Trojan, D. A. Dzivenko, and R. Boehler, *Nat. Mater.* **3**, 558 (2004).
[88] S. Serra, C. Cavazzoni, G. L. Chiarotti, S. Scandolo, and E. Tosatti, *Science* **284**, 788 (1999).
[89] J. Sun, D. Klug, C. Pickard, and R. Needs, *Phys. Rev. Lett.* **106**, 145502 (2011).
[90] A. A. Helmy, *J. Phys. Condens. Matter* **6**, 985 (1994).
[91] M. Santoro and F. A. Gorelli, *Chem. Soc. Rev.* **35**, 918 (2006).
[92] Y. Akahama, H. Kawamura, D. Häusermann, M. Hanfland, and O. Shimomura, *Phys. Rev. Lett.* **74**, 4690 (1995).
[93] V. M. Giordano and F. Datchi, *EPL (Europhysics Letters)* **77**, 46002 (2007).
[94] C. S. Yoo, *Phys. chem. chem. phys.* **15**, 7949 (2013).
[95] A. Simon and K. Peters, *Acta. Crystallogr. B* **36**, 2750 (1980).
[96] B. Olinger, *J. Chem. Phys.* **77**, 6255 (1982).
[97] C. Yoo, H. Cynn, F. Gygi, G. Galli, V. Iota, M. Nicol, S. Carlson, D. Häusermann, and C. Mailhiot, *Phys. Rev. Lett.* **83**, 5527 (1999).
[98] B. Kuchta and R. D. Etters, *Phys. Rev. B* **38**, 6265 (1988).
[99] H. Olijnyk, H. Däufer, H. J. Jodl, and H. D. Hochheimer, *J. Chem. Phys.* **88**, 4204 (1988).
[100] B. Kuchta and R. D. Etters, *Phys. Rev. B* **47**, 14691 (1993).
[101] F. Datchi, B. Mallick, A. Salamat, and S. Ninet, *Physical Rev. Lett.* **108**, 125701 (2012).
[102] C.-S. Yoo, M. Kim, W. Morgenroth, and P. Liermann, *Phys. Rev. B* **87**, 214103 (2013).
[103] A. Sengupta and C.-S. Yoo, *Phys. Rev. B* **82** (2010).
[104] C.-S. Yoo, M. Kim, W. Morgenroth, and P. Liermann, *Phys. Rev. B* **87**, 214103 (2013).
[105] B. O. Hall and H. M. James, *Phys. Rev. B* **13**, 3590 (1976).
[106] A. Serdyukov, M. Vetter, A. Brodyanski, and H. J. Jodl, *Low Temp. Phys.* **36**, 424 (2010).
[107] A. I. Katz, D. Schiferl, and R. L. Mills, *J. Phys. Chem.* **88**, 3176 (1984).
[108] R. L. Mills, B. Olinger, and D. T. Cromer, *J. Chem. Phys.* **84**, 2837 (1986).
[109] A. E. Carlsson and N. W. Ashcroft, *Phys. Rev. Lett.* **50**, 1305 (1983).
[110] M. Somayazulu, P. Dera, A. F. Goncharov, S. A. Gramsch, P. Liermann, W. Yang, Z. Liu, H.-k. Mao, and R. J. Hemley, *Nat. Chem.* **2**, 50 (2010).

[111] M. Santoro, F. Gorelli, J. Haines, O. Cambon, C. Levelut, and G. Garbarino, *Proc. Natl. Acad. Sci. U S A* **108**, 7689 (2011).
[112] B. Mallick, S. Ninet, G. Le Marchand, P. Munsch, and F. Datchi, *J. Chem. Phys.* **138** (2013).
[113] E. Bitzek, P. Koskinen, F. Gähler, M. Moseler, and P. Gumbsch, *Phy. Rev. Lett.* **97**, 170201 (2006).
[114] Stéphane Bernard, Guido L. Chiarotti, Sandro Scandolo, and E. Tosatti, *Phys. Rev. Lett.* **81**, 2092 (1998).
[115] W. F. Chan, G. Cooper, and C. E. Brion, *Chem. Phys.* **178**, 401 (1993).
[116] A. Spielfiedel, N. Feautrier, C. Cossart-Magos, G. Chambaud, P. Rosmus, H. J. Werner, and P. Botschwina, *J. Chem. Phys.* **97**, 8382 (1992).
[117] A. Spielfiedel, N. Feautrier, G. Chabaud, N. Feautrier, and H. J. Werner, *Chem. Phys. Lett.* **216**, 162 (1993).
[118] R. J. Buenker, M. Honigmann, H.-P. Liebermann, and M. Kimura, *J. Chem. Phys.* **113**, 1046 (2000).
[119] R. Martonak, D. Donadio, A. R. Oganov, and M. Parrinello, *Nat. Mater.* **5**, 623 (2006).
[120] K. Aoki, H. Yamawaki, M. Sakashita, Y. Gotoh, and K. Takemura, *Science* **263**, 356 (1994).
[121] G. Kresse and J. Furthmüller, *Phys. Rev. B* **54**, 11169 (1996).
[122] X. Yong, H. Liu, M. Wu, Y. Yao, J. S. Tse, R. Dias, and C. S. Yoo, *Proc. Natl. Acad. Sci. U S A* (2016).
[123] C. Kittel, *Introduction to Solid State Physics*, (Wiley, 7th edn.
[124] D. A. Evans, A. G. McGlynn, B. M. Towlson, M. Gunn, D. Jones, T. E. Jenkins, R. Winter, and N. R. J. Poolton, *J. Phys. Condens. Matter* **20**, 075233 (2008).
[125] E. J. Gamboa *et al.*, *INIS Repository* **47** (2016).
[126] M. Ceppatelli, R. Bini, M. Caporali, and M. Peruzzini, *Angew. Chem. Int. Edit.* **52**, 2313 (2013).
[127] R. Martoňák, in *Modern Methods of Crystal Structure Prediction* (Wiley-VCH Verlag GmbH & Co. KGaA, 2010), pp. 107.
[128] H. Liu, L. Zhu, W. Cui, and Y. Ma, *J. Chem. Phys.* **137**, 074501 (2012).
[129] R. Martoňák, *EP. J. B* **79**, 241 (2011).
[130] A. Togo and I. Tanaka, *Scripta Mat.* **108**, 1 (2015).
[131] Russell J. Hemley, Charles T. Prewitt, and Kathleen J. Kingma, in *Silica: Physical Behavior, Geochemistry, and Materials Applications*, edited by P. J. Heaney1994), pp. 41
[132] Y. Tsuchida and T. Yagi, *Nature* **347**, 267 (1990).
[133] K. J. Kingma, R. J. Hemley, H.-k. Mao, and D. R. Veblen, *Phys. Rev. Lett.* **70**, 3927 (1993).
[134] J. Haines, J. M. Léger, F. Gorelli, and M. Hanfland, *Phys. Rev. Lett.* **87**, 155503 (2001).
[135] Y. Kuwayama, K. Hirose, N. Sata, and Y. Ohishi, *Science* **309**, 923 (2005).
[136] N. Nishiyama *et al.*, *Sci. Rep.* **4**, 6558 (2014).
[137] S. B. Holmquist, *J. Am. Ceram. Soc.* **44**, 82 (1961).
[138] F. Liu, S. H. Garofalini, D. King-Smith, and D. Vanderbilt, *Phys. Rev. B* **49**, 12528 (1994).
[139] A. C. D. Chaklader and A. L. Roberts, *J. Am. Ceram. Soc.* **44**, 35 (1961).
[140] R. Zhou, B. Qu, J. Dai, and X. C. Zeng, *Phys. Rev. X* **4**, 011030 (2014).
[141] M. Marques, A. Morales-Garcia, J. M. Menendez, V. G. Baonza, and J. M. Recio, *Phys. Chem. Chem. Phys.* **17**, 25055 (2015).

[142] A. Morales-García, M. Marqués, J. M. Menéndez, D. Santamaría-Pérez, V. G. Baonza, and J. M. Recio, *Theor. Chem. Acc.* **132** (2012).
[143] J. M. Matter *et al.*, *Science* **352**, 1312 (2016).
[144] K. Z. House, D. P. Schrag, C. F. Harvey, and K. S. Lackner, *Proc. Natl. Acad. Sci. U S A* **103**, 12291 (2006).
[145] C. L. Washbourne, P. Renforth, and D. A. C. Manning, *Sci. Total Environ.* **431**, 166 (2012).
[146] K. AlKaabi, D. L. V. K. Prasad, P. Kroll, N. W. Ashcroft, and R. Hoffmann, *J. Am. Chem. Soc.* **136**, 3410 (2014).
[147]http://serc.carleton.edu/NAGTWorkshops/mineralogy/mineral_physics/phase_equilibria.html.
[148] J. Haines, O. Cambon, C. Levelut, M. Santoro, F. Gorelli, and G. Garbarino, *J. Am. Chem. Soc.* **132**, 8860 (2010).
[149] A. Holewinski, M. A. Sakwa-Novak, and C. W. Jones, *J. Am. Chem. Soc.* **137**, 11749 (2015).
[150] S. Elomari, A. Burton, R. C. Medrud, and R. Grosse-Kunstleve, *Microp. Mesop. Mater.* **118**, 325 (2009).
[151] R. Hill, *Proc. Phys. Soc. Section A* **65**, 349 (1952).
[152] H. Wang, Q. Li, Y. Li, Y. Xu, T. Cui, A. R. Oganov, and Y. Ma, *Phys. Rev. B* **79** (2009).
[153] T. H. DiStefano and D. E. Eastman, *Solid State Commun.* **9**, 2259 (1971).
[154] Z. A. Weinberg, G. W. Rubloff, and E. Bassous, *Phys. Rev. B* **19**, 3107 (1979).
[155] V. J. Nithianandam and S. E. Schnatterly, *Phys. Rev. B* **38**, 5547 (1988).
[156] Y. P. Li and W. Y. Ching, *Phys. Rev. B* **31**, 2172 (1985).
[157] Y.-n. Xu and W. Y. Ching, *Phys. Rev. B* **44**, 11048 (1991).
[158] L. E. Ramos, J. Furthmuller, and F. Bechstedt, *Phys. Rev. B* **69**, 085102 (2004).
[159] C. Sevik and C. Bulutay, *J. Mater. Sci.* **42**, 6555 (2007).
[160] http://www.crystran.co.uk/optical-materials/quartz-crystal-sio2.
[161] H. J. Osburn, *Powder Metallurgy* **12**, 471 (1969).
[162] J. Zhang, B. Li, W. Utsumi, and R. Liebermann, *Phys Chem Minerals* **23**, 1 (1996).
[163] W. Sinclair and A. E. Ringwood, *Nature* **272**, 714 (1978).
[164] E. C. T. Chao, J. J. Fahey, J. Littler, and D. J. Milton, *J. Geophys. Res.* **67**, 419 (1962).
[165] L. Huang, M. Durandurdu, and J. Kieffer, *Nat. Mater.* **5**, 977 (2006).
[166] G. Kresse and D. Joubert, *Phys. Rev. B* **59**, 1758 (1999).
[167] M. Wu, Y. Liang, J.-Z. Jiang, and J. S. Tse, *Sci. Rep.* **2**, 398 (2012).
[168] V. V. Brazhkin, *Phys. Rev. Lett.* **102**, 209603 (2009).
[169] V. Swamy, S. K. Saxena, B. Sundman, and J. Zhang, *J. Geophys. Res-Sol. Ea* **99**, 11787 (1994).
[170] P. J. Heaney, *Rev. Mineral. Geochem.* **29**, 1 (1994).
[171] L. Levien, C. T. Prewitt, and D. J. Weidner, *Am. Mineral.* **65**, 920 (1980).
[172] A. R. Lang, A. P. W. Makepeace, and M. Moore, *Mineral. Mag.* **58**, 87 (1994).
[173] M. Akaogi, H. Yusa, K. Shiraishi, and T. Suzuki, *J. Geophys. Res-Sol. Ea.* **100**, 22337 (1995).
[174] E. Bourova and P. Richet, *Geophys. Res. Lett.* **25**, 2333 (1998).
[175] K. de Boer, A. P. J. Jansen, R. A. van Santen, G. W. Watson, and S. C. Parker, *Phys. Rev. B* **54**, 826 (1996).
[176] N. H. de Leeuw, F. M. Higgins, and S. C. Parker, *J. Phys. Chem. B* **103**, 1270 (1999).

[177] A. A. Skelton, P. Fenter, J. D. Kubicki, D. J. Wesolowski, and P. T. Cummings, *J. Phys. Chem. C* **115**, 2076 (2011).
[178] D. W. Fuerstenau and Pradip, *Adv. in Coll. Inter. Sci.* **114–115**, 9 (2005).
[179] M. Sulpizi, M.-P. Gaigeot, and M. Sprik, *J. Chem. Theor. Comput.* **8**, 1037 (2012).
[180] G. W. Morey, R. O. Fournier, and J. J. Rowe, *Geochim. Cosmochim. Acta* **26,** 1029 (1962).
[181] G. M. Anderson and C. W. Burnham, *Am. J. Sci.* **263**, 494 (1965).
[182] A. Shinozaki, H. Kagi, N. Noguchi, H. Hirai, H. Ohfuji, T. Okada, S. Nakano, and T. Yagi, *Am. Mineral.* **99**, 1265 (2014).
[183] A. C. T. van Duin, S. Dasgupta, F. Lorant, and W. A. Goddard, *J. Phys. Chem. A* **105**, 9396 (2001).
[184] A. C. T. van Duin, A. Strachan, S. Stewman, Q. Zhang, X. Xu, and W. A. Goddard, *J. Phys. Chem. A* **107**, 3803 (2003).
[185] S. Plimpton, *J. Comput. Phys.* **117**, 1 (1995).
[186] K. Chenoweth, A. C. T. van Duin, and W. A. Goddard, *J. Phys. Chem. A* **112**, 1040 (2008).
[187] H. M. Aktulga, J. C. Fogarty, S. A. Pandit, and A. Y. Grama, *Parallel Comput.* **38**, 245 (2012).
[188] G. J. Martyna, M. L. Klein, and M. Tuckerman, *J. Chem. Phys.* **97**, 2635 (1992).
[189] S. Jang and G. A. Voth, *J. Chem. Phys.* **107**, 9514 (1997).
[190] A. C. Mitchell and W. J. Nellis, *J. Chem. Phys.* **76**, 6273 (1982).
[191] E. Schwegler, G. Galli, F. Gygi, and R. Q. Hood, *Phys. Rev. Lett.* **87**, 265501 (2001).
[192] A. Falenty, T. C. Hansen, and W. F. Kuhs, *Nature* **516**, 231 (2014).
[193] C. G. Salzmann, P. G. Radaelli, A. Hallbrucker, E. Mayer, and J. L. Finney, *Science* **311**, 1758 (2006).
[194] J. Schmidt, J. VandeVondele, I. F. W. Kuo, D. Sebastiani, J. I. Siepmann, J. Hutter, and C. J. Mundy, *J. Phys. Chem. B* **113**, 11959 (2009).
[195] J. Klimeš, D. R. Bowler, and A. Michaelides, *Phys. Rev. B* **83**, 195131 (2011).
[196] B. Santra, J. Klimes, D. Alfe, A. Tkatchenko, B. Slater, A. Michaelides, R. Car, and M. Scheffler, *Phys. Rev. Lett.* **107**, 185701 (2011).
[197] J. Wang, G. Roman-Perez, J. M. Soler, E. Artacho, and M. V. Fernandez-Serra, *J. Chem. Phys.* **134**, 024516 (2011).
[198] V. S. Dozhdikov, A. Y. Basharin, and P. R. Levashov, *J. Chem. Phys.* **137**, 054502 (2012).
[199] J. S. Tse and D. D. Klug, *Phys. chem. chem. phys.* **14**, 8255 (2012).
[200] M. Ceriotti, W. Fang, P. G. Kusalik, R. H. McKenzie, A. Michaelides, M. A. Morales, and T. E. Markland, *Chem. Rev.* **116**, 7529 (2016).
[201] O. Mishima, L. D. Calvert, and E. Whalley, *Nature* **314**, 76 (1985).
[202] T. Loerting, C. Salzmann, I. Kohl, E. Mayer, and A. Hallbrucker, *Phys. Chem. Chem. Phys.* **3**, 5355 (2001).
[203] R. J. Nelmes, J. S. Loveday, T. Strassle, C. L. Bull, M. Guthrie, G. Hamel, and S. Klotz, *Nat. Phys.* **2**, 414 (2006).
[204] R. J. Hemley, A. P. Jephcoat, H. K. Mao, L. C. Ming, and M. H. Manghnani, *Nature* **334**, 52 (1988).
[205] J. P. Itie, A. Polian, G. Calas, J. Petiau, A. Fontaine, and H. Tolentino, *Phys. Rev. Lett.* **63**, 398 (1989).
[206] M. B. Kruger and R. Jeanloz, *Science* **249**, 647 (1990).
[207] O. Mishima, *Nature* **384**, 546 (1996).
[208] O. Mishima and H. E. Stanley, *Nature* **396**, 329 (1998).

[209] J. S. Tse *et al.*, *Nature* **400**, 647 (1999).
[210] E. L. Gromitskaya, O. V. Stal'gorova, V. V. Brazhkin, and A. G. Lyapin, *Phys. Rev. B* **64** (2001).
[211] T. Strassle, A. M. Saitta, S. Klotz, and M. Braden, *Phys. Rev. Lett.* **93** (2004).
[212] T. Strassle, S. Klotz, G. Hamel, M. M. Koza, and H. Schober, *Phys. Rev. Lett.* **99** (2007).
[213] T. Strassle, A. Caviezel, B. Padmanabhan, V. Y. Pomjakushin, and S. Klotz, *Phys. Rev. B* **82** (2010).
[214] R. J. Hemley, L. C. Chen, and H. K. Mao, *Nature* **338**, 638 (1989).
[215] J. F. Nye, *Physical Properties of Crystals* (Oxford, 1957).
[216] J. S. Tse, *J. Chem. Phys.* **96**, 5482 (1992).
[217] K. Amann-Winkel, M. C. Bellissent-Funel, L. E. Bove, T. Loerting, A. Nilsson, A. Paciaroni, D. Schlesinger, and L. Skinner, *Chem. Rev.* **116**, 7570 (2016).
[218] R. A. DiStasio, B. Santra, Z. Li, X. Wu, and R. Car, *J. Chem. Phys.* **141**, 084502 (2014).
[219] K. J. Kingma, R. J. Hemley, H. K. Mao, and D. R. Veblen, *Phys. Rev. Lett.* **70**, 3927 (1993).
[220] J. Haines, J. M. Leger, F. Gorelli, and M. Hanfland, *Phys. Rev. Lett.* **87** (2001).
[221] J. A. Hayward and J. R. Reimers, *J. Chem. Phys.* **106**, 1518 (1997).
[222] J. S. Tse *et al.*, *Nature* **400**, 647 (1999).
[223] K. Hoshino, T. Yoshikawa, and S. Munejiri, *Computer Phys. Commun.* **182**, 49 (2011).
[224] U. Essmann, L. Perera, M. L. Berkowitz, T. Darden, H. Lee, and L. G. Pedersen, *J. Chem. Phys.* **103**, 8577 (1995).
[225] J. S. Tse, D. D. Klug, M. Guthrie, C. A. Tulk, C. J. Benmore, and J. Urquidi, *Phys. Rev. B* **71** (2005).
[226] E. G. Noya, C. Vega, L. M. Sese, and R. Ramirez, *J. Chem. Phys.* **131**, 124518 (2009).
[227] H. L. Pi, J. L. Aragones, C. Vega, E. G. Noya, J. L. F. Abascal, M. A. Gonzalez, and C. McBride, *Mol. Phys.* **107**, 365 (2009).
[228] T. Morawietz, A. Singraber, C. Dellago, and J. Behler, *Proc. Natl. Acad. Sci. U S A* **113**, 8368 (2016).
[229] I. C. Lin, A. P. Seitsonen, M. D. Coutinho-Neto, I. Tavernelli, and U. Rothlisberger, *J. Phys. Chem. B* **113**, 1127 (2009).
[230] B. Santra, J. Klimes, A. Tkatchenko, D. Alfe, B. Slater, A. Michaelides, R. Car, and M. Scheffler, *J. Chem. Phys.* **139**, 154702 (2013).
[231] M. Dion, H. Rydberg, E. Schröder, D. C. Langreth, and B. I. Lundqvist, *Phys. Rev. Lett.* **92**, 246401 (2004).
[232] K. Rottger, A. Endriss, J. Ihringer, S. Doyle, and W. F. Kuhs, *Acta Crystall. B* **50**, 644 (1994).
[233] K. Krynicki, C. D. Green, and D. W. Sawyer, *Faraday Discuss. Chem. Soc.* **66**, 199 (1978).
[234] E. H. Hardy, A. Zygar, M. D. Zeidler, M. Holz, and F. D. Sacher, *J. Chem. Phys.* **114**, 3174 (2001).
[235] R. Mills, *J. Phys. Chem.* **77**, 685 (1973).
[236] A. K. Soper, *ISRN Phys. Chem.* **2013**, 67, 279463 (2013).
[237] F. Corsetti, E. Artacho, J. M. Soler, S. S. Alexandre, and M.-V. Fernández-Serra, *J. Chem. Phys.* **139**, 194502 (2013).
[238] M. Ceriotti, J. More, and D. E. Manolopoulos, *Computer Phys. Commun.* **185**, 1019 (2014).
[239] T. Spura, C. John, S. Habershon, and T. D. Kühne, *Mol. Phys.* **113**, 808 (2014).
[240] C. Vega, C. McBride, E. Sanz, and J. L. F. Abascal, *Phy. Chem. Chem. Phys.* **7**, 1450 (2005).

[241] P. Mark and L. Nilsson, *J. Phys. Chem. A* (2001).
[242] G. C. Lie and E. Clementi, *Phys. Rev. A* **33**, 2679 (1986).
[243] P. Jedlovszky, *J. Chem. Phys.* **111**, 5975 (1999).
[244] R. Kumar and T. Keyes, *Theor. Chem. Acc.* **131**, 1 (2012).
[245] F. Paesani, S. Iuchi, and G. A. Voth, *J. Chem. Phys.* **127**, 074506 (2007).
[246] F. Paesani and G. A. Voth, *J. Phys. Chem. C* **112**, 324 (2008).
[247] J. A. Morrone and R. Car, *Phys. Rev. Lett.* **101**, 017801 (2008).
[248] G. S. Fanourgakis, G. K. Schenter, and S. S. Xantheas, *J. Chem. Phys.* **125**, 141102 (2006).
[249] C. Vega, J. L. F. Abascal, E. Sanz, L. G. MacDowell, and C. McBride, *J. Phys. Condens. Matter* **17**, S3283 (2005).
[250] J. Wang, S. Yoo, J. Bai, J. R. Morris, and X. C. Zeng, *J. Chem. Phys.* **123**, 36101 (2005).
[251] R. García Fernández, J. L. F. Abascal, and C. Vega, *J. Chem. Phys.* **124**, 144506 (2006).
[252] P. Wernet *et al.*, *Science* **304**, 995 (2004).
[253] J. Lobaugh and G. A. Voth, *J. Chem. Phys.* **106**, 2400 (1997).
[254] L. Hernández de la Peña and P. G. Kusalik, *J. Chem. Phys.* **121**, 5992 (2004).
[255] X.-Z. Li, M. I. J. Probert, A. Alavi, and A. Michaelides, *Phys. Rev. Lett.* **104**, 066102 (2010).
[256] C. Vega, E. Sanz, J. L. F. Abascal, and E. G. Noya, *J. Phys. Condes. Matter* **20**, 153101 (2008).
[257] E. G. Noya, C. Vega, and E. de Miguel, *J. Chem. Phys.* **128**, 154507 (2008).
[258] H. Nada, J. P. van der Eerden, and Y. Furukawa, *J. Crystal. Growth* **266**, 297 (2004).
[259] E. Whalley, D. D. Klug, and Y. P. Handa, *Nature* **342**, 782 (1989).
[260] N. J. English, *J. Chem. Phys.* **141**, 234501 (2014).
[261] S. Liang and P. G. Kusalik, *J. Phys. Chem. B* **114**, 9563 (2010).
[262] P. A. Moreira and M. de Koning, *Phys. chem. chem. physics* **17**, 24716 (2015).
[263] R. H. McKenzie, C. Bekker, B. Athokpam, and S. G. Ramesh, *J. Chem. Phys.* **140**, 174508 (2014).
[264] X. Wang, J. Li, N. Xu, H. Zhu, Z. Hu, and L. Chen, *Sci. Rep.* **5**, 16677 (2015).
[265] J. Teixeira, *J. Phys. IV* **03**, C1 (1993).
[266] A. Nilsson and L. G. Pettersson, *Nature commun.* **6**, 8998 (2015).
[267] F. Franks, *in Water A comprehensive treatise* **1**, 225 (1972).
[268] http://www.openmp.org.
[269] R. Chandra, L. Menon, D. Kohr, D. Maydan, J. McDonald, and R. Menon, *Parallel Programming in OpenMP* (Morgan Kaufmann Publishers (Elsevier Science and Technology Books, Inc.), 2000).